NOVEL NANOCRYSTAL-INTEGRATED LEDs UTILIZING RADIATIVE AND NONRADIATIVE ENERGY TRANSFER FOR HIGH-QUALITY EFFICIENT LIGHT GENERATION

A THESIS
SUBMITTED TO THE DEPARTMENT OF ELECTRICAL AND ELECTRONICS ENGINEERING
AND THE INSTITUTE OF ENGINEERING AND SCIENCES
OF BILKENT UNIVERSITY
IN PARTIAL FULLFILMENT OF THE REQUIREMENTS
FOR THE DEGREE OF
DOCTOR OF PHILOSOPHY

By
Sedat Nizamoğlu
March 2011

I certify that I have read this thesis and that in my opinion it is fully adequate, in scope and in quality, as a thesis for the degree of Doctor of Philosophy.

_____

Assoc. Prof. Dr. Hilmi Volkan Demir (Supervisor)

I certify that I have read this thesis and that in my opinion it is fully adequate, in scope and in quality, as a thesis for the degree of Doctor of Philosophy.

_____

Prof. Dr. Ayhan Altıntaş

I certify that I have read this thesis and that in my opinion it is fully adequate, in scope and in quality, as a thesis for the degree of Doctor of Philosophy.

_____

Assist. Prof. Dr. Ali Kemal Okyay

I certify that I have read this thesis and that in my opinion it is fully adequate, in scope and in quality, as a thesis for the degree of Doctor of Philosophy.

_____

Assoc. Prof. Dr. Oğuz Gülseren

I certify that I have read this thesis and that in my opinion it is fully adequate, in scope and in quality, as a thesis for the degree of Doctor of Philosophy.

_____

Prof. Dr. İskender Yılgör

Approved for the Institute of Engineering and Sciences:

_____

Prof. Dr. Levent Onural

Director of Institute of Engineering and Science

ABSTRACT

NOVEL NANOCRYSTAL-INTEGRATED LEDs UTILIZING RADIATIVE AND NONRADIATIVE ENERGY TRANSFER FOR HIGH-QUALITY EFFICIENT LIGHT GENERATION

Sedat Nizamoğlu
Ph.D. in Electrical and Electronics Engineering
Supervisor: Assoc. Prof. Dr. Hilmi Volkan Demir

March 2011

To combat environmental issues escalating with the increasing carbon footprint, combined with the energy problem of limited resources, innovating fundamentally new ways of raising energy efficiency and level of energy utilization is essential to our energy future. Today, to this end, achieving lighting efficiency is an important key because artificial lighting consumes about 19% of total energy generation around the globe. There is a large room for improving lighting efficacy for potential carbon emission cut. However, the scientific challenge is to reach simultaneously high-quality photometric performance. To address these problems, we proposed, developed and demonstrated a new class of color-conversion light emitting diodes (LEDs) integrated with nanophosphors of colloidal quantum dots. The favorable properties of these semiconductor nanocrystal quantum dots, including size-tuneable and narrow-band emission with high photostability, have provided us with the ability of achieving high-quality, efficient lighting. *Via* using custom-design combinations of such nanocrystal emitters, we have shown that targeted white luminescence spectra can be generated with desired high photometric performance, which is important for obtaining application-specific white LEDs, *e.g.*, for indoors lighting, street

lighting, and LED-TV backlighting. Furthermore, dipole-dipole coupling capability of these semiconductor nanocrystals has allowed us to realize novel device designs based on Förster-type nonradiative energy transfer. By mastering exciton-exciton interactions in color-conversion LEDs, we have demonstrated enhanced color conversion *via* recycling of trapped excitons and white light generation based on nonradiative pumping of nanocrystal quantum dots for color conversion.

This research work has led to successful demonstrators of semiconductor nanocrystal quantum dots that photometrically outperform conventional rare-earth phosphor powders in terms of color rendering, luminous efficacy of optical radiation, color temperature and scotopic/photopic ratio for the first time.

Keywords: Light emitting diodes, solid state lighting, nanocrystals, quantum dots, color conversion, nonradiative energy transfer, exciton-exciton interactions.

ÖZET

YÜKSEK KALİTELİ, VERİMLİ IŞIK ÜRETİLMESİ İÇİN IŞINIMSAL OLAN VE OLMAYAN ENERJİ TRANSFERİ KULLANAN, NANOKRİSTAL İLE TÜMLEŞTİRİLMİŞ ÖZGÜN LED'*LER*

Sedat Nizamoğlu
Elektrik ve Elektronik Mühendisliği Doktora
Tez Yöneticisi: Doç. Dr. Hilmi Volkan Demir
Mart 2011

Artan karbon salınımı ile oluşan çevre sorunları ile birlikte sınırlı kaynaklardan dolayı ortaya çıkan enerji sorunu ile mücadele etmek için, enerji verimLiliğini ve enerji faydalanma düzeyini artıran yeni yolların bulunması enerji geleceğimiz açısından gereklidir. Günümüzde bu amaçla aydınlatma verimLiliği elde etmek özellikle önemLidir; çünkü bugün yapay aydınlatma dünyadaki toplam enerji üretiminin yaklaşık %19'unu tüketmektedir. Potansiyel karbon salınımını azaltmak amacı ile aydınlatma etkinliğini iyileştirmek için geniş yer bulunmaktadır. Ancak, bilimsel zorluk, aynı zamanda yüksek kaliteli fotometrik performansa ulaşmaktır. Bu problemLerin çözümü için, yarıiletken kuvantum noktacıklarından oluşan nanofosfor ile tümLeştirilmiş yeni nesil ışık yayan diyotlar – LED'ler önerdik, geliştirdik ve gösterdik. Yüksek ışık kararlılığı ile, boyutla ayarlanabilir ve dar-bantlı ışımaya sahip bu yarıiletken nanokristallerin olumLu özellikleri, yüksek kaliteli ve verimLi aydınlatma yeteneğine ulaşmamızı sağlamıştır. Nanokristal ışıyıcıların özel tasarım kombinasyonlarını kullanarak, yüksek fotometrik performansa sahip, uygulamaya özgü beyaz LED'leri (örneğin, iç aydınlatma, sokak aydınlatması ve LED –TV için) elde etmek üzere hedeflenen beyaz ışıma tayfını oluşturulabildiğini gösterdik.

Ayrıca, bu yarıiletken nanokristallerin dipol-dipol etkileşim yetisi, Förster-tipi ışınımsal olmayan enerji transferine dayalı özgün aygıt tasarımLarı gerçekleştirmemize olanak verdi. Renk dönüşümLü LED'lerdeki eksiton-eksiton etkileşimLerini kontrol altına alarak, tuzağa düşmüş eksitonlari geri çevrimi ile artırılmış renk dönüşümünü ve nanokristal kuvantum noktacıklarını ışınımsal olmayan pompalanmasıyla beyaz ışık üretimini gösterdik.

Bu tez araştırma çalışmaları, dünyada ilk defa yarıiletken nanokristal kuvantum noktacıklarının renk dönüşümü, ışıksal verim, renk sıcaklığı ve skotopik/fotopik oranı cinsinden fotometrik performans olarak bilinen eser fosfor tozlarını geçtiğini başarılı şekilde göstermiştir.

Anahtar Sözcükler: Işık yayan diyotlar, katı hal aydınlatma, nanokristal, kuvantum noktacıkları, renk dönüşümü, ışınımsal olmayan enerji transferi, eksiton-eksiton etkileşimleri

Acknowledgements

During my PhD study at Bilkent I lived a beautiful story that is both technically and emotionally satisfactory. I had the opportunity to interact with many scientists around the world and I worked with many talented and smart people with a lot of fun. Advisors, teammates, colleagues, friends and family members had their unique and highly valuable contribution for this thesis in your hand. Therefore, I owe many thanks…

First, I would like to thank Prof. Hilmi Volkan Demir for being my advisor and mentor. It is for me a great honor and privilege being Prof. Hilmi Volkan Demir's graduate student. His kind, positive, friendly and warm personality and management embraced us, and his invaluable guidance, motivation, encouragement, confidence, understanding, and endless support made him more than a supervisor for me. He spreads his joy and positive energy to people around him. I learnt a lot from him and I hope I can apply them myself.

I owe my special thanks to thank Prof. İskender Yılgör for his endless support during my both undergraduate and graduate studies. When I had a problem, he always been there to advice and support. I felt very privileged because he came for my PhD thesis defence for a daily visit from Koç to Bilkent as a member of my thesis committee. I give my thanks to our department chair Prof. Ayhan Altıntaş for his support during my both undergraduate and graduate studies at Bilkent University. I would like to thank Prof. Ali Kemal Okyay and Prof. Ceyhun Bulutay for their valuable discussions during our PhD monitoring committee meetings. I give my thanks to Prof. Oğuz Gülseren for his useful comments and suggestions as a member of my thesis committee.

I would like to thank Prof. Mehmet Şahin for his warm and kind friendship and for his contribution to improve our quantum mechanical simulations. He felt me very honored and privileged because he came from Konya to Ankara to support

me for my PhD thesis defense. I would like to thank Dr. Koray Aydın and Dr. Aşkın Kocabaş for their support, advices and friendship.

I would like to thank Prof. Efrat Lifshitz, her husband Prof. Ray Lifshitz and her co-workers for their great hospitality and support during our research visit in fall 2010 semester at Technion. I give my thanks to Prof. Alexander Eychmüller, Dr. Nikolai Gaponik, Dr. Stephen Hickey and Dr. Sameer Sapra for nanocrystal synthesis at Technical University of Dresden. I would like to thank Prof. In-Hwan Lee and Dr. Jong-Hyeob Baek from Korea for the growth of our epitaxial designs. I would like to also give my thanks to Prof. Xiaowei Sun for his support.

I want to thank to my lovely father Alican and my lovely mother Aynur, who raised me with great love, mercy and patience and who supported me in every moment of my life. I would like to thank my lovely sister İrem. She is both my sister and my sweaty child. She always gives her love to me and makes my life happy. I owe my thanks to all of my family members.

I would like to thank to my wife İrem. Her love is like a sun in my life. She always trusted me and supported me with great patience. I would like to thank my brother-in-law Emre Ünal, who is very special for me. He is always friendly, positive, considerate and kind. I also would like to thank my wife İrem`s parents Belğin and Fevzi. I owe my thanks to all of my wife`s family members.

During my graduate studies I had excellent office mates like my family members. I want to thank to my dear friend Evren Mutlugün, who was also my home mate at Bilkent. We have a great friendship and we had very nice days in research, courses and friendship. I give my thanks to Tuncay Özel, who was also my home mate at Bilkent. He is always kind, considerate and helpful, and he is also a very special friend of mine. With Evren and Tuncay we had very nice days during IEEE Photonics Society Annual Meeting in San Jose, research visit at Technical University of Dresden and workshop in Florence, Italy. I would like

to thank İlkem Özge Özel, who is very kind and positive. I owe my thanks to Rohat Melik, who is always helpful and friendly. I give my thanks to Emre Sarı, who is encouraging, kind and considerate. I would like to thank Evren`s wife Sümeyye, Tuncay`s wife Özge, Rohat`s wife Bahar and Emre`s wife Serpil for making my friends happy. I would like to thank Can Uran and Atilla Özgür Çakmak, who are very friendly, kind and considerate. I would like to thank our young teammates Talha Erdem and Burak Güzeltürk. When I needed help, they were with me and they were always kind, positive and respectful.

I want to thank to all current and former students and researchers supervised by Prof. Hilmi Volkan Demir. I would like to thank Nihan Kosku Perkgöz, İbrahim Murat Soğancı, Urartu Ö. Şeker, Pedro L. Hernandez, Özgün Akyüz, Ersin Doğan, Cüneyt Eroğlu, Onur Akın, Mustafa Akın Sefünç, Refik Sina Toru, Hatice Ertuğrul, Neslihan Çiçek, Veli Tayfun Kılıç, Sayim Gökyar, Kıvanç Güngör, Ahmet Fatih Cihan, Yasemin Coşkun, Shahab Akhavan, Yusuf Keleştemur, Aydan Yeltik, Togay Amirahmadov, Durmuş Uğur Karatay, Ozan Yerli, Mustafa Yorulmaz.

I owe my thanks to all professors, researchers, staffs and students in the Department of Electrical and Electronics Engineering, Department of Physics, Institute of Material Science and Nanotechnology (UNAM), Nanotechnology Research Center (NANOTAM) and Advanced Research Laboratory (ARL) at Bilkent.

Finally, I would like to acknowledge the generous support by European Technology Platform for Photonics21 Student Innovation Award, IEEE for Photonics Society Graduate Student Fellowship and SPIE for Scholarship Award in Optical Science and Engineering. This thesis work is supported by Turkish Academy of Sciences–Young Scientists Award Program, Scientific and Technological Research Council of Turkey (TUBITAK)–Department of Scientist Support, TUBITAK 110E0217, 110E010, 109E004, 109E002, 100E002, 107E297, 107E088, 106E020, 104E114, European Science

Foundation–European Young Investigator Awards, European Science Foundation–European Cooperation in Science and Technology, European Countries Nanophotonics for Energy Efficiency Network of Excellence and Arçelik.

Table of Contents

List of Figures

List of Tables

This thesis is dedicated to my parents Alican and Aynur, my sister İrem and my wife İrem for their love, patience and support…

Chapter 1

Introduction

Today it is estimated that ~19% of the global electricity production is consumed for lighting [1]. If the entire conventional white light sources are to be replaced with energy-efficient light emitting diodes (LEDs), the total energy consumption can potentially be decreased by ca. 1,000 TW h yr^{-1}, which corresponds to the power generation by 230 of typical 500-MW coal plants. This implies that carbon emission can possibly be cut by 200 million tons annually [2], [3]. Therefore, solid state lighting offers a potential solution to help addressing economical and environmental challenges we are now facing due to the energy problem. Furthermore, today approximately one third of the world population (about two billion people) have no or limited access to electricity and relies on fuel-based lighting in under-developed countries [1]. However, fuel-based lighting provides an unhealthy and costly means of illumination with low light quality. Thus, the advancement of LEDs (*e.g.*, in self-powered packages using solar cells) is a key to the human development (*e.g.*, for the improvement of literacy and education). To this end, this worldwide strong demand for the development of high-quality white LEDs (WLEDs) motivates our research work on the investigation of high-quality and efficient light generation presented in this thesis.

To date different approaches of solid state lighting for color-conversion WLEDs have extensively been investigated [4-6]. Among these, WLEDs based on conventional rare-earth phosphor powder coating were first commercialized in 1996 [7]. Such a color-conversion LED utilizes electroluminescence (EL) of the LED platform and photoluminescence (PL) of luminescent phosphor film integrated on this platform. Today although phosphors are commonly used as

color converters, there are problems associated with their usage [8]. These problems arise due to the difficulties in controlling granule size and in mixing and depositing uniform films of phosphors, which lead to undesired visible color variations as one of the main disadvantages. Also, the color rendering index of such phosphor-based color conversion can be undesirably low for high-quality lighting. For example, yellow phosphor-based white LEDs typically exhibit color-rendering indices of about 70, whereas the future solid-state lighting requirements dictate a color rendering index above 80 [9]. Although the peak emission of such phosphors can be shifted by substituting different chemicals (*e.g.*, Gd for Y, Ga for Al) and red-emitting phosphor can be used for color temperature adjustment and color rendering index improvement, their broad-emission spectrum makes it technically impossible to fully tune and optimize the photometric properties of the generated white light at the same time, as is required to achieve optimal lighting conditions specific to particular applications (*e.g.*, for indoors lighting, street lighting, and LED-TV backlighting). For instance, to improve color rendering, it is possible to use red phosphors; but, this comes at the cost of significantly reduced luminous efficacy (due to the emission tail above 650 nm). Therefore, conventional phosphors do not allow for optimal photometric design. In addition, China presently controls 95% of the rare-earth supply of the world, which raises a strategically critical issue for the supply security of phosphors in color-conversion LEDs.

As a possible remedy to overcome these disadvantages, we propose, develop and demonstrate a new class of color-conversion LEDs integrated with nanophosphors of semiconductor nanocrystals (NCs) for efficient and high-quality lighting [10], [11]. The favorable properties of colloidal quantum dots including size-tuneable and narrow emission with high photostability enable us to achieve high-quality, tuneable and efficient white light generation. By using combinations of these nanocrystal emitters the desired luminescence spectra can be obtained. This is essential for making application-specific LEDs.

Furthermore, Förster-type nonradiative energy transfer (NRET) capability of nanocrystals allows us to realize novel device designs. By using this energy transfer process, we achieve enhanced color conversion via recycling of trapped excitons in nanocrystals. Moreover, we show nonradiative pumping of nanocrystal quantum dots for color conversion. White light generation is generally achieved through only optical pumping (*i.e.*, radiative energy transfer) that involves two recombination processes. The first radiative recombination process occurs in the electrically driven quantum wells of the LED and, subsequently, their emitted photons excite nanocrystal luminophors that further luminescence via a second radiative recombination process. Instead of two recombination processes, we investigate and demonstrate an efficient excitation of nanocrystals with a single-step process using nonradiative resonance energy transfer.

The rest of this thesis is organized as follows. In Chapter 2, we explain the scientific background to easily follow the technical content of this thesis. This includes the general concepts and parameters about light sources, white light emitting diodes, and Förster-type nonradiative energy transfer.

In Chapter 3, we discuss colloidal nanocrystals in general and then nanocrystal emitters for light emitting diode application. Furthermore, we explain synthesis of nanocrystals, quantum mechanical calculation of nanocrystals via effective mass approximation, and experimental techniques.

In Chapter 4, we continue with the investigation of superior white light emitting diodes hybridized with nanocrystal quantum dots for high photometric performance. Here we demonstrate three different light emitting diodes that exhibit high-quality photometric parameters. The first hybrid white LED achieves a high color rendering index higher than 80 while generating warm-white light for indoor lighting application. The second hybrid LED achieves the state-of-the-art photometric performance with a color rendering of around 90

while achieving a luminous efficacy of optical radiation higher than 350 lm/W_{opt}. In the last subchapter, we present energy-efficient light emitting diodes with high scotopic/photopic ratio and color rendering index at the same time for street lighting, despite the fundamental trade-off between scotopic/photopic ratio and color rendering index.

In Chapter 5, we introduce white light emitting diodes integrated with exotic nanocrystal emitters. We first make quantum mechanical investigation of CdSe/ZnS/CdSe/ZnS core/shell/shell/shell nanocrystals (*i.e.*, onion-like heteronanocrystals) to understand their multi-color emission and other optical properties. We hybridize these multi-color emitting nanocrystals on blue LEDs for tuning the optical properties of color-conversion LEDs.

In Chapter 6, we demonstrate LEDs enhanced with nonradiative energy transfer. We investigate the optimized donor-acceptor ratio for the highest possible efficiency enhancement by using recycling of trapped excitons. We further show light emitting diodes based on NRET-enhanced color conversion at different colors including green and red as well as white.

In Chapter 7, we study light generation based on NRET-conversion. For this we exhibit white light generation with nonradiative energy transfer from quantum wells to nanocrystal quantum dots. To enhance NRET-conversion we hybridize nanocrystals with multiple quantum well nanopillars and exhibit that energy transfer efficiency is increased to around 83%. Furthermore, we present efficient conversion from Mott-Wannier to Frenkel excitons at room temperature in a hybrid semiconductor quantum dot/polymer.

In Chapter 8, we conclude our thesis by describing and remarking our achievements.

Chapter 2

Scientific Background

2.1 General concepts and parameters about light sources

2.1.1 *(x,y)* chromaticity coordinates

(x,y) tristimulus coordinates allow us to determine the perceived color of the light source by the human eye by using the chromaticity diagram shown in Figure 2.1.1. In fact, the widely reported *(x,y)* coordinates consist of x, y and also the z coordinate values. However, since the z value is a dependent variable of x and y values, it is not given on a two dimensional chromaticity diagram and instead only x and y values are shown. The perceived color is determined by looking at the corresponding coordinates on the standard CIE (Commission Internationale d l'Eclairage – The International Commission for Illumination) chromaticity diagram. CIE defines the international standards for color science, and chromaticity diagram and CIE 1931 color matching functions (shown in Figure 2.1.1 and 2.1.2, respectively) are the most widely used standards in both industrial production and scientific research [4]. However, it is also worth mentioning that the color matching functions are not unique, *e.g.*, Judd and Vos [12], [13]. Each tristimulus value corresponds to an approximate response of red-, green-, or blue-sensitive retinal cones. Equations (2.1.1), (2.1.2) and (2.1.3) are used to determine the strength of each perceived red, green and blue colors (*i.e.*, X, Y and Z, respectively), where the $x(\lambda)$, $y(\lambda)$ and $z(\lambda)$ are the color matching functions and P(λ) is the power spectral density.

$$X = \int_{\lambda} x(\lambda)P(\lambda)d\lambda \qquad (2.1.1)$$

$$Y = \int_{\lambda} y(\lambda)P(\lambda)d\lambda \tag{2.1.2}$$

$$Z = \int_{\lambda} z(\lambda)P(\lambda)d\lambda \tag{2.1.3}$$

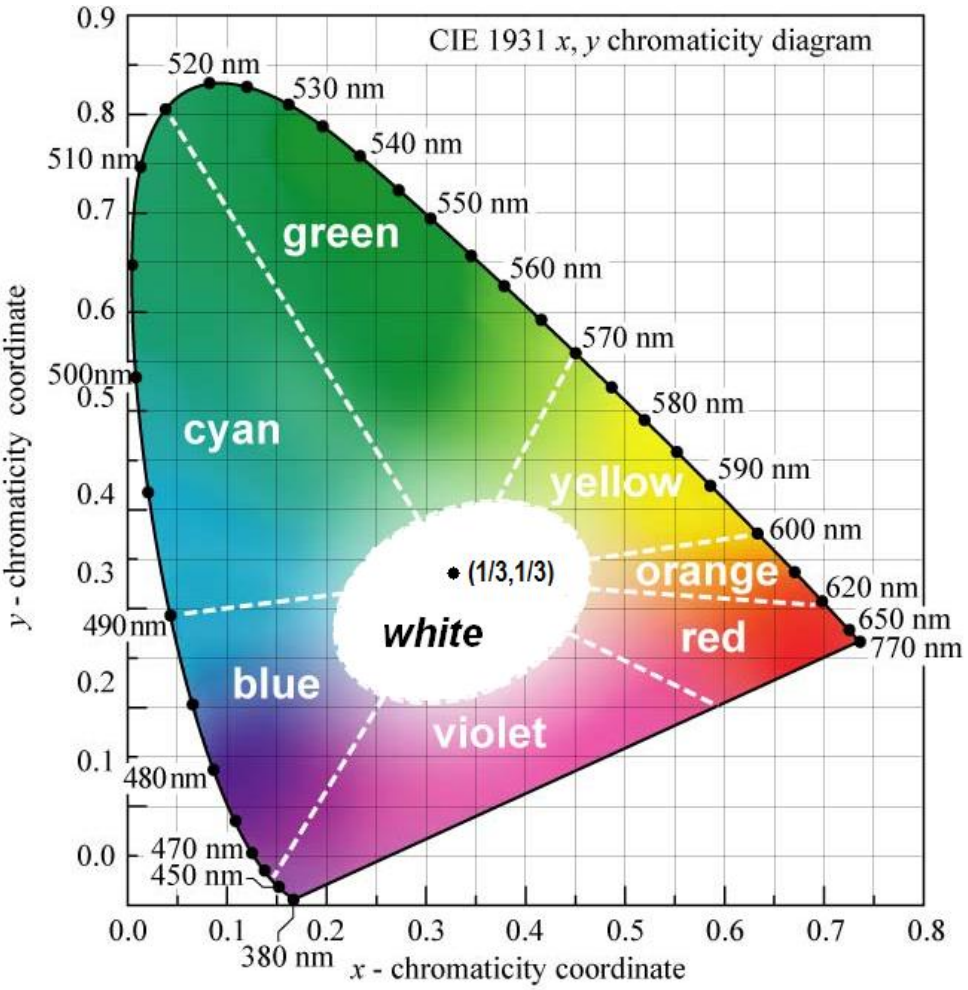

Figure 2.1.1 CIE 1931 (x,y)chromaticity diagram [4].

The *(x,y)* and z chromaticity coordinates are calculated using Equations (2.1.4), (2.1.5) and (2.1.6), respectively. The color of the spectrum can be understood by looking at *(x,y)* coordinates on the chromaticity diagram. Furthermore, the z chromaticity value can also be obtained by using x and y coordinates as shown in Equation (2.1.6), but it does not provide any new information. The equal-energy point located in the center of the chromaticity diagram at (x, y, z) = (1/3,

1/3, 1/3), but this operating point does not have a significant meaning in terms of quality and efficiency of LEDs.

$$x = \frac{X}{X + Y + Z} \tag{2.1.4}$$

$$y = \frac{Y}{X + Y + Z} \tag{2.1.5}$$

$$z = \frac{Z}{X + Y + Z} = 1 - x - y \tag{2.1.6}$$

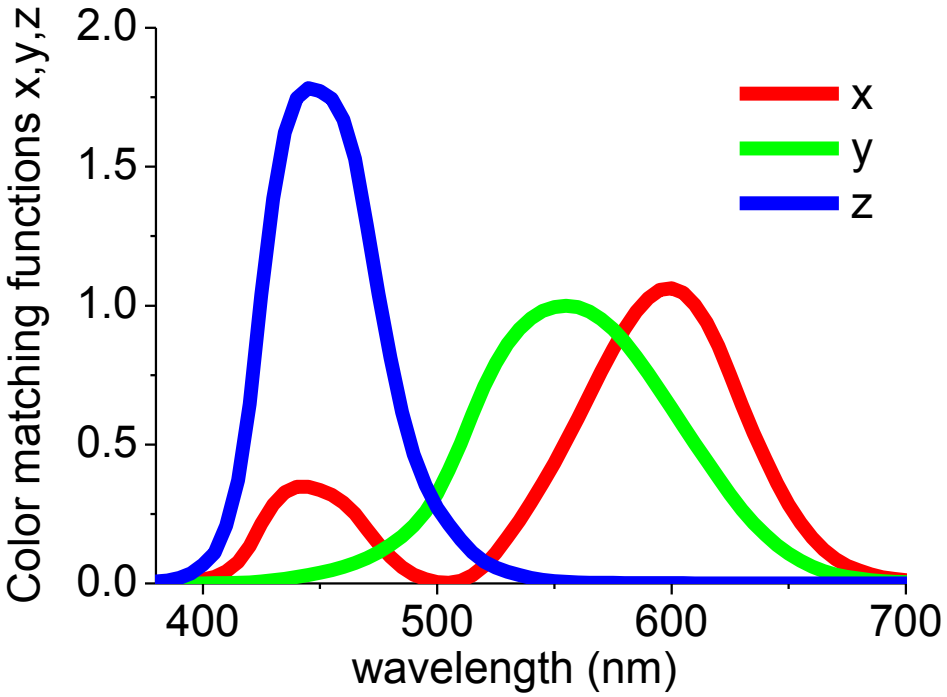

Figure 2.1.2 Spectral distribution of color matching functions [4].

2.1.2 Color temperature

The relation between the color and temperature stems from the blackbody radiation and the black-body spectrum is given as follows [4]:

$$I(\lambda) = \frac{2hc^2}{\lambda^5[\exp(\frac{hc}{\lambda kT}) - 1]} \tag{2.1.7}$$

The change in color is opposite natural human body change. For example, as we run, we get warmer and redder. However, the opposite is true for color temperature. As the color temperature decreases, the appearance shifts from bluish white, white, yellowish white, orange and red. This can be understood while a metal plate is heated, its heat increases and we observe its color first as red, then orange and finally as yellow.

The *(x,y)* tristimulus coordinates of the blackbody radiators form the Planckian locus as shown in Figure 2.1.3 and the color temperature of a light source is determined by looking at the coordinates of corresponding blackbody radiation temperature, whose unit is Kelvin. However, in Figure 2.1.3 the Planckian locus is only a small portion of *(x,y)* chromaticity diagram and there exist many operating points outside the Planckian locus. If coordinates of a light source does not fall on the Planckian locus, the correlated color temperature (*CCT*) is used to define the color temperature of the light source. *CCT* is calculated by transforming the *(x,y)* coordinates of the light source to (u',v') by using Equations (2.1.8) and (2.1.9), and by determining the temperature of the closest point of the Planckian locus to the light source on the (u',v') uniform chromaticity diagram shown in Figure 2.1.4 [4], [14]. To better visualize *CCT*, some light sources with their corresponding *CCTs* are provided in Table 2.1.1.

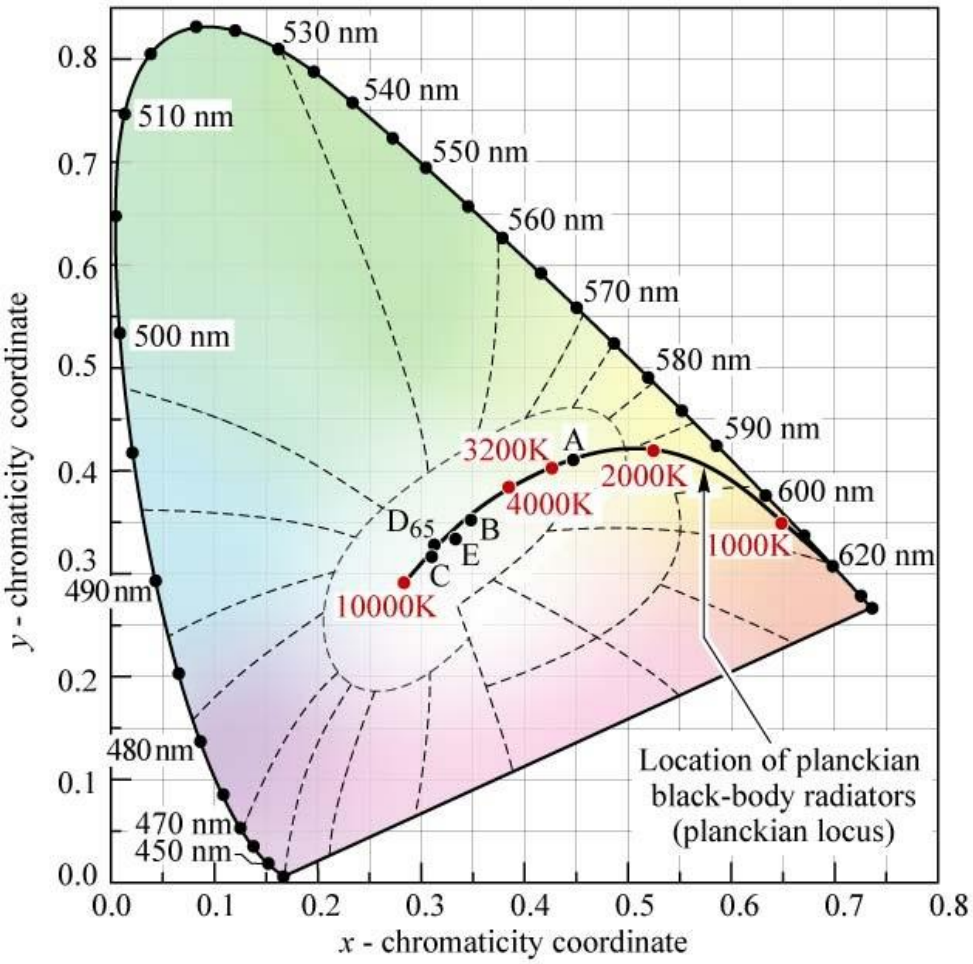

Figure 2.1.3 *(x,y)* chromaticity diagram showing the Planckian locus [4].

$$u' = \frac{4x}{-2x + 12y + 3} \tag{2.1.8}$$

$$v' = \frac{9y}{-2x + 12y + 3} \tag{2.1.9}$$

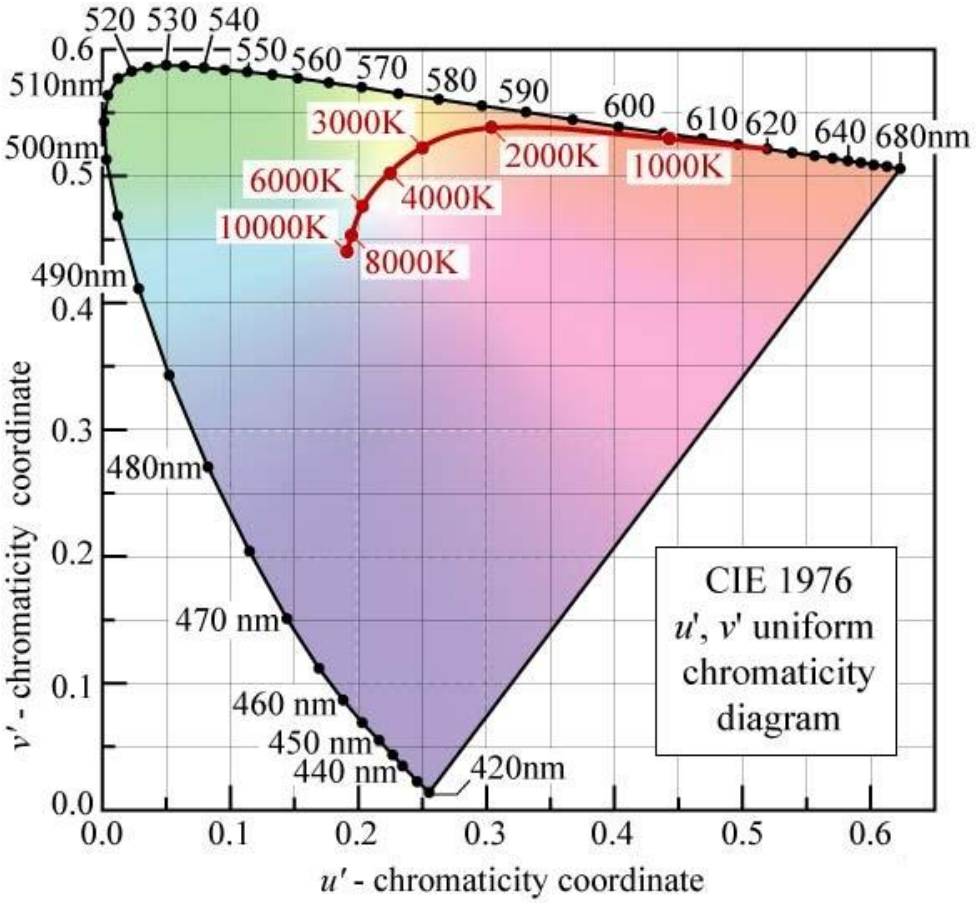

Figure 2.1.4 (u`,v`) chromaticity diagram showing the Planckian locus [4].

Table 2.1.1 Light sources and their correlated color temperatures [4].

Light source	**Correlated color temperature (K)**
Wax candle flame	1,500 to 2,000
“Cool daylight white” flourescent tube	4,300
Xenon Arc	6,000
Direct sun	5,700-6,500
Clear blue sky	8,000-27,000

2.1.3 Color rendering index

Color rendering index (*CRI*) is the measure of how well a light source shows the true colors of the illuminated objects. *CRI* is a measure ranging from -100 to 100 [15]. The best color rendering index is 100, whereas the *CRI* of the poorest color rendition is -100. High *CRI* is required for museum, architectural lighting,

indoor lighting, *etc*., but for outdoor applications such as street lighting a lower *CRI* is sufficient. For future SSL application Sandia National Laboratories announced that LEDs should have *CRI* higher than 80 [9]. *CRI* of a test light source is a relative measure with respect to a reference light source, for which blackbody radiators with excellent *CRI* of 100 are used in general. The incandescent lamps, which are also blackbody radiators, have perfect color rendering capability. However, because of their high energy consumption their use has been or will be prohibited in some countries such as Canada, Australia, Europe, *etc*.

14 internationally agreed test color samples are used to measure *CRI* and these test color samples are defined according to their spectral reflectivity. The general *CRI* is calculated by using CIE test color sample objects from 1 to 8 [15]. The six CIE test color sample objects from 9 to 14 are used to further evaluate *CRI* of the test light source. For test light sources blackbody radiators with the same color temperature or correlated color temperature are used depending whether tristimulus coordinates of test light source is on the Planckian locus or not. Color rendering index is calculated according to the test color spectral reflectivity difference under the test light source illumination and reference light source illumination.

To determine the *CRI* of a test light source, in addition to the test-color samples, test color samples are needed. In international standardization, 14 test color samples has been agreed to measure the *CRI*, but the general *CRI* is an average calculated according to the 8 test-color samples with the following formula [4]:

$$CRI_{general} = \frac{1}{8}\sum_{i=1}^{8} CRI_i \tag{2.1.10}$$

The special color-rendering indices are calculated according to:

$$CRI_i = 100 - 4.6\Delta E_i^* \tag{2.1.11}$$

where ΔE_i^* is the quantitative color change that occurs when a test-color sample is illuminated with the reference source and then with the test source. The special *CRI* is 100 if there is no difference of the test-color sample in color under test and reference light source. Color rendering index of some light sources are indicated in Table 2.1.2.

Table 2.1.2 Color rendering indices of various light sources [4]

Light source	**Color rendering index**
Incandascent light bulb	100
Yellow-phosphor based LED	70-80
High pressure Na vapor light	22
Green light	-50

2.1.4 Color Quality Scale

Recently a new color rendition metric of color quality scale (*CQS*) has also introduced by Davis and Ohno [16-18]. Although color rendering index is widely used in the lighting community, *CQS* also provides a scale for color rendering capability of various spectra. Similarly *CQS* is also based on the use of a reference light source like *CRI*. Different from *CRI*, *CQS* uses 15 reflective Munsell samples and it contains a saturation factor, which becomes effective when light sources enhance object chroma. In addition, *CQS* ranges from 0 to 100. *CQS* and *CRI* of the current technologies and simulated LEDs are analyzed and summarized in Table 2.1.3 [16-18]. According to the analysis, *CQS* results are in agreement with *CRI* results for traditional lamps and, for LED spectra there exists a higher difference between *CQS* and *CRI*. Ohno states that *CQS* is a better measure for color rendering of the LED sources [16-18]. Today *CQS* is not widely used by the lighting community, but in the future with further improvements it may be replace *CRI*.

Table 2.1.3 CQS and *CRI* of the current technologies and simulated LEDs

Light source	Color quality scale	Color rendering index
Incandascent	98	100
Mercury	53	53
Cool White Florescence	61	59
RGB LED (470-525-630)	55	31
RGB LED (464-538-613)	85	80
RGB LED (467-548-616)	82	90
RGB LED (464-562-626)	78	59
RGB LED (457-540-605)	74	80
RGB LED (455-547-623)	79	73

2.1.5 Luminous efficacy of optical radiation and luminous efficiency

Luminous efficacy of optical radiation (*LER*) of a light source represents the fraction of emission spectra useful for human eye and its unit is lumen per optical watt. It is calculated by using Equation (2.1.12) where where v(λ) is the eye sensitivity function (as shown in Figure 2.1.5) and $P_{optical}(\lambda)$ is the power spectral density (*i.e.*, the light power emitted per unit wavelength) [4].

$$LER = \left(683 \frac{lm}{W}\right) \frac{\int P_{optical}(\lambda) v(\lambda) d\lambda}{\int P_{optical}(\lambda) d\lambda} \tag{2.1.12}$$

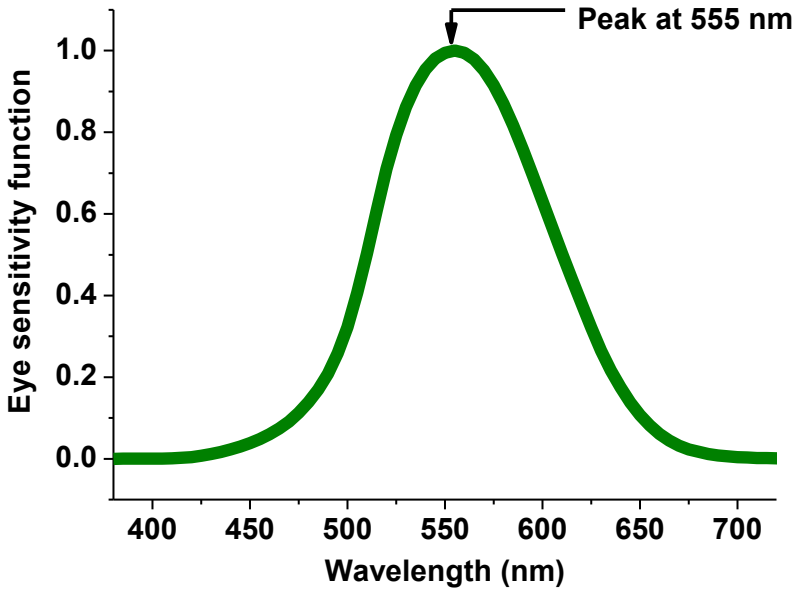

Figure 2.1.5 (u',v') Eye sensitivity function spectrum.

In lighting community, luminous efficacy of optical radiation can be misused and confused with luminous efficiency (*LE*). *LE* reveals the strength of useful emission spectra for electrical power so that its unit is lumen per electrical watt. *LE* can be calculated by multiplying *LER* by power conversion efficiency of LED. This is given by Equation (2.1.13), where v(λ) is the eye sensitivity function, P(λ) is the power spectral density (*i.e.*, the light power emitted per unit wavelength), I is the current injection level and V is the applied voltage level at the operating point of LED.

$$LE = \left(683 \frac{lm}{W}\right) \frac{\int P_{optical}(\lambda) v(\lambda) d\lambda}{VI} \qquad (2.1.13)$$

2.1.6 Scotopic/Photopic ratio

Experiments supported by the U.S. Department of Energy indicate that rod photoreceptors, which are considered to be responsible for scotopic (dark adapted) vision, may also affect photopic (photon adapted) vision [19]. These studies argue that the variation of pupil size strongly follows a scotopic-like

spectrum at interior lighting power levels [20-24]. According to these studies, it could therefore be possible to improve vision and lighting energy efficiency by accounting for the role of these rods, for example, in designing light emitting diodes. The figure-of-merit showing the rod activity under the illumination of a light source is quantified in terms of the ratio of eye response to the light source under the scotopic conditions to that in the photopic case, referred to as the scotopic/photopic (*S/P*) ratio of the source [25]. This difference in the scotopic and photopic luminous efficacy of the source results from the shift of eye sensitivity function peaking at 555 nm (under photopic lighting conditions) to 507 nm (under scotopic lighting conditions), also known as the Purkinje shift. The *S/P* ratio of a light source is calculated by using Equation (2.1.14), where $V(\lambda)$ is the photopic eye sensitivity function and $V`(\lambda)$ is the scotopic one, and the *S/P* ratio of some light sources are summarized in Table 2.1.4.

$$\mathrm{S/P} = \frac{1700\int E(\lambda)V'(\lambda)d\lambda}{683\int E(\lambda)V(\lambda)d\lambda} \tag{2.1.14}$$

Table 2.1.4 Light sources and their *S/P* ratios [24].

Light source	***S/P* ratio**
Incandascent light bulb	1.40
Fluorescent (Cool White)	1.50
Daylight fluorescent	2.22
Mercury vapor (coated)	0.80

2.2 White light emitting diodes

Lighting poses an increasing market demand as one of the next great solid-state frontiers [26] and the new generation lighting systems are required to possess high-quality white light generation with high efficiency and color rendering, high power capability, low manufacturing cost, environmental friendliness and reliability. For that, white light emitting diodes (WLEDs) have attracted both

scientific attention and commercial interest with their potential widescale use, for example, in architectural lighting, decorative lighting, flashlights and backlighting of large displays [27]. To date, multi-chip WLEDs, monolithic WLEDs and color-conversion WLEDs have been extensively exploited [4], [5], [7].

2.2.1 Multi-chip white light emitting diodes

In multi-chip white light emitting diodes, LEDs with different colors are integrated together to generate the desired white light. For this purpose, InGaN based blue- and green-LEDs, and an AlGaInP based red-LED are jointly packaged [5]. The advantageous of these LEDs are color flexibility, both in multi-color displays and different shades of white and potentially very high color rendering. However, there exist also some drawbacks of these LEDs. Individual colored LEDs respond differently to drive current, operating temperature and operating time. Thus, control systems are required for color consistency and these leads to complex driving circuitry and increased expense. Furthermore, the low external quantum efficiency of LEDs at green wavelengths (shown in Figure 2.2.1) also negatively affects the performance of these white LEDs.

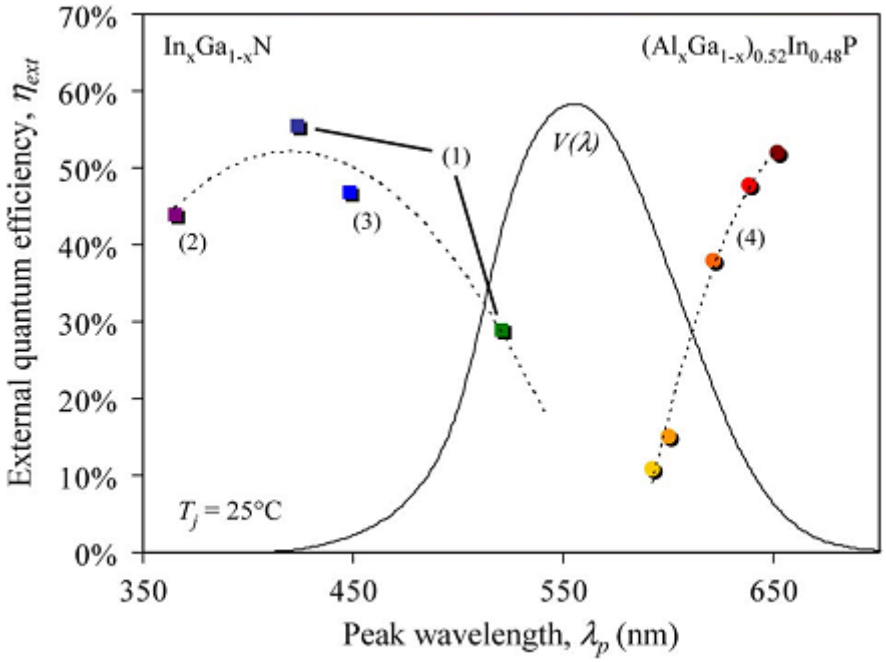

Figure 2.2.1 External quantum efficiency of light emitting diodes in visible [2].

2.2.2 Monolithic white LEDs

In monolithic white light emitting diodes, multiple quantum wells emitting at distinct wavelengths are used for white light generation. For example, Lee *et al.* demonstrated WLEDs including blue, green and amber InGaN/GaN quantum wells as the active layers. Monolithic WLEDs advantageously have simple circuitry and high color rendering index potential. However, these type of LEDs exhibit undesired temperature dependent white light parameters and show different emission spectra at different current injection levels [28].

2.2.3 White light emitting diodes based on color conversion

The working principle of this type of white light emitting diodes is different from both the multichip and monolithic WLEDs. In multichip and monolithic WLEDs, color conversion relies on the electroluminescence originated from the active region of light emitting diodes, but LEDs based on color conversion

utilize both the electroluminescence originated from the active region of LED and photoluminescence of the color conversion layer. Furthermore, multichip and monolithic WLEDs are fully inorganic, but LEDs based on color conversion use both organic and inorganic materials. The working principle of these WLEDs is as follows: Electroluminescence in blue or near-ultraviolet is generated via current injection and this pumps integrated color conversion layer. Consequently the color conversion layer makes photoluminescence. As a result, the electroluminescence and photoluminescence collectively generates white light.

Materials including phosphors, dyes and polymers and can be used for the photoluminescent layer. For example, dyes and polymers can be used as color converter for white LED applications. They can be selected from violet to red colors. They have high quantum efficiencies in solution. They can be jointly used in epoxy resin. However, the drawback of these organic substances is their stability problem, which limits their use in LED application [4], [29], [30].

Today the current WLED market is dominated by the phosphors, especially phosphors with yttrium aluminum garnet (YAG). They exhibit high quantum efficiency (*i.e.*, photon conversion efficiency approaching 100%). They can be easily hybridized on inorganic LEDs and are stable materials to be used in LED application. They provide a wide emission spectra covering from blue to deep-red shown in Figure 2.2.2. The optical characteristics of YAG phosphor with the chemical formula of $(Y_{1-a}Gd_a)(Al_{1-b}Ga_b)_5O_{12}$: Ce can be shifted by substituting Gadolinium (Gd) for Yttrium (Y), Gallium (Ga) for Aluminum (Al) and doping with cerium (Ce) [4]. For white light generation they can be both integrated on top of n-UV and blue LEDs. The spectral tunability is important to use WLEDs for the desired application; however, the main disadvantage of the phosphors is that the white light parameters cannot be sensitively tuned. Furthermore, the deep-red emission of the phosphors decreases the luminous efficacy of optical radiation due to the broad emission spectrum of phosphors.

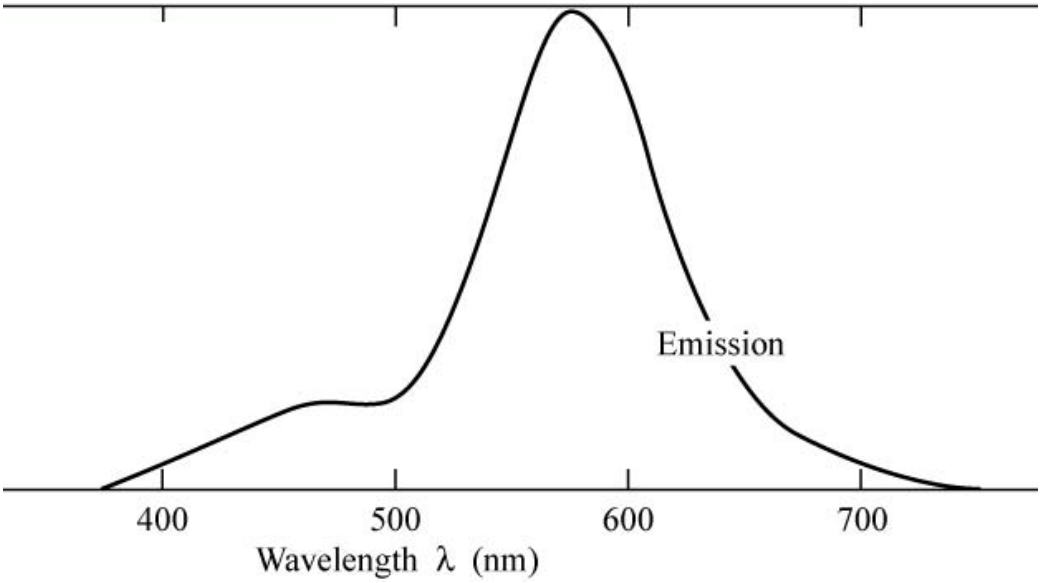

Figure 2.2.2 Photoluminescence spectrum of a phosphor [4].

2.3 Förster-type nonradiative energy transfer

Förster-type nonradiative energy transfer is an important process for communication and energy transport at nanometer scales [31]. In living plants, this allows the transfer of energy from absorbing chlorophyll antenna complexes to the reaction centers. This nonradiative, directional and fast energy transfer has found many applications including medical diagnostics, bio-imaging, analysis of DNA, and recently in optoelectronics and nanophotonics [32].

Förster-type nonradiative energy transfer is a virtual photon process where excitation energy is nonradiatively transferred from an energy donor with wider band gap to an energy acceptor with narrower band gap. This incoherent process is the result of dipole–dipole interactions between the donor and acceptor, and takes place without the involvement of a free emitted photon. The process is as follows: After the optical absorption, electron and hole pair is generated in the donor, which subsequently relaxes to their ground states in their respective

conduction and valance bands. Using NRET the energy is transferred to the acceptor and finally the interband recombination occurs in the acceptor.

The energy transfer rate between a donor and an acceptor is calculated by using Equation (2.3.1), where R_0 is the Förster radius, τ_D is the donor lifetime in the absence of acceptor, and r is the interspacing between the donor and the acceptor [33]. The Förster energy transfer rate is significantly affected by the distance between the acceptor and the donor quantum dots (in Equation (2.3.1)). For example, if the interspacing between the dots is less than one Förster radius, then most of the excitonic energy is transferred to the acceptor nanocrystal (where generally the Förster radius is less than 10 nm), However, when the interspacing decreases, the transfer rate decreases with the sixth power. Therefore, the interspacing between the donor and acceptors should be carefully adjusted. On the other hand, for even smaller distances less than 1 nm, the dipole-quadrupole and quadrupole-quadrupole interactions become effective and the wavefunctions of the particles may start to overlap and tunneling becomes probable. As a result, the NRET may turn into Dexter-type transfer process. Because of that, both time-resolved and steady-state spectroscopies are important in understanding NRET process.

The Förster radius (thus energy transfer rate) is dependent on the refractive index of the medium (n), quantum efficiency of the donor (Q_D), overlap of donor emission with acceptor absorption and absorption of the acceptor (J) and transitional dipole moment (κ^2) as given in Equation (2.3.2). For an isotropic orientation of transitional dipole moment, κ^2 is equal to 2/3, which is the case for nanocrystals. Furthermore, the spectral overlap is calculated by using Equation (2.3.3), where $F_D(\lambda)$ is the corrected fluorescence intensity of the donor and $\varepsilon_A(\lambda)$ is the extinction coefficient of the acceptor at the wavelength of λ. The energy transfer efficiency can be calculated by using Equation (2.3.4), which is significantly dependent both on Förster radius and interspacing. The dependence of Förster energy transfer efficiency on distance is shown in Figure 2.3.1 and

after two Förster radii the energy transfer efficiency becomes insignificant (almost zero). In addition, the transfer efficiency can be calculated based on the recombination rate of donor without acceptor and the transfer efficiency as given in Equation (2.3.5).

$$k_{ET}(r) = \frac{1}{\tau_D}\left(\frac{R_0}{r}\right)^6 \tag{2.3.1}$$

$$R_0 = 0.211(\kappa^2 n^{-4} Q_D J(\lambda))^{1/6} \quad \text{(in Angstrom)} \tag{2.3.2}$$

$$J(\lambda) = \int_0^\infty F_D(\lambda)\varepsilon_A(\lambda)\lambda^4 d\lambda \tag{2.3.3}$$

$$\eta = \frac{R_0^{\,6}}{R_0^{\,6} + r^6} \tag{2.3.4}$$

$$\eta = \frac{k_{ET}}{k_{ET} + k_D} \tag{2.3.5}$$

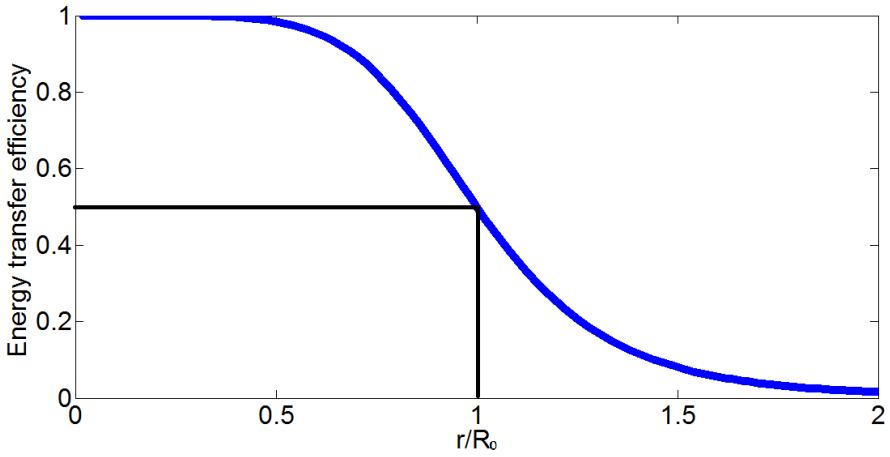

Figure 2.3.1 Dependence of the energy transfer efficiency on distance (R_0 is the Förster distance).

Chapter 3

Colloidal Nanocrystal Quantum Dots

3.1 Introduction

Semiconductor nanocrystals, also known as colloidal quantum dots, are nanosized sphere-like crystal structures with diameters ranging from 2 to 10 nanometers. For example, in Figure 3.1.1 the transmission electron microscopy (TEM) images of mono-dispersed CdSe nanocrystal quantum dots with diameters around 5 nm are shown.

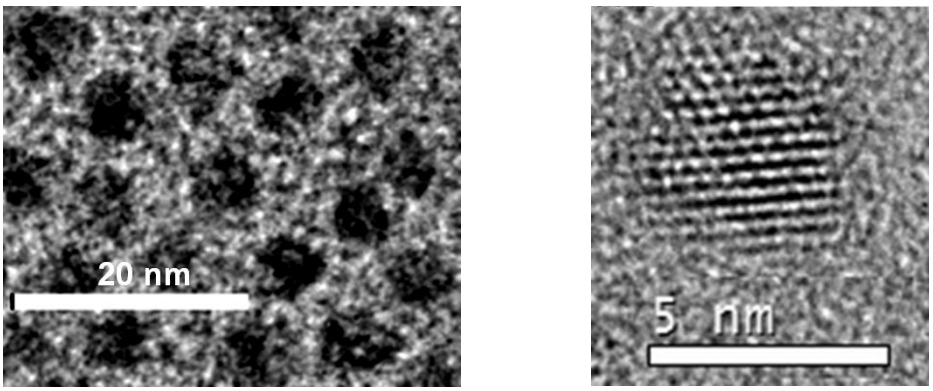

Figure 3.1.1 Transmission electron microscopy (TEM) images of NC solid films,

Nanocrystals can be composed of periodic groups of II-VI, III-V, or IV-VI materials. It is possible to control the electronic structure and optical properties of these nanomaterials by changing their size [11]. In the bulk case, the energy levels in valence and conduction bands are more continuous like (ignoring discrete k`s given the size of the crystal). However, while the size of the nanocrystal shrinks, the continuous energy levels start to be discrete. In other

words, when the nanorystals are synthesized in a size comparable to or smaller than the Bohr radius, the quantum size effect (quantum confinement) begins to be strongly observed. As a result, by using the size effect, NC emission peak can be tuned. If this band gap energy corresponds to the photons in visible, the emission color and spectrum of NCs can be shifted to red while increasing the NC size as shown in Figure 2.3.2(a) and 2.3.2(b). These tuneable nanoparticles can be synthesized using hot-injection method where the reaction temperature, material and time are significant parameters to modify and control the material characteristics.

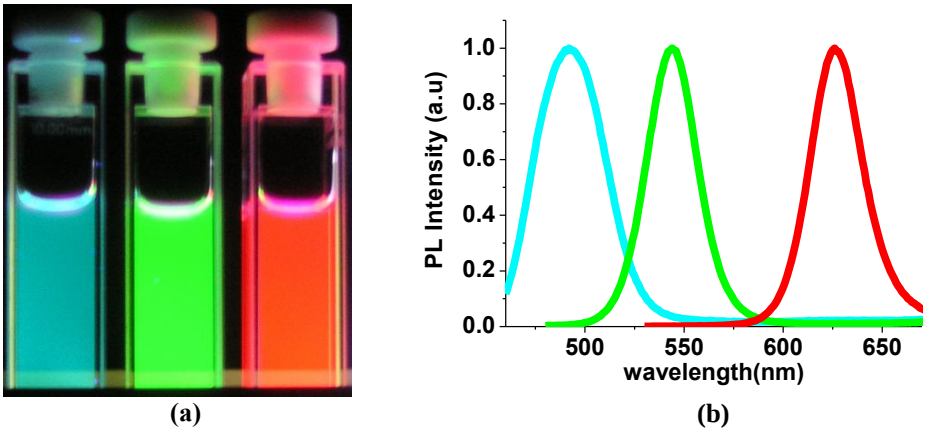

(a) (b)

Figure 3.1.2 (a) Photograph of nanocrystal quantum dots emission under UV light excitation and (b) spectral tuning of these dots while gradually changing their size.

Today different kinds of nanocrystal structures including only core, core with single shell, and core with multi-shells are synthesized by using the hot-injection method [34]. Here shell provides a potential barrier both for electron and hole. This electron and hole confinement can be achieved in different kinds of band alignment including type-I and type-II band alignment [35-36]. In type-I, both electron and hole wavefunctions mainly localize in the same spatial location (*e.g.*, in CdSe/ZnS core/shell NCs both the electron and hole mainly confine in the CdSe core) resulting in high oscillator strength, which is significant for obtaining high quantum efficiency. Therefore, NCs with type-I alignment are good candidates to be used in LED applications and CdSe/ZnS core/shell NCs are widely used in hybrid LEDs. In type-II band alignment, electron and hole

confine in different spatial positions. These NCs are more promising for lasing and nonlinear optical applications.

3.2 Colloidal nanocrystal quantum dots for light emitting diodes

In lighting applications, nanocrystals offer important benefits for color conversion LEDs. Their emission properties can be conveniently adjusted through quantum size effect, and using different material systems and shape [37]. Furthermore, nanocrystals can be easily integrated on substrates using common techniques (*e.g.*, spin-coating and layer-by-layer assembly) and they favorably exhibit high quantum efficiency, photostability and photobleaching thresholds [38]. Furthermore, they provide high spectral purity because of their narrow emission linewidths. These favorable properties enable us to custom-design a desired emission spectrum by using proper combinations of differently sized nanocrystals [39]. Because of these important benefits and continuing developments in their colloidal synthesis, nanocrystals are strong candidates for use in color conversion LEDs as shown in Figure 3.2.1.

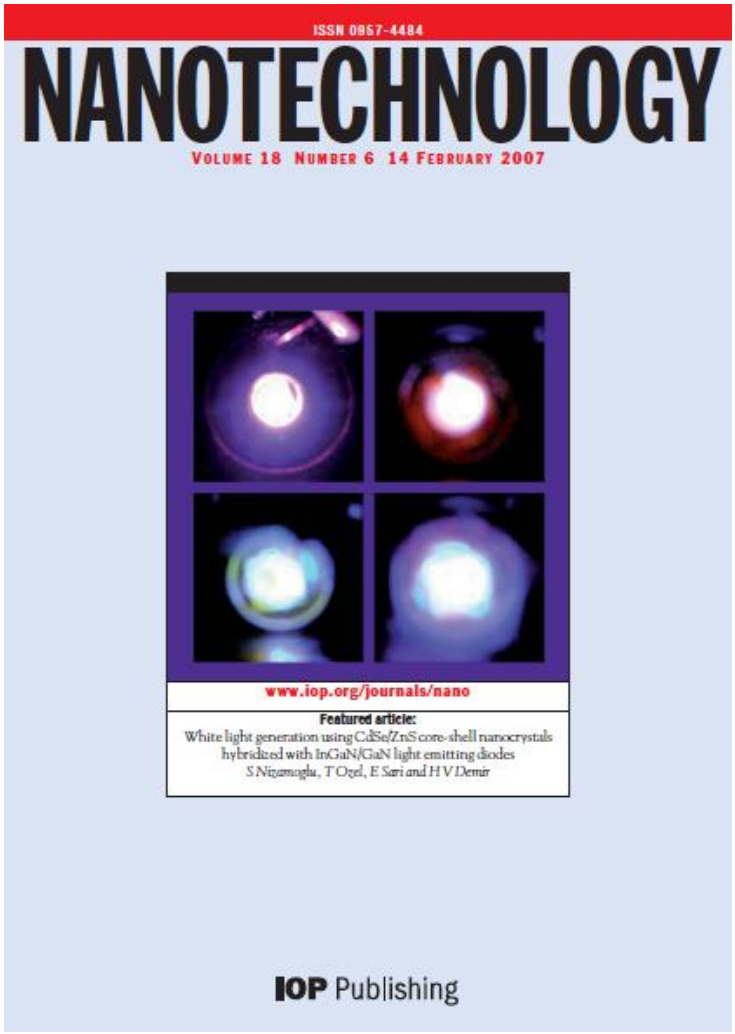

Figure 3.2.1 Our paper is highlighted as a featured article on the front cover of the journal Nanotechnology by Institute of Physics (vol. 18, no. 6 in the issue of 14 February 2007).

The use of combinations of nanocrystals at different emission colors with narrow emission linewidths having full-width-at-half-maximum of 40 nm or less at room temperature enables us to make easy adjustment of the white light parameters. To fine-tune the generated white light spectrum, the size and density of NCs and the thickness and order of the NC films are needed to be carefully adjusted. The size of NCs determines the colors that will contribute for white light generation. The NC density and NC film thickness affects color conversion of electroluminescence from the LED. Furthermore, the order of differently sized NCs affects the reabsorption of radiation by the previous NCs. Therefore,

the capability to set such device parameters allows one to form the aimed white light spectrum, which makes these color converters favorable compared to others.

3.3 Synthesis

Colloidal nanocrystal quantum dots can be synthesized with III-V, II-VI and IV-VI materials by using hot-injection method. During our research study, here we concentrated on the synthesis of colloidal nanocrystal quantum dots made of II-VI materials, which we will explain in the following sections.

3.3.1 CdSe core nanocrystals

For CdSe core synthesis, we prepare a cadmium stock solution consisting of 513.6 mg cadmium oxide (CdO), 6.3mL oleic acid (OA) and 40 mL octadecene (ODE). Subsequently, we prepare 1 M solution of selenium powder in trioctylphosphine (TOP) in glove box to prevent it from oxidation. Into a 25mL 3-neck flask equipped with a stirrer load, we mix 2 g tri-n-octylphosphine oxide (TOPO), 2 g (hexadecylamine) HDA, 8 mL ODE and 4 mL Cd-stock solution as shown in Figure 3.3.1.1. We slowly increase the temperature up to 300 ^{o}C under inert atmosphere and stirring to obtain clear colorless solution. Afterward, we prepare injection mixture in the glove box shown in Figure 3.3.1.2. We take 0.4 mL Se-stock solution, 1.6 mL TOP and 2 mL ODE. Then, we decrease temperature in the reaction flask to 270-280 ^{o}C and inject the selenium mixture. By adjusting the reaction time and temperature, we can tune the emission to the desired wavelength. Finally, we cool the reaction solution and stop the synthesis.

In Figure 3.3.1.3, the emission and absorption spectra of CdSe core nanaocrystal quantum dots are indicated. The emission peak is at 621 nm and the emission shape is a Gaussian profile. The emission linewidth comes from both the homogenous and inhomeogenous broadening (*e.g.*, phonon-exciton coupling and

size-distribution, respectively). Furthermore, there exists an approximately 7 nm red-shift of the first excitonic peak of absorption with respect to the photoluminescence peak, which is called the Stokes shift. The absorption strength of the nanocrystal quantum dots increases toward the shorter wavelengths.

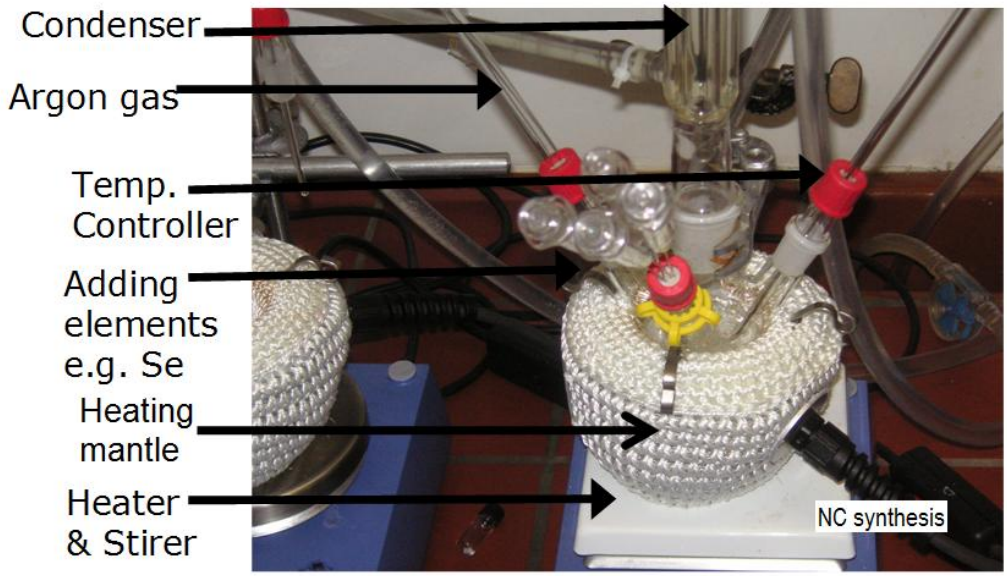

Figure 3.3.1.1 Photograph of nanocrystal synthesis flask equipped with condenser, temperature controller, heating mantle, and stirrer.

Figure 3.3.1.2 Photograph of glove box to work in oxygen-free environment.

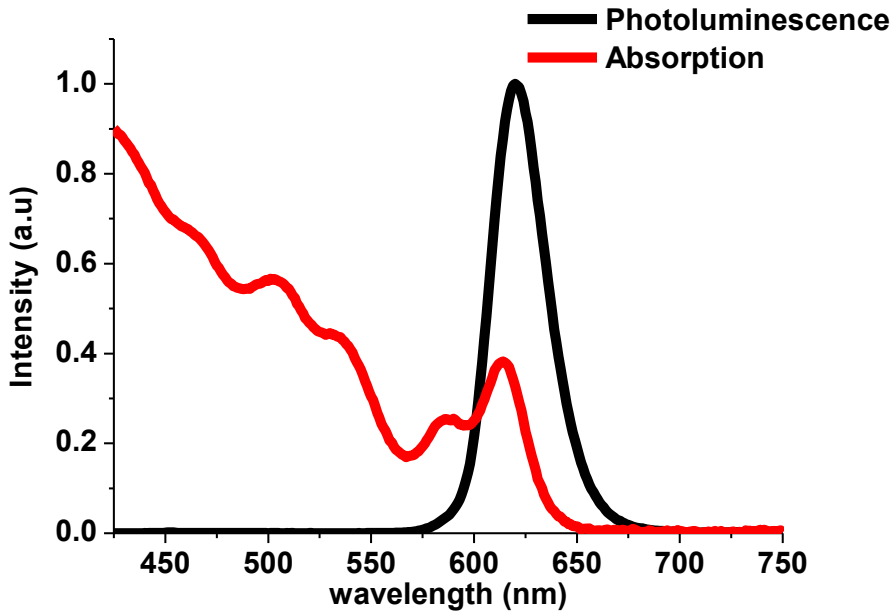

Figure 3.3.1.3 Absorption and photoluminescence spectra of our synthesized CdSe core nanocrystal quantum dots.

3.3.2 Shell growth surrounding CdSe nanocrystals

There exist many shell options that can be formed on top of CdSe core nanocrystals. For example, type-II band alignment can be obtained with CdTe shell and type-I band alignment can be obtained with CdS and/or ZnS shell. For shell synthesis, we need to determine the material amount that can cover the surface of the nanocrystal. Therefore, from the core diameter (which is determined from the first excitonic absorption peak, *e.g.*, by using reference [40]) we calculate the necessary number of atoms and consequently amount of material by using the reference [41]. For CdS shell, we heat reaction solution with nanocrystals to 240 ^{o}C. We slowly inject the necessary amount of Cd stock solution and then after five minutes we add S stock solution. We wait 25-30 min for one monolayer shell formation. We repeat this for each monolayer of shell growth. Growing shell that covers core nanocrystals positively affects the material quality in terms of both the stability and efficiency of the nanocrystals in general.

3.3.3 CdTe/CdSe core/shell nanocrystals

CdTe/CdSe core/shell nanocrystal quantum dots have type-II band alignment. However, depending on the purpose, if the CdSe shell is grown thin enough, the behavior of electron and hole approaches a quasi-type-II configuration, which means that the electron and hole wavefunction are distributed over the entire core/shell material. This behavior is a state between type-I and type-II configuration. In type-I configuration, electron and hole mainly localize in the same spatial position either in the core or in the shell whereas in type II configuration electron and hole localize in different spatial positions; for example, electrons localize in the core, but holes localize in the shell. These quasi-type-II CdTe/CdSe core/shell nanocrystals are favorable materials for multi-exciton generation and Prof. Efrat Lifshitz and co-workers exhibited the multi-exciton bands in steady state using these core/shell materials [38].

For CdTe/CdSe core/shell nanocrystal quantum dot synthesis we prepare a solution of Se, TOP and octadecene and another solution of CdO, oleic acid and octadecene. At room temperature we mix these two solutions, we heat up to 310 ^{o}C until we observe a gray solution and inject another solution including Te, TOP and octadecene. Then, we decrease the temperature to 190 ^{o}C and another solution containing Te, TOP and octadecene. By adjusting the time properly we can tune the characteristics of nanocrystals. After our synthesis, the photoluminescence peak wavelength shifts from 675 to 688 nm. In fact, if the shell thickness is increased, then the photoluminescence peak wavelength can even shift to 800 nm. We also check the time-resolved behavior of CdTe core and CdTe/CdSe core/shell nanocrytal quantum dots as shown in Figure 3.3.3.1. As expected, the lifetime of the core/shell nanocrystals increases with respect to the only core case due to the transition from type-I configuration to quasi-type-II configuration. We further check the blinking behavior of these nanocrystals as presented in Figure 3.3.3.2. We can see that the quasi-type-II CdTe/CdSe core/shell nanocrystals positively exhibit constant emission intensity without blinking within the time scale shown in the Figure, while nanocrystals with type-I band configuration shows strong intensity fluctuations. Although today the reason of the blinking is not certainly known, it is attributed to the Auger recombination. Therefore, suppression of Auger process in quasi-type-II nanocrystals is important to enhance the efficiency of nanoparticles and generate multi-excitons. Today another solution to suppress Auger recombination is making thick enough shell (>10 monolayers) around the core nanocrystals [42].

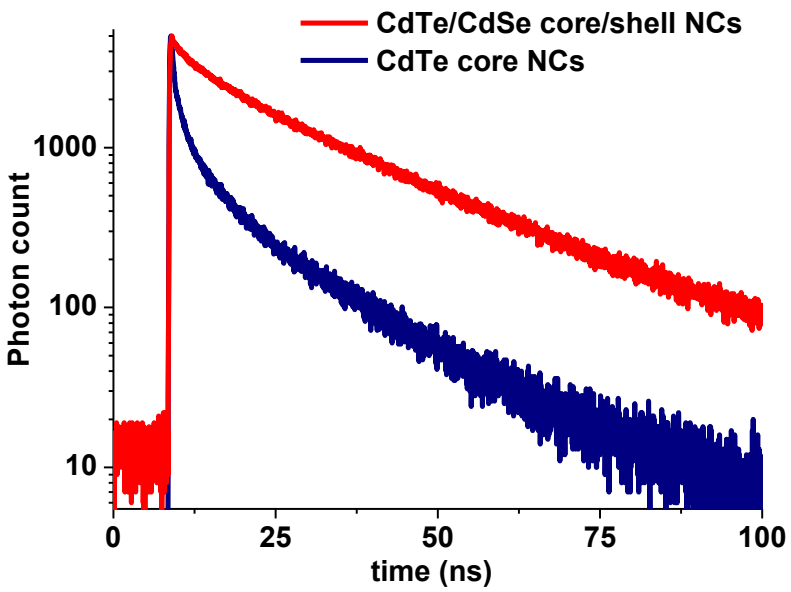

Figure 3.3.3.1 Absorption and photoluminescence spectra of our synthesized CdTe core and CdTe/CdSe core/shell nanocrystal quantum dots.

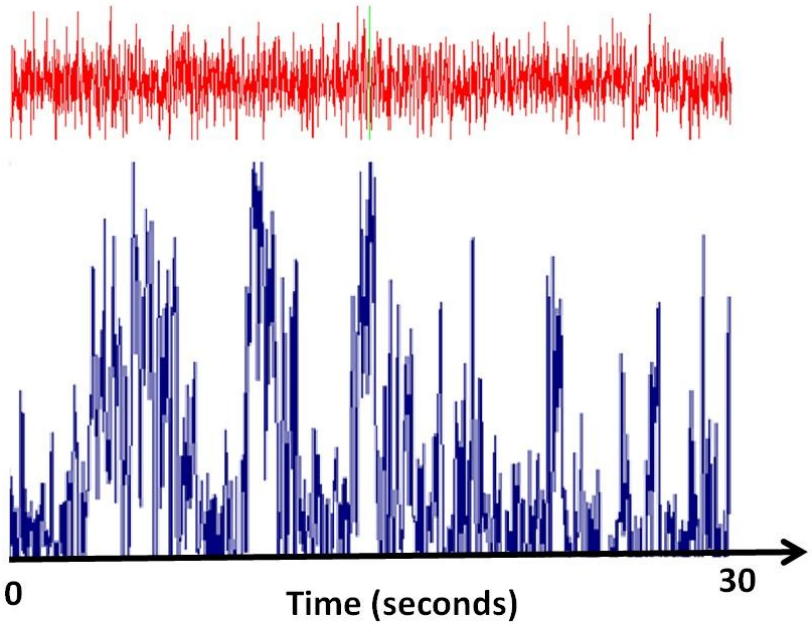

Figure 3.3.3.2 Time-trace of quasi-type-II nanocrystals (red line) and type-I nanocrystals (blue line).

3.3.4 Exotic nanoparticles: CdSe/ZnS/CdSe core/shell/shell nanocrystals

Although CdSe core and CdSe/$Cd_xZn_{1-x}S$ core/shell materials have single emission peak, by continuing the growth of the shell with a CdSe shell, dual peak emission can be generated as depicted in Figure 3.3.4.1 (The physics of dual emission characteristics will be discussed in detail with quantum mechanical simulations in Section 5.1). These CdSe/ZnS/CdSe core/shell/shell nanocrystal quantum dots are also called as onion-like nanocrystals as well.

Their synthesis starts with making CdSe core NCs [43]. For that, 0.1 mmol CdO is dissolved in 0.83 mmol OA and 4 mL ODE and heated at 300 ^oC under Ar atmosphere. Another solution of Se/TOP/ODE (0.05 mmol/0.5 mL/0.5 mL) is dissolved at 100 ^oC. The Se/TOP/ODE solution is then injected into the colorless Cd/OA/ODE solution at 300 ^oC. The temperature is dropped to 280 ^oC and heating is continued for 30 s at this temperature. The nanocrystals are separated by precipitation and redissolved in hexane. 10^{-7} mol of these NCs, 3 g hexadecylamine (HDA) and 3 mL ODE are added and heated to 200 ^oC. Subsequently, a colorless solution (0.1 M) of ZnO and OA (1:4 ratio) in 10 mL ODE is prepared by heating the mixture to 300 ^oC. The Cd/OA, S, and Se/TBP solutions, all 0.1 M, are used for overcoating to make shells. Adequate amounts of the Zn (Cd) and S (Se) solutions required for one shell growth are added to the core CdSe NC solution and the heating is continued for 30 min. Small aliquots of the reaction mixture are recovered, precipitated with acetone, and finally dissolved in toluene.

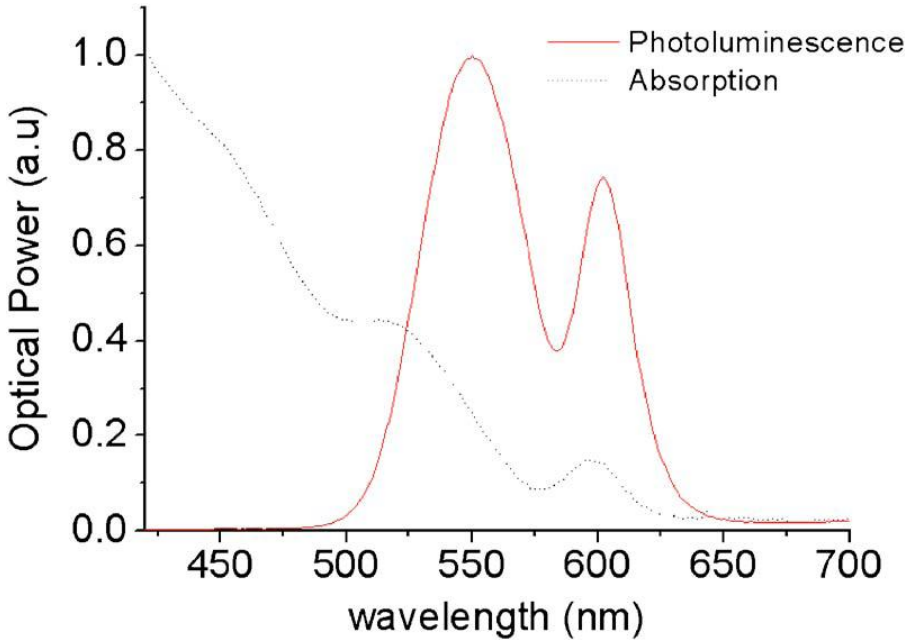

Figure 3.3.4.1 Absorption photoluminescence and absorption spectra of onion-like (CdSe)ZnS/CdSe (core)shell/shell nanocrystals in solution.

3.3.5 Exotic nanoparticles: CdS trap-rich nanocrystals

For white light generation we synthesize trap-rich CdS nanocrystal luminophores. The synthesis of CdS nanocrystals is carried out at a Schlenck line under Argon atmosphere. 0.1 mmol CdO is dissolved in 4 mL octadecene using 0.6 mmol oleic acid at ~200 °C. The temperature is then raised to 250 °C. A 0.1 M sulfur solution is prepared separately by dissolving elemental S in octadecene. 0.5 mL of the S solution is injected into the hot Cd solution at 250 °C and heated for 5 minutes. The solution is immediately cooled down and the nanocrystals precipitated and redissolved in toluene.

The surface states of these luminophores give rise to a broad emission band that spans the entirety of the visible spectrum. When pumped by a light source at a higher photon energy than their effective band gap energy, the radiative recombination through the interband and mid-gap states takes place and, as a

result, white light is generated. Here the particle diameter of CdS luminophores is about 2.4 nm, as inferred from the absorption edge at 400 nm [44], [45]. The narrow peaks of their absorption spectrum (with a half-width-at-half-maximum (HWHM) of 14 nm) and their emission spectrum (with a full-width-at-half-maximum (FWHM) of 22 nm) indicate a very narrow size distribution of these nanocrystals. The photoluminescence of CdS NCs presented in Figure 3.3.5.1 corresponds to chromaticity coordinates of (x = 0.34, y = 0.35), a correlated color temperature of 5146 K, and a color rendering index of 82.5, when in toluene solution. For example, well-known magic-sized CdSe nanocrystals with a diameter of 1-2 nm generate white light, but their quantum efficiency (QE) is restricted to 2-3% [45]. Different from CdSe nanocrystals, CdS surface state emitting (SSE) nanocrystals with a dot diameter of 2-3 nm generate white light emission exhibiting a relatively high QE of 17% [45].

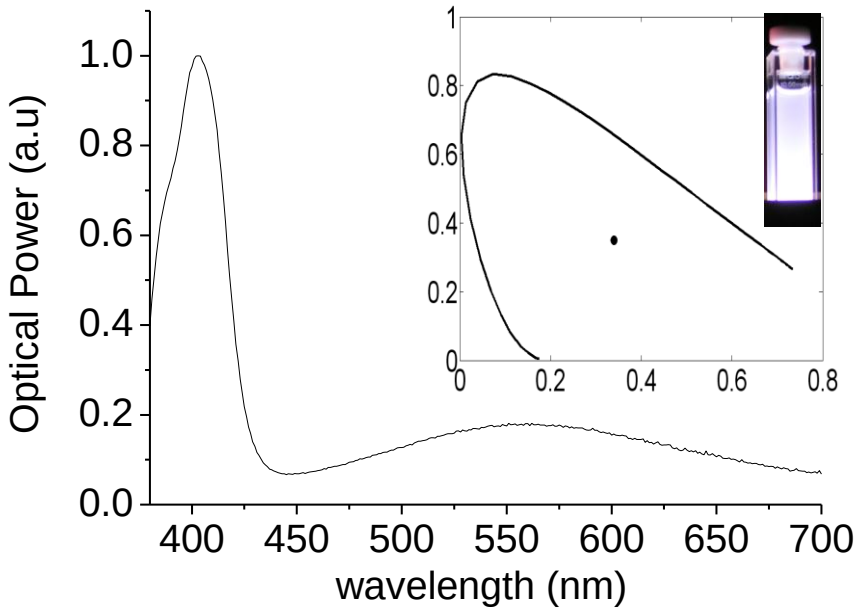

Figure 3.3.5.1 The photoluminescence spectrum of CdS surface state emitting nanocrystals in toluene solution. The corresponding *(x,y)* chromaticity coordinates and a photograph of the white light generated by these CdS nanocrystals in toluene solution under UV excitation are also provided in the inset.

3.3.6 CdTe nanocrystals in aqueous solution

The previously explained nanocrystal quantum dots are soluable in nonpolar solvents such as toluene, hexane, chloroform, *etc*. They can be transferred to aqueous solution by ligand exchange. Another possibility is the synthesis directly in aqueous environment, as is performed in Prof. Alexander Eychmüller`s lab in Technical University of Dresden. For the synthesis of CdTe nanocrystal quantum dots in aqueous medium, we mix $Cd(ClO_4)_2 \cdot 6H_2O$ and milli-Q water. We add thioglycolic acid (TGA) to the solution and the TGA:Cd^{2+} ratio is crucial for the stability and quality of NCs and should be equal to 1:3. From the glove box, we take Al_2Te_3 and add it to the solution. In a separate bottle we prepare H_2SO_4 solution and inject dropwise H_2SO_4 solution into the reaction solution. Then, we start to heat the solution and the nanocrystals start to grow. Since this reaction takes place in water, the reaction temperature is not as high as the temperature in nonpolar solvents. Thus, the reaction time in aqueous medium is slower. Another disadvantage of this synthesis is that growing shell on top of the nanocrystals in aqueous medium is not easy.

3.4 Quantum mechanical calculation of nanocrystal quantum dots

Nanocrystals such as (CdSe)ZnS (core)shell quantum dots typically reveal almost spherical, slightly elongated shapes according to the high-resolution transmission electron microscopy (HRTEM) measurements [46]. In our theoretical formalism, for simplicity we consider a spherically symmetric heteronanocrystal structure to separate its wavefunctions into the radial and angular parts, as presented in Equation (3.4.1) in spherical coordinates (r,θ,ϕ). In Equation (3.4.1), $R_{nl}(r)$ is the radial wavefunction, $Y_{lm}(\theta,\phi)$ is the spherical harmonic, n is the principal quantum number, and l and m are the angular momentum numbers. Here, in the case that a particular eigenenergy (E_{nl}) of the

heteronanocrystal is higher than the potential in its q^{th} layer, *i.e.*, $E_{nl}>V_q$, then the corresponding radial wavefunction $R_{nl,q}(r)$ (the radial wavefunction in the q^{th} layer) for the associated energy state E_{nl} is a linear combination of spherical Bessel and Neumann functions. On the other hand, in the case of $E_{nl,q}<V_q$, the solution $R_{nl,q}(r)$ is a linear combination of Hankel functions.

For our theoretical analysis, we apply effective mass approximation, which is a widely-used method in quantum mechanical analysis. It has been previously shown that the effective mass approximation works well even for few-monolayer quantum structures [47]. Thus, the effective mass approximation has been used for a number of spherical nanocrystal heterostructures [48]. Also, in our theoretical analysis as a valid approach, we solve for the energy levels (eigenvalues) and wavefunctions (eigenfunctions) of the CdSe-ZnS heteronanocrystal using effective mass approximation. The associated wavefunction solutions must then satisfy the continuity condition at all boundaries of the heteronanocrystal layers (*i.e.*, the boundary conditions) as in Equations (3.4.2) and (3.4.3).

$$\psi_{nlm}(r,\theta,\phi) = R_{nl}(r)Y_{lm}(\theta,\phi) \qquad (3.4.1)$$

$$R_{nl,q}(r)|_{r=r_q} = R_{nl,q+1}(r)|_{r=r_q} \qquad (3.4.2)$$

$$\frac{1}{m_q^*}\frac{dR_{nl,q}(r)}{dr}\bigg|_{r=r_q} = \frac{1}{m_{q+1}^*}\frac{dR_{nl,q+1}(r)}{dr}\bigg|_{r=r_q} \qquad (3.4.3)$$

For example, the origin and physics of dual-color emission (CdSe)ZnS/CdSe/ZnS (core)shell/shell/shell nanocrystal quantum dots are not understood. Therefore, we quantum-mechanically investigate these heteronanocrystals in detail to understand their optical properties. In (CdSe)ZnS/CdSe/ZnS (core)shell/shell/shell hetero-NC (that will be discussed in Section 5.1 in detail), there are four layers and three boundaries, as

schematically shown in Figure 5.1.1. Because $R_{nl}(r)$ has to be regular at r = 0 and has to converge to zero when $r \to \infty$, there are six unknown coefficients for its basis functions, and there are six equalities coming from Equations (3.4.2) and (3.4.3) applied at its three boundaries. To find nontrivial solution, the determinant of these coefficients should be zero, *i.e.*, $D_l=D_l(E_{nl})=0$. Restricting our consideration to only S-symmetry states (with zero angular momentum), the wavefunction depends on the radial part $R_{n,l=0}(r)$ that makes $l=0$ and $m=0$, and thus the wavefunction becomes only dependent on r. By using the normalization condition for $R_{nl}(r)$, all the coefficients of the basis functions are then determined [49], [50].

After solving for energy levels and wavefunctions, we calculate the exciton binding energy due to the Coulomb interaction between the electron and hole pair using the first-order perturbation theory [50]. The binding energy is given in Equation (3.4.4), where *e* and *h* subscripts refer to electron and hole, respectively, and ε is the high frequency dielectric constant. After expanding the $1/|r_e-r_h|$ term in Equation (3.4.4) in the form of spherical harmonics and integrating over the angular coordinates, the binding energy is written as in Equation (3.4.5), where $\bar{\varepsilon}_r$ is the mean dielectric constant.

$$E_c = -\int\int dr_e dr_h \frac{\psi_e^*(r_e)\psi_h^*(r_h)\psi_e(r_e)\psi_h(r_h)}{|r_e - r_h|\,\varepsilon(r_e, r_h)} \tag{3.4.4}$$

$$E_c = -\frac{e^2}{4\pi\varepsilon_0}\int\int dr_e dr_h r_e^{\,2} r_h^{\,2} \frac{|R_e(r_e)|^2 |R_h(r_h)|^2}{\max(r_e, r_h)\bar{\varepsilon}_r(r_e, r_h)} \tag{3.4.5}$$

The material parameters used in our quantum mechanical analysis is summarized in Table 3.4.1 [51], [52]. When a single monolayer of CdSe (or ZnS, by the same token) is added surrounding an existing spherical dot, the expansion of the resulting dot occurs in all three directions (x,y,z). However, (CdSe)ZnS/CdSe/ZnS hetero-NC is made of a wurtzite structure, in which the

lattice constants in x and y directions are equal and the lattice constant in z direction is different from the others. Therefore, we calculate the mean of lattice constants in x-y plane and z direction. As a result, we take 1 monolayer (ML) CdSe to be 0.56 nm thick [53] and 1 ML ZnS to be 0.49 nm thick [54], given in Table 3.4.1. For our simulations we use a CdSe core of 2.75 nm radius and subsequently add alternative layers of ZnS and CdSe shells, each with changing thickness from 1 to 3 monolayers around this CdSe core. To find bounded solutions, we complete the onion-like structure with an infinitely thick ZnS barrier.

Table 3.4.1 Material parameters of CdSe and ZnS

Material	$\mathbf{m_e^*}$	$\mathbf{m_h^*}$	**Monolayer thickness (nm)**	**Band discontinuity (eV)**
CdSe	0.13	0.45	0.56	-
ZnS	0.28	0.49	0.49	1.75 with respect to CdSe)

3.5 Measurement techniques

3.5.1. Time-resolved spectroscopy

We use a fluorescence lifetime system of FluoTime 200 spectrometer (shown in Figure 3.5.1.1) by PicoQuant to measure time-resolved dynamics of luminescent materials. The system uses a time-correlated single photon counting (TCSPC) system of PicoHarp 300, which provides a highly stable and crystal calibrated time resolution of 4 ps [55]. As the detector, the system has a photon multiplier detector array (PMA) that is based on the Hamamatsu H5783 series photosensor module. PMA unit consists of built-in high voltage power supply, signal pre-amplifier and a gold plated iron allowing for optimal timing performance. For the pump, the system has a LDH-D-C-375 laser head controlled by a PDL-800B driver that provides picosecond laser pulses at 375 nm. As a result, our system achieves an instrument response function (IRF) FWHM of 200 ps, as shown in Figure 3.5.1.2.

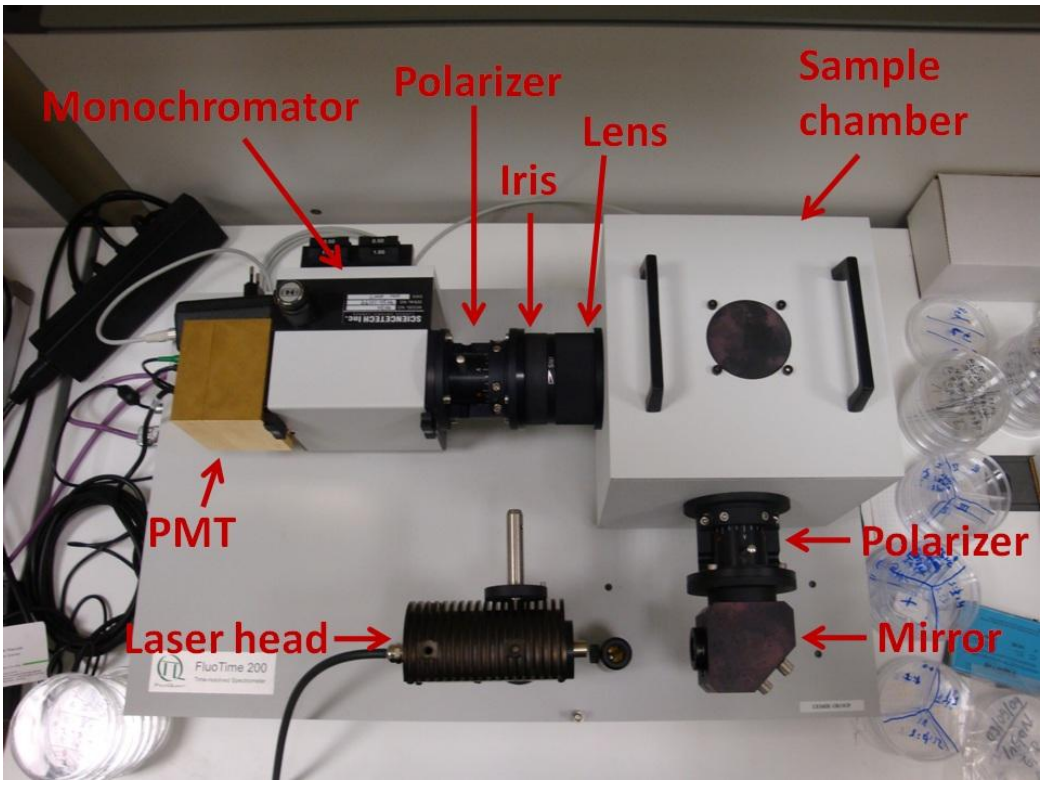

Figure 3.3.5.1 Time-resolved measurement setup (FluoTime 200 spectrometer).

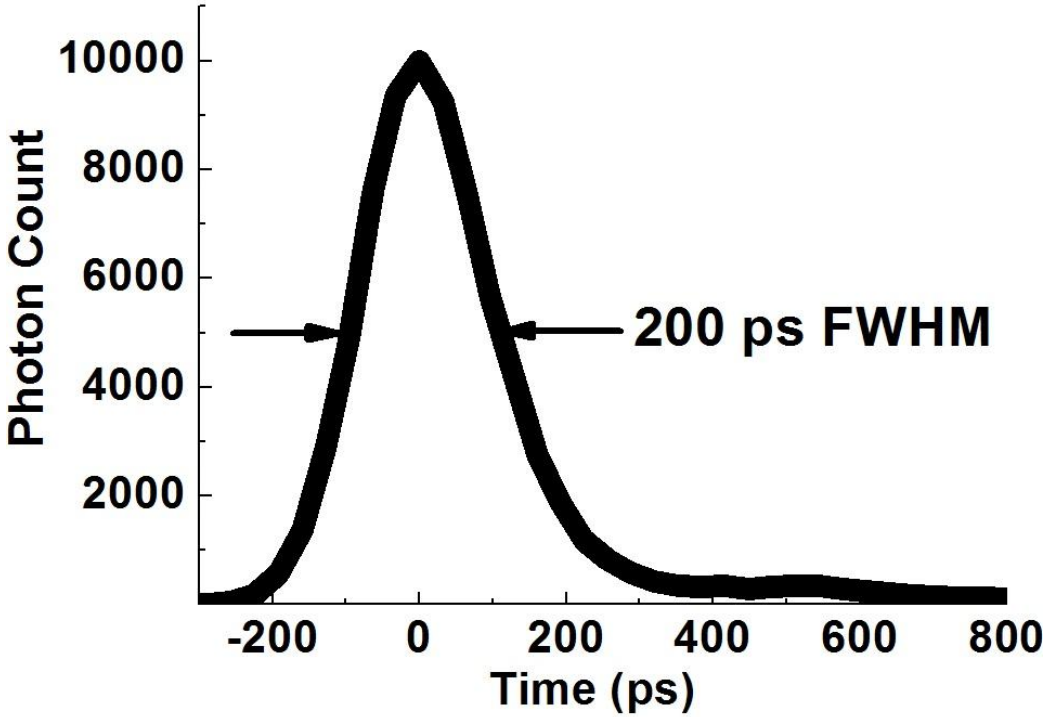

Figure 3.5.1.2 Instrument response function and full-width-at-half-maximum (FWHM) of our time-resolved system.

Because of the finite temporal response of IRF, the exhibited decays are the actual response of materials response convoluted with the IRF response. Thus, the time-resolved emission decays may not seem as perfect exponentials. In our analysis, we take this case into account in our calculations and make fits to the measured decays accordingly. For fitting which we use Equation (3.5.1.1), where IRF(t) is the instrument response function, A is the amplitude, and τ_i is the lifetime of the samples. The time-resolved spectroscopy system helps us to extract the rates of radiative and nonradiative recombination, and of energy transfer and quenching of material systems.

$$I(t) = \int_{-\infty}^{t} IRF(t') \sum_{i=1}^{n} A_i e^{-\frac{(t-t')}{\tau_i}} dt' \qquad (3.5.1.1)$$

3.5.2 Photoluminescence spectroscopy

For photoluminescence spectroscopy the materials are excited through a light source with photon energy higher than the band gap of the material. Consequently, the material makes photoluminescence and the emission is detected with a photodetector. The photoluminescence allows us to extract information about the recombination energy, relative efficiency and size-distribution of nanocrystal quantum dots.

3.5.3. Absorption spectroscopy

The absorption spectrum of the materials is measured with respect to a reference sample (*e.g.*, air, water, glass, *etc*.) by determining the transmitted light intensity at each wavelength in the chosen interval. By using absorption spectroscopy, we can obtain an idea on the quality and size of the nanocrystal quantum dots. In nanocrystal quantum dots, 4-5 different excitonic transitions can be resolved from optical density (*i.e.*, absorbance). Furthermore, we can determine the Stokes shift by using the difference of the first excitonic peak energy and

photoluminescence peak energy. The spectrometer provides data of absorbance and by using Equation (3.5.3.1) the ratio of the transmitted light to the incoming light can be extracted.

$$\text{Absorbance} = -\log(\text{transmittance}) \qquad (3.5.3.1)$$

3.5.4. Quantum efficieny measurement

For quantum efficieny measurement, we use a light source integrated with monochromator to excite the nanoparticles and an integrating sphere to collect the total emission coming from nanocrystals as shown in Figure 3.5.4.1. The quantum effiency of nanocrystal quantum dots is calculated by dividing the total number of photons generated by the nanocrystals to the number of photons absorbed by the materials. Although two decades ago the efficiency of nanocrystals were generally less than 10%, today nanocrystals with quantum efficiency higher than 80% can be synthesized due to the increased understanding on their electrical and optical properties and with optimized synthesis procedures. We also use the integrating sphere to calculate the efficiency of light emitting diodes by injecting current to the diodes.

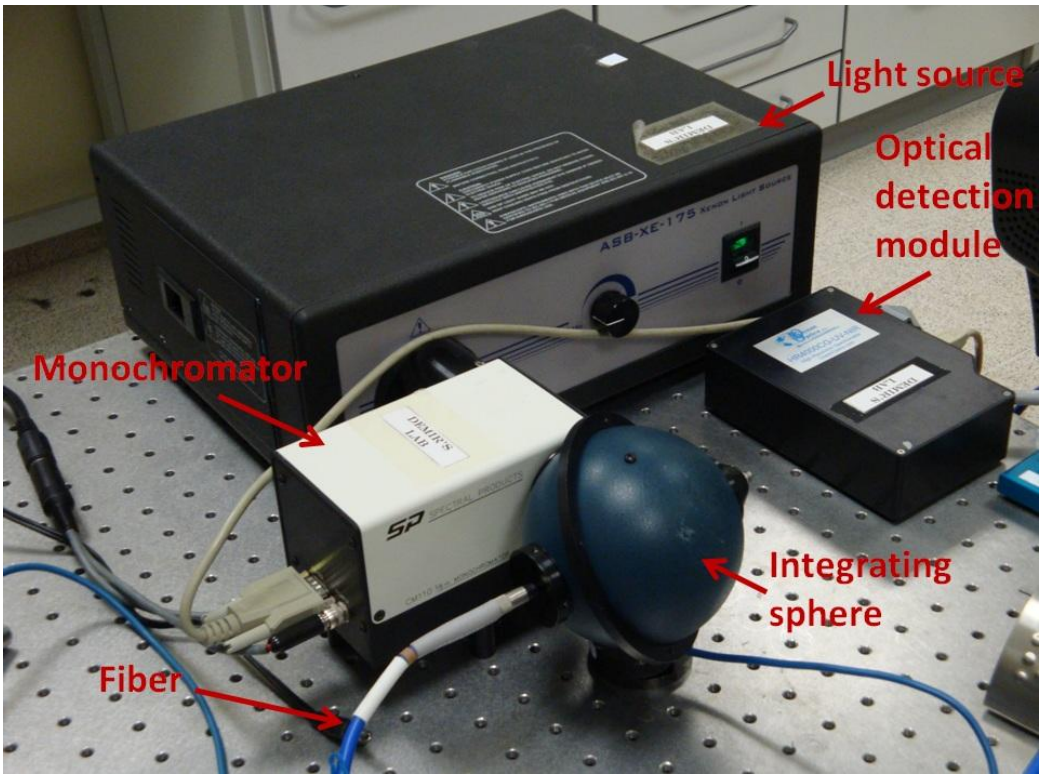

Figure 3.5.4.1 A home-made quantum efficiency measurement setup.

3.5.5. Electroluminescence

The resulting hybrid LEDs are characterized on a probe station with dc probes placed on the LED to electrically drive them by a current power supply (HP4142B Modular dc Source/Monitor), while collecting the emitted light through an optical system to couple into a multimode fiber connected to an optical spectrum analyzer setup (Ocean Optics PC2000 with an optical resolution of 0.5 nm). A photograph taken during an electroluminenscence measurement of nanocrystal integrated white LED is shown in Figure 3.5.5.1.

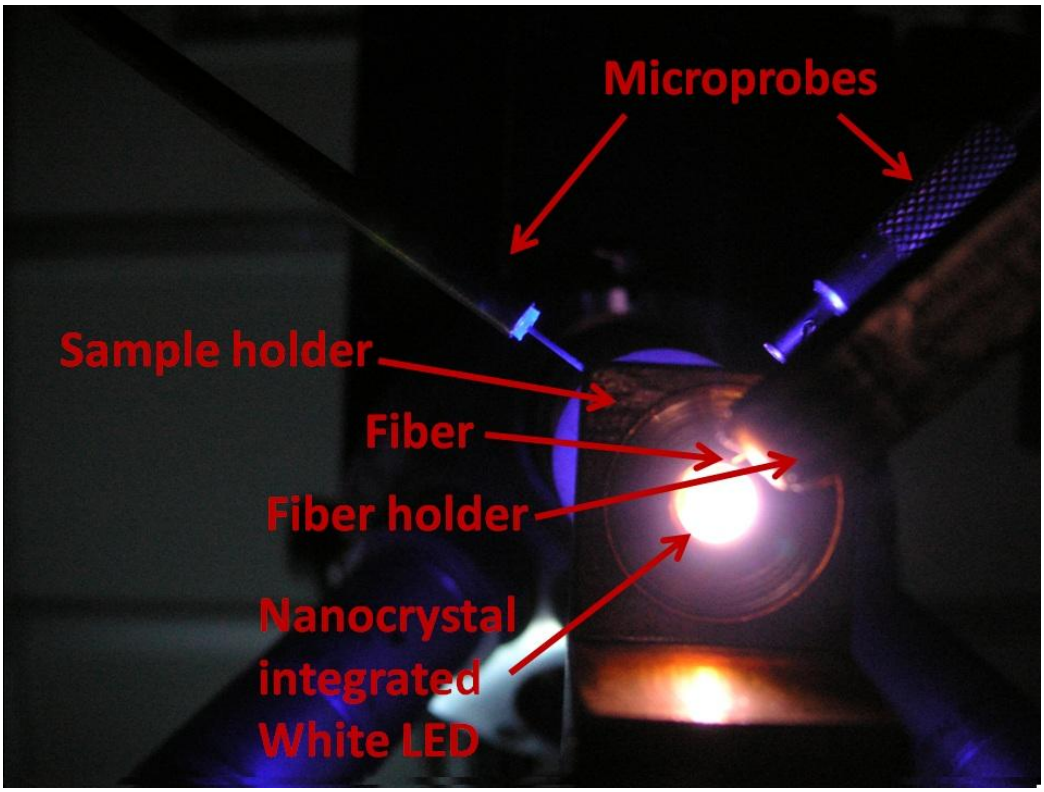

Figure 3.5.5.1 A home-made electroluminescence measurement setup.

Chapter 4

Superior white light emitting diodes hybridized with nanocrystal quantum dots for high photometric performance

4.1 Hybrid white-LEDs with high color rendering index utilizing color-converting combinations of nanocrystal emitters

This section is based on the publication "Color-converting combinations of nanocrystal emitters for warm-white light generation with high color rendering index" **S. Nizamoglu**, G. Zengin, and H. V. Demir, Applied Physics Letters 92, 031102 (2008). Reproduced (or 'Reproduced in part') with permission from American Institute of Physics.

Warm-white light emitting diodes with high color rendering indices are required for the widespread use of solid state lighting (SSL) especially indoors. To meet these requirements, in this section we propose and demonstrate warm-white hybrid light sources that incorporate the right color-converting combinations of CdSe/ZnS core-shell nanocrystals hybridized on InGaN/GaN LEDs for high color rendering index. Three sets of proof-of-concept devices are developed to

generate high-quality warm-white light with 1.) tristimulus coordinates *(x,y)*=(0.37,0.30), luminous efficacy of optical radiation *LER*=307 lm/W_{opt}, color rending index *CRI*=82.4, and correlated color temperature *CCT*=3228 K; 2.) *(x,y)*=(0.38,0.31), *LER*=323 lm/W_{opt}, *CRI*=81.0, and *CCT*=3190 K; and 3.) *(x,y)*=(0.37,0.30), *LER*=303 lm/W_{opt}, *CRI*=79.6, and *CCT*=1982 K, as shown on the CIE 1931 chromaticity diagram in Figure 4.1.1.

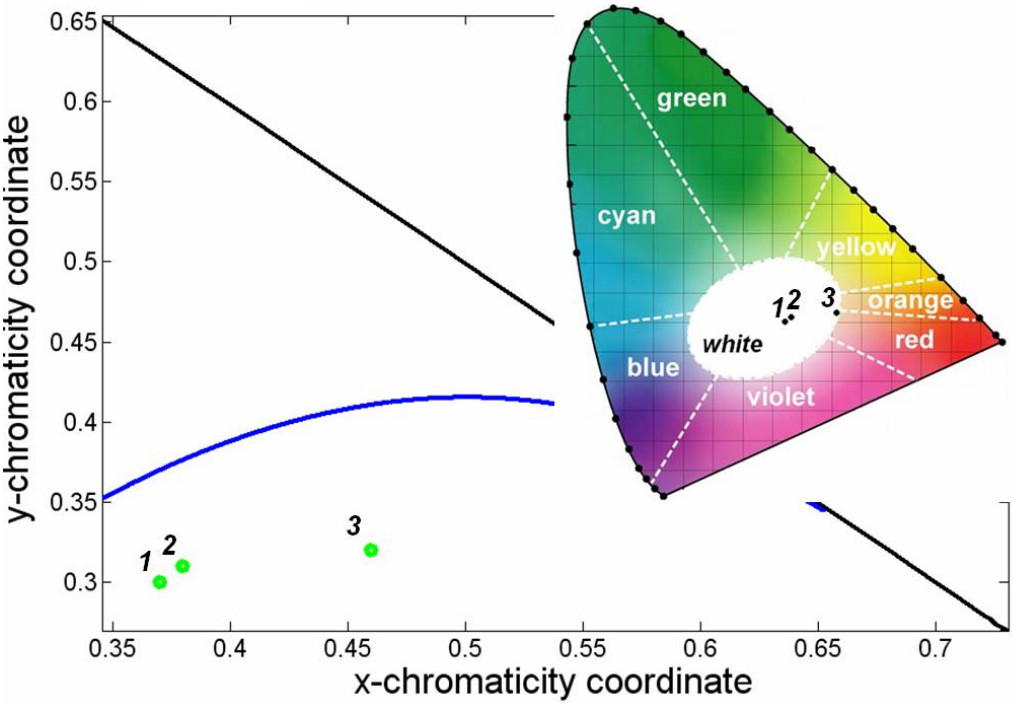

Figure 4.1.1 CIE chromaticity diagram zoomed-in for the loci of the tristimulus coordinates of our nanocrystal-hybridized warm-white light emitting diodes (green points) along with the Planckian locus (blue line). A complete CIE 1931 chromaticity diagram, *e.g.*, as in Ref. [4], is also given with the tristimulus coordinates of our hybrid warm-white light emitting diodes in the inset.

4.1.1 Introduction

Solid state lighting offers an effective way to deal with the challenge of reducing greenhouse gas emission and combating climate change. Today the most commonly used SSL sources are based on the integration of yttrium aluminum

garnet (YAG) phosphors on blue InGaN/GaN light emitting diodes [4], [7]. The broad yellowish emission of YAG phosphors along with blue LED yields white light generation with correlated color temperatures of 4000-8000 K, corresponding to the neutral- and cool-white intervals, and color rendering indices typically lower than 80 [2], [9]. However, especially for wide-scale use in indoor illumination applications, white light emitting diodes (WLEDs) are required to provide warm enough *CCT* (< 4000 K) with high enough *CRI* (> 80) [1], [2], [9] .

Nanocrystal emitters are particularly advantageous for use in white light sources because they feature tunable and relatively narrow emission across the visible spectral range and small overlap between their emission and absorption spectra, and also provide the ability to be easily and uniformLy deposited in solid films with common techniques (*e.g.*, spin casting, dip coating). In the previous reports, white light generation using CdSe/ZnS core-shell nanocrystals of single, dual, trio, and quadruple combinations on blue InGaN/GaN LEDs have been demonstrated [56]. A blue/green two-wavelength InGaN/GaN LED coated with a single type of red NC and a blue InGaN/GaN LED with a single type of yellow NC and a dual type of red and green NCs have been also reported [6], [57]. In our previous work, white light generation with high color rendering index > 80 using dual hybridization of nanocrystals and polymers on LEDs has been achieved [58]. Additionally, WLEDs have been realized by integrating NCs with polymethylmethacrylate (PMMA) on ultraviolet LEDs [59]. These NC-based white LEDs have been shown to exhibit high *CRI*. But in the previous studies of our group and others, using such high-*CRI* nanocrystal-based hybrid LEDs, warm correlated color temperature along with high *CRI* has not been demonstrated, although such high-quality white light is required for the future according to the SSL roadmap [1], [2], [9].

4.1.2 Design strategy

The use of such nanocrystal emitters facilitates achieving low correlated color temperature, while maintaining the chromaticity operating point within the white region and keeping color rendering index high. This is primarily because nanocrystals have relatively narrow emission in the visible (*e.g.*, full width at half maximum <30 nm in solution) and their peak emission wavelength can be fine-tuned with the size effect as necessary. Therefore, using a right color-converting combination of nanocrystals, it is possible in principle to generate and adjust any emission spectrum as desired. Also, in the case of using such nanocrystal emitters, the red emission above 650 nm can be significantly avoided, unlike using the phosphors, which exhibits strong emission tail in the red above 650 nm and reduces its luminous efficacy of optical radiation (because of the eye sensitivity function decreasing quickly above 650 nm). The hybrid NC-LED luminescence can thus be carefully tuned by taking into account the eye sensitivity function to achieve high luminous efficacy.

The operating principle of these hybrid NC-WLEDs is based on the mutual use of the integrated NC film as the photoluminescent layer and the LED as the pump light source. The integrating LED platform optically excites the NC emitters when it is electrically driven. Consequently, the NC photoluminescence and the LED electroluminescence collectively contribute to the white light generation. We use InGaN/GaN based blue light emitting platform as the excitation source at 452 nm. We design and grow the epitaxial structure of these InGaN/GaN LEDs and fabricate them using the standard microfabrication techniques similar to those described in our previous work [56], [60]. Such InGaN/GaN LEDs are demonstrated to achieve long lifetime (up to 20,000 hours) [7].To make the hybrid warm-WLEDs, we integrate green- and red-emitting CdSe/ZnS core-shell NCs (at λ_{PL}=555 and 613 nm, respectively) in the PMMA matrix on top of the blue LEDs. The optical properties of these nanocrystals and their hybridization method are also explained in our previous work [56]. Such nanocrystal emitters have been investigated to study their

photostability; typical shelf lifetime of these nanocrystals is reported to be longer than 15,000 hours. To obtain white light generation with warm color temperature and high color rendering index, we analyze the blackbody radiators on the planckian locus of CIE chromaticity diagram, which are used as the reference sources. Based on this analysis, we set the correct amount of NC emitters for the LED hybridization to achieve high performance. In Figure 4.1.2 we show the spectrum of blackbody radiators at the color temperature of the fabricated hybrid warm-white light emitting diodes (Samples 1-3). As the color temperature of the radiators decreases (getting warmer in color), the red part in the visible becomes more dominant. Therefore, to achieve warmer color temperatures, we increase the red luminescence in the visible spectrum, while maintaining the chromaticity point in the white region and sustaining high color rendering index.

4.1.3 Experimental characterization of hybrid white LEDs and discussions

In the first experimental proof-of-concept demonstration, for their hybridization on blue LED (λ_{EL}=452 nm), we design to incorporate 0.22 mg (0.578 nmoles) of red-emitting CdSe/ZnS core-shell NCs and subsequently 0.26 mg (2.166 nmoles) of green-emitting NCs. These nanocrystals are selected with sizes of 9.6 nm and 7.7 nm in diameter (with a size distribution of ±5%) to emit at the peak wavelengths of 613 nm and 555 nm, respectively. These red nanocrystal emitters are carefully chosen to provide sufficiently red emission to increase the color temperature, which is not too red in color to contribute significantly to emission above 650 nm and undesirably reduce the luminous efficacy. On the other hand, the green nanocrystal emitters are chosen to balance out the red emission conveniently at 555 nm along with the blue LED emission at 452 nm and, consequently, keep the operating chromaticity coordinates within the white region and the color rendering index high enough. We obtain the luminescence of the resulting hybrid LED at various current injection levels as shown in

Figure 4.1.2. As the injected current increases, the luminescence of the hybrid LED increases, while maintaining the relative peak levels in the blue, green, and red. At all current injection levels, the emission of the LED leads to (x, y)=(0.37, 0.30), *LER*=307 lm/W_{opt}, *CRI*=82.4, and *CCT*=3228 K. This corresponds to a warm-white LED with a high color rendering index of 82.4, satisfying the future SSL criterion of *CRI* ~ 80.[4,7,8]

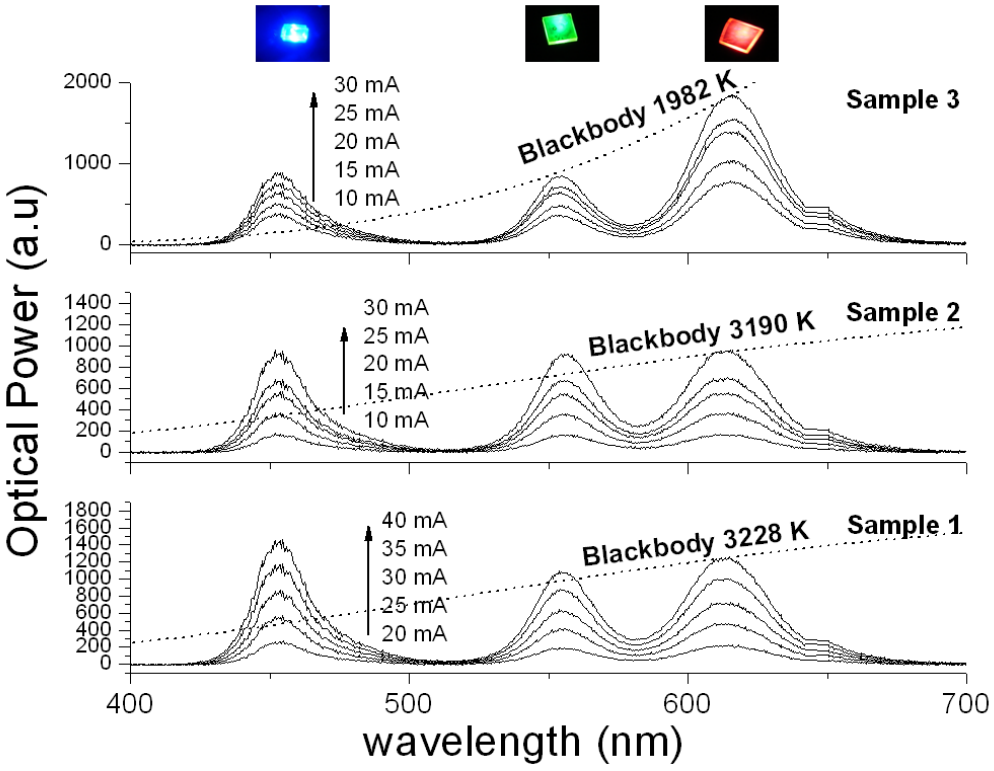

Figure 4.1.2 Luminescence spectra of our nanocrystal hybridized warm-white light emitting diodes (Samples 1-3).

For the second demonstration, we design to integrate 0.13 mg (1.083 nmoles) of green-emitting CdSe/ZnS core-shell NCs (λ_{PL}=555 nm) and then 0.44 mg (1.156 nmoles) of red-emitting NCs (λ_{PL}=613 nm) on the top of blue LED (λ_{EL}=452 nm). Again, the nanocrystal emitters are carefully chosen to mimic the optical spectrum of the associated black-body radiator as much as possible. We show the luminescence of the hybrid LED at various current injection levels in Figure

4.1.2. This implementation experimentally leads to (x, y)=(0.38, 0.31), *LER*=323 lm/W_{opt}, *CRI*=81.0, and *CCT*=3190 K. Here the tristimulus coordinates shift to the red side of the CIE chromaticity diagram and the correlated color temperature decreases to 3190 K because of the increased relative intensity of the red-emitting nanocrystals. Therefore, this light source achieves warmer-white light generation while maintaining its chromaticity point in the white. The color rendering index slightly drops to 81.0, which still satisfies the criterion for the future SSL sources, and the luminous efficacy reaches a relatively high value of 323 lm/W_{opt}.

As the last demonstration, we design to hybridize 0.13 mg (1.083 nmoles) of green-emitting CdSe/ZnS core-shell NCs (λ_{PL}=555 nm) and 0.66 mg (1.734 nmoles) of red-emitting NCs (λ_{PL}=613 nm) on the blue LED (λ_{EL}=452 nm). The resulting emission spectra at various levels of current injection are shown in Figure 4.1.2, corresponding to (x, y)=(0.37, 0.30), *LER*=303 lm/W_{opt}, *CRI*=79.6, and *CCT*=1982 K. This operating point stands approximately on the boundary of white region near to the red color end as shown in Figure 4.1.2. Therefore, this hybrid white LED generates highly warm-white light at an extra-low correlated color temperature of 1982 K.

Hybridizing CdSe/ZnS core–shell NC emitters on InGaN/GaN-based blue LEDs, we demonstrate three warm-white light sources with *CCT* ranging from 3227 to 1982 K. In these proof-of-concept demonstrations, the color rendering indices as high as 82.4 and luminous efficacies as high as 327 lm/W_{opt} are achieved. Table 4.1.1 provides a list of these hybrid nanocrystal-based warm-white light emitting diodes along with their corresponding (x, y) coordinates, *LER*, *CRI*, and *CCT*.

Table 4.1.1 Optical properties of our nanocrystal hybridized warm-white light emitting diodes.

Sample #	x	y	*LER* (lm/W_{opt})	*CRI*	*CCT* (K)
1	0.37	0.30	307	82.4	3228
2	0.38	0.31	323	81.0	3190
3	0.46	0.32	303	79.6	1982

4.1.4 Conclusion

In this section, we presented nanocrystal-hybridized warm-white light emitting diodes with high color rendering index. In this work the use of nanocrystal emitters in the right color-converting combinations enabled such hybrid white light sources to achieve highly warm correlated color temperature, while maintaining their operating chromaticity coordinates in the white region and sustaining their high color rendering index. Our proof-of-concept demonstrations indicate that such nanocrystal-based warm-white light emitting diodes with high-quality white light properties hold great promise especially for future indoor lighting applications.

4.2 Warm-white LEDs integrated with colloidal quantum dots for high luminous efficacy and color rendering

This section is based on the publication "Warm-white light-emitting diodes integrated with colloidal quantum dots for high luminous efficacy and color rendering" **S. Nizamoglu**, T. Erdem, X. W. Sun and H. V. Demir, Optics Letters 35, 3372-3374 (2010). Reproduced (or 'Reproduced in part') with permission from Optical Society of America. Copyright 2010 Optical Society of America.

Warm-white light-emitting diodes with high spectral quality and efficiency are required for lighting applications, but the current experimental performances are limited. In this section, we report on nanocrystal quantum dot hybridized WLEDs with high performance, which exhibit a high luminous efficacy of optical radiation exceeding 350 lm/W_{opt} and a high color rendering index close to 90 at a low correlated color temperature <3000 K. These spectrally-engineered WLEDs are obtained using a combination of CdSe/ZnS core/shell NC nanophosphors integrated on blue InGaN/GaN LEDs.

4.2.1 Introduction

Theoretical emission spectra of white light-emitting diodes have been investigated to achieve efficient solid state lighting with a high color rendering index approaching 90 and a luminous efficacy higher than 350 lm/W_{opt} [61]. However, the reported sets of experimental luminous efficacy of optical radiation and color rendering index have been limited [2], [37], [62]. A high color rendering index approaching 90 is important for general purpose lighting. A high *LER* exceeding 350 lm/W_{opt} is also essential to ensure that the light source provides an efficient spectral content for the human eye. As the current state-of-the-art, a warm-WLED with a *LER* of 274 lm/W_{opt} and a *CRI* of 89 at a

correlated color temperature of 3100 K has previously been demonstrated by using nitride-based Eu^{2+} phosphors on a blue LED [2]. For the current study, to outperform conventional phosphors in terms of *LER*, we developed photometric models, made new WLED designs, and experimentally demonstrated warm-WLEDs combined with nanophosphors of semiconductor nanocrystal quantum dots on LED chips to achieve *LER* >350 lm/W_{opt} with *CRI* =89.2 at *CCT* <3000 K.

4.2.2 Simulation and design

Since we use nanocrystals in a host medium (PMMA- poly(methyl methacrylate)), the environmental and dipole-dipole interactions prevent us from exactly predicting the peak emission wavelength shifts, emission broadenings and relative emission strengths. Thus, we need to perform a numerical analysis to study whether the intended high-quality white light generation can be achieved by using our green-, yellow- and red-emitting CdSe/ZnS core/shell nanocrystals. These nanocrystals are coated with long chain amine capping agents and exhibit respective photoluminescence peak wavelengths at 528, 560 and 609 nm in toluene. We employed the emission spectrum of each color source as a Gaussian function [4] and changed the emission peaks of each color with a 10 nm step size in the range of 450-470 nm for blue, 535-555 nm for green, 557-577 nm for yellow, and 610-630 nm for red. Furthermore, we varied the full-width at half-maximum (FWHM) of blue emission with a 10 nm step size from 25 to 55 nm and used a FWHM variation from 30 to 50 nm with the other color components. We also varied the peak amplitudes of each color from 430 to 470 units for blue, 750 to 790 units for green, and 470 to 510 units for yellow with a 20 unit step size; for red, the variation was set between 1400 and 1500 units with a 50 unit step size. As a result, we generated and simulated a total number of 1,180,980 hybrid LED designs using experimentally realistic input parameters in our simulations. In this analysis, we optimized our WLED performances for daytime vision (with a peak eye sensitivity response at 555 nm in photopic mode) rather than for nighttime vision (with a peak eye sensitivity

response at 507 nm in scotopic mode due to the Purkinje shift). To understand feasible performance of LEDs using these specific nanocrystals, the simulation results of *CRI* vs. *LER* are presented in Figure 4.2.1(a), including only those with the resulting photometric performances of *LER* >300 lm/W_{opt} and *CRI* >60. Consequently, these simulation results show that our NC nanophosphors are capable of achieving spectrally efficient and high-quality white light generation.

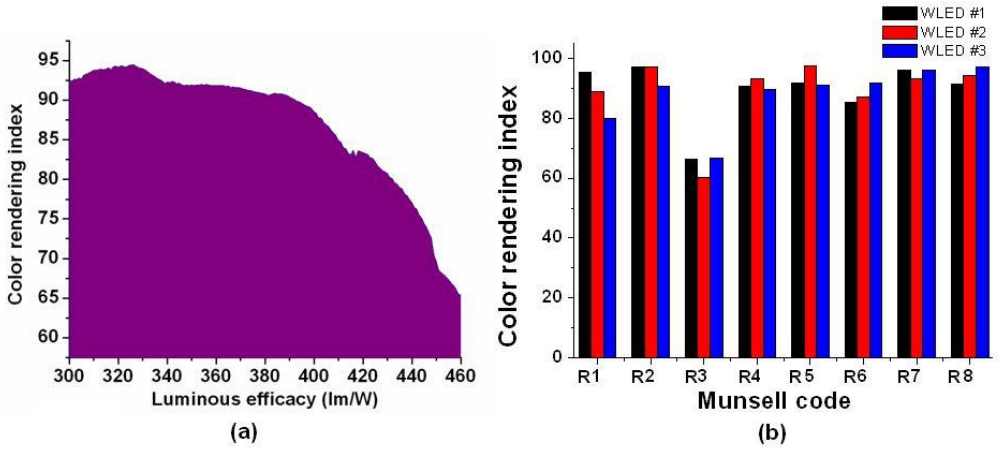

Figure 4.2.1 (a) Feasible sets of color rendering indices (*CRI*) vs. luminous efficacy of optical radiation (*LER*) for WLEDs integrated with NC nanophosphors, and (b) color rendering indices of NC-integrated warm-WLEDs (WLED #1, #2 and #3) analyzed at different Munsell hues.

4.2.3 Experimental characterization of hybrid white LEDs and discussions

For our first design of NC integrated WLEDs (WLED #1), we hybridized 31.91 nmoles of green-emitting nanocrystals, 1.42 nmoles of yellow-emitting nanocrystals and 0.37 nmoles of orange-emitting nanocrystals on our blue LED. The orange-emitting nanocrystals decrease the color temperature for warm-white light generation and balance the luminescence of the green-emitting nanocrystals along with the blue LED. As a result, the chromaticity coordinates remain inside the white region while keeping *LER* and *CRI* high. Figure 4.2.2 presents the resulting collective emission and chromaticity properties of the hybrid LED at different current injection levels. The operating point at 12 mA

corresponds to (x,y)=(0.425,0.378), *LER*=357 lm/W_{opt}, *CRI*=89.2, and *CCT*=2982 K. This makes a warm-WLED with a desirably low *CCT* of less than 3000 K. This NC-LED also satisfies the *CRI* need for future SSL applications (with a *CRI* > 80) [62]. Furthermore, this hybrid LED reaches a *LER* of 357 lm/W_{opt} achieving a high spectral efficiency because these nanocrystal emitters enable us to reduce the deep-red emission at wavelengths longer than 650 nm, where the eye sensitivity function quickly decays and the luminous efficacy decreases in the case of broad emitters with emission tail towards long wavelengths. To investigate the device power conversion efficiency we use the following equation [2], [4]:

$$\eta_{power} = t*\eta_{LED}+(1-t)*\eta_{NC}*(\lambda_{LED}/\lambda_{NC}) \qquad (4.2.1)$$

where η_{power} is the power conversion efficiency of the NC-integrated LED; t is the power fraction of the transmitted radiation of the blue LED; η_{LED} is the external quantum efficiency of the blue LED; η_{NC} is the quantum efficiency of the nanocrystal quantum dots; and λ_{LED} and λ_{NC} are the center emission wavelengths of blue LED and the nanocrystal quantum dots, respectively. For our calculation we used the following values for our device parameters: λ_{LED}= 452 nm, λ_{NC}= 588.4 nm, η_{LED}= 0.10, η_{NC}= 0.15, and t= 0.20, which results in a power conversion efficiency of 0.11. Thus, this hybrid WLED achieves a luminous efficiency of approximately 40 lm/$W_{electrical}$. Also, we predict that a luminous efficiency of 100 lm/$W_{electrical}$ is attainable by using optimized blue LEDs and nanocrystals as it is possible to obtain η_{LED}= 0.50 and η_{NC}= 0.35.

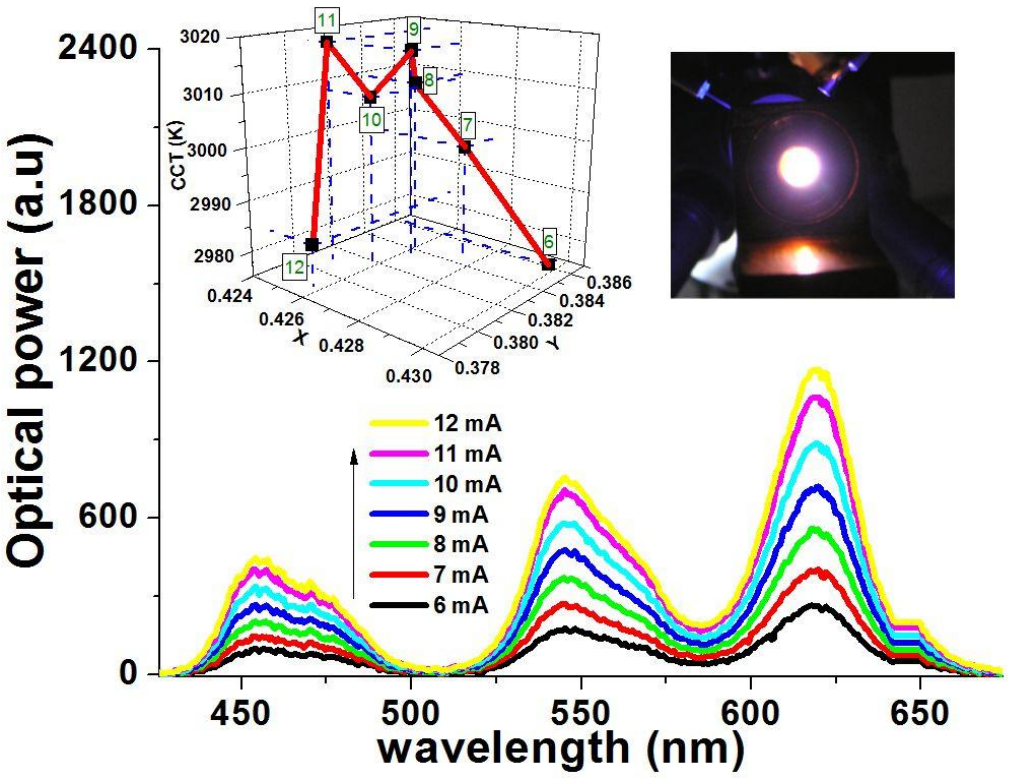

Figure 4.2.2 Electroluminescence spectra of the first NC-LED design (WLED #1) integrated with green-, yellow- and orange-emitting CdSe/ZnS core/shell NC nanophosphors on blue LED chips (λ_{EL} = 452 nm) driven at different levels of current injection at room temperature, along with the corresponding (x, y) coordinates vs. correlated color temperature (*CCT*) and a picture of NC-LED while generating white light (In the inset, the values given in the squares represent the current injection levels at that operating point.).

For our second set of NC based WLEDs (WLED #2), we integrated 31.91 nmol of green-emitting, 1.42 nmol of yellow-emitting and 0.55 nmol of orange-emitting nanocrystals. We measured the emission spectra of this hybrid LED with the corresponding optical properties at different injected current levels, as shown in Figure 4.2.3. The experimental operating point at 12 mA led to (x,y)=(0.445,0.382), with *LER*=349 lm/W_{opt}, *CRI*=88.9, and *CCT*=2781 K. This second set of results corresponds to a warm-WLED with a lower correlated color temperature because the optical intensity coming from orange-emitting nanocrystals is increased. The color rendering index, despite a slight decrease, is

88.9, satisfying the need for *CRI* >80 for future WLEDs. The luminous efficacy is 349 lm/W_{opt}, which is also higher than the previous best results of conventional powder phosphors [2].

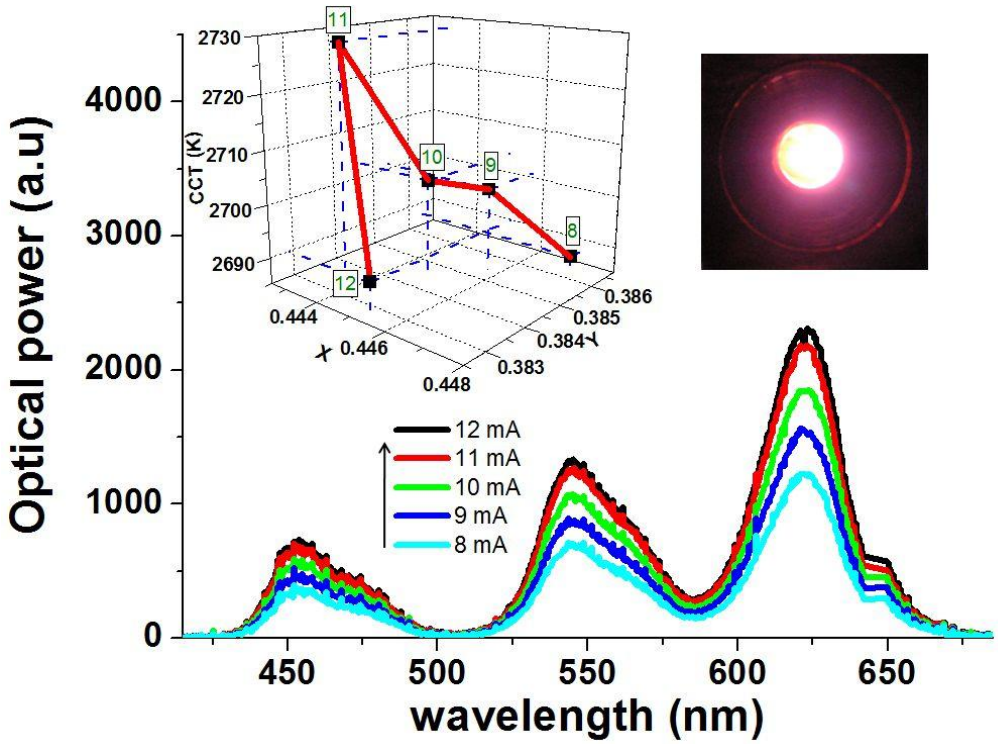

Figure 4.2.3 Electroluminescence spectra of the second NC-LED design (WLED #2) integrated with green-, yellow- and orange-emitting CdSe/ZnS core/shell NC nanophosphors on blue LED chips (λ_{EL} = 452 nm) driven at different levels of current injection at room temperature, along with the corresponding (x, y) coordinates *vs.* correlated color temperature (*CCT*) and a picture of NC-LED while generating white light (In the inset, the values given in the squares represent the current injection levels at that operating point.).

In our last set of NC-integrated WLEDs (WLED #3), we incorporated 31.91 nmol of green-emitting, 1.42 nmol of yellow-emitting and 0.74 nmol of orange-emitting nanocrystals. We obtained the collective emission spectra and optical properties at various current injection levels, as depicted in Figure 4.2.4. The emission spectrum at 12 mA led to (*x*,*y*)=(0.452,0.376), with *LER*=339 lm/W_{opt}, *CRI*=87.8, and *CCT*=2390 K. For this sample we achieved a warm-WLED at an

even lower correlated color temperature of 2390 K. The color rendering index and luminous efficacy slightly decreased to 87.8 and 339 lm/W_{opt}, respectively. Nevertheless, this warm-WLED still meets high *LER* and *CRI* requirements.

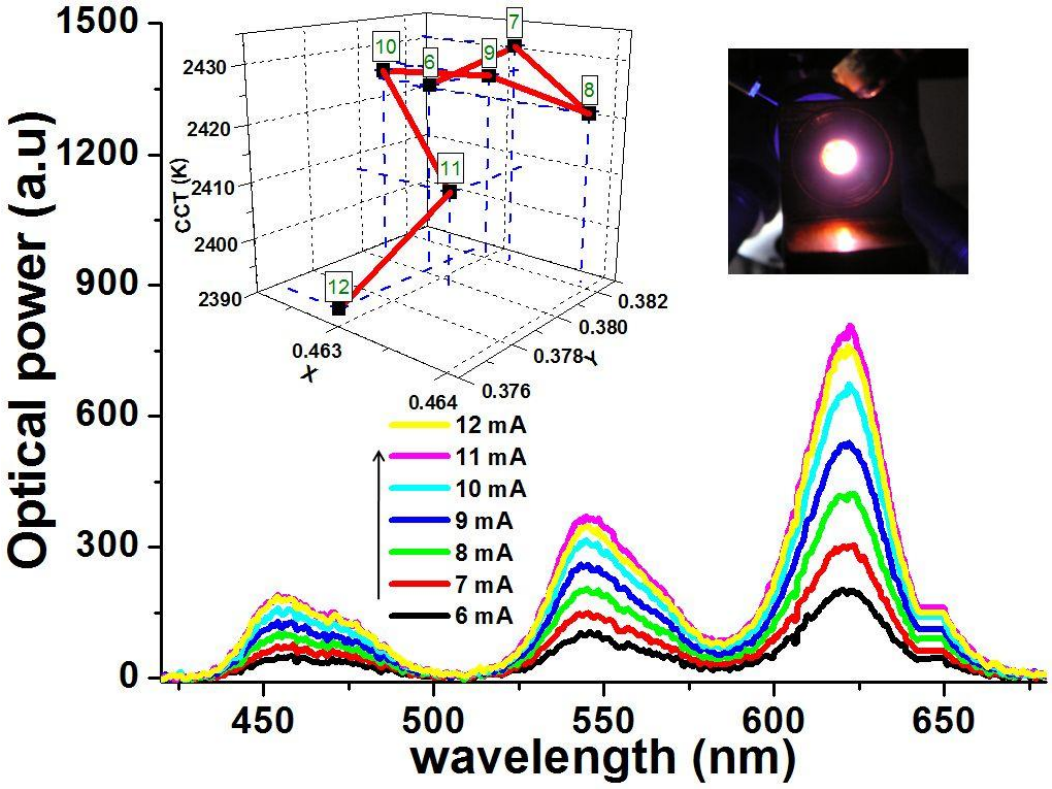

Figure 4.2.4 Electroluminescence spectra of the third NC-LED design (WLED #3) integrated with green-, yellow- and orange-emitting CdSe/ZnS core/shell NC nanophosphors on blue LED chips (λ_{EL} = 452 nm) driven at different levels of current injection at room temperature, along with the corresponding (x, y) coordinates *vs.* correlated color temperature (*CCT*) and a picture of NC-LED while generating white light (In the inset, the values given in the squares represent the current injection levels at that operating point.).

In all of these three implementations (WLED#1-3), it is worth mentioning that we observe slight shift of both chromaticity coordinates and correlated color temperature in response to changing current injection level. However, these small changes are difficult to clearly distinguish by the naked human eye. These WLEDs exhibit reasonable color stability under the reported current injection levels. We further analyzed the experimental color rendering index performance

of WLED#1-3 at each Munsell color as shown in Figure 4.2.1(b). These internationally accepted Munsell test color samples are defined according to their spectral reflectivity [4]. The color rendering index is calculated by taking the average color rendering of each Munsell code. The color rendering index for each Munsell code is above 80, except for the Munsell color of R3. At R3 there is a decrease corresponding to halfway between the green and yellow color spectral ranges. This means that there is room for improvement in *CRI* by increasing the color rendering capability of the green-yellow color range.

4.2.4 Conclusion

To summarize, we developed nanocrystal integrated warm-WLEDs with high luminous efficacy of optical radiation and high color rendering index at the same time. These NC-hybridized WLEDs demonstrated significantly improved spectral performance with *LER* of 357 lm/W_{opt} and *CRI* of 89.2 at *CCT* of 2982 K. These hybrid LEDs hold great promise for future SSL applications.

4.3 High scotopic/photopic ratio white-LEDs integrated with semiconductor nanophosphors of colloidal quantum dots

This section is based on the publication "High scotopic/photopic ratio white-LEDs integrated with semiconductor nanophosphors of colloidal quantum dots" **S. Nizamoglu**, T. Erdem and H. V. Demir, Optics Letters 36, 7 (2011). Reproduced (or 'Reproduced in part') with permission from Optical Society of America. Copyright 2011 Optical Society of America.

In this section we propose and demonstrate single-chip white light-emitting diodes (WLEDs) integrated with semiconductor nanophosphors of colloidal quantum dots for high scotopic/photopic (*S/P*) ratio. These color conversion WLEDs achieve *S/P* ratios over 3.00, which exceeds the current limit of 2.50 in common lighting technologies, while sustaining sufficient levels of color rendering index.

4.3.1 Introduction

Today light sources are commonly specified by photopic vision. For solid state lighting the role of rod activity in vision has not been studied in LED chips. The difference in the scotopic and photopic luminous efficacy of the source stems from the Purkinje shift. According to this theory, if there are two light sources emitting at the same optical power, the one exhibiting higher *S/P* ratio is predicted to yield better perceived brightness along with better visual acuity [24]. This means that light sources with higher *S/P* ratios may potentially provide the equivalent levels of perceived brightness and visual acuity at a lower output power level. High *S/P* ratio, which provides higher correlated color temperature, yields relatively smaller pupils at a given photopic light level so that the object light rays are collected more at the central region of the eye,

which may possibly result in improved optical vision [63]. Therefore, in that case, this may potentially provide means for energy saving. There are still ongoing investigations and discussions on the possible effects of *S/P* ratio. Regardless the extent of their effects under debate, looking from the device perspective, it is not straightforward to make high *S/P* ratio light sources with sufficient level of color rendering, which enables color differentiation. There exists a trade-off between *S/P* ratio and color rendering index. This trend, which is observable for various light sources, makes it challenging to make both *S/P* ratio and *CRI* high at the same time.

In terms of *S/P* ratio and *CRI*, the performance of current lighting technologies is typically limited [9], [64]. The *S/P* ratios of common white light sources range from 0.8 to 2.5 [64]. For example, incandescent light bulbs have a poor *S/P* ratio of 1.41 despite featuring a high perfect *CRI* of 100. As for today's commercially available SSL sources, among the most widely used ones are color conversion LEDs that integrate yellow YAG phosphors; these white LEDs also exhibit poor *S/P* ratios typically ranging from 1.68 to 2.38 [4], [19]. To date single-chip light sources achieving high *S/P* ratios have not been demonstrated or realized. Different phosphors may in principle be integrated to improve a certain photometric property (*e.g.*, *S/P* ratio or *CRI*), but this may come at the cost of reducing performance levels of other photometric parameters (*e.g.*, a decreased luminous efficacy depending on their emission linewidths).

As an alternative luminophor, for future white LEDs, semiconductor nanocrystal quantum dots are strong candidates with their size-tuneable and narrow emission nature, also accompanied with reasonably large photoluminescence quantum efficiency [11], [65]. Therefore, nanocrystals have recently been exploited for various color conversion light emitting diode applications [56], [62], [66]. Especially their color tuning capability allows for adjustable white light generation using combinations of NC emitters (*e.g.*, CdSe/ZnS core-shell NCs) integrated on InGaN/GaN LEDs [56]. In these previous studies using

nanocrystals or others (*e.g.*, using four-color mixing of polychromatic lamps [67]), however, none of the reported white LEDs features high *S/P* ratio.

4.3.2 Design strategy

For the purpose of obtaining a high *S/P* ratio with a reasonable color rendering index, our design strategy relies on mimicking blackbody radiators with high color temperatures. This is because such high temperature blackbody radiators have dominantly blue-cyan emission meaning that their *CCT* is high, while also characteristically exhibiting a high *CRI*. Therefore, the optical spectrum design with dominant blue-cyan emission can be carefully adjusted to use appropriate combinations of nanocrystal emitters to obtain a similar spectrum of these blackbody radiators with high *S/P* ratios and *CRI*s. The operating principle of these hybrid NC LEDs relies on using the combined electroluminescence of LEDs and photoluminescence of nanocrystal color convertors. The fabrication details of our blue LED are explained in our previous study [56]. Since the blue and cyan emissions are required be dominant as in the case of blackbody radiators with high *CCT*s, we employ a blue emitting LED and cyan emitting nanocrystals appropriately with strong enough color components iteratively determined to increase sufficiently the color temperature and make the *S/P* ratio high. On the other hand, the green, yellow, and red nanocrystal emitters are strategically chosen to balance the blue and cyan emission for white light generation.

4.3.3 Experimental characterization of hybrid white LEDs with high scotopic/photopic ratio and discussions

For a proof-of-concept demonstration of such spectrally enhancing nanocrystal based white LEDs, we incorporate cyan-, green-, yellow-, and red-emitting

CdSe/ZnS core/shell NCs with the photoluminescence peaks of λ_{PL}=490, 540, 580, and 620 nm in toluene solution, respectively, in layers integrated directly on our blue InGaN/GaN LED chips with the electroluminescence peak of λ_{EL}= 452 nm by making their close-packed films through evaporating the excess toluene solvent. For our hybrid device, we integrate 119.7 nmol cyan-, 4.652 nmol green-, 0.990 nmol yellow- and 0.158 nmol red-emitting NCs on the blue LED and the total thickness of the color converting layer is approximately 50 μm. We experimentally obtain the white light generating hybrid LED driven at various current injection levels at room temperature as shown in Figure 4.3.1. The luminescence of this hybrid LED increases, as the injected current increases in this regime, leading to the following photometric properties at 25 mA at room temperature: tristimulus coordinates *(x,y)*=(0.251,0.246), *LER*=266.83 lm/W_{opt}, *S/P*=3.04, *CRI*=71.7, and *CCT*=45 kK. These *LER* and *S/P* values reported here (as well as all of those in the rest of this section) are computed using Equations (4.3.1) and (4.3.2) presented in Table 4.3.1 respectively. This white light spectrum satisfies both of the figure-of-merits simultaneously for scotopic enhancement and reasonable color rendering for the first time, by achieving an *S/P* ratio >2.50 at a color rendering index of 71.7. Furthermore, the operating point of our WLED is expectedly close to the blue and white color intersection meaning that this WLED achieves a sufficiently cool white tint to increase the *S/P* ratio.

Table 4.3.1 Photopic luminous efficacy of optical radiation (*LER*), *S/P* ratio (*S/P*), relative brightness (*RB*), and relative nighttime vision (*RNV*) of two sources (where V(λ) is the photopic eye sensitivity function (for photon adapted vision), V′(λ) is the scotopic eye sensitivity function (for dark adapted vision), and E(λ) is the optical spectral power density).

Equation #	Equation
4.3.1 [12]	$\mathrm{LER} = 683\frac{lm}{W}\frac{\int V(\lambda)E(\lambda)d\lambda}{\int E(\lambda)d\lambda}$
4.3.2 [7]	$\mathrm{S/P} = \frac{1700\int E(\lambda)V'(\lambda)d\lambda}{683\int E(\lambda)V(\lambda)d\lambda}$
4.3.3 [32]	$\mathrm{RB} = \left(\frac{\text{S/P ratio of light source 1}}{\text{S/P ratio of light source 2}}\right)^{0.5}$
4.3.4	$\mathrm{RNV} = \frac{\text{S/P ratio of light source 1}}{\text{S/P ratio of light source 2}}$

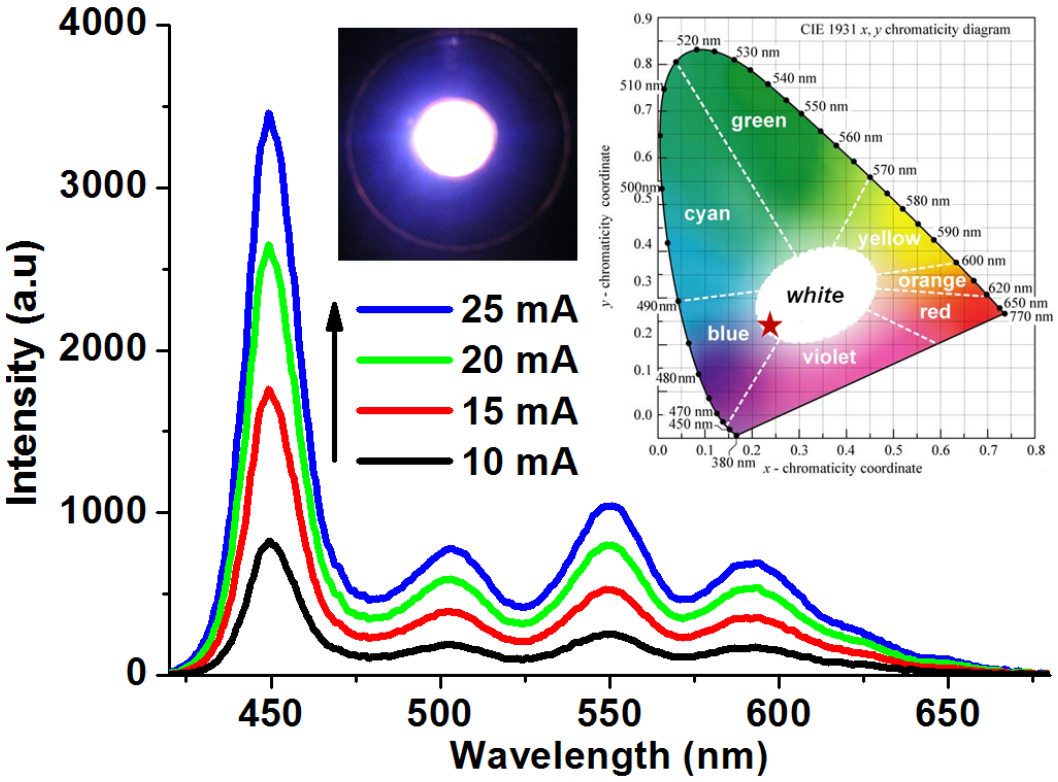

Figure 4.3.1 Emission spectra of our nanocrystal integrated white LED achieving a high *S/P* ratio of 3.05 at a *CRI* of 71.0 under various current injection levels at room temperature, along with its *(x,y)* tristimulus coordinates on CIE 1931 chromaticity diagram and a photograph presented in the insets.

At such elevated color temperatures, *CRI* may, however, not reflect the actual color rendering performance. To address this issue, Ohno and Davis have recently developed the so-called color quality scale (*CQS*) having a similar but more sophisticated calculation method [16-18]. Using this approach, our NC integrated white LED exhibits a *CQS* of 70.3, also implying that our hybrid LED achieves a reasonable color rendering level. This shows that the indicated *CRI* value is relatively successful in terms of expressing the color rendering performance of the source in this case. By comparing our WLED against those of a typical phosphor based white LED operating at the same optical power with an average *S/P* ratio of 2.03 (=[1.68+2.38]/2), our nanocrystal luminophors is predicted to provide a 22.5% brighter view and a 50% better nighttime vision (using Equations (4.3.3) and (4.3.4) given in Table 4.3.1, respectively). Such

strong spectral enhancement is possible using nanocrystal emitters as a result of their conveniently size-tuneable and precisely controllable emission thanks to the quantum size effect. Figure 4.3.2 also compares this nanocrystal based white LED against different light sources available in common lighting technologies including phosphor based white LEDs, along with their references. For example, the standard daylight source D65 yields a *S/P* ratio of 2.47 [64]. As clearly observed in Figure 4.3.2, all common light sources lie below the *S/P* ratio barrier of 2.50, and our nanocrystal integrated source exceeds this barrier. This shows that white light generation using nanocrystal luminophors outperforms current lighting technologies in terms of scotopic/photopic vision while achieving sufficiently high color rendering.

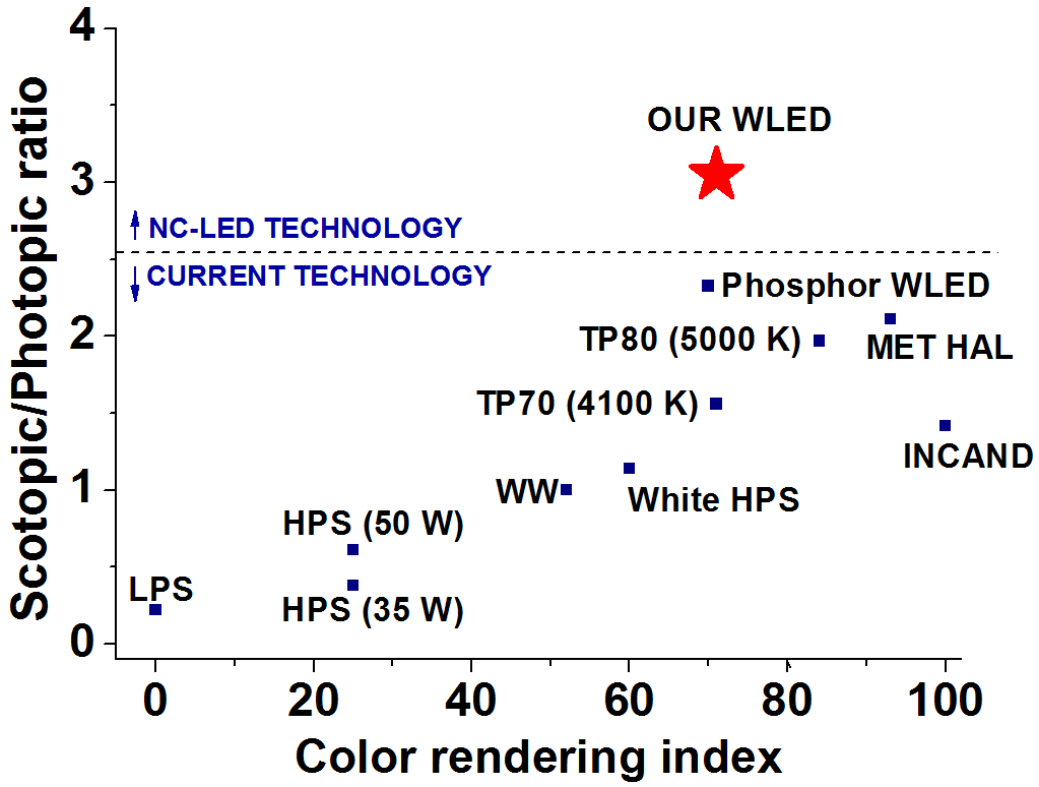

Figure 4.3.2 Scotopic/Photopic ratio versus color rendering index given for our NC based single-chip white LED, also compared with common lighting technologies [2] (including LPS: low pressure sodium, HPS: high pressure sodium, WW: warm white fluorescent, TP70: tri-phosphor fluorescent (70<*CRI*<80), TP80: tri-phosphor fluorescent (80<*CRI*<90), INCAND: incandescent light bulb, MET HAL: metal halide (Thal/Dys/Hol) [10] and also a typical yellow phosphor based WLED [9]).

We further investigate the *S/P* ratio of other NC hybridized LEDs (dubbed Samples A, B and C). Table 4.3.2 summarizes the integrated amount of each nanocrystal color component in these samples. Their resulting emission spectra and *(x,y)* tristimulus coordinates are shown in Figure 4.3.3 and their optical properties are presented in Table 4.3.3. Sample A exhibits an *S/P* ratio of 3.75 and, when we further enhance the blue emission in the spectrum, we achieve an increased *S/P* ratio of 4.72 for Sample B and of 5.15 for Sample C. Therefore, via increasing the blue content of the emission spectrum, LEDs with higher *S/P* ratio can be obtained. However, since the *(x,y)* tristimulus coordinates of these samples are then out of the chromaticity region spanned by the correlated color temperature iso-curves as depicted in Figure 4.3.3, their *CCT*s cannot be defined. Thus, we cannot cite *CRI* values for these sources because we cannot utilize a reference spectrum to calculate their *CRI*. On the other hand, while falling outside the defined region of *CCT*, these LEDs are very close in spectral content to the LED design whose spectra are shown in Figure 4.3.1. Therefore, Samples A-C are also expected to provide reasonable color rendering in practice, although their *CRI* is not technically definable.

Table 4.3.2 Amounts of integrated nanocrystals emitting at different colors (given in nmol) for Sample A, B and C.

Samples	Cyan	Green	Yellow	Red
A	239.4	2.326	0.247	0.052
B	59.8	2.326	0.495	0.158
C	119.7	2.326	0.495	0.158

Table 4.3.3 Photometric properties of Sample A, B and C.

Samples	*S/P*	*LER*	*x*	y
A	3.75	228.24	0.226	0.212
B	4.72	178.48	0.211	0.154
C	5.15	201.04	0.169	0.192

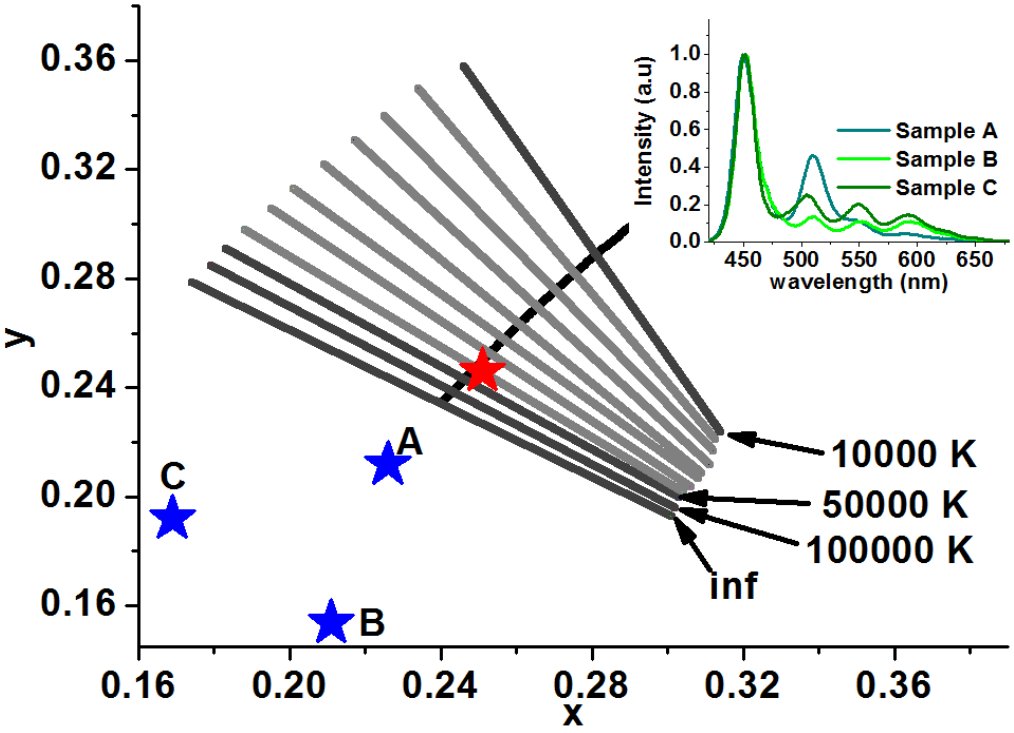

Figure 4.3.3 Lines of constant correlated color temperature on the *(x,y)* chromaticity diagram with the emission spectra of Samples A, B and C. The red star is the *(x,y)* tristimulus coordinates of the white LED shown in Figure 4.3.1.

Lines of constant correlated color temperature on the *(x,y)* chromaticity diagram with the emission spectra of Samples A, B and C. The red star is the *(x,y)* tristimulus coordinates of the white LED shown in Figure 4.3.1.

4.3.4 Conclusion

In this section, this work demonstrated the first proposal and demonstration of scotopically enhancing single-chip white LEDs with nanocrystal luminophors to achieve a scotopic/photopic ratio exceeding the common barrier of 2.50. These photometric properties show that these devices outperform common lighting technologies in terms of scotopic/photopic vision.

Chapter 5

Hybrid white light emitting diodes integrated with exotic nanocrystal quantum dots

5.1 Multi-layered onion-like (CdSe)ZnS/CdSe/ZnS quantum-dot-quantum-well heteronanocrystals for investigation of their multi-color emission

This section is based on the publication "Onion-like (CdSe)ZnS/CdSe/ZnS quantum-dot-quantum-well heteronanocrystals for investigation of multi-color emission" **S. Nizamoglu** and H. V. Demir, Optics Express 16, 3515-3526 (2008). Reproduced (or 'Reproduced in part') with permission from Optical Society of America. Copyright 2008 Optical Society of America.

In this section we investigate multi-color spontaneous emission from quantum-dot-quantum-well heteronanocrystals made of onion-like (CdSe)ZnS/CdSe/ZnS (core)shell/shell/shell structures, with our theoretical results explaining experimental measurements for the first time. In such multi-layered heteronanocrystals, we discover that the carrier localization is tuned from type-I-like to type-II-like localization by controlling CdSe and ZnS shell thicknesses, and that 3-monolayer ZnS barriers are not necessarily sufficient for carrier localization, unlike in conventional (CdSe)ZnS (core)shell structures. We

demonstrate that exciton localization in distinct layers of (CdSe)ZnS/CdSe/ZnS heteronanocrystals with high transition probability (for n=1 states in CdSe core and n=2 states in CdSe shell) is key to their multi-color emission.

5.1.1 Introduction

Quantum structures are of fundamental interest to study the modification of light-material interactions through quantum confinement. Among the examples of such quantum confined structures are semiconductor nanocrystal quantum dots that exhibit size-tunable optical and electronic properties because of their exciton confinement [11], [68], [69]. Thanks to these adjustable features, nanocrystal emitters have attracted great attention for different device applications [56], [64-68], [76], [92], [93]. Today various core-shell nanocrystal structures (*e.g.*, in CdSe-ZnS and CdSe-CdS material systems) are commonly synthesized in high-boiling organic solvents [36], [37], [59]. In recent years complex quantum structures that include layers of concentric shells in alternating materials surrounding the core, the so-called quantum-dot-quantum-well (QDQW) systems, have been investigated. The first achievement in QDQW systems was obtained using CdS particles with an embedded layer of HgS in 1993 [54]. Afterward (CdS)CdSe/CdS and (ZnS)CdS/ZnS (barrier-core)well-shell/barrier-shell, and (ZnSe)CdSe (barrier-core)well-shell structures were successfully synthesized, and some of those QDQW systems were also theoretically investigated [62], [94-96]. However, all of these early QDQW systems had the ability to luminescence only in mono-color.

On the other hand, there has been a strong demand for QDQW systems that provide multi-color light emission to cover a broader emission spectrum across the visible. Multi-color emission from such QDQW heteronanocrystals (hetero-NCs) is essential for their use as white emitting luminophors in solid state lighting applications. Such multi-color luminescence possibly allows for white light generation with higher color rendering index, which is one of the critical requirements yet to be met for future solid state lighting. As the state of the art,

white light generation using mono-color emitting nanocrystals is achieved using the collective photoluminescence contributed from the combination of different types of such nanocrystals or on the luminescence arising from the combination of such nanocrystals and LEDs. In all of these device implementations with these mono-color emitting nanocrystals, however, the hybrid device parameters including the type and concentration of NCs as well as the thickness and order of the NC films are required to be engineered at the device level to obtain white light.

As a conceptual advance the multi-color emitting heteronancorsyals facilitiates fabrication of white light emitting diodes with simple device hybridization using only a single type of heteronanocrystals and heteronanocrystals provide tuneable broad emission for high-quality white light generations. Only recently multi-color emission in the visible has been accomplished in CdSe-ZnS based QDQW systems to generate white light [51], [97]. In these structures, around a core made of CdSe, a ZnS shell barrier is synthesized, and subsequently CdSe shell quantum well is added surrounding this ZnS barrier. Only for certain QDQW structures, emission from their CdSe core at the longer wavelength and from their CdSe shell at the shorter wavelength together contributes to the white light generation [51].

However, to date the conditions of multi-color spontaneous emission from a single type of such heteronanocrystals have not been completely understood. Furthermore, these multi-layered heteronanocrystal systems (including the multi-color emitting (CdSe-core)ZnS-shell/CdSe-shell heteronanocrystals) have not been theoretically investigated till date. There are still fundamental questions left unanswered for such multi-color emitting QDQW systems: For instance, why can the multi-color emission not be observed for specific shell thicknesses of these heteronanocrystals; what are the necessary conditions for multi-color emission from such heteronanocrystals; how do their ZnS and CdSe shell thicknesses affect the carrier localization and the corresponding energy states;

how do the relative two peaks of the emission spectrum change with respect to each other; and are the electron and hole wavefunctions at n=1 and n=2 localized or delocalized in these heteronanocrystals?

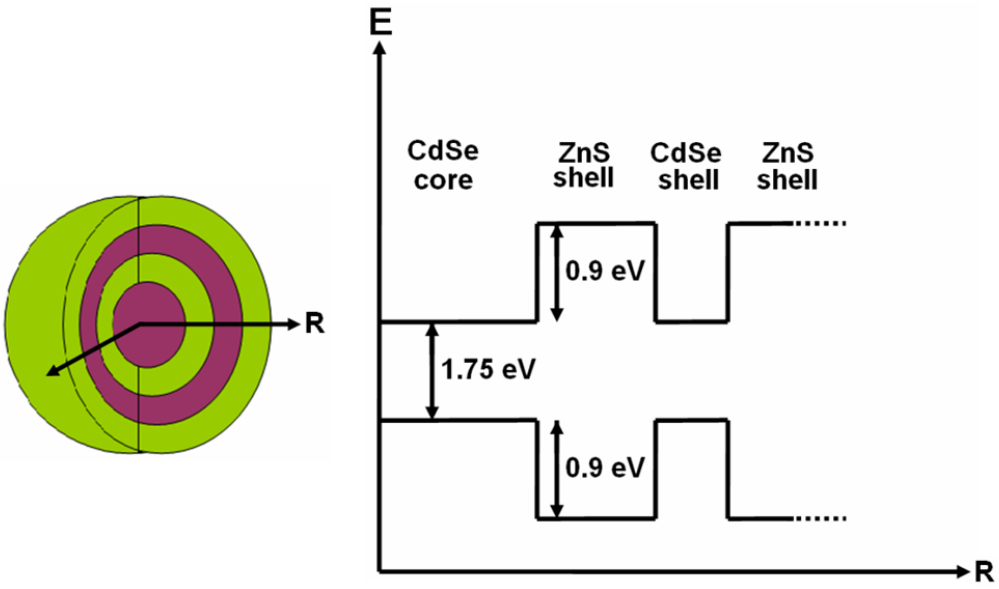

Figure 5.1.1 Schematic of an onion-like (CdSe)ZnS/CdSe/ZnS heteronanocrystal structure (with violet regions representing CdSe and green regions representing ZnS) along with the corresponding radial energy diagram (not drawn to scale).

In this section, to seek answers for these fundamental questions, we investigate multi-color spontaneous emission from quantum-dot-quantum-well heteronanocrystals in CdSe-ZnS material system. For this purpose, we quantum mechanically analyze multi-layered heteronanocrystals made in the generic form of onion-like (CdSe)ZnS/CdSe/ZnS (core)shell/shell/shell structures, as schematically shown in Figure 5.1.1. Using our quantum mechanical analysis as a tool, we investigate their electronic properties (wavefunctions and excitons) and the resulting optical properties (photoluminescence peak and relative oscillation strength). We further identify the conditions of multi-color spontaneous emission from a single multi-layered heteronanocrystal in CdSe-ZnS material system, with our theoretical results explaining experimental measurements for the first time. For (CdSe)ZnS/CdSe/ZnS heteronanocrystals,

we demonstrate that the distinct spatial localization of excitons in their separate layers (in their CdSe core and CdSe shell) is key to their multi-color luminescence, which is of fundamental importance to generate white light from a single heteronanocrystal. Additionally, although CdSe-ZnS interface is well known to lead to only type-I band alignment, we find out that the carrier localization is surprisingly tuned from type-I-like localization (with both electron and hole primarily residing in the same layer of the heterostructure) to type-II-like localization (with electron and hole primarily residing in different layers of the heterostructure) by controlling the combination of CdSe and ZnS shell thicknesses. Furthermore, in spite of the well-known fact that a 3-monolayer ZnS shell barrier is sufficient for full carrier confinement in conventional (CdSe)ZnS (core)shell structures, we discover that the carriers in the CdSe core and CdSe shell in a multi-layered heteronanocrystal might be still coupled despite the use of 3-monolayer ZnS shells as the barrier.

5.1.2 Analysis of electronic structure in multi-layered heteronanocrystals

For our theoretical analysis, we apply effective mass approximation, which is discussed in Section 3.4. Beginning with the analysis of 2S states in (CdSe)ZnS/CdSe/ZnS heteronanocrystals, Figure 5.1.2 shows the probability distribution of the electron $|\psi_{e,200}(r)|^2$ and the hole $|\psi_{h,200}(r)|^2$ (normalized with respect to the peak for easy visual inspection) at the first excited states n=2. Here again note that these (CdSe)ZnS/CdSe/ZnS heteronanocrystals are analyzed with the thickness of their inner ZnS and CdSe shells varied from 1 monolayer (ML) to 3 monolayers (MLs), while their CdSe core is kept fixed and the outmost ZnS shell is taken infinitely thick. At these n=2 energy states, we observe that the carrier distribution is tuned between the localization regimes of type-I and type-II by changing the thickness of the shell layers. In the cases of 1

ML ZnS and 1 ML CdSe shells (indicated as 1-1 in our notation in Figure 5.1.2), 1 ML ZnS and 2 ML CdSe shells (1-2), 1 ML ZnS and 3 ML CdSe shells (1-3), and 2 ML ZnS and 1 ML CdSe shells (2-1), both the electron and hole mainly reside in the CdSe core, with their distribution maxima overlapping in the center of the core, showing type-I-like localization. However, for the cases of 2 ML ZnS and 3 ML CdSe shells (2-3) and 3 ML ZnS and 1 ML CdSe shells (3-1), the distribution maxima of the electron and the hole are clearly separated, with one type of the carrier mainly residing in the CdSe core while the other residing mainly in the CdSe shell, showing type-II-like localization. In the cases of 2 ML ZnS and 2 ML CdSe shells (2-2), 3 ML ZnS and 2 ML CdSe shells (3-2), and 3 ML ZnS and 3 ML CdSe shells (3-3), both the electron and hole mainly reside in the CdSe shell, which shows type-I-like carrier localization again. Here it is worth noting that the electron and hole localize in the CdSe shell rather than in the CdSe core in the final type-I-like localization cases. As a result, by varying the thickness of ZnS and CdSe shells, we observe that it is possible to tune the carrier localization from type-I to type-II regime and from type-II back to type-I regime again.

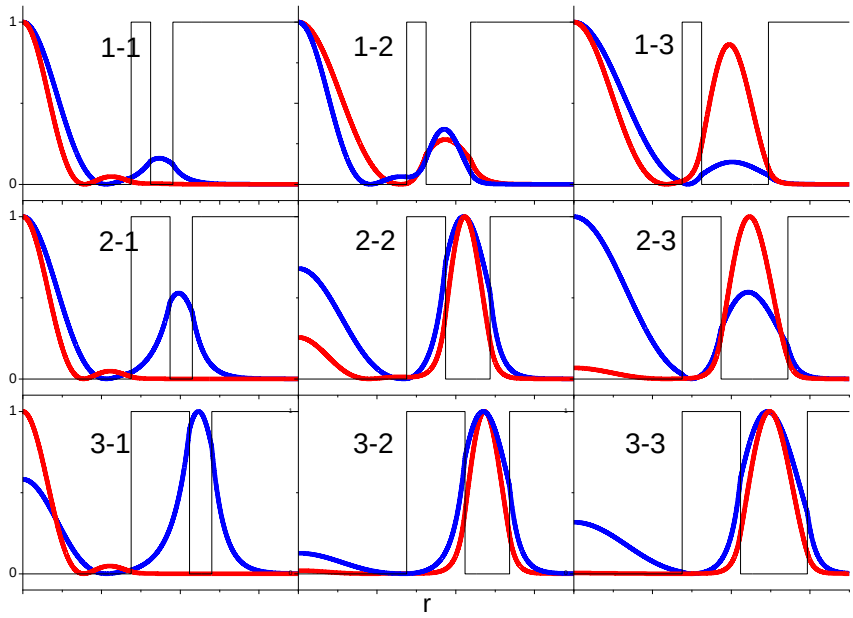

Figure 5.1.2 2S relative probability distribution of electron $|\psi_{e,200}(r)|^2$ (in blue) and hole $|\psi_{h,200}(r)|^2$ (in red) for n=2, l=0, m=0 states (with their peaks normalized to 1 for easy visualization) across the radial potential profile V(r) (in black) of the entire heteronanocrystal. On each plot, the thicknesses of the inner ZnS shell (the first shell) and the CdSe shell (the second shell) in monolayers (*e.g.*, x ML ZnS and y ML CdSe) are labeled as a pair (in the convention of x-y) in our notation. (For instance, 1-3 indicates (CdSe)ZnS/CdSe/ZnS heteronanocrystal with a 1-monolayer ZnS inner shell and a 3-monolayer CdSe shell.)

At n=2 energy states, both the electron and hole tunnel to the CdSe shell, as shown in Figure 5.1.2. This situation plays a critical role in multi-color emission, as will be explained in the next section. Although in conventional mono-color emitting (CdSe)ZnS (core)shell NCs a 3 ML ZnS barrier provides sufficient isolation for carrier confinement [36], this may not be sufficient for full carrier localization at n=2 in (CdSe)ZnS/CdSe/ZnS heteronanocrystals. When ZnS thickness CdSe shell thicknesses are varied, at n=2 energy level the hole tends to localize mainly either in the CdSe core or in the CdSe shell layer. When ZnS barrier thickness is fixed to 1 ML, as the CdSe shell thickness is

increased, the hole tunnels further more and more toward the CdSe shell, and when the CdSe shell thickness is increased to 3 MLs, the hole localization in the shell becomes as distinguishable as it is in the core. Similar behavior is also observed for 2 ML ZnS shell with increasing CdSe shell thickness. For example, in the case of 2 ML ZnS and 3 ML CdSe shells (2-3), the probability of the hole residing in the CdSe shell is higher than in the CdSe core. Similarly, when we have 3 ML ZnS and 1 ML CdSe shells (3-1), the hole is localized in the core, but as we increase CdSe thickness to 2 MLs (3-2) and then further to 3 MLs (3-3), the probability distribution of the hole in the core eventually decays almost to zero and the hole localization in the CdSe shell dominates.

Analyzing 1S states in (CdSe)ZnS/CdSe/ZnS heteronanocrystals, we observe that both electron and hole are mainly localized in the core at the ground state (n=1) as shown in Figure 5.1.3. One of the important characteristics of the mono-color emitting (CdSe)ZnS (core)shell NCs is that they confine electrons and holes in the core with strong localization, leading to high quantum efficiencies (*e.g.*, up to 66% [98]). In hetero-NCs at the ground state, ZnS makes a good barrier for both the electron and hole as well. Only, in the case of 1 ML ZnS and 3 ML CdSe shells (1-3), the electron tunnels with a relatively low probability to the CdSe shell. Nevertheless, we conclude that the ZnS barrier in general provides significant isolation for both carriers in (CdSe)ZnS/CdSe/ZnS hetero-NCs at the ground state, like (CdSe)ZnS (core)shell NCs.

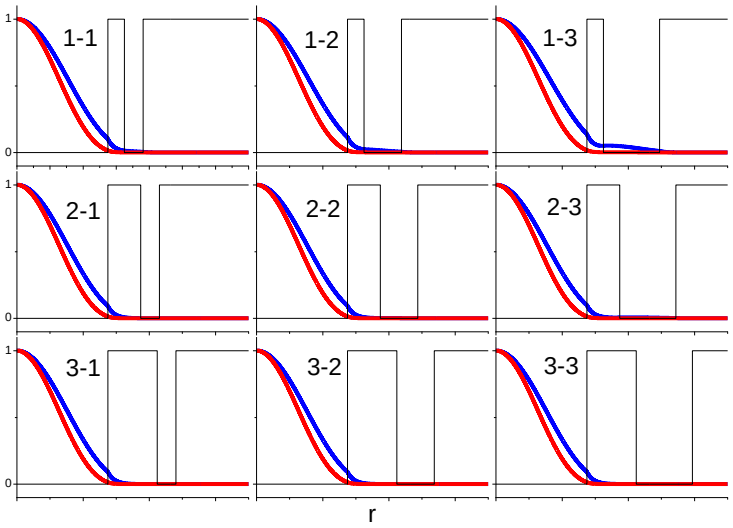

Figure 5.1.3 1S relative probability distribution of electron $|\psi_{e,100}(r)|^2$ (in blue) and hole $|\psi_{h,100}(r)|^2$ (in red) for n=1, l=0, m=0 states (with their peaks normalized to 1 for easy visualization) across the radial potential profile V(r) (in black) of the entire heteronanocrystal. On each plot, the thicknesses of the inner ZnS shell (the first shell) and the CdSe shell (the second shell) in monolayers (*e.g.*, x ML ZnS and y ML CdSe) are labeled as a pair (in the convention of x-y) in our notation. (For instance, 1-3 indicates (CdSe)ZnS/CdSe/ZnS heteronanocrystal with a 1-monolayer ZnS shell and a 3-monolayer CdSe shell.)

5.1.3 Analysis of optical properties and multi-color emission in multi-layered heteronanocrystals

In multi-color emitting heteronanocrystals, lower-energy photons originate from the CdSe core and higher-energy photons from the CdSe shell. Battaglia *et al.* demonstrated multi-color emitting onion-like structures by changing ZnS and CdSe shells from 1 ML to 3 MLs [97]. However, some structures surprisingly did not exhibit multi-color emission, instead they featured only mono-color emission from CdSe core through 1S transition. To achieve multi-color emission from such hetero-NCs, according to our simulation we find out that lower-

energy excitons should be localized in the CdSe core at n=1 states, and higher-energy excitons should be localized in the CdSe shell at n=2 states. In addition, the overlaps of these electron-hole wavefunctions for the corresponding optical transitions between the associated energy states should be relatively high (because the optical transition probability is directly proportional to the electron and hole wavefunction overlap [60]). For (CdSe)ZnS/CdSe/ZnS heteronanocrystal, the electron-hole spatial overlaps calculated for n=1 are relatively high (near to 1) as summarized in Table 5.1.1 and the associated excitons are mainly localized in the CdSe core at n=1 as shown in Figure 5.1.4, which is the same situation for mono-color emitting (CdSe)ZnS (core)shell nanocrystals.

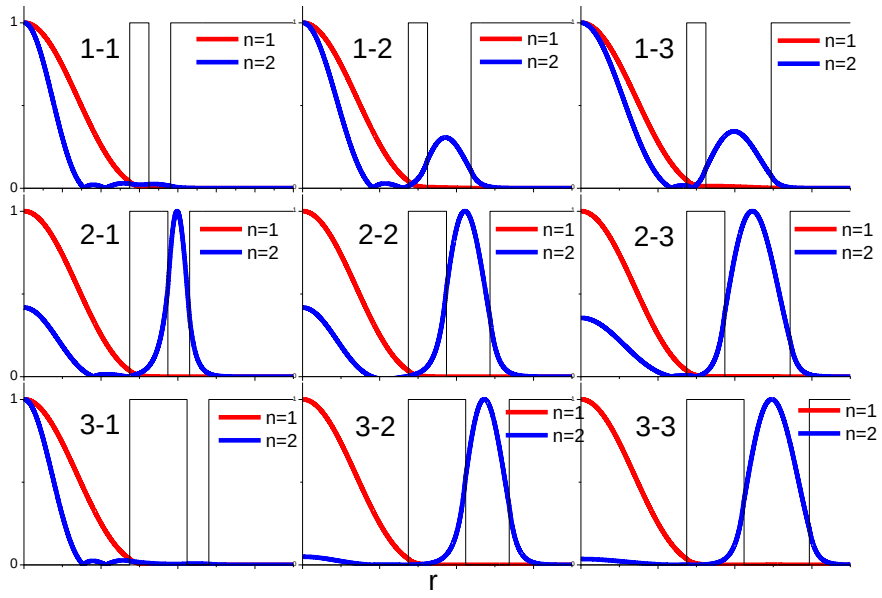

Figure 5.1.4 The electron-hole spatial wavefunction multiplication (exciton) distribution $|\psi_{e,n00}(r)\psi_{h,n00}(r)|$ **for n=1 (in red) and n=2 (in blue), l=0, m=0 states (with their peaks normalized to 1 for easy visualization) across the radial potential profile V(r) (in black) of the entire heteronanocrystal. On each plot, the thicknesses of the inner ZnS shell (the first shell) and the CdSe shell (the second shell) in monolayers (*e.g.*, x ML ZnS and y ML CdSe) are labeled as a pair (in the convention of x-y) in our notation. (For instance, 1-3 indicates (CdSe)ZnS/CdSe/ZnS heteronanocrystal with a 1-monolayer ZnS shell and a 3-monolayer CdSe shell.)**

Battaglia *et al.* did not obtain multi-emission specifically for the cases of 1 ML ZnS and 1 ML CdSe shells (1-1), 1 ML ZnS and 2 ML CdSe shells (1-2), 1 ML ZnS and 3 ML CdSe shells (1-3), 2 ML ZnS and 1 ML CdSe shells (2-1), and 3 ML ZnS and 1 ML CdSe shells (3-1) [97]. For all of these cases at n=2, both the electron and hole are confined in the core rather than in the shell, as demonstrated in Figure 5.1.4. We consider that the excitons possibly relax to n=1 state from n=2 state before they recombine. Thus, the emission occurs only between 1S states. On the other hand, the cases of 2 ML ZnS and 2 ML CdSe shells (2-2), 2 ML ZnS and 3 ML CdSe shells (2-3), 3 ML ZnS and 2 ML CdSe shells (3-2), and 3 ML ZnS and 3 ML CdSe shells (3-3) exhibit radiative 2S transitions, as also Battaglia *et al.* experimentally observed [97]. In these cases, the excitons are localized in the CdSe shell for n=2 states as demonstrated in Figure 5.1.4, and the associated overlaps are relatively high (near to 1) as shown in Table 5.1.2.

We know that heteronanocrystal structures achieving multi-color emission exhibit that electrons and holes are mainly localized in the core and in the shell for n=1 and n=2 states, respectively. In this material system generally the spontaneous emission lifetime is around tens of nanoseconds (around 20 ns), the Auger recombination is about tens of picoseconds (around 50 ps) and the intersubband relaxation time is about hundreds of femtoseconds (around 100 fs). In our case we consider that the intersubband relaxation transition of carriers at n=2 states primarily localized in the shell to n=1 states is weak due to the low probability distribution of electrons and holes in the shell at n=1 state and this situation results multi-color emission. In addition, according to the Battaglia *et al.* and Sapra *et al.* in (CdSe)ZnS/CdSe/ZnS multi-layered heteronanocrystals there is energy transfer (with uncertainity whether with Föster or Dexter energy transfer), but according to our knowledge, for these structures the energy transfer rate has not been investigated to date. Furthermore, we compare the overlaps for 1S and 2S transitions with the experimentally measured relative

peak luminescences [97]. For example, the overlap in the case of 2 ML ZnS and 3 ML CdSe shells (2-3) is higher than the overlap in the case of 2 ML ZnS and 2 ML CdSe shells (2-2) for 2S transition, and the luminescence from n=2 states of (2-3) is theoretically predicted to be relatively higher than (2-2), as also previously experimentally shown. We observe similar confirmation of our theoretical predictions with the experimental measurements also for the cases of 3 ML ZnS and 3 ML CdSe shells (3-3) and 3 ML ZnS and 2 ML CdSe shells (3-2).

Table 5.1.1 1S electron-hole wavefunction overlaps $<\psi_{e,100}(r)|\psi_{h,100}(r)>$ for different numbers of monolayers of the ZnS shell in rows and the CdSe shell in columns at n=1 states. In parenthesis in each cell where overlap is presented, the thicknesses of the inner ZnS shell (the first shell) and the CdSe shell (the second shell) in monolayers (*e.g.*, x ML ZnS and y ML CdSe) are indicated as a pair (in our notation of x-y.) (For instance, 1-3 represents (CdSe)ZnS/CdSe/ZnS heteronanocrystal with a 1-monolayer ZnS shell and a 3-monolayer of CdSe shell.)

CdSe shell (ML) / **ZnS shell (ML)**	**1 ML**	**2 ML**	**3 ML**
1 ML	0.963 (1-1)	0.944 (1-2)	0.898 (1-3)
2 ML	0.970 (2-1)	0.969 (2-2)	0.946 (2-3)
3 ML	0.971 (3-1)	0.968 (3-2)	0.969 (3-3)

Table 5.1.2 2S electron-hole wavefunction overlaps at n=2 states $<\psi_{e,200}(r)|\psi_{h,200}(r)>$ for different numbers of monolayers of the ZnS shell in rows and the CdSe shell in columns. In parenthesis in each cell where overlap is presented, the thicknesses of the inner ZnS shell (the first shell) and the CdSe shell (the second shell) in monolayers (*e.g.*, x ML ZnS and y ML CdSe) are indicated as a pair (in our convention of x-y). (For instance, 1-3 represents (CdSe)ZnS/CdSe/ZnS heteronanocrystal with a 1-monolayer ZnS shell and a 3-monolayer CdSe shell.)

ZnS shell (ML) \ CdSe shell (ML)	**1 ML**	**2 ML**	**3 ML**
1 ML	0.586 (1-1)	0.926 (1-2)	0.144 (3-1)
2 ML	0.286 (2-1)	0.970 (2-2)	0.946 (2-3)
3 ML	0.144 (3-1)	0.976 (3-2)	0.975 (3-3)

Examining the energy levels of (CdSe)ZnS/CdSe/ZnS heteronanocrystals we observe that both the core and shell energy levels change when the thicknesses of the ZnS and CdSe shells are changed, as Battaglia *et al.* also experimentally demonstrated [97]. For 1S transitions, we find similar levels of energy change in our theoretical work with respect to the case of mere CdSe core as shown in Figure 5.1.5 (a), excluding the binding energy due to the Coulomb interaction. For 1 ML ZnS, as the CdSe shell thickness is increased, the photoluminescence shifts with an increasing slope towards red. The increase of the PL peak shift for the case of 1 ML ZnS is larger than for the cases of 2 ML ZnS and 3 ML ZnS because, in the 3 ML ZnS shell case, the electron and hole wavefunctions slightly leak into the CdSe shell. In 3 ML ZnS shell, the change in PL is almost zero because 3 ML ZnS shell is a good barrier for carrier confinement for n=1 states. These calculated results match the experimental results very well within a precision of 2-5 nm range.

When we take the Coulomb interaction into account to investigate the change of the core CdSe emission as shown in Figure 5.1.5 (b), although the difference between the measured and calculated results increases to a range of 1-11 nm, we observe the blue shift for 3 ML ZnS, as was also observed in the experiment [97]. In the hetero-NC, in each case, the binding energy is smaller in magnitude than the only core case (-95 meV), as shown in Table 5.1.3. Therefore, because of the weaker Coulomb interaction in hetero-NCs, the red shift due to the exciton confinement is reduced. In other words, as a result of the Coulomb interaction, in the hetero-NC structure, there exists a relative blue shift with respect to the mere CdSe core case. The binding energies between 2S transitions for different ZnS and CdSe shells (by taking into account the Coulomb interaction) are summarized in Table 5.1.4.

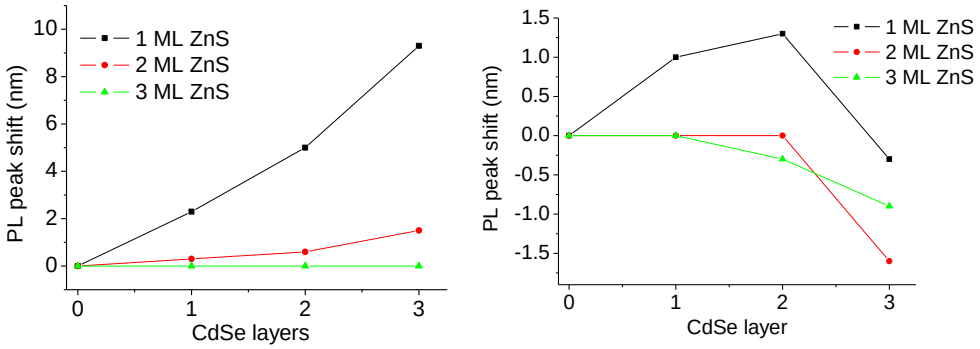

(a) **(b)**

Figure 5.1.5 Theoretical energy level shifts of (CdSe)ZnS/CdSe/ZnS heteronanocrystal for different thicknesses of the ZnS shell and the CdSe shell with respect to the mere core CdSe NC (a) without and (b) with taking the Coulomb interaction into account.

Table 5.1.3 Exciton binding energy due to the Coulomb interaction at n=1 states.

2nd shell CdSe (ML) / 1st shell, ZnS (ML)	1 ML	2 ML	3 ML
1 ML	-90 meV (1-1)	-82 meV (1-2)	-63 meV (1-3)
2 ML	-94 meV (2-1)	-92 meV (2-2)	-85 meV (2-3)
3 ML	-94 meV (3-1)	-93 meV (3-2)	-91 meV (3-3)

For 2S transition energies, we observe good agreement between our theoretically calculated data and the experimentally measured data [97]. In the cases of 1 ML ZnS and 1 ML CdSe shells (1-1), 1 ML ZnS and 2 ML CdSe shells (1-2), 1 ML ZnS and 3 ML CdSe shells (1-3), 2 ML ZnS and 1 ML CdSe shells (2-1), and 3 ML ZnS and 1 ML CdSe shells (3-1), we theoretically explained in the previous sections that these samples should not have luminesce for 2S. In Table 5.1.5, we present the calculated and measured optical emission wavelengths for 2S transitions. For example, particularly for the case of 3 ML ZnS and 3 ML CdSe shells (3-3), we calculate the PL wavelength to be 578 nm, whereas the experimentally measured PL peak is approximately at 575 nm. Also, in the cases of 2 ML ZnS and 3 ML CdSe shells (2-3), and 3 ML ZnS and 2 ML CdSe shells (3-2), we observe similar agreement between the experimental and theoretical results.

Table 5.1.4 Exciton binding energy due to the Coulomb interaction at n=2 states.

2nd shell, CdSe (ML) / 1st shell, ZnS (ML)	1 ML	2 ML	3 ML
1 ML	-30 meV (1-1)	-23 meV (1-2)	-21 meV (1-3)
2 ML	-9 meV (2-1)	-23 meV (2-2)	-24 meV (2-3)
3 ML	-2 meV (3-1)	-21 meV (3-2)	-23 meV (3-3)

Table 5.1.5 Comparison of our theoretical PL peaks and the experimental PL peaks for different CdSe and ZnS thicknesses for 2S transitions.

2nd shell, CdSe (ML) / 1st shell, ZnS (ML)	1 ML		2 ML		3 ML	
	Theo.	**Exp.** [a]	**Theo.**	**Exp.** [a]	**Theo.**	**Exp.** [a]
1 ML	- (1-1)	- (1-1)	- (1-2)	- (1-2)	- (1-3)	- (1-3)
2 ML	- (2-1)	- (2-1)	520nm (2-2)	550nm (2-2)	576nm (2-3)	580nm (2-3)
3 ML	- (3-1)	- (3-1)	520nm (3-2)	535nm (3-2)	578nm (3-3)	575nm (3-3)

[a] Reference: [97].

We further investigate the possibility of triple-color emission from multi-layered hetero-NCs based on CdSe-ZnS material system. According to our theoretical

investigations given any possible combination of shell thickness, we do not observe any case that confines excitons for n=1 state in the core, for n=2 state in the first CdSe shell, and for n=3 state in the second CdSe shell, disabling potential triple-color emission. For instance, we examine a (CdSe)ZnS/CdSe/ZnS/CdSe/ZnS (core)shell/shell/shell/shell/shell heterostructure by adding ZnS shell (as the third shell) and CdSe shell (as the fourth shell) of various thicknesses surrounding the three-shell hetero-NC with 3 ML ZnS and 3 ML CdSe shells (3-3) that achieves dual-color emission. Even for the case of 3 ML of the third shell and 3 ML of the fourth shell, we do not observe triple-color emission because electrons at n=2 and n=3 states are confined together either in the second shell or in the fourth shell depending on the fifth shell thickness. Thus, this situation prevents the formation of localized excitons for n=2 and n=3 states separately in different layers. Therefore, according to our investigations, we do not encounter a case that would potentially provide triple-color emission from a five-shell hetero-NC in CdSe-ZnS material system.

5.1.4 Conclusion

In this section, we quantum mechanically investigated the electronic properties and the resulting optical properties of multi-layered (CdSe)ZnS/CdSe/ZnS (core)shell/shell/shell nanocrystals and verified our theoretical results with the previous experimental measurements. We showed that the carrier localization at the first excited state is tuned from type-I-like to type-II-like localization and from type-II-like to type-I-like localization back again, by varying the first shell (ZnS) and the second shell (CdSe) thicknesses. We revealed that ZnS barrier used in the first shell (even for 3 monolayers) does not necessarily fully confine electron and hole at n=2 state, though providing significant electron and hole isolation at n=1 state. We showed that the distinct spatial localization of excitons at n=1 and n=2 is key to achieve multi-color emission, in addition to the requirement of relatively high electron-hole wavefunction overlaps.

Furthermore, we investigated the possibility of triple-color emission from multi-layered hetero-NCs based on CdSe-ZnS material system and we did not observe any case that would potentially achieve triple-color emission.

5.2 Dual-color emitting quantum-dot-quantum-well CdSe-ZnS heteronanocrystals hybridized on InGaN/GaN light emitting diodes for high-quality white light generation

This section is based on the publication "Dual-color emitting quantum-dot-quantum-well CdSe-ZnS heteronanocrystals hybridized on InGaN/GaN light emitting diodes for high-quality white light generation" **S. Nizamoglu**, E. Mutlugun, T. Özel, H. V. Demir, S. Sapra, N. Gaponik, A. Eychmüller, Applied Physics Letters 92, 113110 (2008). Reproduced (or 'Reproduced in part') with permission from American Institute of Physics. Copyright 2008 American Institute of Physics.

In this section we report white light generation by hybridizing green-red emitting (CdSe)ZnS/CdSe (core)shell/shell quantum-dot-quantum-well heteronanocrystals on blue InGaN/GaN light emitting diodes with the resulting photometric properties of tristimulus coordinates (x, y)=(0.36,0.30), luminous efficacy of optical radiation LER=278 lm/W, correlated color temperature CCT=3929 K, and color-rendering index CRI=75.1. We present the photometric analysis and the quantum mechanical design of these dual-color emitting heteronanocrystals synthesized to achieve high-quality white light when hybridized on light emitting diodes. Using such multi-color emitting heteronanocrystals facilitates simple device implementation while providing good photometric properties.

5.2.1 Introduction

To date by employing nanocrystals various device applications have been demonstrated including sensors, scintillators, and lasers [92], [93], [99], [100].

But in particular, white light emitting diodes (WLEDs) have achieved significant progress. White light generation using single-color emitting (CdSe)ZnS (core)shell nanocrystals of single, dual, trio, and quadruple combinations hybridized on blue-emitting InGaN/GaN LEDs has been demonstrated [45], [76]. White light generation with the dual hybridization of nanocrystals and fluorescent polymers has also been realized [65]. Utilization of a blue/green dual-wavelength InGaN/GaN LED integrated with a single type of red NCs, and a blue InGaN/GaN LED with a single type of yellow NCs and a dual type of red and green NCs have been reported [6], [64]. Furthermore, a white LED has been fabricated by integrating a UV-LED with a mixture of CdSeS NCs in polymethyl methacrylate (PMMA) and also by using layer-by-layer assembly of (CdSe)ZnS NCs on a near-UV LED [66-68]. However, these WLEDs are all based on the use of mono-color emitting nanocrystals or of their multiple combinations. Recently complex nanocrystal structures that achieve multi-color emission have been investigated [37]. For example, by using a quantum-dot-quantum-well structure in the CdSe-ZnS material system dual emission in the visible spectrum has been accomplished by Battaglia *et al*. [97]. Such a heteronanocrystal consists of a quantum dot core made of CdSe, then a ZnS shell barrier surrounding the core, and finally a CdSe shell quantum well around the barrier. Sapra *et al.* has also previously demonstrated white light emitting heteronanocrystals in solution by using dual-color emission in cyan and red [51]; however, only these cyan and red color emitting nanocrystals in solution are not sufficient for lighting applications, *e.g.*, due to their low color rendering index.

In this section we present high-quality white light generation by hybridizing dual-color heteronanocrystals, made of (CdSe)ZnS/CdSe in (core)shell/shell structure emitting in red from the CdSe cores and green from the CdSe shells, on blue InGaN/GaN light emitting diodes. Employing these onion-like heteronanocrystals, we achieve the photometric properties of tristimulus coordinates (x,y)=(0.36,0.30), luminous efficacy of optical radiation (the ratio of

emitted luminous flux to radiant flux in units lumen per optical power) *LER*=278 lm/W_{opt}, correlated color temperature *CCT*=3929 K, and color rendering index *CRI*=75.1, with the emission spectrum as shown in Figure 5.2.1. We also report the quantum mechanical design and the photometric analysis of these dual-color emitting quantum-dot-quantum-well heteronanocrystals integrated on light emitting diodes to obtain high-quality white light.

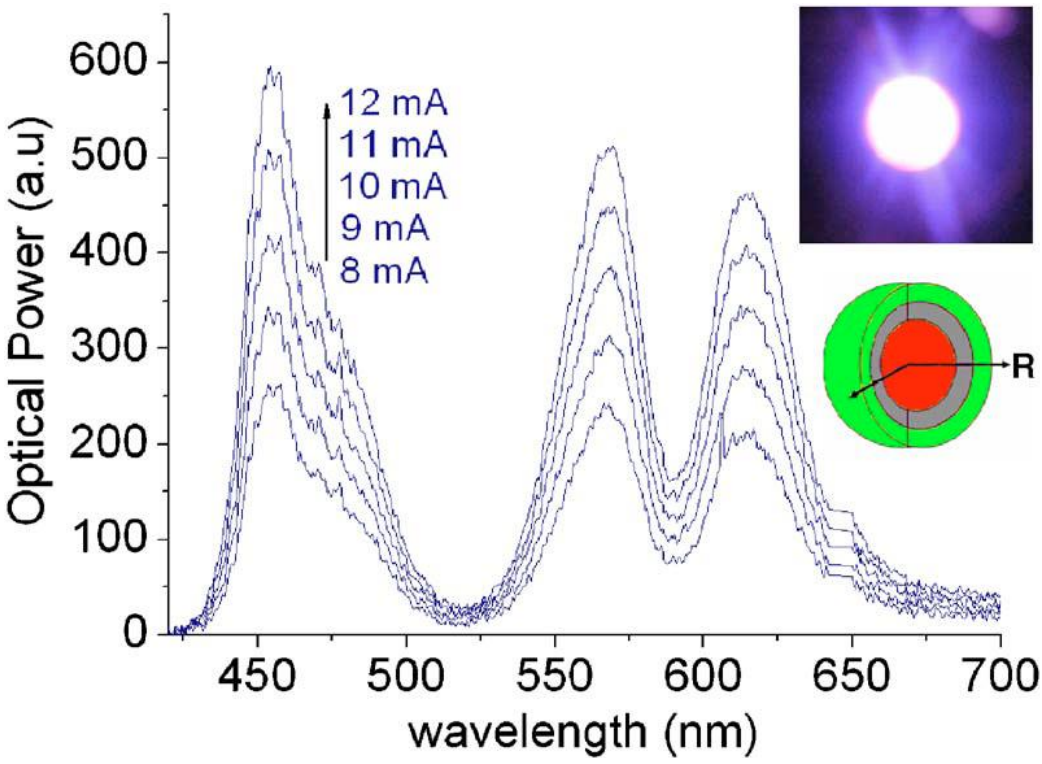

Figure 5.2.1 Luminescence spectra of onion-like (CdSe)ZnS/CdSe (core)shell/shell heteronanocrystals hybridized on a blue light emitting diode driven at different levels of current injection at room temperature, along with a schematic structure of the heteronanocrystals (not drawn to scale) and a picture of the resulting hybrid NC-WLED while generating white light.

5.2.2 Simulation and design

The operating principle of these hybrid NC-WLEDs relies on the use of the integrated NC film as the photoluminescent layer pumped by the LED platform. When electrically driven, the LED pump source excites the NC emitters. As a

result, the dual-color photoluminescence from the NC emitters in conjunction with the single-color electroluminescence from the LED contributes to the white light generation. However, to achieve such white light generation with high-quality photometric properties, these NC emitters along with their integrating LEDs need to be very carefully analyzed and designed. For that purpose, in our photometric analysis, by taking into account the possible emission ranges of our heteronanocrystals and light emitting diodes for white light generation, as in the case of conventional red-green-blue (RGB) white LEDs, we consider a peak emission wavelength of 450 nm in the blue region to be provided by the InGaN/GaN LED, and two peak wavelengths of 550 nm in the green and 620 nm in the red region to be provided by the heteronanocrystals. For feasible implementation, we take the emission in each color with identical peak levels and with a typical variance of 20 nm (corresponding to a full width half maximum of 33 nm). The photometric analysis of these design parameters then leads to white light generation with the optical properties of (x, y)=(0.34, 0.30), *LER*= 315 lm/W_{opt}, *CCT*=4979 K, and *CRI*=75.5. This shows in principle that the use of such green-red emitting heteronanocrystals on blue LED enables achieving high-quality WLEDs, if designed properly. To obtain green and red emission from our heteronanocrystals at the targeted wavelengths when cast into solid thin films, we also consider a typical in-film red shift of approximately 20 nm with respect to in-solution emission (due to the interactions [101] between the nanocrystals when in film, *e.g.*, re-absorption, dipole-dipole interaction, energy transfer, *etc*.). This means that the red emission from the CdSe core must be at around 600 nm in solution. This requires a quantum dot radius of approximately 2.22 nm [46]. Surrounding the core, we then need to add 2 monolayers of ZnS, which provides a sufficiently high potential barrier. Finally, surrounding the ZnS shell, we need to add the CdSe shell to obtain the green emission as desired.

For the quantum mechanical analysis of our dual-color emitting heteronanocrystals, we consider only s-symmetry states (with zero angular

momentum) in which the wavefunction depends on the radial part $R_{n,l=0}(r)$. The material parameters used in our design are summarized in Table 3.4.1 [36], [59], [60-62]. After solving for the energy levels (eigenvalues) and wavefunctions (eigenfunctions) assuming the effective mass approximation, we calculate the energy difference in each transition by adding the respective hole and electron energy eigenvalues, and the Coulomb interaction as a first-order perturbation [54]. As a result, the emission from the CdSe core is computed to be at 602 nm as expected for a radius of 2.22 nm and the green emission from the CdSe shell is obtained at 518 nm when 2 ML of CdSe shell is used. (Since in our simulation the last ZnS barrier is taken to be infinitely thick to find bounded solutions, we further expect to have a red shift for this 518 nm peak because of the reduced confinement of the electrons and holes due to the finite barrier in the implementation.) The probability distribution and the spatial product of the electron and hole wavefunctions for this heteronanocrystal structure are presented in Figure 5.2.2(a) and (b) for the ground states (n=1) and for the first excited states (n=2), respectively. Also the wavefunction overlaps and overlap squares (oscillator strength), the exciton binding energy due to the Coulomb interaction, and the resulting optical transition energies are listed in Table 5.2.1.

In both n=1 and n=2 transition energies, our analysis predicts that the oscillator strengths are near to 1 showing that the transition probability is high, and that the ground state excitons are localized in the core for the red emission and the first excited state excitons are mainly localized in the CdSe shell for the green luminescence possibly to lead to dual-color emission. But at this juncture it is also worth mentioning that although the theoretical calculations predict dual emission and these onion-like structures have been shown to exhibit dual emission in the solutions, a further study on a single-particle level needs to be performed to confirm the dual nature of this emission. Nevertheless, the present working parameters for the device will still remain valid whether the single particles exhibit dual emission or not.

Table 5.2.1 Electron and hole wavefunction overlaps ($<\psi_{electron}(r)|\ \psi_{hole}(r)>$), their overlap squares ($<\psi_{electron}(r)|\ \psi_{hole}(r)>^2$), the exciton binding energy due to their Coulomb interaction and the resulting optical transition energies for the ground states (n=1) and for the first excited states (n=2).

	Overlap	Overlap square	Coulomb interaction (meV)	Transition energy (eV)
Ground state (n=1)	0.9390	0.8817	99.1	2.0622
First excited state (n=2)	0.9505	0.9035	25.8	2.3913

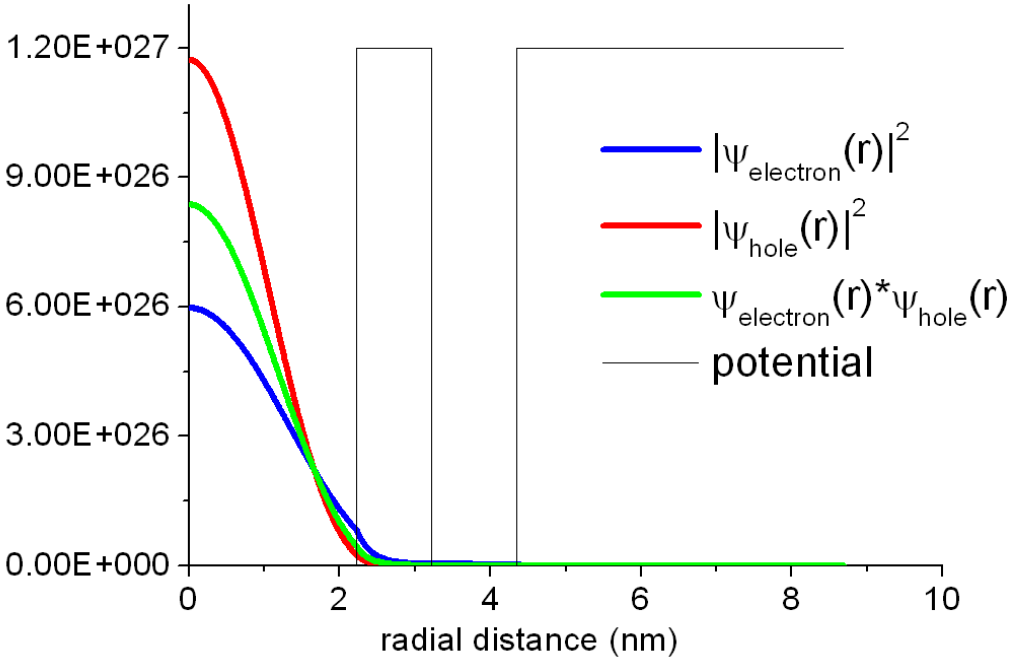

(a)

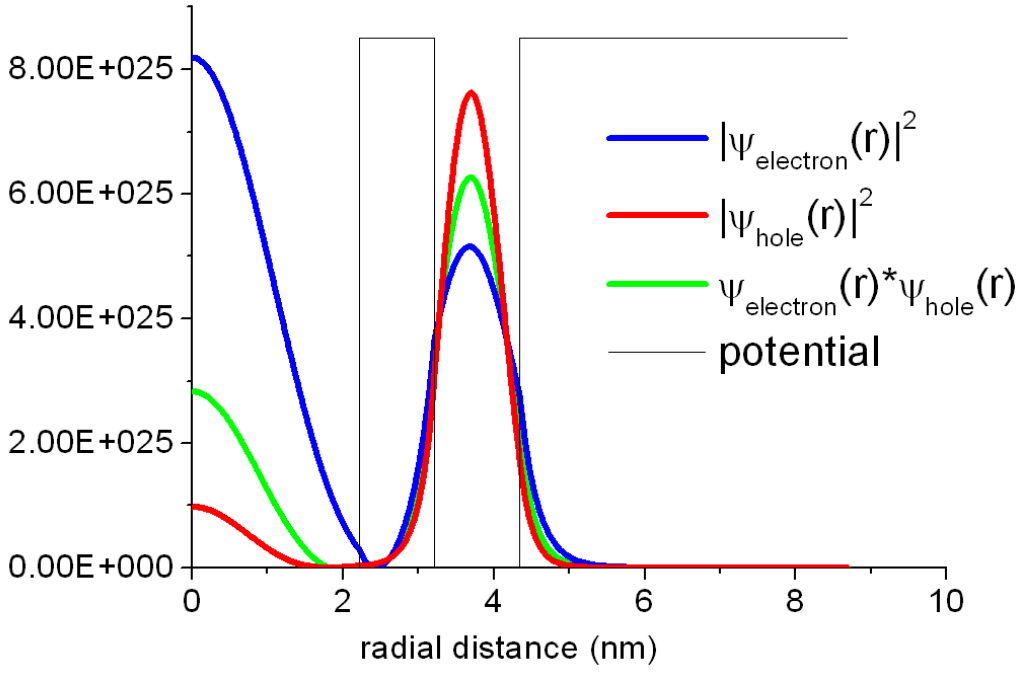

(b)

Figure 5.2.2 $|\psi_{electron}(r)|^2$ (in blue) and $|\psi_{hole}(r)|^2$ (in red) show the probability distribution of electron and holes in the (CdSe)ZnS/CdSe (core)shell/shell, respectively, while $\psi_{electron}(r)^*\psi_{hole}(r)$ (in green) indicates the relative spatial localization of excitons, with respect to the potential profile (in black): (a) for the ground state (n=1), and (b) for the first excited state (n=2).

To realize our heteronanocrystal design, we synthesize (CdSe)ZnS/CdSe (core)shell/shell nanocrystals by following the procedure given in Section 3.3.4. The absorption and emission spectra of the resultant nanocrystals are given in Figure 3.3.4.1. In solution, it is significant to obtain the red peak lower than the green peak because, when the nanocrystals are closely packed in film, the green light emitted by the nanocrystal shells is partially reabsorbed by the nanocrystal cores that re-emit in red, and as a result, the lower red peak increases. For the blue InGaN/GaN LED, we use a GaN dedicated metal organic chemical vapor deposition (MOCVD) system (Aixtron RF200/4 RF-S). For this LED emitting at 452 nm, similar design, growth, fabrication, and characterization are explained in our previous work [69], [70], [71], [102]. Further for the hybridization of nanocrystals and LED, we make closely-packed nanocrystal films on the LED platform.

5.2.3 Characterization of onion-like nanocrystals hybridized white LEDs

For the hybrid NC-WLED, we use 0.83 nmol of these dual-color emitting heteronanocrystals to achieve white light generation. The resulting luminescence spectra under different current injection levels are given in Figure 5.2.1, which correspond to (x, y)=(0.36, 0.30), *LER*=278 lm/W_{opt}, *CCT*=3929 K, and *CRI*=75.1 at all current levels. These experimental results are in good agreement with our photometric simulation. The hybrid WLEDs based on such onion-like heteronanocrystals are advantageous because they provide a reasonable color rendering index due to their broad emission while the nanocrystal hybridization is simple due to the need for the integration of only a single type of multi-color emitting heteronanocrystals instead of the integration of multiple combinations of various single-color emitting nanocrystals.

5.2.4 Conclusion

In this section, we presented white light generation by hybridizing dual-color green and red emitting heteronanocrystals made of (CdSe)ZnS/CdSe (core)shell/shell on a blue emitting InGaN/GaN light emitting diode. We showed the photometric and quantum mechanical analyses of these onion-like heteronanocrystals integrated on blue LEDs to achieve high-quality white light generation. The hybrid WLEDs based on such multi-color emitting heteronanocrystals prove to be beneficial because of simple device hybridization requiring the integration of only a single type of nanocrystals rather than the integration of various combinations of single-color emitting nanocrystals.

5.3 Tuning shades of white light with multi-color quantum-dot-quantum-well emitters based on onion-like CdSe-ZnS heteronanocrystals

This section is based on the publication "Tuning shades of white light with multi-color quantum-dot-quantum-well emitters based on onion-like CdSe-ZnS heteronanocrystals" H. V. Demir, **S. Nizamoglu**, E. Mutlugun, T. Özel, S. Sapra, N. Gaponik, A. Eychmüller, Nanotechnology 19, 335203 (2008). Reproduced (or 'Reproduced in part') with permission from Institute of Physics. Copyright 2008 Institute of Physics.

In this section we present white light generation controlled and tuned by multi-color quantum-dot-quantum-well emitters made of onion-like CdSe/ZnS/CdSe core/shell/shell heteronanocrystals integrated on InGaN/GaN light emitting diodes. We demonstrate hybrid white LEDs with *(x,y)* tristimulus coordinates tuned from (0.26,0.33) to (0.37,0.36), correlated color temperature from 27,413 to 4,192 K, and luminous efficacy of optical radiation from 202 to 370 lm/W_{opt} by controlling the number of their integrated red-green emitting heteronanocrystals. We investigate the modification of in-film emission from these multi-layered heteronanocrystals with respect to their in-solution emission, which plays a significant role in hybrid LED applications. Our proof-of-principle experiments indicate that these complex heteronanocrystals hold promise for use as nanoluminophors in future hybrid white LEDs.

5.3.1 Introduction

Only recently multi-color emitting semiconductor heteronanocrystals (hetero-NCs) have been demonstrated by Battaglia *et al.* using a quantum-dot-quantum-well (QDQW) structure in CdSe-ZnS material system [97]. In this nested structure, first a CdSe core, then a ZnS barrier shell, and finally a CdSe well

shell are synthesized one after the other, outer layers surrounding inner ones. By using these multi-layered CdSe-ZnS hetero-NCs in solution, white light generation with multi-color emission from their CdSe cores (in yellow-orange) and from their CdSe shells (in cyan) has been accomplished [51]. However, these orange-cyan emitting heteronanocrystals in solution are not sufficient for white light generation on a LED platform in the solid state. For that reason, emission properties of these heteronanocrystals need to be carefully analyzed in the solid form for proper integration on a LED platform to generate white light [103]. In this section, unlike the previous work of ours and others, we present white light generation precisely controlled and tuned by multi-color emitting quantum-dot-quantum-well heteronanocrystals integrated on InGaN/GaN light emitting diodes. In this section, tuning photometric properties of white light with such multi-color emitters enables application-specific lighting with optimal spectral content, *e.g.*, for street lighting at nights and museum display lighting indoors.

5.3.2 Design and fabrication

Our multi-color light emitters, made of onion-like CdSe/ZnS/CdSe core/shell/shell heterostructure, are designed and synthesized to emit in red (around 600 nm) from the CdSe core and in green (around 550 nm) from the CdSe shell. By careful design and hybridization of these multi-layered red-green emitting heteronanocrystals on blue emitting LEDs, we demonstrate hybrid integrated WLEDs on a single chip. These hybrid hetero-NC-WLEDs are implemented in a well controlled manner with their *(x,y)* tristimulus coordinates tuned from (0.26,0.33) to (0.37,0.36) across CIE chromaticity diagram as shown in Figure 5.3.1, along with their corresponding correlated color temperature tuned from 27,413 to 4,192 K and the luminous efficacy of their optical radiation tuned from 202 to 370 lm/W_{opt}. The tuning of these photometric properties is conveniently controlled with the number of integrated heteronanocrystals. Related to tuning, we investigate the modification of in-film emission from these multi-layered heteronanocrystals with respect to their in-

solution emission. This plays an important role in the use of these complex heteronanocrystals in hybrid LED applications.

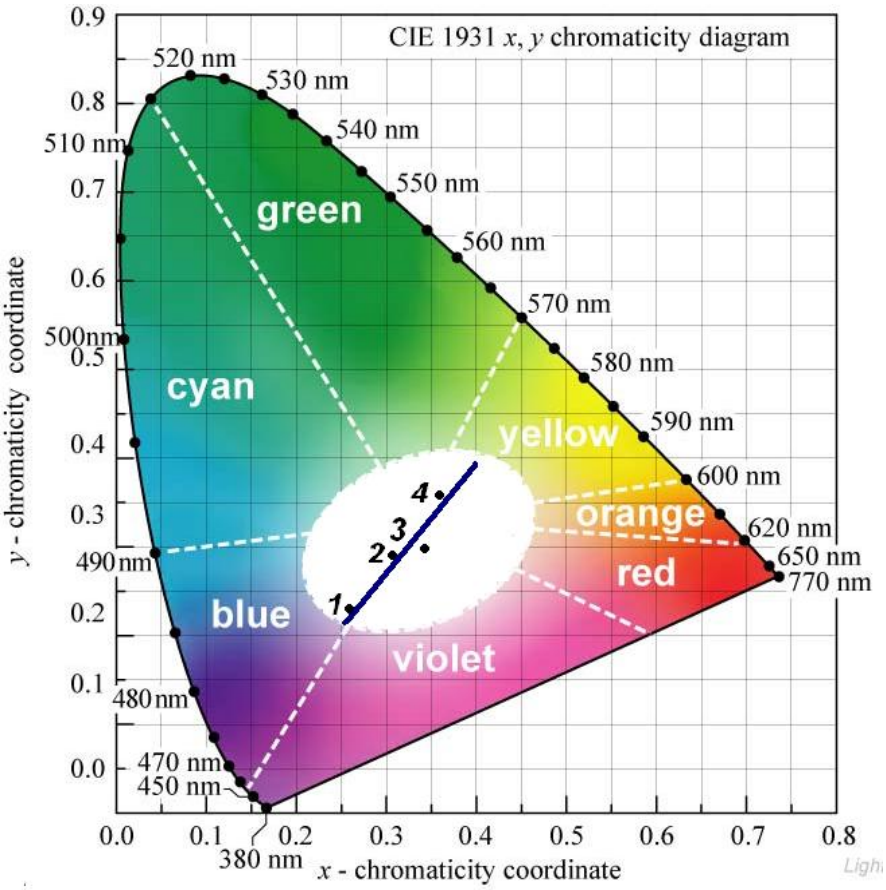

Figure 5.3.1 Tuning shades of white light with multi-color quantum-dot-quantum-well emitters made of onion-like CdSe/ZnS/CdSe core/shell/shell heteronanocrystals integrated on InGaN/GaN light emitting diodes (Hetero-NC-WLEDs 1-4) across CIE (1931) chromaticity diagram.

For blue InGaN/GaN light emitting diodes, we use a GaN dedicated metal organic chemical vapor deposition (MOCVD) system (Aixtron RF200/4 RF-S). We first grow a 14 nm thick GaN nucleation layer and a 200 nm thick GaN buffer layer. Then follows a 690 nm thick, Si doped n-type contact layer. Subsequently, we continue the epitaxial growth with five 4–5 nm thick InGaN/GaN quantum structures as the active layers of our LEDs. We use an

active region growth temperature of 661 °C to obtain electroluminescence peak around 450 nm. Finally, we finish our growth with p-type layers that contain Mg-doped, 50 nm thick $Al_{0.1}Ga_{0.9}N$ and 120 nm thick GaN layers as the contact cap. Following the growth, we activate Mg dopants at 750 °C for 15 minutes. To construct device mesas and electrical contacts, we use the standard semiconductor processing procedures including photolithography, thermal metal evaporation, reactive ion *etc*h, and rapid thermal annealing, as also performed in our previous works [69-71]. The p-contacts consist of Ni/Au (15 nm/100 nm) annealed at 700 ^{o}C for 30 s under N_2 and the n-contacts consist of Ti/Al (100 nm/2500 nm) annealed at 600 ^{o}C for 60 s under N_2. For the integration of the hetero-NCs on the LEDs with a cross-sectional active area of 300 μm x 300 μm, we make relatively uniform closely-packed heteronanocrystal films on them, controlling the film thickness with the account of starting NC solution. Taking the necessary amount from heteronanocrystal-toluene solution, we add acetone and centrifuge the resulting mixture to precipitate the hetero-NCs. We then disperse the heteronanocrystals in solvent chloroform and drop-cast them on the LED in controlled amounts. By post-baking over 10 min, we completely evaporate the solvent for proper hetero-NC film formation. InGaN/GaN LEDs are demonstrated to achieve long lifetime around ten thousands of hours and nanocrystal emitters exhibit typical shelf lifetime to be thousands of hours [76].

5.3.3 Our hybrid white LEDs

Table 5.3.1 Photoluminescence peak wavelengths of the synthesized onion-like CdSe/ZnS/CdSe heteronanocrystals in solution and in film (Samples 1-4).

Peak wavelengths (nm) / Samples	Shell emission peak	Core emission peak
Reference (in solution)	**558.42**	**613.32**
Sample 1 (in film)	**561.75**	**602.17**
Sample 2 (2 x hetero-NCs in Sample 1)	**562.74**	**604.64**
Sample 3 (4 x hetero-NCs in Sample 1)	**560.48**	**612.62**
Sample 4 (9 x hetero-NCs in Sample 1)	**569.44**	**621.53**

Table 5.3.2 Photoluminescence relative peak intensities of the synthesized onion-like CdSe/ZnS/CdSe heteronanocrystals in solution and in film (Samples 1-4).

Relative intensity (a.u.) / Samples	Shell emission peak	Core emission peak
Reference (in solution)	**0.695**	**0.156**
Sample 1 (in film)	**0.573**	**0.152**
Sample 2 (2 x hetero-NCs in Sample 1)	**0.609**	**0.145**
Sample 3 (4 x hetero-NCs in Sample 1)	**0.228**	**0.668**
Sample 4 (9 x hetero-NCs in Sample 1)	**0.136**	**0.820**

A variety of physical mechanisms including reabsorption, dipole-dipole interaction, energy transfer, and effective dielectric constant change of the environment significantly alter optical emission properties of the nanocrystals, typically leading to a red shift, in their luminescence when cast in solid film with respect to their luminescence when in solution. To investigate these

luminescence modifications of the heteronanocrystals in film compared to in solution and its significance in device implementation of WLEDs, we synthesize CdSe/ZnS/CdSe heteronanocrystals with emission originating from the CdSe core and CdSe shell. The in-solution luminescence that comes from CdSe core has its peak at 613 nm, and the one from the shell at 558 nm. The long-wavelength emission from the core is confirmed by only red emission after the synthesis of the core.

For investigating in-film luminescence red shift with respect to in-solution luminescence, we prepare four samples of heteronanocrystal films with different heteronanocrystal amounts precisely in integer multiples (1, 2, 4, and 9 multiples) of the starting sample (ca. 1 nanomoles). Tables 5.3.1 and 5.3.2 show the photoluminescence peak wavelengths and relative peak intensities of these samples (Samples 1-4) excited with a He-Cd laser at 325 nm at room temperature. As the number of heteronanocrytals in each sample increases, we observe that all emission peaks experience red shifts in the film and that the relative intensities of emission at shorter wavelengths decrease (due to the re-absorption, dipole-dipole interaction, energy transfer, *etc*.). However, with respect to the in-solution PL (reference), the peak (with emission at 613 nm in solution) generated by the CdSe core in the thin films (Samples 1-4) experiences a blue shift as shown in Table 5.3.1. Here this significant blue shift is attributed to the effect of the substrate, which decreases with increasing number of nanocrystals [101]. The effect of the substrate as blue shift in photoluminescence is valid for excitons localized both in CdSe core and shell resulting red and green emission, respectively. However, since the spatial localization of excitons in the shells are closer to each other, the red shift due to the dipole interaction is higher resulting a dominant red shift for the shell emission.

Moreover, for Samples 1-4, it is interesting to note that although the peak coming from the CdSe core experiences a red shift of 8.2 nm going from Sample 1 to Sample 4, the peak (with emission 558 nm in solution) coming from the

CdSe shells experience a red shift of 11.0 nm. As a result, the shells exhibit a larger red shift in comparison to the core in the thin films. We consider the additional red shift compared to the core is due to the collectivization of the electronic states as our hetero-NCs do not have any outmost ZnS potential barrier that can prevent occurrence of the coupled states. At this point, it is also worth discussing that, although these onion-like heteronanocrystals have been previously by others [97] and also in our work [51], [103] shown to exhibit multi-color emission in solutions and in films, a further study on a single-nanocrystal level needs to be conducted to verify the multiple nature of this emission. However, these present discussions will still remain valid regardless the single heteronanocrytals exhibit multiple color emission or not.

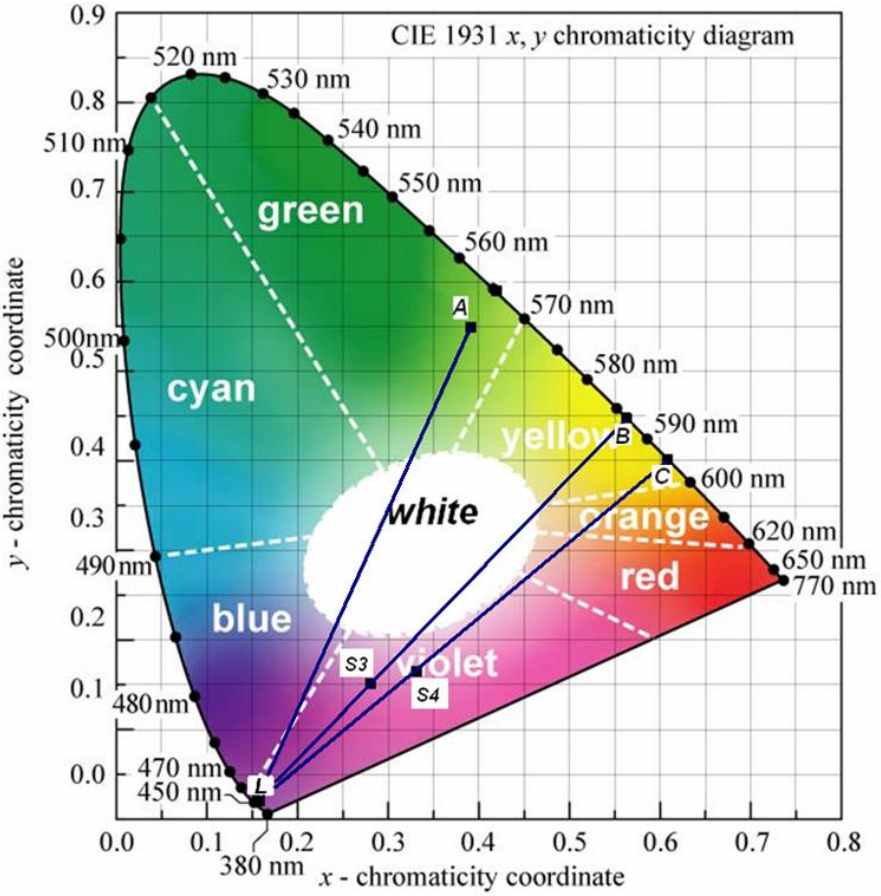

Figure 5.3.2 The tristimulus coordinates of electroluminescence from the blue LED (*L*), the tristimulus coordinates of photoluminescence from the heteronanocrystals in solution (*A*), the tristimulus coordinates of the total emission from the integrated hybrid hetero-NC-LEDs (*S3* and *S4*), and the effective tristimulus coordinates of the photoluminescence only contributed from the heteronanocrystals integrated on the blue LED for *S3* and *S4* (*B* and *C*, respectively), for the investigation of the resulting red shift (from *A* to *B* to *C*) across CIE (1931) chromaticity coordinates.

To further analyze the effect of the red shift in the solid form in device implementation we hybridize hetero-NCs with the same amounts of Samples 3-4 on the blue LED and investigate the resulting shift of the effective *(x,y)* tristimulus coordinates across CIE chromaticity diagram. In Figure 5.3.2, the point *L* represents the operating point of the starting blue LED at (0.14,0.03), while the points *S3* and *S4* at (0.27,0.10) and (0.33,0.12) represent the coordinates of the hybrid WLEDs integrated with the heteronanocrystals (with the amounts of Sample 3 and Sample 4) integrated on the blue LED,

respectively. On the other hand, the point *A* at (0.39,0.55) indicates the in-solution luminescence of the heteronanocrystals, while the point *B* at (0.52,0.45) and the point *C* at (0.61,0.40) show the effective *(x,y)* tristimulus coordinates of the collective luminescence contributed only from the integrated heteronanocrystals (excluding the LED contribution itself) on the hybrid devices of *S3* and *S4*, respectively.

Here we determine the effective tristimulus coordinates (*B* and *C*) by extrapolating a line from the blue LED operating point at (0.14,0.03) through the hybrid device operating points (*S3* and *S4*, respectively); the resulting end points of these extrapolated lines crossing the boundary on the chromaticity diagram give the effective tristimulus points to represent the effective color contribution solely from the hetero-NCs in the film on these hybrid platforms. The conventional boundary of the chromaticity coordinate is drawn by transforming each mono-color in the visible represented as a Dirac function using the color matching functions. Since we define these effective tristimulus coordinates on the boundary of the chromaticity diagram, they represent their effective contributing colors, each being mathematically equivalent to a specific Dirac function on the chromaticity diagram.

When we look at the shift of these coordinates from *A* to *B* to *C*, we clearly observe the effect of the heteronanocrystals' in-film red shift with respect to their in-solution luminescence on the chromaticity diagram. This red shift makes it harder to obtain white light generation in film in general. In Figure 5.3.2, the line that connects the operating points of the blue LED and the in-solution PL of hetero-NCs passes through the white region, implying that white light generation were possible with these hetero-NCs should there be no red shift in the film. However, in Figure 5.3.2, the in-film red shift makes it impossible to obtain white light generation for the hybrid device implementations with these heteronanocrystals in the film because the lines *L-S3* and *L-S4* do not intersect the white region at all. Therefore, this red shift in the luminescence of the solid

heteronanocrystals, which is inevitable, should be carefully taken into account to obtain white light using solid heteronanocrystals on a LED platform.

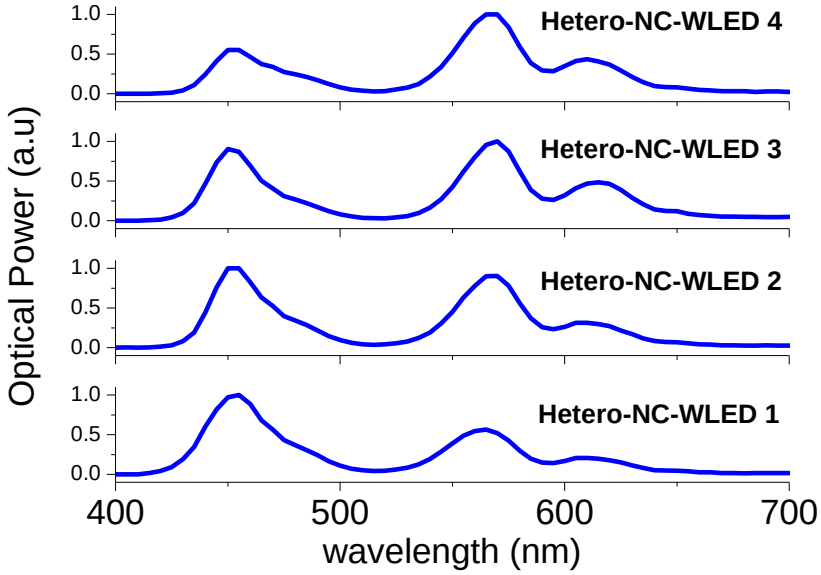

Figure 5.3.3 Emission spectra of our hybrid white light emitting diodes (hetero-NC-WLEDs 1-4).

To obtain white light generation, by considering the luminescence red shift in film with respect to solution, we synthesize heteronanocrystals with the core emission at 602 nm and the shell emission at 550 nm. For sample hetero-NC-WLED 1, we hybridize 0.33 nmol heteronanocrystals on the blue LED. We obtain the white light emission spectrum shown in Figure 5.3.3 with the tristimulus coordinates of (0.26,0.23) falling in the white region of the CIE choromaticity diagram as depicted in Figure 5.3.1, along with a color temperature of 27,413 K, and a luminous efficacy of the emitted spectrum of 258 lm/W_{opt}. From hetero-NC-WLED 1 to 4, we gradually increase the number of the hybridized heteronanocrystals on the blue LED as shown in Table 5.3.3. As a result, the color temperature decreases because the relative contribution coming from the heteronanocrystals with respect to the blue LED emission

increases. Finally, for hetero-NC-WLED 4, we integrate 0.50 nmol heteronanocrystals to generate white light with a warmer color temperature. The operating point corresponds to the tristimulus coordinates of (0.50,0.37) in the white region, the correlated color temperature decreases to 4,192 K, and the luminous efficacy of the emitted spectrum reaches a relatively high value of 375 lm/W_{opt}. As a result, from hetero-NC-WLED 1 to 4 we tune the optical properties of the generated white light with varying *(x,y)* tristimulus coordinates from (0.26,0.33) to (0.37,0.36), correlated color temperature from 27,413 to 4,192 K, and luminous efficacy of the emitted spectra from 202 to 370 lm/W_{opt} by precisely controlling the number of integrated heteronanocrystals.

Table 5.3.3 Photometric characteristics of our hybrid white hetero-NC-WLEDs (1-4).

Hetero-NC-WLED	Number of nanocrystals (nmol)	*x*	*y*	Correlated color temperature (K)	Optical luminous efficacy (lm/W_{opt})
1	0.33	0.26	0.23	27413	258
2	0.40	0.31	0.29	6780	313
3	0.46	0.34	0.30	4635	315
4	0.50	0.37	0.36	4192	375

5.3.4 Conclusion

In section, we presented white light generation controlled and tuned by hybridization of CdSe/ZnS/CdSe core/shell/shell multi-color emitting heteronanocrystals on blue emitting InGaN/GaN LEDs. We showed white hybrid hetero-NC-LEDs with varying *(x,y)* tristimulus coordinates from (0.26,0.33) to (0.37,0.36), correlated color temperature from 27,413 to 4,192 K, and luminous efficacy of optical radiation from 258 to 375 lm/W_{opt} by controlling the number of integrated heteronanocrystals. Furthermore, we discussed that the red shift in-film emission of the heteronanocrystals with

respect to the in-solution emission, which has significant effect on hybrid WLED implementation and has to be carefully taken into account for the proper design of such hybrid hetero-NC-WLEDs.

Chapter 6

Light emitting diodes based on NRET-enhanced color conversion

6.1 Nonradiative energy transfer in CdSe/ZnS core/shell nanocrystal solids enhances hybrid white light emitting diodes

This section is based on the publication "Resonant nonradiative energy transfer in CdSe/ZnS core/shell nanocrystal solids enhances hybrid white light emitting diodes" **S. Nizamoglu** and H. V. Demir, Optics Express 16, 13961-13968 (2008). Reproduced (or 'Reproduced in part') with permission from Optical Society of America. Copyright 2008 Optical Society of America.

We propose and demonstrate hybrid white light emitting diodes enhanced with nonradiative energy transfer in CdSe/ZnS core/shell nanocrystal solids integrated on near-UV InGaN/GaN LEDs. We observe a relative quantum efficiency enhancement of 13.2 percent for the acceptor nanocrystals in the energy gradient mixed assembly, compared to the monodisperse phase. This enhancement stems from the ability to recycle trapped excitons into nanocrystals using nonradiative energy transfer. We present the time-resolved photoluminescence of these nanocrystal solids to reveal the dynamics of their energy transfer and their steady-state photoluminescence to exhibit the resulting quantum efficiency enhancement.

6.1.1 Introduction

Semiconductor NCs have been extensively exploited in a wide range of applications [6], [64-68], [76], [81], [92], [93], [100], [104-107]. However, in those device applications, nanocrystals typically suffer from relatively low quantum efficiency when they are cast into solid form [101]. To address this problem, we investigate the use of Förster energy transfer in nanocrystal solids to increase their spontaneous emission rate in hybrid white light emitting diodes. The emission enhancement based on such carefully designed energy transfer systems is critically important especially for white light emitting diodes in solid state lighting application, which is considered to make one of the next solid state frontiers.

The Förster-type nonradiative energy transfer is the nonradiative transfer of excitation energy from an excited molecule (donor) to a ground-state molecule (acceptor) [108]. Kagan *et al.* first demonstrated ET in spin-cast films of closely packed CdSe core nanocrystals with different sizes [109], [110]. Crooker *et al.* showed bilayer light-harvesting quantum dot films with an effective energy bandgap gradient structure with monolayer assemblies of CdSe/ZnS core/shell nanocrystals [111]. This energy gradient structure efficiently transported energy between nanocrytals in a submicron range much faster than their radiative decay rates [31], [111].

Franzl *et al.* demonstrated energy transfer using bilayers of CdTe NCs by using oppositely charged polyelectrolyte linkers [112] and then without using any linker they revealed ET by making bilayers of oppositely charged NCs with directly linked water-soluble CdTe NCs [113]. They further showed a cascaded energy transfer having a funnel-like band gap profile structure by using distinctly sized CdTe nanocrystals [114]. Then, Klar *et al.* showed super efficient exciton funneling structure using layer-by-layer nanocrystals [108]. In

that study it is demonstrated that using energy gradient structure not only excitons in radiative states are transferred, but also the trapped excitons that are generally nonradiatively recombined are recycled that results an overall emission increase. Also, Achermann *et al.* demonstrated a none-white light emitting diode by pumping a single type of CdSe/ZnS nanocrystals using epitaxial quantum wells, *i.e.*, excitation from quantum wells to nanocrystals [91]. However, the use of the NRET particularly in nanocrystal solids of white light emitting diodes has not been studied or demonstrated for solid state lighting to date.

In this section, for white light emitting diodes we propose and demonstrate the enhancement of spontaneous emission in integrated nanocrystal solids by recycling their trapped excitons on hybrid WLED platforms. We use closely packed CdSe/ZnS core/shell nanocrystals of two carefully selected sizes with sufficient energy gradient (approximately 160 meV) hybridized on our near-UV InGaN/GaN LEDs for enhanced quantum efficiency of quantum dot solids. In such designed mixture of nanocrystal solids, the small quantum dots serve as donors and the large quantum dots as acceptors, leading to energy transfer from the small ones to the large ones. As a result, we observe an emission enhancement of 46% for the large dots residing in the mixed energy gradient assembly of small and large dots, with respect to the emission of only large dots. This corresponds to a 13.2% increase in the quantum efficiency of the large dots in the presence of the small dots because of their recycled excitons, compared to the large dots alone. Here we investigate NRET using both steady-state and time-resolved spectroscopy of these nanocrystal solid samples. Their time-resolved photoluminescence, which reveals the dynamics of the energy transfer, and their spontaneous emission at the steady state, which exhibits the resulting quantum efficiency enhancement, together prove the action of energy transfer in nanocrystal solids.

6.1.2 Materials and experimental method

To investigate Förster energy transfer, we use CdSe/ZnS core/shell nanocrystals with diameters of 7.7 nm and 8.2 nm emitting at 540 and 580 nm in solution, respectively. For control groups, we prepare two test solid films that consist of only small and only large quantum dots. For NRET, we prepare mixed assembly of both small and large nanocrystals by making their closely packed film. This solid film contains exactly the same total amount of large and small nanocrystals as in the control groups. For time-resolved spectroscopy measurements (shown in Figure 6.1.1), we use a FluoTime 200 spectrometer (PicoQuant) with a time-correlated single photon counting (TCSPC) system of PicoHarp 300 with a calibrated time resolution of 4 ps. To pump nanocrystal solids, we use a laser head at an emission wavelength of 375 nm with light pulses as short as 70 ps and a photon multiplier tube (PMT) as the detector. Using an output monochromator, we characterize all of the prepared NC solids at 550 nm and 612 nm, corresponding to the peak emission wavelengths of the small NCs and the large NCs in the film, respectively. For the data analysis we use the software FluoFit to deconvolute the instrumental response. For steady-state spectroscopy measurements (shown in Figure 6.1.2), we use a Xenon halogen lamp in a monochromator as the excitation light source and an integrating sphere for collecting the total emission from the nanocrystal solids.

6.1.3 Analysis of the nanocrystal layer

Figure 6.1.1(a) shows the time-resolved photoluminescence of only small nanocrystal solids along with that of mixed large and small solids, both at the emission wavelength of small dots (around 550 nm). Figure 6.1.1(b), on the other hand, depicts the time-resolved photoluminescence of only large nanocrystal solids along with that of mixed large and small solids, both at the emission wavelength of large dots (around 612 nm). In Figure 6.4.1(a), the decay rate of the mixed nanocrystal solids at 550 nm is clearly observed to increase with respect to the only small dots because the small dots serving as

donors in the mixture quench as a result of their excitation energy transferred to the acceptor large dots in the mixture. In contrast, in Figure 6.4.1(b) the decay rate of the mixed nanocrystal solids at 612 nm is clearly observed to decrease with respect to the only large dots because the acceptor large dots take the transferred energy from the donor small dots. We fit our decay curves in Figure 6.4.1(a) and (b) using a multiexponential model fit with convolution of the laser diode response at 375 nm and the fitting parameters are summarized in Table 6.4.1. Here the lifetime 1 (*i.e.*, τ_1) is the general lifetime of the nanocrystals that is on the order of tens of nanoseconds [91], [101]. However, there exists another decay lifetime (*i.e.*, τ_2) more than 40 ns. The amplitude of the long decay component is relatively weak when we compare its amplitude around hundreds with the general nanocrystal decay time amplitude around thousands. We attribute the slow and weak decay component to environmental effects. Furthermore, for mixed small and large nanocrystal case at 612 nm we have a third lifetime component (*i.e.*, τ_3) as 2.84 ns. This third component is an additional decay for small dots as donors, but it is an additional energy increase for large dots as acceptors in mixed case (In Table 6.4.1 to differentiate the energy increase component, we put a minus sign for its amplitude). In addition, we also calculate the intensity averaged lifetime components with Equation (6.1.1) (where A_i and τ_i refer to amplitudes and lifetimes, respectively) to see the quenching for small dots and lifetime increase in large dots. The intensity weighted average decay time constant for the small dots at 550 nm is found to decrease from 15.53 to 10.58 ns as a consequence of quenching when the small dots are placed in the close vicinity of the large dots in the mixed assembly. On the other hand, the intensity weighted average decay time constant of large dots in the mixed assembly at 612 nm is found to increase from 17.66 to 22.59 ns with respect to only large dots as a result of the energy transfer. Furthermore, we calculate the amplitude weighted average lifetime (*i.e.*, using Equation (6.1.2)) of only small nanocrystals and mixed small and large nanocrystals case at 550 nm to determine the efficiency of energy transfer (*i.e.*, using Equation (6.1.3)) where $\tau_{amp\_av\_DA}$ refers to the amplitude weighted average lifetime of mixed

small (donor) and large (acceptor) nanocrystals and $\tau_{amp\_av\_D}$ refers to the amplitude weighted average lifetime of only small (donor nanocrystal case) [115]. As a result, the efficiency of energy transfer for mixed small and large nanocrystals achieves a relatively high value of 55.58%.

$$\tau_{av} = \frac{\sum_i A_i \tau_i^{\,2}}{\sum_i A_i \tau_i} \tag{6.1.1}$$

$$\tau_{amp\_av} = \frac{\sum_i A_i \tau_i}{\sum_i A_i} \tag{6.1.2}$$

$$E = 1 - \frac{\tau_{amp\_av\_DA}}{\tau_{amp\_av\_D}} \tag{6.1.3}$$

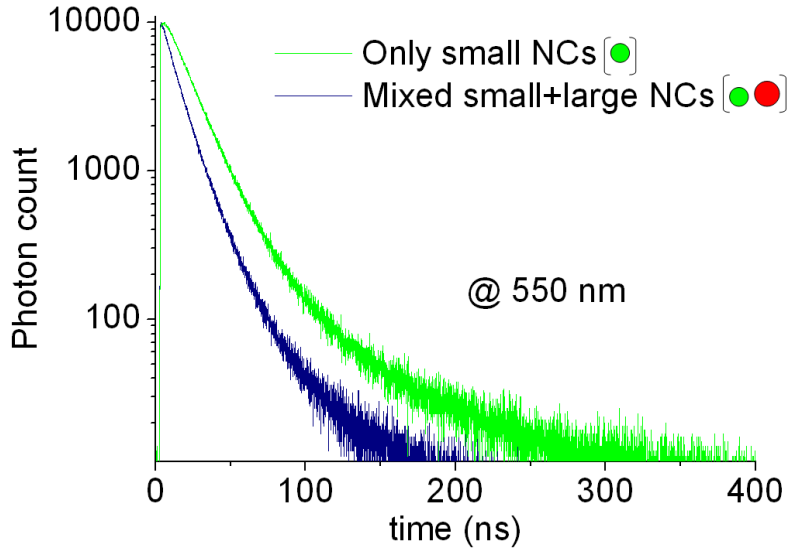

(a)

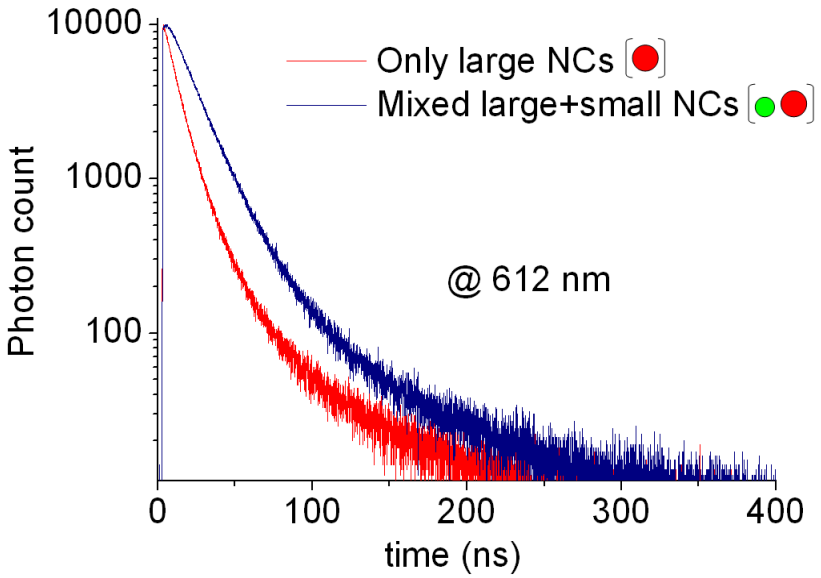

(b)

Figure 6.1.1 Time-resolved photoluminescence of (a) only small nanocrystal solids (with a diameter of 7.7 nm) and mixed nanocrystal solids (with diameters of 8.2 and 7.7 nm) for emission at 550 nm, and (b) only large nanocrystal solids (with a diameter of 8.2 nm) and mixed nanocrystal solids (with diameters of 8.2 and 7.7 nm) for emission at 612 nm.

Table 6.1.1. The fitting parameters of time-resolved spectra in Figure 6.1.1(a)-(b). A_n and τ_n are the amplitudes and decay time constants, for n=1, 2, 3; τ_{av} and τ_{amp_av} are the intensity and amplitude weighted average decay time constants.

	Only small nanocrystals ***(at 550 nm)***	**Mixed small and large nanocrystals** ***(at 550 nm)***	**Only large nanocrystals** ***(at 612 nm)***	**Mixed small and large nanocrystals** ***(at 612 nm)***
A_1 [Counts]	10313.6	4189.2	10171	12588
τ_1 [ns]	12.06	10.00	9.936	16.96
A_2 [Counts]	410.3	110.9	499.9	416.0
τ_2 [ns]	41.133	46.33	42.597	61.90
A_3 [Counts]	-	7248	-	-3298
τ_3 [ns]	-	2.84	-	2.84
τ_{av} [ns]	15.53	10.58	15.62	22.57
τ_{amp_av} [ns]	13.17	5.85	-	-

We also present the steady-state spectroscopy measurements of these nanocrystal solid samples that are taken using an integrating sphere to observe the effect of NRET on the spontaneous emission spectra and the associated quantum efficiencies. In Figure 6.1.2, the photoluminescence and absorption spectra of only large, only small, and mixed large and small nanocrystal assemblies are shown. In the mixed large and small nanocrystal solids, the peak at 550 nm decreases with respect to only small nanocrystal solids due to transferring its excitation energy to the large nanocrystals (*i.e.*, quenching of the small nanocrystals) and, for the same reason, the peak at 612 nm increases as a result of the transferred energy. Although the number of large dots in mixed assembly is the same as only large dots, we observe a 46% enhancement in the emission of large dots in the mixed assembly compared to only large solids.

Furthermore, to investigate the quantum efficiencies (QEs) of these solid samples, we experimentally measure QE of the mixed solids to be 29.1% in the integrating sphere. It is known that the emission spectrum of nanocrystals exhibits a Gaussian like emission line shape on a wavelength scale. This kind of gaussian fit is made also in several references too [116-118]. On the other hand, using Gaussian fits to the steady-state luminescence of the mixed nanocrystal solids and weighting only according to the emission levels of small and large dots alone, without considering energy transfer, we calculate the expected QE of the mixed solids to be only 25.7%. Therefore, we find out that the experimentally measured QE is 13.2 percent better than the predicted one because of the energy transfer.

In defect-rich NCs, excitons are effectively captured in surface traps that result non-radiative recombination, but the defect-poor NCs show a higher probability for radiative recombination. Defect-rich NCs in films may capture excitons from proximal defect-poor NCs. As a result, this difference comes from the portion of trapped excitons recycled by the energy transfer to additionally contribute to the emission. Furthermore, we also observe that the orange emission around 592 nm of only large nanocrystals is blue shifted to shorter wavelengths with respect to mixed large and small nanocrystals, or in other words, the orange emission in mixed structure makes red shift with respect to only large nanocrystals case. This red shift is due to the dipole-dipole interaction. The orange emitting nanocrystals with larger sized ones due to size distribution accepts more energy from green emitting nanocrystals and cause a further red-shift though the size distribution <5%. A similar situation occurs also in single size nanocrystals, a red shifted and modified emission line shape occur due to the electronic energy transfer within inhomogeneous distribution of nanocrystals [110].

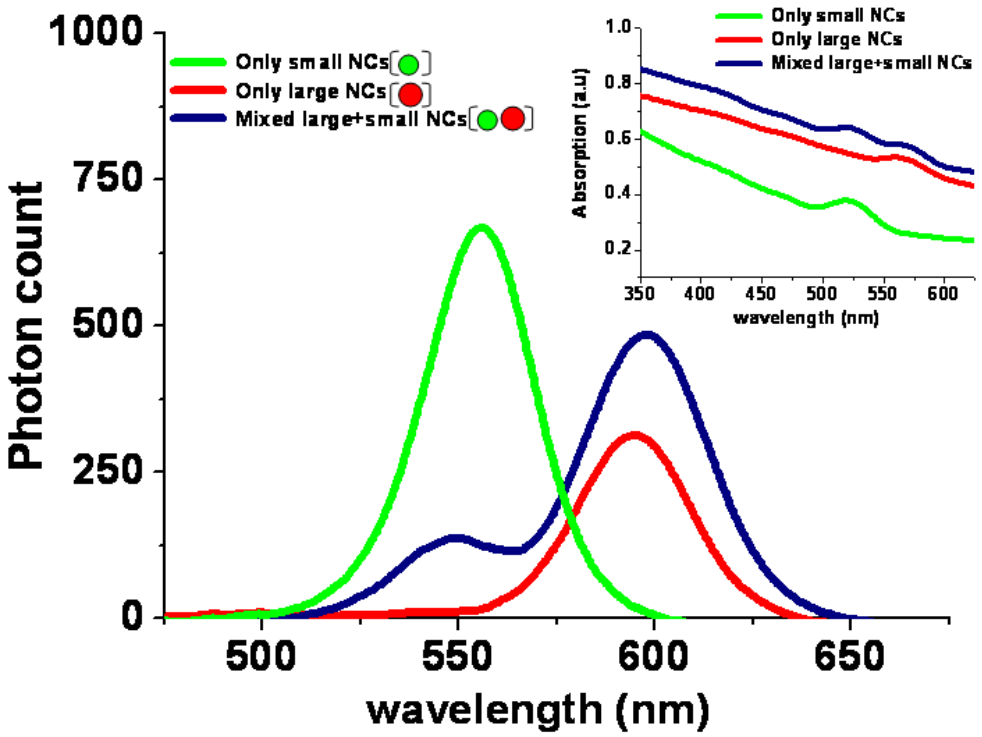

Figure 6.1.2 Photoluminescence spectra of only large nanocrystals (with a diameter of 8.2 nm), only small nanocrystals (with a diameter of 7.7 nm) and mixed large and small nanocrystals (with diameters of 8.2 and 7.7 nm, respectively) and their absorption spectra are shown as an inset.

6.1.4 Hybrid white light emitting diodes enhanced with resonant nonradiative energy transfer in CdSe/ZnS core/shell nanocrystal solids

We employ these mixed large and small nanocrystal assemblies that exhibit Förster energy transfer in white light generation. We use the same amount of nanocrystals in mixed assembly on an InGaN/GaN n-UV LED emitting at 383 nm. Similar device fabrication and characterization methods are given in our previous works [45], [69], [102], [119], [120], and their design and growth are described elsewhere [45]. The operating principle of this white light emitting

diode relies on the hybrid use of the LED as the excitation source and the integrated nanocrystal solid film as the photoluminescent layer. Near-UV LED pumps all the integrated nanocrystal solids that in turn luminescence at their corresponding emission wavelengths, while the excitons in the small nanocrystals and the trapped excitons also further transfer their energy to the large nanocrystals. Consequently, the photoluminescence of these nanocrystals enhanced with the energy transfer and the electroluminescence of the LED contribute altogether to generate white light. In Figure 6.4.3, the emission spectra of the hybrid device driven at various current injection levels at room temperature are shown. Here it is important to carefully balance the levels of green emission (λ_{PL}= 550 nm) and orange emission (λ_{PL}= 592 nm) from these nanocrystals to allow the near-UV tail of the LED emission to shift the tristimulus coordinates to the white region. The emission spectrum of hybrid LED corresponds to *(x,y)* tristimulus coordinates of (0.44,0.40) and a correlated color temperature of 2872 K. This very warm white light emitting diode with such a low correlated color temperature is particularly important for indoor illumination applications [76].

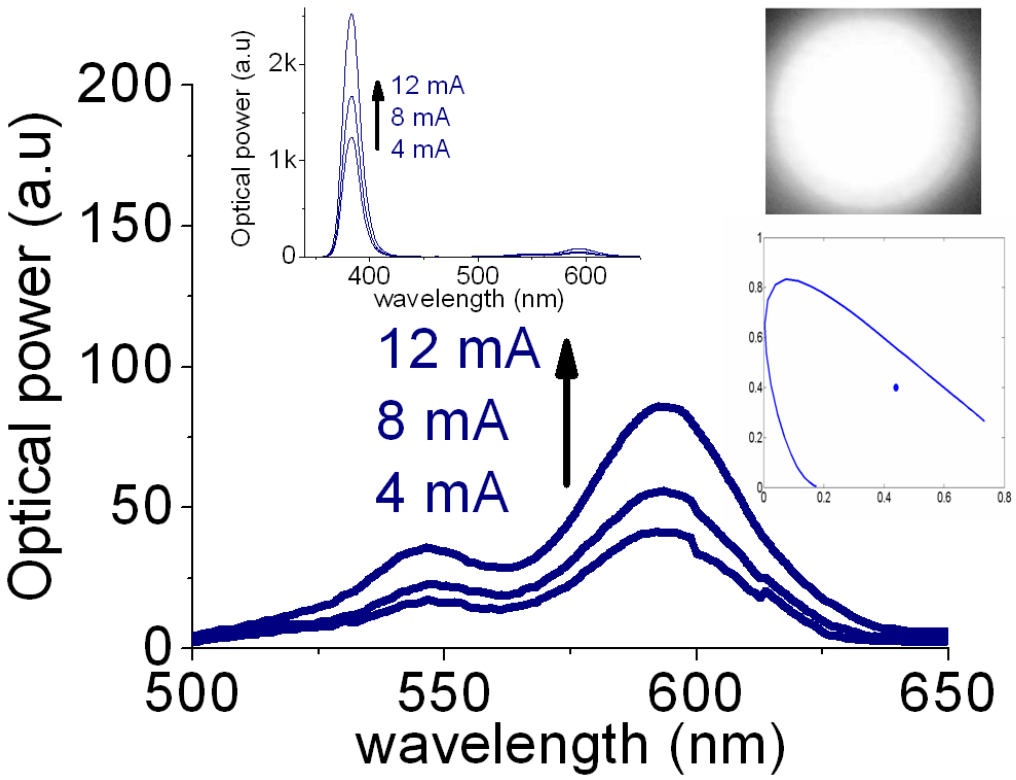

Figure 6.1.3 Emission spectra of mixed CdSe/ZnS core/shell nanocrystals (with diameters of 8.2 nm and 7.7. nm) hybridized on n-UV InGaN/GaN light emitting diode driven at different levels of current injection at room temperature, along with the corresponding (x, y) coordinates and pictures of the hybrid WLED, while generating white light.

6.1.5 Conclusion

In this section, we demonstrated hybrid white light emitting diodes enhanced with resonant nonradiative energy transfer in CdSe/ZnS core/shell nanocrystal solids integrated on near-UV InGaN/GaN light emitting diodes. We observed a relative quantum efficiency enhancement of 13.2% for the acceptor nanocrystals in the energy gradient assembly by comparing with the monodisperse phase. The quantum efficiency enhancement in CdSe/ZnS nanocrystal solids stems from the ability to recycle trapped excitons into nanocrystals using nonradiative energy transfer. We investigated NRET and quantum efficiency enhancement using both steady-state and time-resolved spectroscopy measurements. We believe

that the resonant nonradiative energy transfer offers great potential to improve the efficiency of nanocrystal solids in lighting applications.

6.2 Energy transfer enhanced color conversion using colloidal semiconductor quantum dots for solid state lighting

This section is based on the publication "Förster resonance energy transfer enhanced color-conversion using colloidal semiconductor quantum dots for solid state lighting" **S. Nizamoglu** and H. V. Demir, Applied Physics Letters 95, 151111 (2009). Reproduced (or 'Reproduced in part') with permission from American Institute of Physics. Copyright 2009 American Institute of Physics.

In this section, we present Förster-type nonradiative energy transfer enhanced color-conversion using colloidal semiconductor quantum dot nanocrystals to make reddish-orange light-emitting diodes for use in ultra-efficient solid state lighting. To achieve NRET-enhancement at 614 nm we use an energy gradient hybrid structure made of cyan- and orange-emitting CdSe/ZnS nanocrystals (λ_{PL}=492 and 588 nm in solution, respectively). This enables recycling of trapped excitons using NRET and achieves a relative quantum efficiency enhancement of 15.1% in reddish-orange full color-conversion for the integrated hybrid cyan-orange NC layer with respect to the case of full color-conversion using only orange NCs without NRET.

6.2.1 Introduction

Solid state lighting potentially provides substantial energy saving to allow for efficient energy utilization of the limited energy sources and reduction of carbon emission [1]. To further increase the energy saving of SSL, a photometric design (named "ultra-efficient solid-state lighting") that simultaneously achieves a luminous efficacy of 408 lm/W and a color rendering index of 90 at a warm correlated color temperature of 3000 K has been proposed [72], [73]. To achieve these photometric properties, it is required to have a set of pure color emission

in blue, green, yellow, and orange with the corresponding power levels of 1/8 at 463 nm, 2/8 at 530 nm, 2/8 at 573 nm, and 3/8 at 614 nm, each color having a full-width-at-half-maximum of 1 nm [72], [73]. In this design, the reddish-orange is the strongest color component with the highest relative power (3/8) and at the longest optical wavelength (at 614 nm), thus with the largest number of photons emitted per unit time among the other color components.

However, the internal quantum efficiency of $In_xGa_{1-x}N$ structures begins to significantly drop as approaching from blue to green color in the visible due to the increased In content in multi-quantum-wells, though $In_xGa_{1-x}N$ material system has the capability to cover the whole visible. Therefore, it is not possible to obtain reddish-orange emission at 614 nm by using $In_xGa_{1-x}N$ material system [121-123]. Different from the $In_xGa_{1-x}N$ material system, it is possible to achieve reddish-orange emission by using a quaternary alloy $(Al_xGa_{1-x})_{1-y}In_yP$. However, this material system is different from the $In_xGa_{1-x}N$ based material system, which prevents single-chip implementation of $In_xGa_{1-x}N$ based red color emission. The quantum efficiency of $(Al_xGa_{1-x})_{1-y}In_yP$ is also observed to decrease significantly as going from red to the other colors at shorter wavelengths due to the decreasing barrier energy in their quantum well structure. As a possible solution, color-converters can be used for light generation at 614 nm on $In_xGa_{1-x}N$ material system for reddish-orange emission. Although phosphors are the most commonly used color-converters on InGaN/GaN light-emitting diodes, they are not suitable for generating pure red/orange emission efficiently (*e.g.*, at 614 nm of ultra-efficient SSL) [4], [15] (and also shown in Figure 6.2.1), due to their wide FWHM (of about 100 nm), which undesirably causes the luminous efficacy to drop significantly (down to around 64 lm/W). Therefore, the hybrid use of a relatively narrow color-converter is important to enable the use of $In_xGa_{1-x}N$ LEDs at such long wavelengths.

To achieve this reddish-orange emission needed for ultra-efficient SSL, semiconductor colloidal quantum dot nanocrystals exhibit favorable optical properties with their narrow and symmetric photoluminescence, which is also widely and precisely tunable across the visible using quantum confinement effect for the targeted peak emission wavelengths [11], [81]. In the previous works of our group and the others, a wide range of studies on nanocrystal integrated LEDs, NRET in nanocrystals, and the use of nanocrystals in white and green/yellow LEDs have already been reported [45], [76], [83], [109], [124], [125]. However, NRET-enhanced color-conversion at long wavelengths critically important for ultra-efficient SSL has not been investigated to date. For that, in this section we present nanocrystal based orange color-conversion at long wavelengths (614 nm) that utilizes nonradiative energy transfer in full color-conversion on $In_xGa_{1-x}N$ LEDs for enhanced efficiency. To enable NRET in nanocrystals, we establish an energy gradient hybrid film that embeds a custom-design assembly of cyan- and orange-emitting CdSe/ZnS core/shell nanocrystals. By using this energy gradient, the trapped excitons are recycled into nanocrystals rather than losing them through nonradiative recombination in trap centers. As a result, we achieve a relative quantum efficiency enhancement of 15.1% in full color-conversion for this hybrid cyan-orange nanocrystal film with respect to the full color-conversion layer of only orange NCs without NRET.

6.2.2 Simulation

Figure 6.2.1 presents the color rendering index and luminous efficacy of optical radiation both decreasing as a function of increasing FWHM of 614 nm emission used in solid state lighting as described above. Despite exhibiting FWHM linewidths larger than 1 nm (*e.g.*, 30-40 nm), we find out that the resulting color rendering index of these NC color-converters is reduced only slightly by 11-13 units, and their luminous efficacy of optical radiation, only by 11-17 lm/W_{opt}, compared to the case of 1 nm wide FWHM as illustrated in Figure 6.2.1. Thus, this shows that it is possible to achieve reddish-orange

emission at 614 nm by using nanocrystals with sufficiently high color rendering index and high luminous efficacy as required for ultra-efficient SSL.

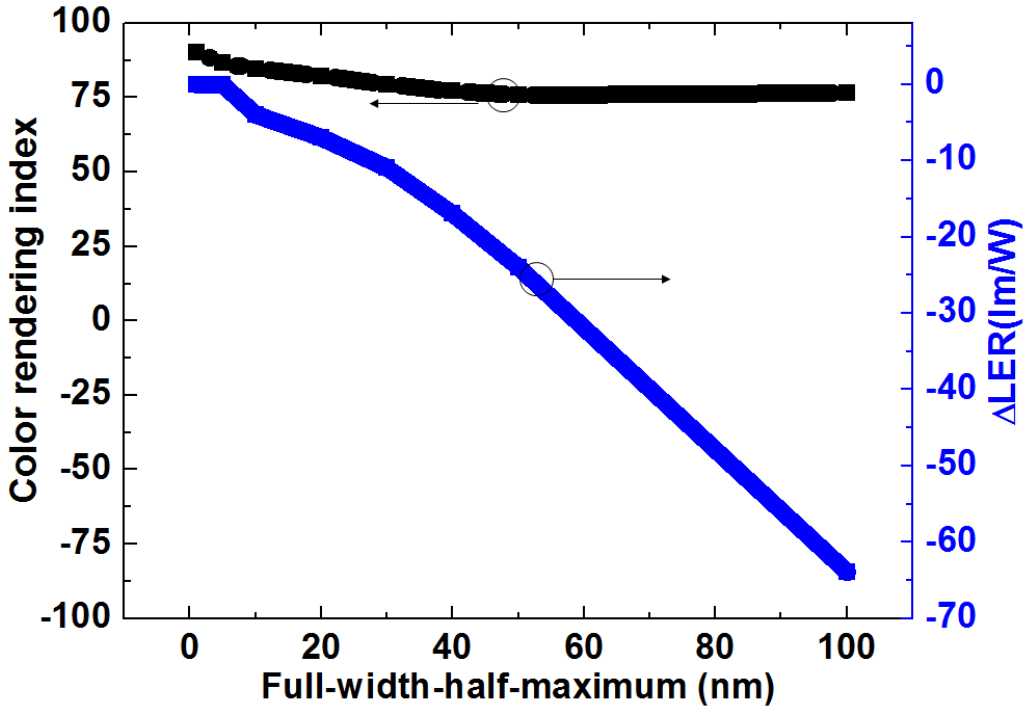

Figure 6.2.1 Investigation of full-width-half-maximum dependent color rendering index and luminous efficacy change of optical radiation (ΔLER) with respect to the case of 1 nm FWHM for ultra-efficient solid-state lighting (with power levels of 1/8 at 463 nm, 2/8 at 530 nm, 2/8 at 573 nm, and 3/8 at 614 nm).

6.2.3 Energy gradient formation

To establish energy gradient, we employ cyan- and orange-emitting CdSe/ZnS core/shell nanocrystals with photoluminescence peaks at 493 and 588 nm in solution, respectively, as depicted in Figure 6.2.2. Our cyan- and orange-emitting NCs have concentrations of 171 nmol/mL and 70 nmol/mL in the toluene solution and molecular weights of 85 μg/nmol and 200 μg/nmol, respectively. Their respective radius is around 3.2 nm and 4.4 nm, both with a size dispersion of <5%, and they exhibit a quantum efficiency of >50% in solution [126]. To achieve full color-conversion, we further integrate closely-packed NCs in film with just sufficient amounts on the near-ultraviolet (near-

UV) InGaN LEDs. To accomplish ultra-efficient photometric properties in solid state lighting, we reach our desired operating point around 614 nm by using the red-shift of these nanocrystals when cast into a solid film due to the resonant coupling and environmental changes. Here in operation the electroluminescence of the near-UV LED excites this integrated NC film and these NCs make photoluminescence so that the desired reddish-orange light at around 614 nm is generated. (The growth, fabrication and characterization of these near-UV LEDs are explained in our previous study [124].)

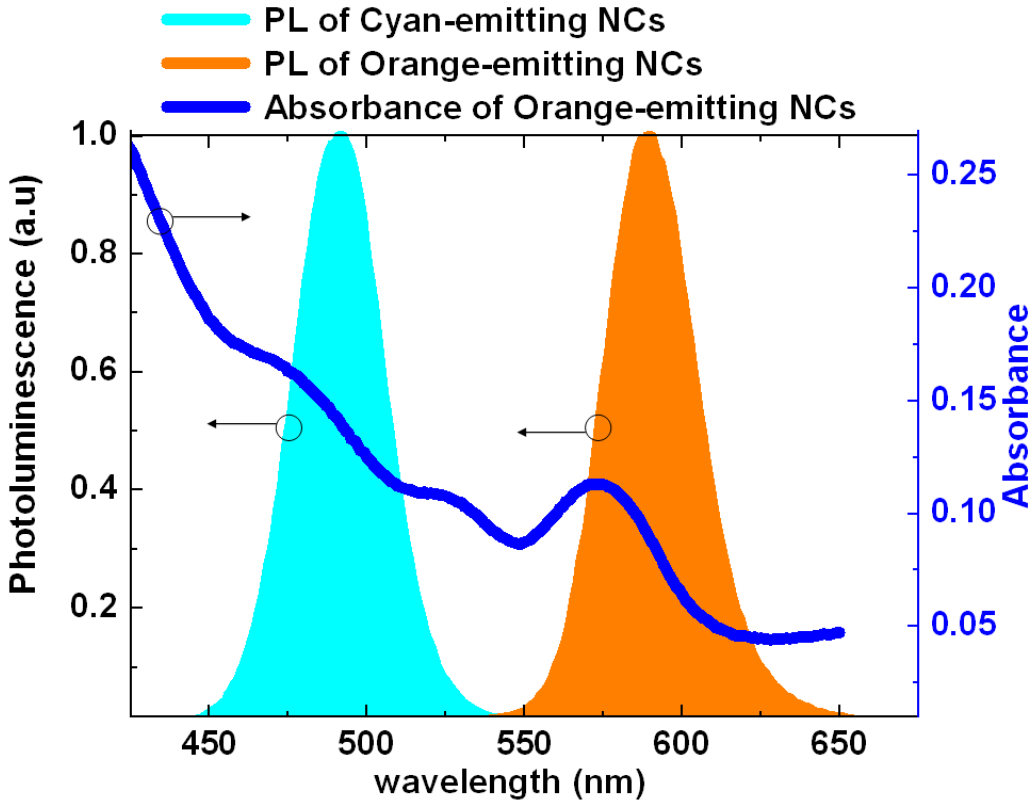

Figure 6.2.2 Emission/absorption spectra of orange-emitting CdSe/ZnS core/shell nanocrystals (acceptors) and emission of cyan-emitting CdSe/ZnS core/shell nanocrystals (donors).

6.2.4 NRET-enhancement in color-conversion using nanocrystals

For NRET-enhancement in color-conversion using nanocrystals, we integrate a carefully designed assembly of 5.6 nmol cyan-emitting donor nanocrystals and 5.6 nmol orange-emitting acceptor nanocrystals, for which the maximum quantum efficiency enhancement is observed at a donor-acceptor ratio of 1:1 [127]. These are the minimum NC amounts that lead to full color-conversion in the reddish-orange, while keeping the 1:1 ratio between the cyan and orange NCs. By using this hybrid assembly of nanocrystals we establish a sufficient energy gradient for nonradiative energy transfer on the near-UV LED. This mixture of nanocrystals further enhance the overall quantum efficiency of the integrated nanocrystal film, while fully converting the incident UV photons to reddish-orange photons (with no UV or green photons coming off the hybrid film). Here the quantum efficiency increase comes from recycling of trapped excitonic energy in defect states of donor nanocrystals into acceptor nanocrystals through Förster-type resonance energy transfer [108], [124], [127].

When the incoming near-UV light is absorbed by these nanocrystals for color-conversion, electron-hole pairs are generated. These photogenerated electron and hole pairs then relax to their respective conduction and valence bands. Some portion of these electron-hole pairs get trapped in the defect states and typically make nonradiative recombination. This decreases the quantum efficiency of the nanocrystal film. Using NRET, some of these trapped excitons are further transferred to the orange-emitting nanocrystals that behave as acceptors for these defect states. Therefore, rather than losing the trapped excitons in defect states, a part of the transferred excitons contributes to the emission by radiative recombination.

To investigate the level of efficiency enhancement in this hybrid nanocrystal film, we also prepare a negative control group using only orange-emitting NCs.

For that, we integrate 7 nmol orange-emitting CdSe/ZnS nanocrystals on our n-UV LED, which is the minimum amount that also achieves full color-conversion in the reddish-orange color. Here for the power measurements to compare quantum efficiencies, we use an integrating sphere (Newport). Initially, we measure the optical output power and the quantum efficiency of the near-UV LEDs; afterwards, we measure those of the nanocrystal integrated LEDs. Then, we obtain the quantum efficiency of the nanocrystal color-converters extracted from these two sets of data, separately for the cases of using hybrid NC film and control NC film. In both cases, it is made sure that it is full photon conversion to the reddish-orange for fair comparison between them.

Figure 6.2.3 shows the time-resolved spectroscopy measurements of the integrated nanocrystals at 614 nm. The system has a calibrated time resolution of 32 ps. We pump our nanocrystals using a laser head at an emission wavelength of 375 nm with light pulses as short as 70 ps. With an output monochromator, we characterize all of the prepared NC solids at 614 nm, corresponding to the approximate peak emission wavelengths of these NC solids. In Figure 6.2.3 the energy rising component (*i.e.*, the exponential increase) in the photoluminescence kinetics of the hybrid film of these mixed cyan-orange nanocrystals is more dominant compared to the case of the control NC film, because of the strong exciton migration to the orange-emitting nanocrystals in the hybrid film. This manifests itself as a slower photoluminescence decay at shorter times for the hybrid NC film. At longer times, the slope of the decay is almost the same for the hybrid film as that of the control film because their interband recombination lifetimes are similar on the order of tens of nanoseconds.

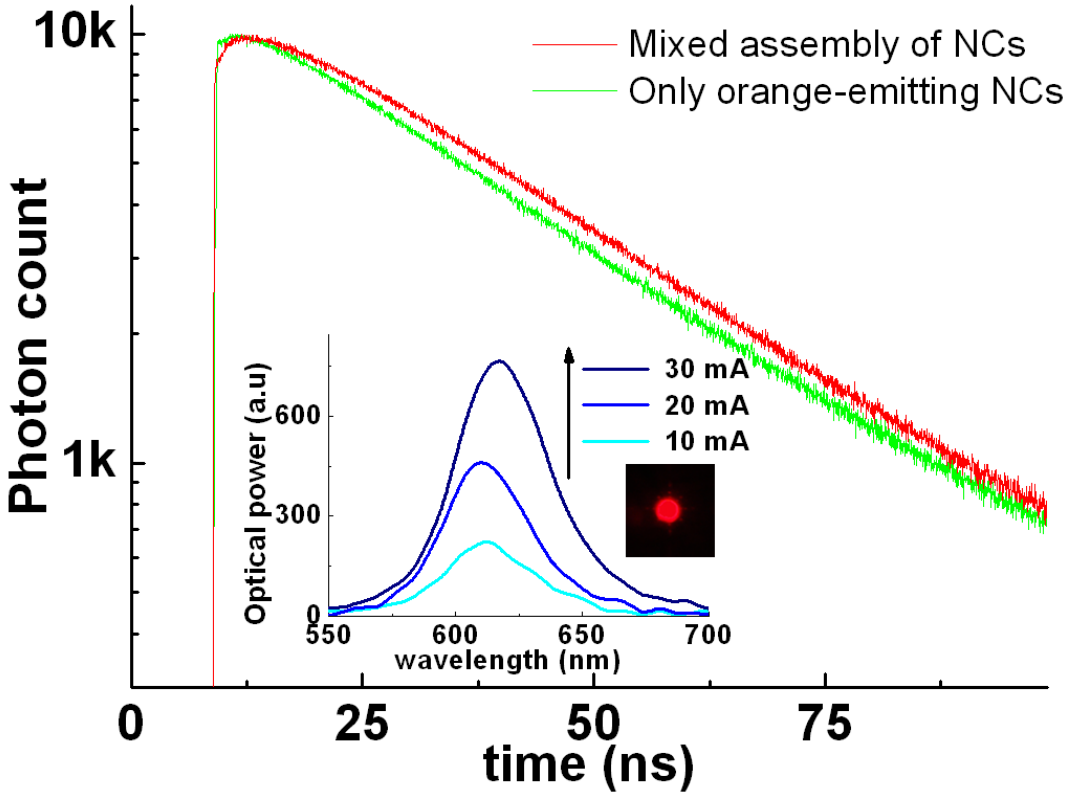

Figure 6.2.3 Time-resolved spectroscopy measurements of the integrated orange-emitting CdSe/ZnS core/shell nanocrystals (λ_{PL}=588 nm) and hybrid cyan- and orange-emitting CdSe/ZnS core/shell nanocrystals (λ_{PL}=492 and 588 nm, respectively) on near-UV LED (λ_{EL}=379 nm) along with the emission spectra at different levels of current injection at room temperature and picture of the hybrid NC-LED when electrically driven.

By using the NRET-enhanced color-conversion, we obtain the resulting luminescence of the hybrid device changing from 612 to 616 nm with the increasing current injection level as shown in the inset of Figure 6.2.3. This nanocrystal based reddish-orange LED leads to a luminous efficacy of optical radiation at 278.7 lm/W_{opt} and its energy gradient hybrid NC film achieves a quantum efficiency of 16.92% in full color-conversion of UV to reddish-orange. On the other hand, the control NC film without using NRET shows a lower quantum efficiency of 14.7%, again in the full color-conversion on the near-UV LED. As a result, the relative quantum efficiency enhancement of the hybrid cyan-orange nanocrystal film is 15.1% in full color-conversion in reddish-orange (with respect to the only orange NCs without NRET). Here it is

important again to note that, because of the strong nonradiative energy transfer, cyan-emitting nanocrystals are fully quenched by transferring their energy to orange-emitting nanocrystals in the hybrid film; therefore, the hybrid film only provides orange emission. This proof-of-concept demonstration shows that nanocrystal based LEDs enable us to reach the desired operating wavelength important for ultra-efficient SSL without making major sacrifices in color rendering and luminous efficiency because of their relatively narrow emission linewidths.

6.2.5 Conclusion

In this section, we presented NRET-enhanced reddish-orange light-emitting diodes in which we integrated colloidal semiconductor nanocrystals as color-converters on near-UV InGaN/GaN LEDs. For that, we made a hybrid assembly of cyan- and orange-emitting CdSe/ZnS core/shell nanocrystals to enhance the efficiency of hybrid NC LED. By recycling of the trapped excitons into nanocrystals we achieved a relative quantum efficiency enhancement of 15.1% in full color-conversion with respect to the negative control group without NRET.

6.3 Quantum efficiency enhancement in nanocrystal solids using nonradiative energy transfer with optimized donor-acceptor ratio for hybrid white light emitting diodes

This section is based on the publication "Quantum efficiency enhancement in nanocrystal solids using nanoradiative energy transfer with optimized donor-acceptor ratio for hybrid white light emitting diodes" **S. Nizamoglu**, O. Akin, and H. V. Demir, Applied Physics Letters 95, 151111 (2009). Reproduced (or 'Reproduced in part') with permission from American Institute of Physics. Copyright 2009 American Institute of Physics.

The quantum efficiency enhancement in nanocrystal solids is critically important for their efficient use as luminophors on color-conversion light emitting diodes. For this purpose, we investigate energy gradient mixture of nanocrystal solids for recycling their trapped excitons by varying their donor-acceptor nanocrystal ratios and study the resulting quantum efficiency enhancement as a function of the donor-acceptor ratio in the solid film for hybrid LEDs. We achieve a maximum quantum efficiency enhancement of 17% in these nanocrystal solids when the donor-acceptor ratio is 1:1, demonstrating their highly-modified time-resolved photoluminescence decays to reveal the kinetics of strong energy transfer between them.

6.3.1 Introduction

Semiconductor nanocrystal quantum dots exhibit attractive properties for use in hybrid white LEDs. They strongly absorb incident blue/UV light and emit with cooperative downconversion at the desired long wavelengths in the visible upon excitation at the short wavelengths. For example, red-emitting nanocrystals

achieve a high photon conversion efficiency, which is larger than the reported level of red phosphors for converting blue into red [128], [129]. Furthermore, nanocrystals feature widely tunable emission across the visible spectral range by quantum confinement effect [11]. They also provide us with the ability to easily and uniformLy deposit them in solid films employing simple techniques (*e.g.*, spin casting, dip coating). As a result, nanocrystal based solid state lighting devices have made important progress in device research in recent years [6], [45], [65], [66], [103]. However, these nanocrystal emitters suffer from the problem of relatively reduced quantum efficiency in film with respect to their high quantum efficiency in solution [101]. To address this problem, the recycling of trapped excitons into the quantum dots by using Förster-type nonradiative resonance energy transfer provides a possible solution to enhance the quantum efficiency of these NC solid films. Although NRET for colloidal nanocrystal emitters are investigated in various studies [88], [91], [108-111], [114], [130], the dependence of quantum efficiency enhancement on the donor-acceptor variation in the solid film and its optimization have not been investigated for hybrid light emitting diodes to date.

In this section, we study the optimal donor-acceptor colloidal nanocrystal ratio for their quantum efficiency enhancement in the solid film for white light emitting diode applications. For that we use carefully selected energy gradient mixtures of CdSe/ZnS core/shell nanocrystals (emitting at 500 and 550 nm) for strong nonradiative energy transfer between them. We investigate the resulting quantum efficiency enhancement of these nanocrystal solids with their varied donor-acceptor ratios in film, *e.g.*, 16:1, 4:1, 1:1, 1:4 and 1:16. All of these energy-gradient structures exhibit quantum efficiency enhancement with respect to the cases of only donor and only acceptor control groups. Here the observed quantum efficiency increase stems from the ability of transferring excitation energy of some of the excitons trapped in the midgap states through NRET. We observe that the mixed donor and acceptor nanocrystals achieve a maximum quantum efficiency enhancement of 17% when the donor-acceptor ratio is 1:1,

implying that NRET is optimized when there is one donor nanocrystal for each acceptor nanocrystal on the average.

6.3.2 Experimental method and sample preparation

For investigating the quantum efficiency enhancement, we use a Xenon halogen lamp in a monochromator as the excitation light source and an integrating sphere for collecting the total emission from the nanocrystal solids as explained in Section 3.5.4. For time-resolved spectroscopy measurements (explained in Section 3.5.1), we use a laser head at an emission wavelength of 375 nm and a photon multiplier tube (PMT) as the detector with a calibrated time resolution of 16 ps. For the numerical analysis of the experimental data, we deconvolute the instrumental response function (IRF).

In our hybrid system, we use cyan-emitting CdSe/ZnS core/shell nanocrystals as the donors and green-emitting nanocrystals as the acceptors for nonradiative energy transfer. Our cyan-emitting NCs have a concentration of 171 nmol/mL in toluene and their diameters are around 3.2 nm with a size dispersion of <5%; our green-emitting NCs have a concentration of 70 nmol/mL in toluene and their diameters are around 3.4 nm with a size dispersion of <5% [126]. Their molecular weights are 85 μg/nmol and 100 μg/nmol for cyan- and green-emitting nanocrystals, respectively, and they exhibit an in-solution quantum efficiency of >50%. After mixing the NC solutions for appropriate donor-acceptor ratios, we prepare the hybrid nanocrystal samples by drop-casting on quartz substrates and post-bake them around 50 ^{o}C to remove excess solvent toluene from the films.

6.3.3 Quantum efficiency enhancement of nanocrystal solids as a function of varying donor-acceptor ratios

Figure 6.3.1 presents the quantum efficiency enhancement of these nanocrystal solids as a function of varying donor-acceptor ratios in film with respect to the control groups. In Figure 6.3.1, we also show the control group samples of only cyan- and only green-emitting nanocrystals as the base line; these points are presented at the far edges of the plot in Figure 6.3.1 for visualization purposes. Using green- and cyan-emitting nanocrystals in any combination as the donor-acceptor pairs, we experimentally observe that the quantum efficiency is effectively enhanced in all samples for any donor-acceptor ratio with respect to the control groups.

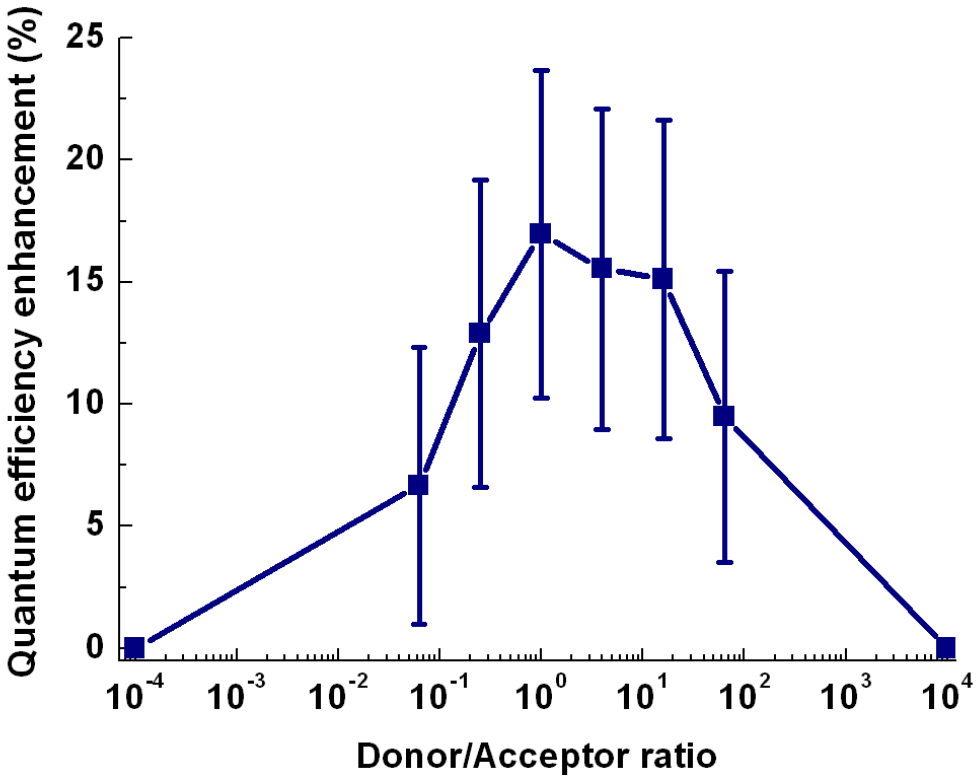

Figure 6.3.1 Nanocrystal donor-acceptor ratio dependent quantum efficiency enhancement of the donor-acceptor hybrid solid films consisting of cyan- and green-emitting CdSe/ZnS core/shell nanocrystals.

It is normally expected to be impossible for the overall efficiency of the hybrid donor-acceptor NC film to exceed that of only donors or that of only acceptors as given in Equation (6.3.1), where the quantum efficiency of the hybrid NC film (QE_{hybrid}) is expressed as a weighted sum of the acceptor and the donor efficiencies (QE_A and QE_D). Given Equation (6.3.1), QE_{hybrid} is required to lie between QE_A and QE_D (when $\tau_{NRET} << \tau_D$ or $\tau_{NRET} >> \tau_D$ corresponding to the far ends of the possible QE_{hybrid} range, respectively). However, we observe in the experiments that QE_{hybrid} exceeds QE_A and QE_D. This is attributed to the recycling of trapped excitons [108], [114]. Following the optical absorption process, the electron and hole pairs rapidly relax to the conduction and valance band ground states (in hundreds of femtoseconds). However, due to the surface defects, there also exist additional midgap trap energy states. Some of these

excitons thus end up with being trapped in these defect states, mostly making nonradiative recombination. Using NRET, though, these trapped excitons may also be transferred, possibly contributing to spontaneous emission in addition to the interband excitons. As a result of such recycling of these trapped excitons, the photoluminescence of the hybrid films is increased.

$$QE_{hybrid}=QE_A\times(1+\tau_{NRET}/\tau_D)^{-1}+ QE_D\times(1+\tau_D/\tau_{NRET})^{-1} \quad (6.3.1)$$

Starting the emission enhancement investigation with a donor-acceptor ratio of 1:16, the quantum efficiency is found to be increased by 6.6% with respect to the control groups. As we increase the donor-acceptor ratio from 1:16 to 1:1, this enhancement increases correspondingly from 6.6% to 17.0%. As we further increase the donor-acceptor ratio beyond 1:1, however, the enhancement begins to decrease from 17.0% to 9.5%. When the number of acceptors (donors) significantly exceeds the number of donors (acceptors) in the limiting cases, the number of donors (acceptors) becomes insignificant. Thus, the energy transfer behavior converges the case of only acceptors (donors). This explains the experimental observations of decreasing enhancement before and after 1:1 ratio. As a result, for hybrid LEDs the donor-acceptor ratio of 1:1 is found to be optimum for the maximum possible quantum efficiency enhancement observed in these nanocrystal emitters.

For investigation of modified photoluminescence kinetics, we present the hybrid sample with the donor-acceptor ratio of 1:1 that reveals the highest in-film emission enhancement among other combinations. Figure 6.3.2 shows the time-resolved photoluminescence of the hybrid donor-acceptor sample and the only cyan-emitting donor nanocrystal solids, both at the donor peak emission wavelength of 500 nm. In Figure 6.3.2, the photoluminescence decay of the hybrid sample at 500 nm drops faster with respect to the only cyan-emitting donors because these donor dots in the hybrid sample quench as a result of their excitation energy transferred to the acceptor dots in the hybrid sample. On the other hand, the inset of Figure 6.3.2 reveals the time-resolved photoluminescence of the hybrid sample and the only green-emitting acceptor

nanocrystal solids, this time both at the acceptor peak emission wavelength of 550 nm. In contrast, in the inset, the decay of the hybrid sample at 550 nm slows down with respect to the only green-emitting acceptors because these acceptor dots are fed with the transferred energy from the donor dots in the hybrid sample.

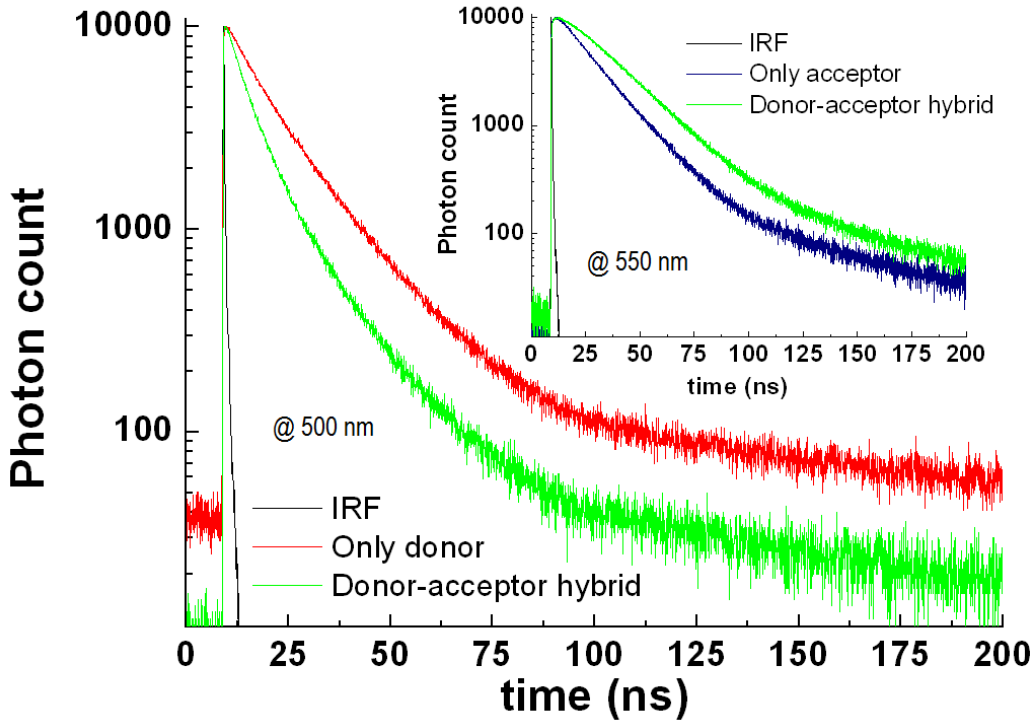

Figure 6.3.2 Time-resolved photoluminescence kinetics of the only donor nanocrystal solids and the donor-acceptor hybrid nanocrystal solids with 1:1 ratio at the donor emission wavelength of 500 nm. Time-resolved photoluminescence kinetics of the only acceptor nanocrystal solids and the donor-acceptor hybrid nanocrystal solids with 1:1 ratio at the acceptor emission wavelength of 550 nm are given in the inset.

We numerically analyze our photoluminescence decay curves in Figure 6.3.2 using a multiexponential model fit. The resulting fitting parameters are summarized in Table 6.3.1. Here the first lifetime (*i.e.*, τ_1) is the interband recombination of the nanocrystals, which is expectedly on the order of tens of nanoseconds [91]. This recombination lifetime component is found to be 13.7 ns for cyan-emitting dots and 17.4 ns for green-emitting dots. In addition to this

interband recombination, the numerical analysis also returns another decay lifetime (*i.e.*, τ_2). This lifetime component exhibits a rather slow decay. It is 63.8 ns for cyan-emitting dots and 103.6 ns for green-emitting dots. This long decay component is weak, exhibiting amplitudes less than 3% of the amplitude of τ_1 for all cases. We therefore attribute this slow and weak decay component to the environmental effects that may potentially be caused by ligands of the nanocrystals in the close vicinity of each other in their close-packed film [48]. Furthermore, for the hybrid sample the numerical analysis gives a third lifetime component (*i.e.*, τ_3), both at the peak emission wavelengths of the donors and the acceptors (at 500 and 550 nm). The numerical analysis reveals that this third component is an additional decay pathway for the small dots serving as the donors and that this is an energy increase for the large dots serving as the acceptors in the hybrid sample (because the analysis returns negative amplitude associated with this component, as presented in Table 6.3.1).

Table 6.3.1 The fitting parameters of time-resolved spectra presented in Figure 6.3.2(a)-(b). (A_n and τ_n are the amplitudes and decay time constants, for n=1, 2, 3, respectively; τ_{av} and τ_{amp_av} are the intensity and amplitude weighted average decay time constants.)

	Only donor nanocrystals ***(at 500 nm)***	**Donor:Acceptor 1:1** ***(at 500 nm)***	**Only acceptor nanocrystals** ***(at 550 nm)***	**Donor:Acceptor 1:1** ***(at 550 nm)***
A_1 **[counts]**	11245	3831	11941	37212
τ_1 **[ns]**	13.7	13.7	17.4	17.4
A_2 **[counts]**	326	109	189	314.2
τ_2 **[ns]**	63.8	63.8	103.6	103.6
A_3 **[counts]**	-	8790	-	-26375
τ_3 **[ns]**	-	4.4	-	14.1
τ_{av} **[ns]**	19.6	13.6	24.9	30.7
τ_{amp_av} **[ns]**	15.1	7.7	18.9	28.9

To further analyze the energy transfer from cyan-emitting dots to green-emitting dots, we calculate the intensity averaged lifetime components using Equation (6.3.2) (where A_i and τ_i refer to the amplitudes and their associated lifetimes, respectively). The intensity weighted average decay time constant for the cyan-emitting dots at 500 nm decreases from 19.6 to 13.6 ns because of the exciton migration from cyan-emitting nanocrystals to green-emitting nanocrystals. On the other hand, the intensity weighted average decay time constant of green-emitting dots at 550 nm is found to increase from 24.9 to 30.7 ns with respect to only green-emitting dots as a result of the energy transfer. Using Equation (6.3.3) we calculate the amplitude weighted average lifetime of the hybrid nanocrystals sample ($\tau_{amp\_av\_DA}$) and the only cyan-emitting nanocrystal case ($\tau_{amp\_av\_D}$) at 550 nm. Furthermore, by using Equation (6.3.4), we determine the efficiency of the energy transfer. As a result, the efficiency of the nonradiative energy transfer in the hybrid nanocrystals achieves a relatively high level of 48%. Here the third decay term for the donors due to the energy transfer quenching is calculated to be 4.4 ns. However, the lifetime of this component for the acceptors because of the exciton migration is computed to be 14.1 ns, which is slower than the quenching lifetime. Since the trap states have energy lower than the interband gap, the overlap of the optical absorption of green-emitting dots with the trapped states is lower because the absorption of nanocrystals increases towards shorter wavelengths. As a result, the rate of energy enhancement decreases and thus the energy transfer lifetime increases.

$$\tau_{avg} = \frac{\sum_i A_i \tau_i^{\,2}}{\sum_i A_i \tau_i} \tag{6.3.2}$$

$$\tau_{amp\_avg} = \frac{\sum_i A_i \tau_i}{\sum_i A_i} \tag{6.3.3}$$

$$\eta_{ET} = 1 - \frac{\tau_{amp\_avg\_DA}}{\tau_{amp\_avg\_D}} \tag{6.3.4}$$

6.3.4 Conclusion

In this section, we presented blended nanocrystal energy gradient structures for recycling of trapped excitons and investigated the quantum efficiency enhancement with in-film donor-acceptor ratios. We exhibited a maximum quantum efficiency enhancement of 17% when the donor-acceptor ratio is 1:1. We studied the time-resolved photoluminescence of the nanocrystal solids with donor-acceptor ratio 1:1 to reveal the kinetics of their energy transfer. The quantum efficiency enhancement of integrated nanocrystal solids proves to be important for achieving efficient hybrid white light emitting diodes.

6.4 Green/yellow solid state lighting via radiative and nonradiative energy transfer involving colloidal semiconductor nanocrystals

This section is based on the publication "Green/yellow solid-state lighting via radiative and non-radiative transfer involving colloidal semiconductor nanocrystals" **S. Nizamoglu**, E. Sari, J.-H. Baek, I.-H. Lee, and H. V. Demir, IEEE Journal of Special Topics in Quantum Electronics 15, 4, 1163-1170 (2009). Reproduced (or 'Reproduced in part') with permission from IEEE. Copyright 2009 IEEE.

LEDs made of $In_xGa_{1-x}N$ and $(Al_xGa_{1-x})_{1-y}In_yP$ suffer from significantly reduced quantum efficiency and luminous efficiency in the green-yellow spectral ranges. To address these problems, in this section we present the design, growth, fabrication, hybridization and characterization of proof-of-concept green/yellow hybrid light emitting diodes that utilize radiative and nonradiative energy transfers in their colloidal semiconductor nanocrystals integrated on near-ultraviolet LEDs. In our first NC-LED, we realize a color converted LED that incorporate green-emitting CdSe/ZnS core/shell nanocrystals (λ_{PL}=548nm) on near-UV InGaN/GaN LEDs (λ_{EL}=379nm). In our second NC-LED, we implement a color-converted NRET-enhanced LED. For that we hybridize a custom-design assembly of cyan-green-emitting CdSe/ZnS core/shell nanocrystals (λ_{PL}=490 and 548nm) on near-UV LEDs. Using a proper mixture of differently-sized NCs, we obtain a quantum efficiency enhancement of 9% by recycling trapped excitons via NRET. With NRET-NC-LEDs, we show that it is possible to obtain a luminous efficacy of 425 lm/W_{opt} and a luminous efficiency of 94 lm/W, using near-UV LEDs with a 40% external quantum efficiency. These proof-of-concept demonstrations show that NRET based NC-LEDs hold promise for efficient solid state lighting in green/yellow.

6.4.1 Introduction

In a recent study the photometric conditions that achieve ultra-efficient solid-state lighting have been investigated [72], [73]. According to this study, a luminous efficacy at 408 lm/W and a color rendering index of 90 at a correlated color temperature of 3000 K are simultaneously achievable. To obtain these photometric properties, light emitting diodes that emit in blue, green, yellow, and red colors (at 463, 530, 573, and 614 nm with relative optical power levels of 1/8, 2/8, 2/8, and 3/8, respectively) are required [72], [73].

$In_xGa_{1-x}N$ material system has the potential to cover the whole visible by changing the In composition (x), however, it has technically been extremely challenging to obtain efficient green and yellow light emitting diodes especially at those wavelengths (*i.e.*, at 530 nm and 573 nm, respectively) [2]. Though blue emitting InGaN/GaN LEDs may reach high external quantum efficiency [4], [7], those LEDs made of the same material system begin to suffer from significantly reduced internal quantum efficiency (and thus substantially reduced luminous efficiency) due to the increased In content in multi quantum wells while approaching green color [121-123]. In addition, the resulting optical emission is further reduced due to the increased internal fields in the quantum wells that separate electron and hole wavefunctions. Furthermore, undesired defects and compositional inhomogeneities also further decrease the efficiency of green LEDs [72].

For red light emitting diodes, it is possible to achieve high quantum efficiencies around 650 nm by utilizing another material system, a quaternary alloy $(Al_xGa_{1-x})_{1-y}In_yP$. By using this quaternary, it is possible to cover from 650 nm to 580 nm. However, the efficiencies significantly decrease approaching the yellow color. Therefore, there exists a significant gap in the green and yellow spectral regions to make efficient light emitting diodes.

To address these problems, we propose and develop proof-of-concept green/yellow hybrid light emitting diodes that use both radiative energy transfer and nonradiative energy transfer in their integrated colloidal semiconductor nanocrystals for color conversion on near-ultraviolet LEDs (Figure 6.4.1). Our experimental demonstrations indicate that the use of NRET in color conversion in green and yellow allows for significant enhancement in efficiency. Such NRET-converted LEDs hold great promise for efficient lighting, especially in green and yellow where the existing material systems and LED technologies suffer from low performance.

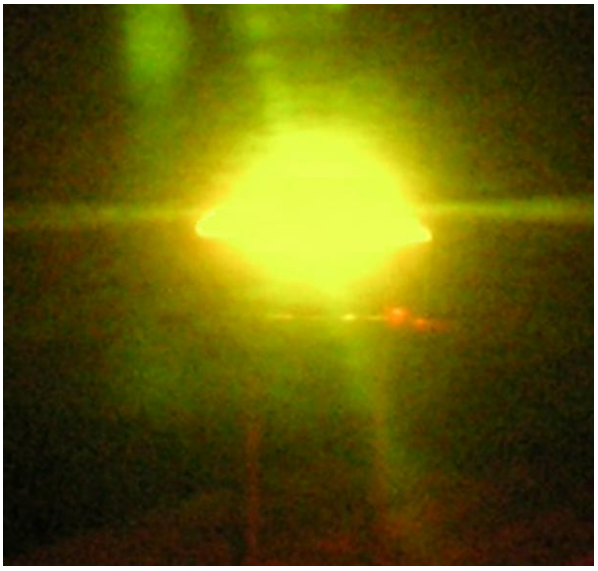

Figure 6.4.1 Exemplary picture of a yellow hybrid light emitting diode while emitting at 573 nm.

In conventional color conversion technique, phosphors are commonly used to generate white light. Phosphors provide wide band emission with high quantum efficiency across the visible. It is, however, difficult to tune their optical emission properties and to obtain a spectrally narrow emission band (*e.g.*, green or yellow emission alone). As an alternative, though, semiconductor nanocrystals exhibit favorable properties for use in light emitting diode

applications. They reveal tuneable emission using quantum confinement effect [11], [81]. They show narrow, symmetric photoluminescence with large photoluminescence quantum yields and high photostability. They exhibit increasing absorption levels towards shorter wavelengths, relatively high photobleaching thresholds, and small spectral overlap between absorption and emission spectra [100]. Furthermore, various film deposition techniques including Langmuir-Blodgett, spin casting, and electrostatic layer-by-layer film deposition can be conveniently used to make good quality film. Therefore, these quasi-zero-dimensional semiconductor materials have been both theoretically and experimentally widely investigated [67], [91], [93], [100], [104], [105], [107]. Because of the tuneable nature of their optical emission they have also been exploited in various light emitting diode applications especially for hybrid white LEDs [6], [45], [64], [65], [68], [76]. Unlike these previous studies of our group and the others, here we demonstrate hybrid light emitting diodes that also employ NRET as a nonradiative means of energy transfer in color-converting colloidal nanocrystals for increased efficiency in green/yellow spectral ranges for the first time.

In this section, we present the design, growth, fabrication, integration and characterization of nanocrystal based light emitting diodes that utilize direct and NRET-enhanced color conversion. Furthermore, we also investigate NRET-converted light emitting structures. In our first NC-LED, we use green-emitting CdSe/ZnS core/shell nanocrystals (λ_{PL}=548 nm) on near-UV InGaN/GaN LEDs (λ_{EL}=379 nm). In our second NC-LED that additionally employs NRET in nanocrystals, we use a custom-design assembly of cyan- and green-emitting CdSe/ZnS core/shell nanocrystals (λ_{PL}=490 nm and 548 nm, respectively) to recycle the trapped excitons into nanocrystals via NRET. In this proof-of-concept NRET-enhanced NC-LED we achieve a quantum efficiency enhancement of 9% with respect to the first NC-LED. Finally, we examine NRET directly from epitaxial quantum wells to colloidal nanocrystals in their

close proximity. Using NRET-pumping in color conversion, a potential efficiency enhancement is predicted in such hybrid LEDs.

6.4.2 Device fabrication

For the growth of our near-UV LED, we employ a GaN dedicated metal organic chemical vapor deposition (MOCVD) system and use a p-i-n epitaxial design for the near-UV LED as shown in Figure 6.4.2. At first, we begin with a 30 nm thick GaN buffer layer and continue with a 0.5 μm thick GaN layer to increase the crystal quality of the device epitaxial layers. Subsequently, we grow a 3 μm thick, Si doped n-type contact layer. We continue with the epitaxial growth of 2.5 nm/7.5 nm InGaN/GaN quantum well/barrier structure. We repeat the well/barrier structure five times for multi quantum well region. Finally, we finish our growth with layers that consist of Mg-doped 70 nm thick AlGaN, 140 nm thick Mg-doped GaN layer and 2.5nm/2.5 nm thick Si doped InGaN/GaN layers. In the device fabrication, we use standard semiconductor processing including photolithography, thermal evaporator (metallization), reactive ion *etc*h (RIE), and rapid thermal annealing. Finally, we make wire bonds to the device contacts in its package.

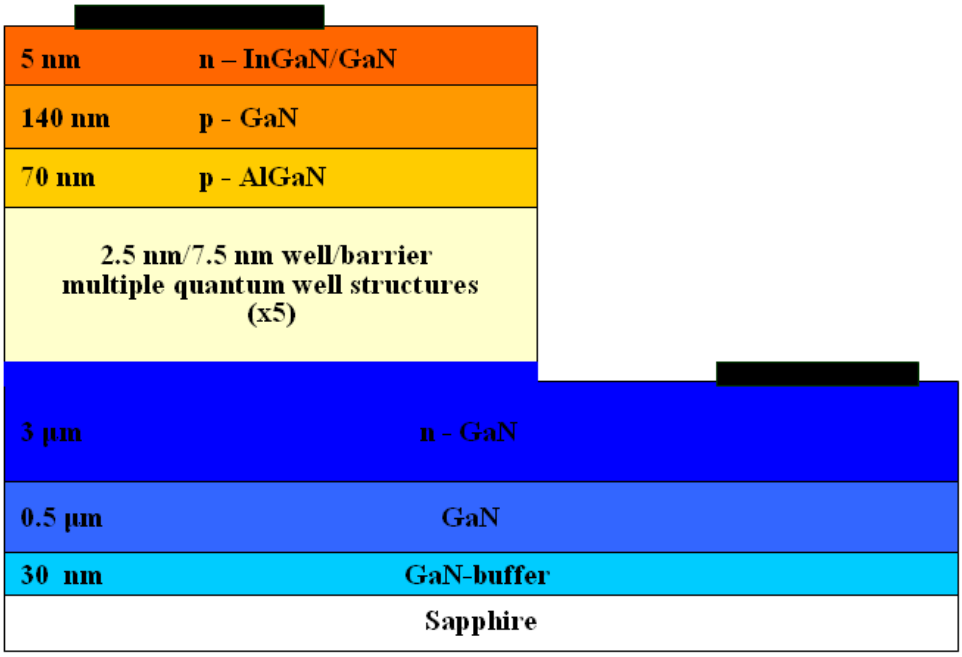

Figure 6.4.2 Epitaxial design of our near-UV InGaN/GaN light emitting diode.

Our near-UV LED has a turn-on voltage approximately at 3 V and an electroluminescence peak wavelength at 379 nm, as shown in the inset of Figure 6.3.3. Our near-UV LED exhibits an external quantum efficiency of around 8% at low current levels. For example, the optical power is 5.8 mW at 19.05 mA. However, we observe a strong rollover in the efficiency with increasing input current, as our packaged LED does not include a heat sink and its full package is not designed for proper heat management. With a decreased level of device efficiency, the near-UV LED reaches an output optical power level of 8.5 mW at 43 mA as shown in Figure 6.4.3.

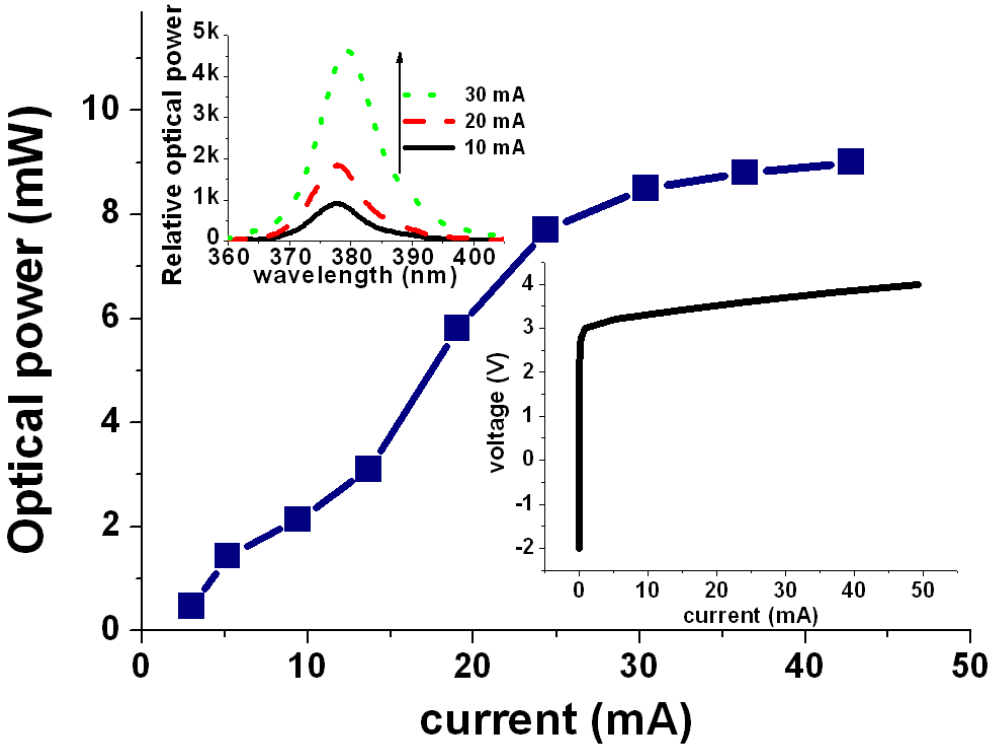

Figure 6.4.3 L-I of our near-UV LED measured in an integrating sphere at room temperature (with no heat sink or active cooling) along with its EL spectra and I-V given in the insets.

6.4.3 Color-Converted LED

For the first NC-LED, we use green-emitting CdSe/ZnS core/shell nanocrystals as the color converters. Our green-emitting NCs have a concentration of 70 nmol/mL in toluene and their diameters are around 3.4 nm with a size dispersion of <5%. Their molecular weight is 100 μg/nmol and they exhibit an in-solution quantum efficiency of >50%. Their emission and absorption spectra are shown in Figure 6.4.4. Towards shorter wavelengths, their optical absorption increases rapidly.

For hybrid light generation, we integrate closely-packed NCs on a near-UV LED. The operating principle for such NC- LEDs relies on the optical excitation of the integrated NC films by the electrically driven near-UV LED. As a result of optical pumping, the NC photoluminescence generates the desired green/yellow light.

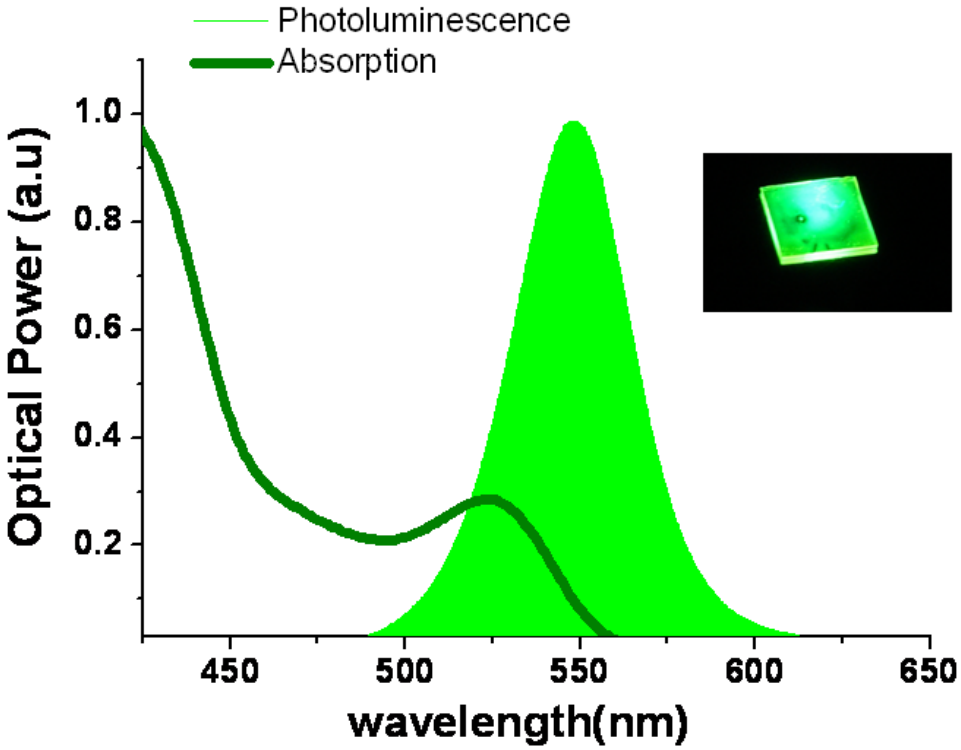

Figure 6.4.4 The emission and absorption spectra of green-emitting CdSe/ZnS core/shell nanocrystals along with their photoluminescence picture given in the inset.

For our first NC-LED, we integrate a carefully determined amount of 9.1 nmol green-emitting CdSe/ZnS nanocrystals on our LED. By using this exact amount of nanocrystals, all of the LED electroluminescence at 379 nm is fully down-converted to NC emission by the nanocrystal luminophors. In Figure 6.4.5, as the current injection level increases, the optical output power of our LED expectedly increases as well. When the current level reaches 19.05 mA, the optical power becomes 1.81 mW, which corresponds to a quantum efficiency of 46% for the integrated nanocrystal layer. The resultant luminescence of the hybrid LED is shown as a function of increasing current injection level in the inset of Figure 6.4.5. Here it is important to note that the green NC emission shifted 20 nm from 548 to 568 nm in the solid film. This is mainly due to the nonradiative energy transfer among nanocrystals because of their size distribution (<5%). This size variance leads to slightly modified effective bandgaps. Consequently, the absorption of the relatively small-sized

nanocrystals and emission of the relatively large-sized nanocrystals overlap, which enables energy transfer among them. However, this is not a fundamental problem. Since the starting NC peak emission can be conveniently set at any desired wavelength across the visible, this red shift can be easily compensated for using NCs with a shorter starting peak emission wavelength.

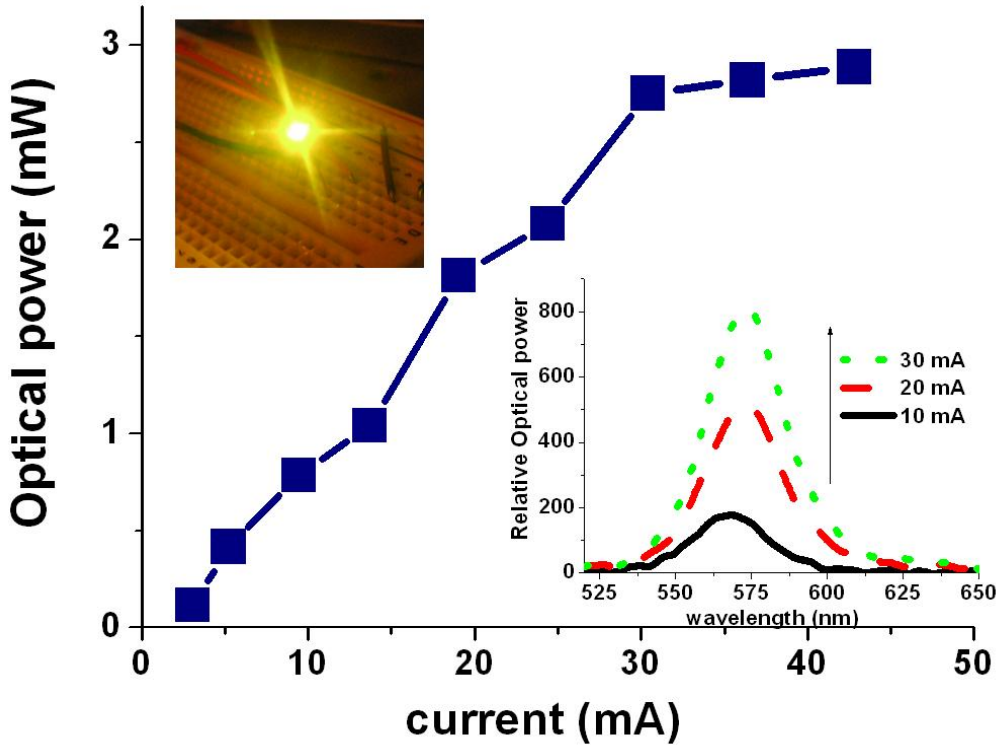

Figure 6.4.5 The total optical power of green NC (λPL=548 nm) hybridized on near-UV LED (λ_{EL}=379 nm) at different levels of current injection at room temperature (with no heat sink or active cooling), along with the emission spectra and picture of the hybrid NC-LED when electrically driven.

As the current injection level increases, the emission of packaged hybrid LED red-shifts due to thermal effects that pushes our operating wavelength closer to 573 nm for yellow LED in ultra-efficient solid state lighting. Thus, *(x,y)* tristimulus coordinates of the hybrid LED moves from (0.42,0.54) to (0.46,0.51) and its correlated color temperature shifts from 4008 to 3260 K, as also summarized in Table 6.4.1. We also measure the luminous efficacy of

optical radiation and luminous efficiency of the source using Equations (2.1.9) and (2.1.10), where $v(\lambda)$ is the eye sensitivity function and and $P(\lambda)$ is the power spectral density (*i.e.*, the light power emitted per unit wavelength) [4]. At 19.05 mA, our color-converted LED exhibits a luminous efficacy of 425 lm/W_{opt} and a luminous efficiency of 17 lm/W.

Table 6.4.1 Photometric properties of our color-converted NC-LED at various current injection levels.

I (mA)	*x*	*y*	*CCT* (K)
9.45	0.42	0.54	4008
19.50	0.45	0.50	3423
30.40	0.46	0.51	3260

Figure 6.4.6 shows the time-resolved spectroscopy measurements of the integrated nanocrystal layers at 556 nm. In Figure 6.4.6, the energy rise (*i.e.*, exponential increase) observed at 9 ns comes from the energy transfer. For these time-resolved spectroscopy measurements, we use a FluoTime 200 spectrometer (PicoQuant) with a time-correlated single photon counting (TCSPC) system of PicoHarp 300 that has a calibrated minimum possible time resolution of 4 ps. To pump nanocrystal solids, we use a laser head at an emission wavelength of 375 nm with light pulses as short as 70 ps and a photon multiplier tube (PMT) as the detector. Using an output monochromator, we characterize all of the prepared NC solids at 556 nm, corresponding to the around peak emission wavelengths of the NCs. For the data analysis we use the software FluoFit to take into account the instrumental response function (IRF).

To further analyze the photoluminescence decay curves of our nanocrystals, we make fits to experimentally measured decay curves in Figure 6.4.6 using a multi-exponential model fit and convoluting with the laser diode response function at 375 nm. The resultant fitting parameters are summarized in Table

6.4.2. Here for our decays we have two distinct lifetime components. The first lifetime component (associated with τ_1) is the general lifetime of the nanocrystals, which is expectedly on the order of tens of nanoseconds [91], [100]. The second lifetime component (associated with τ_2) gives an energy increase, which we conclusively differentiate with its negative amplitude. Here it is worth noting that the distinct negative amplitude stems only possibly from the nonradiative energy transfer among nanocrystals due to their size distribution, as we also previously discussed. For comparison, the cases of mixed green- and cyan-emitting nanocrystals that exhibit intentionally strong energy transfer in Figure 6.4.6 (and also Table 6.4.2) will be discussed in the next section.

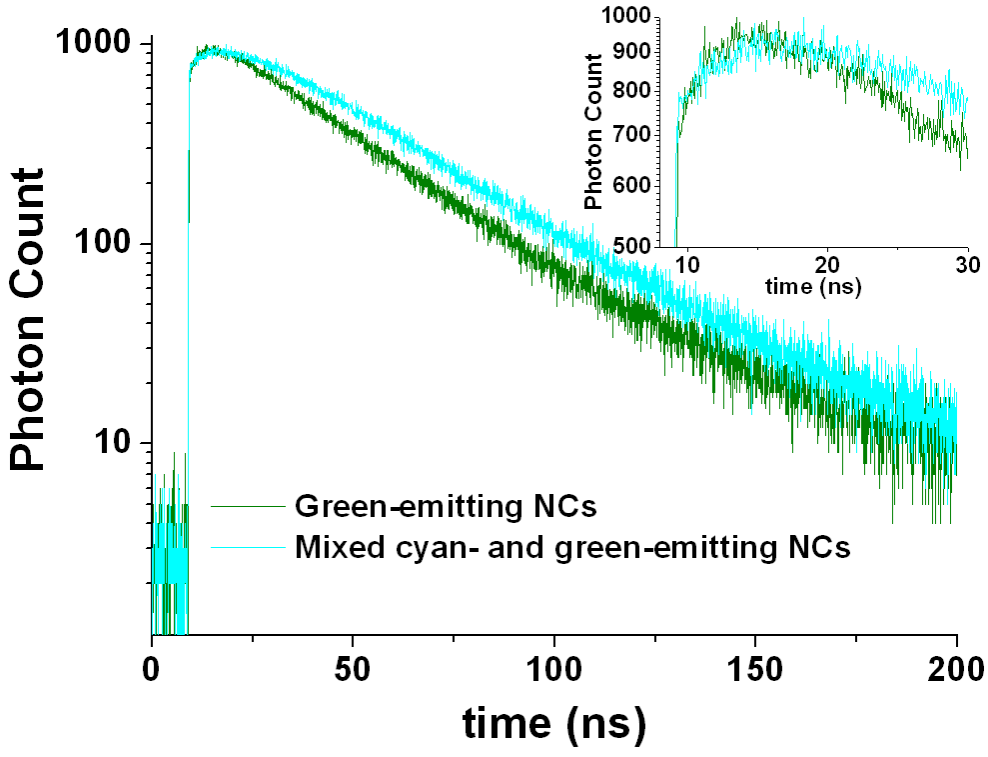

Figure 6.4.6 Time-resolved spectroscopy measurements of the integrated green-emitting CdSe/ZnS core/shell nanocrystals (λ_{PL}=548 nm) and mixed cyan- and green-emitting CdSe/ZnS core/shell nanocrystals (λ_{PL}=490 and 548 nm, respectively) on near-UV LED (λ_{EL}=379 nm).

Table 6.4.2 The multiexponential fitting parameters for transient photoluminescence decays in Figure 6.4.6 (A_n and τ_n are the associated amplitudes and decay time constants of multi-exponential decay fits to the experimental photoluminescence decay curves; n=1, 2.)

	A_1	τ_1 (ns)	A_2	τ_2 (ns)
Only green-emitting NCs	219.69	32.78	-99.70	3.18
Mixed cyan- and green-emitting NCs	309.85	32.78	-166.77	12.10

6.4.4 Color-converted NRET-enhanced LED

To enhance the efficiency of the hybrid LED, we integrate a carefully designed assembly of 3.4 nmol cyan-emitting nanocrystals and 4.9 nmol green-emitting nanocrystals as an energy gradient structure on a similar near-UV LED, which increases the overall quantum efficiency of the integrated nanocrystal layer. Here the physical mechanism of the quantum efficiency enhancement stems from the ability to transfer excitation energy of the trapped excitons captured in defect states of donor nanocrystals into acceptor nanocrystals using nonradiative resonance energy transfer [108], [124]. With the optical excitation by incoming near-UV light, the photogenerated electron and hole pairs relax rapidly (in hundred fs) to their respective conduction and valence bands, some of which subsequently make interband transitions for radiative recombination. However, some of those photogenerated electron-hole pairs get trapped in the defect states, typically leading to nonradiative recombination. Using nonradiative energy transfer, some portion of these trapped excitons are transferred to the green-emitting nanocrystals that serve as acceptors for these defect states, a part of which in turn contribute to photoluminescence of these acceptors. Thus, the overall luminescence increases because of the enhanced emission of the

acceptors by effectively recycling the trapped excitons (and thus otherwise lost excitation energy) in the defect states of donors.

In Figure 6.4.6 the time-resolved spectroscopy measurements of mixed cyan- and green-emitting nanocrystal film is presented. We observe in Figure 6.4.6 (and also in Table 6.4.2) that the energy rise (*i.e.*, the exponential increase) in the energy gradient structure of mixed cyan-green nanocrystals is more dominant with respect to the case of only green nanocrystals, because of the strong exciton migration to green-emitting nanocrystals. By using the physical process of NRET, we obtain the resulting luminescence of the hybrid device as shown in Figure 6.4.7. Here the quantum efficiency of the nanocrystal film is enhanced by 9%.

It is important to note that, because of the strong nonradiative energy transfer, cyan-emitting nanocrystals are fully quenched by transferring their energy to green-emitting nanocrystals. As a result of the enhanced quantum efficiency of the mixed nanocrystal assembly, at 19.05 mA, the NRET-enhanced NC-LED reaches a luminous efficiency of 19 lm/W, while the luminous efficacy of optical radiation is maintained at 425 lm/W_{opt}. This NRET-NC-LED has its chromaticity coordinates at *(x,y)*=(0.46, 0.51). As the current injection level increases, the emission of NRET-NC-LED makes expectedly a red shift from 568 to 573 nm due to the additional heating. Its tristimulus coordinates and correlated color temperature correspondingly shift from (0.40, 0.49) to (0.45, 0.52) and from 4077 to 3441 K, respectively, as given in Table 6.4.3. In our NRET-NC-LED, NCs reach a quantum efficiency level as high as 55%. By using a state-of-the-art near-UV LED with an external quantum efficiency of 40%, this implies that it is possible to obtain color-converted NRET-enhanced LEDs with an expected external quantum efficiency of 22% and a predicted luminous efficiency of 94 lm/W.

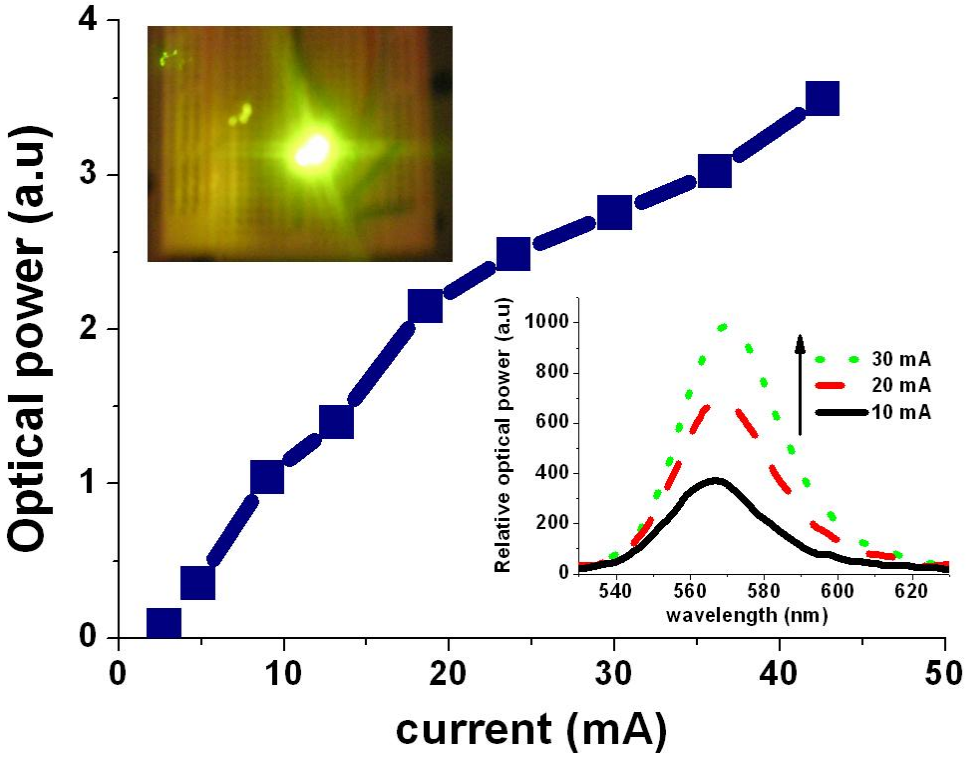

Figure 6.4.7 The total optical power of mixed cyan- and green-emitting NCs (λ_{PL}=490 nm and 548 nm, respectively) hybridized on near-UV LED (λ_{EL}=379 nm) at different levels of current injection at room temperature (with no heat sink or active cooling), along with the emission spectra and picture of the resulting NRET-NC-LED when electrically driven.

Table 6.4.3 Photometric properties of our color-converted NRET-enhanced NC-LED at various current injection levels .

I (mA)	***x***	***y***	***CCT* (K)**
9.45	0.40	0.49	4077
19.50	0.44	0.51	3642
30.40	0.45	0.52	3441

6.4.5 Conclusion

In this section, we presented the design, growth, fabrication, hybridization and characterization of hybrid light emitting diodes that integrate colloidal semiconductor nanocrystal nanocrystals as color converters on near-UV InGaN/GaN LEDs. In our proof-of-concept color-converted NC-LED by hybridizing green-emitting CdSe/ZnS core/shell nanocrystals, we achieved the luminous efficacy of optical radiation to be 425 lm/W_{opt} and the luminous efficiency to be 17 lm/W at a current injection level of 19.05 mA.

In our proof-of-concept color-converted NRET-enhanced NC-LED by hybridizing a custom-design assembly of cyan- and green-emitting CdSe/ZnS core/shell nanocrystals to facilitate nonradiative energy transfer among them, we demonstrated a quantum efficiency enhancement of 9% with respect to the color-converted NC-LED by recycling the trapped excitons into nanocrystals via NRET. At a current injection level of 19.05 mA while keeping the luminous efficacy of optical radiation at 425 lm/W_{opt}, we further improved our hybrid NC-LED to reach a luminous efficiency of 19 lm/W. In our NRET-NC-LED, NCs reach a quantum efficiency level of 55%. Starting with a 40% efficiency near-UV LED, a luminous efficiency of 94 lm/W and an external quantum efficiency of 22% are predicted in yellow/green spectral ranges. These proof-of-principle demonstrations show that these hybrid NC-LEDs are potentially strong candidates for future lighting applications in green/yellow.

Chapter 7

Light generation based on NRET-conversion

7.1 White light generating nonradiative energy transfer from epitaxial InGaN/GaN quantum wells to colloidal CdSe/ZnS core/shell quantum dots

This section is based on the publication "White light generation by resonant nonradiative energy transfer from epitaxial InGaN/GaN quantum wells to colloidal CdSe/ZnS core/shell quantum dots" **S. Nizamoglu**, E. Sari, J.-H. Baek, I.-H. Lee, and H. V. Demir, New Journal of Physics 10, 123001 (2008). Reproduced (or 'Reproduced in part') with permission from Institute of Physics. Copyright 2008 Institute of Physics.

In this section we propose and demonstrate white light generating nonradiative energy transfer from epitaxial quantum wells to colloidal quantum dots in their close proximity. The hybrid color conversion system consists of chemically synthesized red-emitting CdSe/ZnS core/shell heteronanocrystal quantum dots (λ_{PL}= 650 nm) intimately integrated on epitaxially grown cyan-emitting InGaN/GaN quantum wells (λ_{PL}= 490 nm). The white light is generated by the

luminescence of quantum wells and quantum dots in which the dot emission is further increased by 63% with nonradiative energy transfer to set the operating point in the white region of CIE 1931 chromaticity diagram. Using the cyan emission from the quantum wells and red emission from the nanocrystal luminophors we obtain warm white light generation with correlated color temperature *CCT* = 3135 K and tristimulus coordinates of *(x,y)*=(0.42, 0.39) in the white region of CIE chromaticity diagram. By analyzing the time-resolved decay of nanocrystal emitters in our hybrid system with a 16 ps time resolution, the luminescence kinetics reveals an energy transfer with a lifetime of 2 ns using a multiexponential least square fit with χ^2=1.0171.

7.1.1 Introduction

For white light generation, phosphor based color conversion approach has already been commercialized and is most commonly used today [4-6]. In this approach the blue electroluminescence of InGaN/GaN light emitting diode optically pumps the yellowish phosphors, and the electroluminescence of LED and photoluminescence of the phosphors jointly form the perceived white light spectrum. However, this current technology suffers from the major problem of the low level of absorption of blue light by the phosphors and the limited blue absorption in blue causes to use thick color converter [1]. To address this issue in solid state lighting, nonradiative energy transfer from semiconductor quantum wells (QWs) to color converters enables using relatively thinner color converter. Therefore, in our study we investigate white light generating nonradiative energy transfer pumping of colloidal quantum dots by epitaxial quantum wells, as the first proof-of-concept demonstration in solid state lighting. To date only the Förster-type nonradiative energy transfer of excitons and free carriers from a semiconductor quantum well QW to semiconductor nanocrystal quantum dots is shown [91], and temperature dependence of energy transfer from QW to quantum dots is investigated [131].

As the color converter we select semiconductor nanocrystal luminophors because they reveal attractive properties including size-tuneable emission with large photoluminescence quantum yields, high absorption towards shorter wavelengths, high photostability, relatively narrow and symmetric photoluminescence with high photobleaching thresholds, and small spectral overlap between absorption and emission [100], [130]. Furthermore, various film deposition techniques such as Langmuir-Blodgett, spin casting, and electrostatic layer-by-layer film deposition are commonly used. Therefore, these quasi-zero-dimensional semiconductor materials have been both theoretically and experimentally investigated [10], [31], [92], [93], [99], [113], [132-137]. Because of the tuneable nature of their emission they are mainly used in various hybrid white light application. White light generation using single, dual, trio, and quadruple combinations of CdSe/ZnS core-shell nanocrystals hybridized on blue-emitting InGaN/GaN LEDs has been demonstrated. However, in all of these previous white light generating examples, nanocrystals are fully optically pumped by another excitation platform.

As an alternative method, in our study, we propose and demonstrate white light generation enhanced with nonradiative energy transfer pumping of colloidal quantum dots by epitaxial quantum wells. This hybrid color conversion system consists of chemically synthesized red-emitting CdSe/ZnS core/shell nanocrystals (λ_{PL}= 650 nm) integrated on epitaxially grown cyan-emitting InGaN/GaN quantum wells (λ_{PL}= 490 nm). The white light is generated by the luminescence of quantum wells and nanocrystal emitters in which the nanocrystal emission is further increased around 63% with nonradiative energy transfer to set the operating point in the white region of CIE 1931 chromaticity diagram. Using the cyan emission from the quantum wells and red emission from the nanocrystal luminophors we obtain warm white light generation with a correlated color temperature of 3135 K and tristimulus coordinates of *(x,y)*=(0.42, 0.39) in the white region of CIE chromaticity diagram as shown in Figure 7.1.1. By analyzing the time-resolved decay of nanocrystal emitters in

our hybrid system, the luminescence kinetics reveals an energy transfer from quantum wells to nanocrystals with a lifetime of 2 ns that is higher than the recombination lifetime of nanocrystals (around tens of nanoseconds).

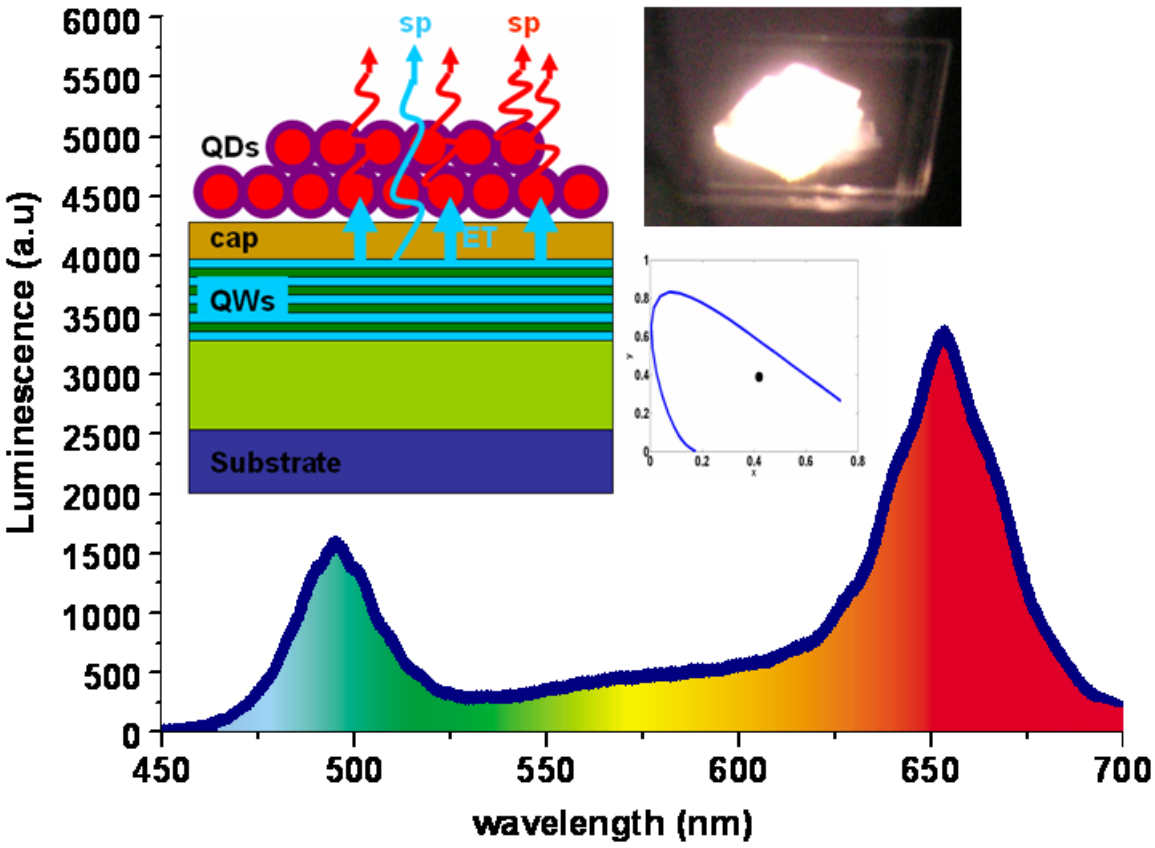

Figure 7.1.1 Luminescence spectrum of our hybrid system improved by using non-radiative energy transfer pumping of red-emitting CdSe/ZnS core/shell nanocrystals (λ_{PL}= 650 nm) by cyan-emitting InGaN/GaN quantum wells (λ_{PL}= 490 nm), along with the corresponding *(x,y)* tristimulus coordinates, the pictures of the cyan emitting wafer, red-emitting nanocrystals and white emitting hybrid system, and hybrid system structure while generating white light.

7.1.2 Materials used for white light generation

To achieve white light generation we use cyan-emitting InGaN/GaN semiconductor quantum wells (λ_{PL}= 490 nm) and red-emitting CdSe/ZnS core/shell nanocrystals (λ_{PL}= 650 nm). For the InGaN/GaN wafer we use the

design shown in Figure 7.1.2(a). On top of the polished sapphire substrate we grow 3.5 μm n-doped GaN. Afterwards we continue with 5 InGaN/GaN well/barrier layers and finally finish our structure with a few monolayers undoped GaN capping layer. According to the X-ray diffraction measurement (XRD) in Figure 7.1.2(b), the well and barrier thicknesses are around 95 nm thick with a well indium mole fraction of 83%. For steady state measurements we use a Jobin Yvon Traix 500 CCD photolumescence system with a He/Cd laser at 325 nm and the photoluminescence of the InGaN/GaN wafer is shown in Figure 7.1.2(c). Its emission peak is around 490 nm in Figure 7.1.2(c) and the observed wavy PL is due to the phase separation in the quantum wells and barriers.

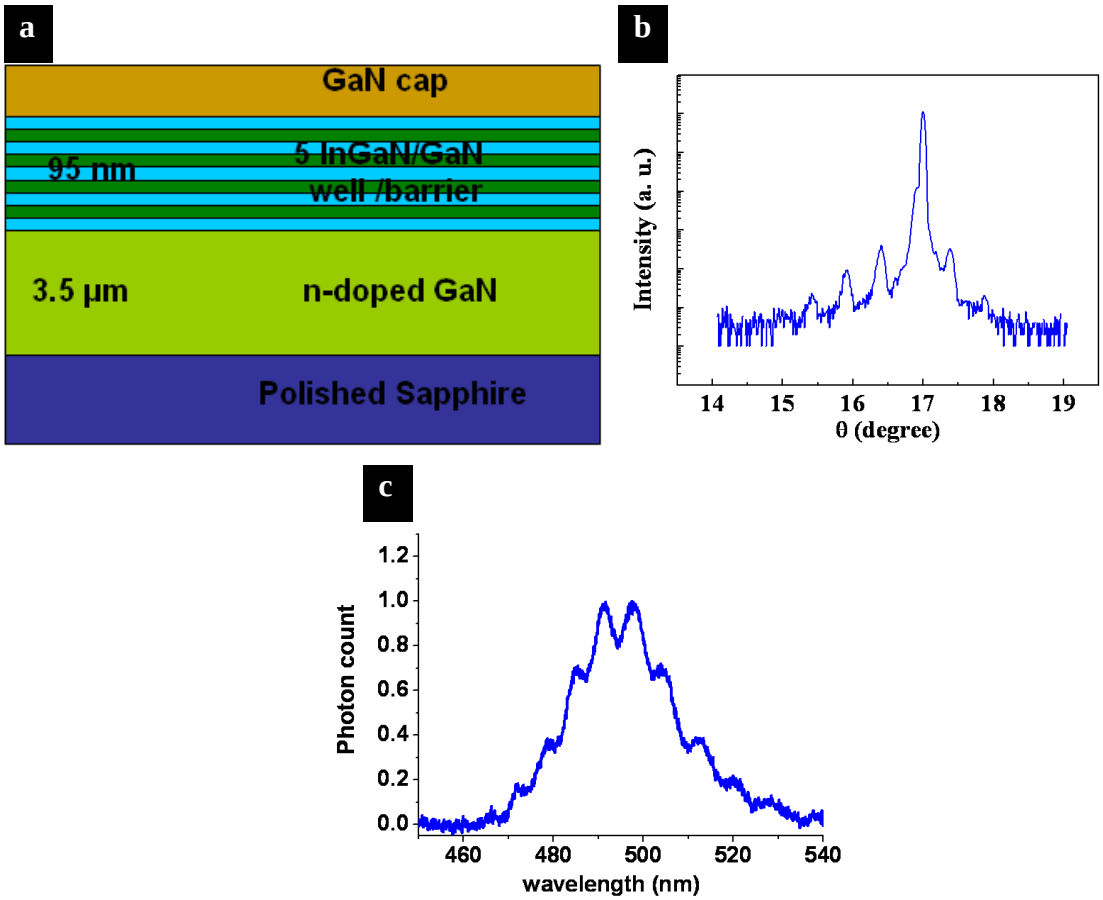

Figure 7.1.2 (a) Epitaxial structure of our cyan-emitting wafer (not drawn to scale), (b) X-ray diffraction measurement (XRD) of the grown wafer, and (c) photoluminescence of the wafer around at 490 nm excited at 325 nm.

For quantum dots, we use red-emitting CdSe/ZnS core/shell nanocrystals with a concentration of 15.85 nmol/mL in toluene. The diameters of quantum dots are around 5.8 nm with size dispersion <5% and the transmission electron microscopy (TEM) image of nanocrystals are shown in Figure 7.1.3(a). As we also see from the TEM image the shapes of quantum dots are not perfect. Using the He/Cd laser at 325 nm the photoluminescence of nanocrystals with its peak around 650 nm are shown in Figure 7.1.3(b). Since the absorption below the emission of NCs increases toward shorter wavelengths shown on the inset of Figure 7.1.3(b), the overlap of the NCs absorption and QWs emission make the electrostatic interaction possible between the transition dipoles of QWs and NCs. For our hybrid structure and control group, we hybridize the NCs with a volume of 3 μL on InGaN/GaN quantum well/barriers (with an area around 1 cm^2) and quartz respectively by evaporating the toluene on top of the QW resulting a mean NC solid film thickness of 270 nm by using atomic force microscopy (AFM) measurement (which is also consistent with the thickness calculation of <300 nm by considering the TOPO ligands <2 nm).

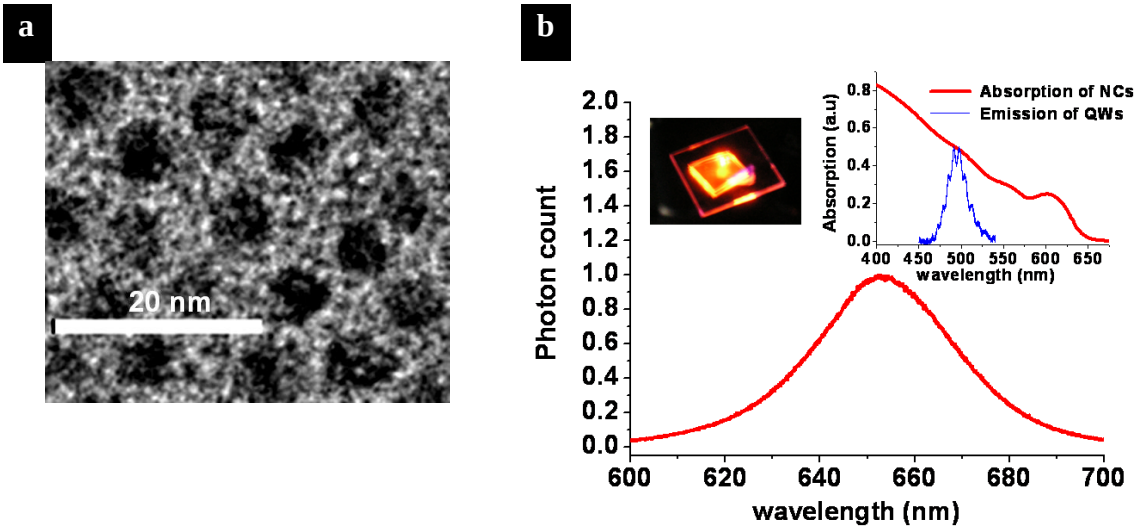

Figure 7.1.3 (a) Transmission electron microscopy image and (b) photoluminescence of the nanocrystals excited at 325 nm with absorption and luminescence photograph as given in the inset.

7.1.3 Characterization and analysis of the hybrid structure

In Figure 7.1.4, the steady-state photoluminescence of hybrid system (*i.e.*, nanocrystals integrated on quantum wells) and only nanocrystals are shown. We observe that the emission of the nanocrystals in the hybrid system is increased by 63% with respect to the only NCs case because of the energy transfer from quantum wells to nanocrystals. Furthermore, in the hybrid system the emission of nanocrystals is disturbed and this asymmetry is another evidence of the energy transfer from the quantum wells to the quantum dots. It is a fact that there exists homogeneous energy transfer among the nanocrystals due to size distribution (<5%), but this kind of energy transfer would not result in such a wavy symmetry break in the PL.

Here cyan-emitting quantum wells and red-emitting nanocrystals are carefully selected to provide the operating point in the white region. For white light generation using dual-color emission, the line that connects both of the operating wavelengths should intersect the white region. As shown in the inset of Figure 7.1.4, since the connecting line of cyan and red emission intersect the white region, we can obtain our operating point in white region. Thus, the resultant white light corresponds to the tristimulus coordinates (x,y)=(0.42, 0.39) and correlated color temperature of 3135 K in white region of CIE 1931 chromaticity coordinate.

The energy transfer provides an efficient balance mechanism that maintains the operating point in the white region while shifting the tristimulus coordinate to a warmer color temperature. Furthermore, in our hybrid structure the energy transfer is a result of the electrostatic interaction between quantum wells and quantum dots rather than the delocalized behavior of excitons or free carriers, because the ZnS barrier of our nanocrystals prevent tunneling and make electronic isolation [138]. The advantage of this hybrid structure is that in

previous studies [45], [6], [64-66], [68], [103] white light generation is achieved with platforms in which the recombination process occurs in quantum well and the resultant photon excites the quantum dot again. In other words, there should exist two radiative recombination processes to generate a photon from a nanocrystal. However, in our approach for white light generation the recombination occurs directly in the nanocrystal (*i.e.*, after the quantum well absorbs the light, then the quantum well transfers its excitation energy to the quantum dot and the recombination occurs in the dot.) Therefore, for white light generation using nonradiative energy transfer is a relatively efficient process.

Furthermore, although we did not observe any stability problem during our study, we did not make any stability measurement. However, it is well-known that packaged InGaN/GaN QWs can operate hundred thousands of hours. Nanocrystals also exhibit high photostability. They are compared with commonly used color converters such as rhodamine, fluorescein, and Alexa-Fluor and the high photostability makes NCs very attractive among various color converters [139]. Thus, it is expected that the hybrid system has high stability.

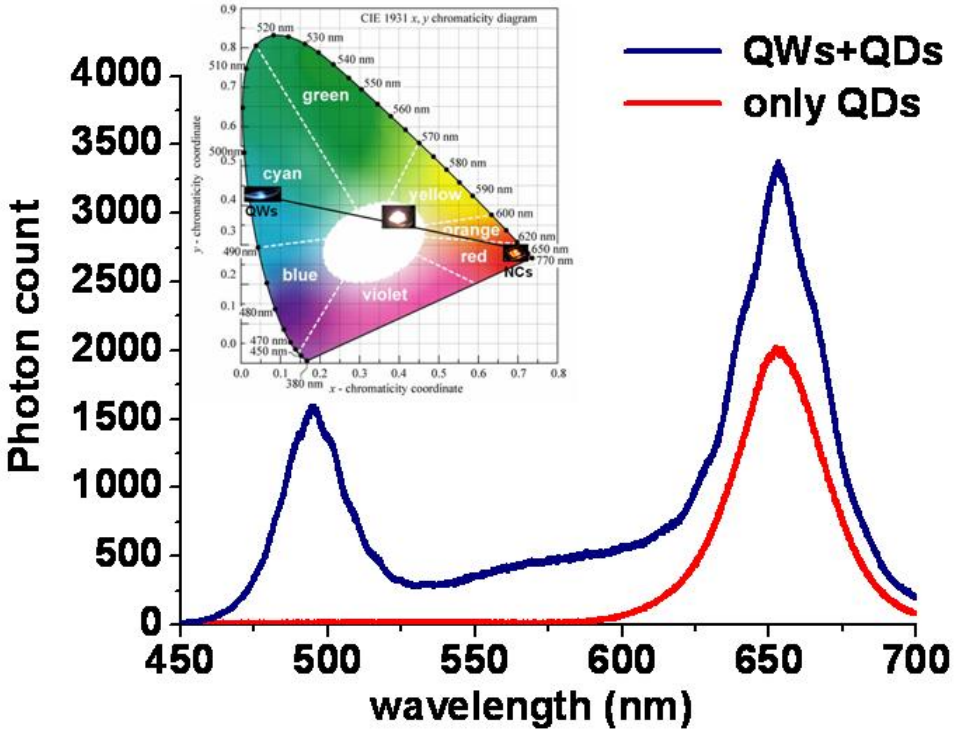

Figure 7.1.4 Steady state emission spectrum of hybrid system (QWs+QDs) improved by using non-radiative energy transfer pumping of red-emitting CdSe/ZnS core/shell nanocrystals (λ_{PL}= 650 nm) by cyan-emitting InGaN/GaN quantum wells (λ_{PL}= 490 nm) with respect to the only nanocrystals on quartz case (only QDs). The inset shows the 1931 CIE chromaticity diagram presenting the *(x,y)* operating point by using the combination of cyan-emitting wafer and red-emitting nanocrystals .

For the time resolved spectroscopy measurements, we use a FluoTime 200 spectrometer from PicoQuant with a time-correlated single photon counting (TCSPC) system of PicoHarp 300. For pumping nanocrystal solids, we use a laser head at a wavelength of 375 nm and a photon multiplier tube (PMT) as the detector. For the data analysis we use the software of FluoFit to solve the fitting decay parameters. For these measurements we use time resolution of 16 ps that is sufficiently high to resolve the luminescence kinetics. We measure the hybrid system at 650 nm to determine the energy transfer to the quantum dots rather than investigating the quenching of quantum well. This is because the quenching can occur because of environmental impurities. However, the energy increase in

quantum dots can surely occur only due to the energy transfer from quantum well.

Figure 7.1.5 shows time-resolved spectroscopy of hybrid system and only nanocrystal solids on quartz substrate case. The emission increase for the hybrid structure shows a smoother change from rise to decay around from 8 to 10 ns because of the energy-transfer feeding component of the luminescence as also zoomed in the inset of Figure 7.1.5. For the decay fit we use a multiexponential model fit with deconvolution of the laser diode response as shown in Equation 7.1.1. For only NCs on quartz substrate, we use double exponential fit with a χ^2 near 1 (χ^2=0.9369). The lifetimes are 12.870 and 49.990 ns as also summarized in Table 7.1.1. The 12.870 decay component is the general lifetime of the nanocrystals that are on the order of tens of nanoseconds [109-111]. However, there exists another decay lifetime as 49.990 ns. The amplitude of the long decay component is relatively weak when we compare its amplitude 88.30 with 1120.9 of the general nanocrystal decay time. We attribute the slow decay component to trap states. When we analyze the white light generating hybrid system QWs and NCs together, we already have double exponential lifetimes 12.870 and 49.990 ns, which are same with the only nanocrystal case. Additionally, there is another third increasing exponential with a lifetime of 2 ns, possessing a negative amplitude (*i.e.*, an energy increase) that is attributed to the nonradiative energy transfer from quantum well to nanocrystals for white light generation, as the fitting parameters summarized in Table 7.1.1. These fitting parameters result also in a χ^2 around 1 (χ^2=1.0171). The lifetime of the increasing emission component is around 2 ns meaning energy transfer faster than the recombination time of CdSe/ZnS core/shell nanocrystals around tens of nanoseconds. The lifetime of the hybrid system increases and the white light is enhanced with respect to the only NCs case because of the energy transfer and, as a result, the intensity weighted average time constant of hybrid system at 650 nm increases from 21.567 ns to 22.665 ns when compared to only nanocrystals.

$$I(t) = \int_{-\infty}^{t} IRF(t') \sum_{i=1}^{n} A_i \exp(-\frac{t-t'}{\tau_i}) dt' \qquad (7.1.1)$$

Table 7.1.1 The multiexponential fitting parameters to only nanocrystal on quartz substrate (only QDs) and hybrid system consisting of quantum wells and nanocrystals together (QWs+QDs) by convolution of the laser diode source at 375 nm.

	A_1	τ_1(ns)	A_2	τ_2 (ns)	A_3	τ_3 (ns)
Only NCs	88.30	49.990	1120.9	12.870	-	-
QWs+NCs	102.35	49.990	1174.7	12.870	-200.0	2.000

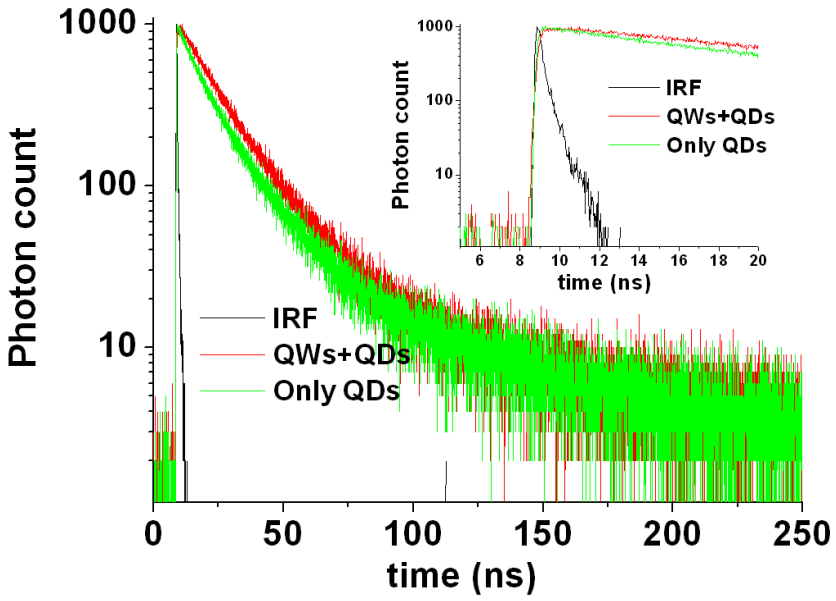

Figure 7.1.5 Time resolved spectroscopy measurement of hybrid system consisting of quantum wells and nanocrystals together (QWs+QDs), only nanocrystals on quartz substrate (only QDs) and instrument response function (IRF) of the laser diode at 375 nm using a time-correlated single photon counting (TCSPC) system of PicoHarp 300 with a time resolution of 16 ps.

7.1.4 Conclusion

In this section, we presented white generation with the nonradiative energy transfer pumping of colloidal quantum dots by epitaxial quantum wells. We investigated the energy transfer both by steady state and time resolved

spectroscopy measurements. We obtained warm white light generation with a correlated color temperature of 3135 K and tristimulus coordinates of (0.42, 0.39) by obtaining an 63% increase in nanocrystal emission because of energy transfer. We believe that white light generation enhanced with nonradiative energy transfer from quantum wells to nanocrystals hold promise for future lighting applications.

7.2 Efficient nonradiative energy transfer from InGaN/GaN nanopillars to CdSe/ZnS core/shell nanocrystals

This section is based on the publication "Efficient nonradiative energy transfer from InGaN/GaN nanopillars to CdSe/ZnS core/shell nanocrystals" **S. Nizamoglu,** B. Guzelturk, D-W. Jeon, I-H. Lee, and H. V. Demir, Applied Physics Letters 98, 1 (2011). Reproduced (or 'Reproduced in part') with permission from American Institute of Physics. Copyright 2011 American Institute of Physics.

In this section, we propose and demonstrate efficient electron-hole pair injection from InGaN/GaN multiple quantum well nanopillars (MQW-NPs) to CdSe/ZnS core/shell nanocrystal quantum dots via Förster-type nonradiative energy transfer. For that we hybridize red-emitting nanocrystals with blue-emitting MQW-NPs and electron-hole pair transfer reaches a maximum rate and efficiency of $(0.192\ ns)^{-1}$ and 83.0%, respectively. By varying the effective bandgap of nanocrystals, we conveniently control and tune the electron-hole pair transfer rate for these core/shell nanocrystals integrated hybrids, and our measured and computed electron-hole pair transfer rates are in good agreement for all hybrid cases.

7.2.1 Introduction

Nanocrystal quantum dots exhibit favorable properties to be exploited for light emitting device applications. They feature size-tuneable effective band gap, high photoluminescence, high photostability and easy means of film deposition [43], [44], [140]. Electrical current injection into these nanocrystals is possible via using mixture of nanocrystal-polymer composites or hybridization of

nanocrystal monolayers into diode structure [41], [141]. However, high potential barriers due to surfactants around nanocrystals and the charge transport differences between electron and hole limit the efficiency of electrically driven NC based devices. Alternatively, NRET can solve both charge injection and transport problems. In addition, NRET also has the potential to provide significant energy savings for light emitting diodes [125], [142-144]. Today current white light emitting diode technology relies on color-conversion step involving two recombination processes [2], [4], [7]. The first radiative recombination process occurs in multiple quantum wells of LED, and subsequently, their emitted photons excite color conversion layer that luminescence via a second radiative recombination process. NRET advantageously eliminates recombination in MQWs, photon extraction from MQWs and absorption by the color conversion layer [132]. However, the reported experimental performances in terms of transfer efficiency and percentage of generated electron–hole pairs experiencing nonradiative energy transfer from QWs to NCs are limited.

Achermann *et al.* demonstrated NRET pumping of semiconductor nanocrystals using an epitaxial quantum well with a transfer efficiency of 65% [91]. However, in this structure the limitation was that only single quantum well could contribute to the color conversion through the NRET process. Furthermore, since the energy transfer coupling scales with d^{-4}, the topmost layer was required to be extremely thin (typically <10 nm). However, thinning the top contact layer undesirably increases the nonradiative carrier losses in the QW. As a solution, Chanyawadee *et al.* demonstrated to use the epi-wafer having holes with elliptical cross-sections that reach down to the active multiple quantum wells for efficient energy transfer [145]. However, in this structure only 18% of the generated electron-hole pairs experience nonradiative ET with an efficiency of 82%.

Different from the previous studies, we hybridize arrays of InGaN/GaN multiple quantum well nanopillars (MQW-NPs) with CdSe/ZnS core/shell nanocrystals to enhance Förster-type nonradiative energy transfer. We integrate red-emitting nanocrystals on blue-emitting MQW-NPs for efficient and fast NRET. As a result, electron-hole pair transfer efficiency of 83.0% with a rate of $(0.192\ ns)^{-1}$ is achieved in this hybrid system, while 41% of generated electron–hole pairs in MQW-NPs undergo nonradiative ET. By changing the effective bandgap of nanocrystals, we conveniently adjust electron-hole pair transfer rate for these core/shell nanocrystals integrated hybrids. We also compute electron-hole pair transfer rates for all hybrid cases and both calculated and measured NRET rates are in agreement.

7.2.2 Materials and spectroscopy

InGaN/GaN MQW epitaxial structure was grown by metal organic chemical vapor deposition (MOCVD) technique. Trimethylgallium (TMGa), trimethylindium (TMIn) and NH_3 were used as precursors for Ga, In and N, respectively. A thermal annealing of c-plane sapphire substrate was performed at 1000 ^oC for 10 min, followed by the growth of a low temperature GaN buffer layer. A 1 μm-thick undoped GaN layer and a 2 μm-thick n-type GaN layer were grown at 1060 ^oC. Subsequently, five pairs of InGaN/GaN MQW were grown on high quality GaN epitaxial layers and a 150 nm-thick p-GaN layer was directly grown on MQW layer. A 100 nm thick SiO_2 layer and 10 nm-thick Ni mask were deposited on the surface of LED by plasma-enhanced CVD and e-beam evaporator, respectively. This sample was subsequently annealed under flowing N_2 at temperatures of 800 ^oC for 1 min to form the Ni clusters. Then, the SiO_2 and GaN layer were *etc*hed for 120 s and 5 min using an ICP-RIE process, respectively. Finally, Ni metal and SiO_2 layer were removed by buffered oxide *etc*hant (BOE).

The nanopillar formation steps are schematically illustrated in Figure 7.2.1(a). In Figure 7.2.1(b) the scanning electron microscopy image reveals that the

nanopillars are finely formed. Furthermore, the existence of multiple quantum wells in both planar structure and nanopillars are shown by using the x-ray diffraction measurements depicted in Figure 7.2.1(c). One of the main advantages of nanopillar formation is that the MQW-NPs exhibit stronger photoluminescence than the planar case [146], [147]. In Figure 7.2.1(d) the PL of MQW nanopillar structure is presented and the nanopillar structure shows approximately a two-fold PL enhancement.

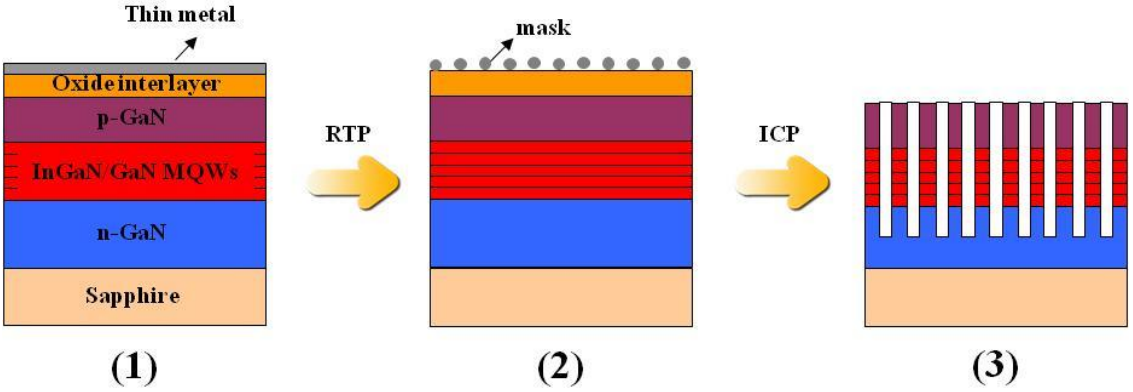

(a)

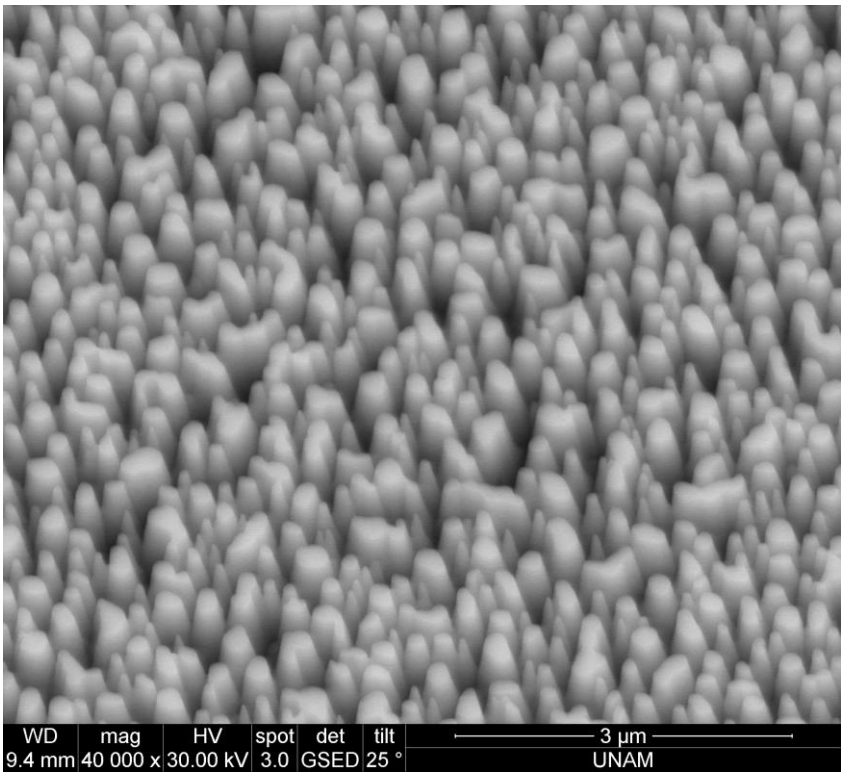
WD
mag
HV
spot
det
tilt
9.4 mm
40 000 x
30.00 kV
3.0
GSED
25 °
3 µm
UNAM

(b)

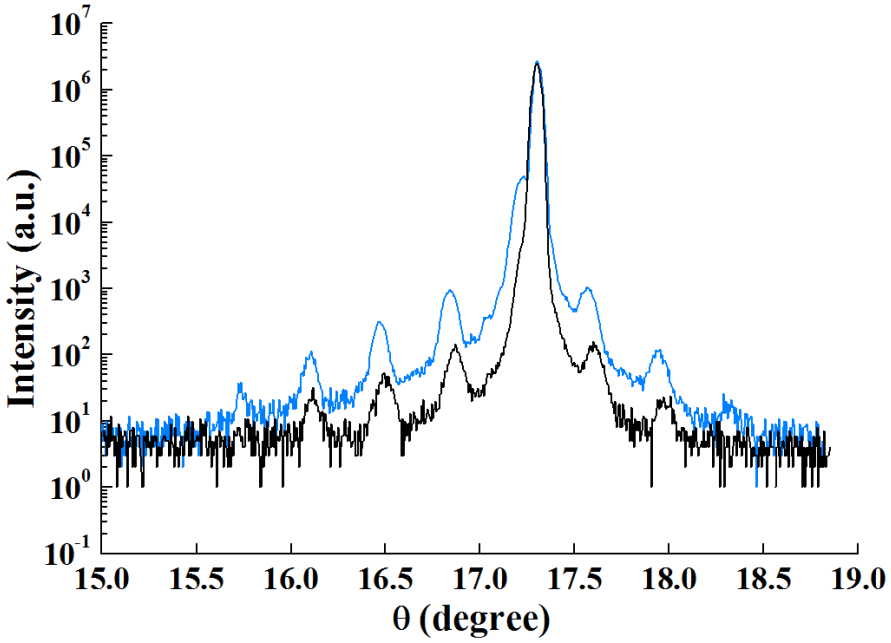
Intensity (a.u.)
θ (degree)
10^7
10^6
10^5
10^4
10^3
10^2
10^1
10^0
10^-1
15.0
15.5
16.0
16.5
17.0
17.5
18.0
18.5
19.0

(c)

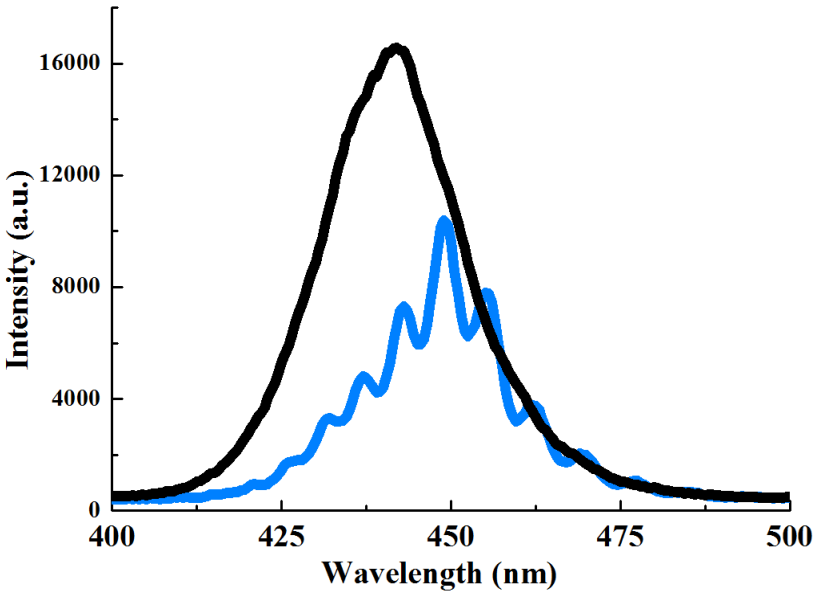

(d)

Figure 7.2.1 (a) Schematic representation of the nanopillar formation, (b) scanning electron microscopy image of fabricated InGaN/GaN multiple quantum well nanopillars, (c) x-ray diffraction measurement, and (d) photoluminescence spectra of both planar (blue line) and nanopillar (black line) structures.

For exciton migration we use trioctylphosphineoxide (TOPO) capped green-, yellow- and red-emitting CdSe/ZnS core/shell nanocrystals emitting at 540, 590 and 620 nm, respectively. The absorption and photoluminescence spectra of nanocrystals in toluene (measured with Varian flouremeter and spectrometer, respectively) are shown in Figure 7.2.2. They have a concentration of 10 mg/mL and exhibit in-solution quantum efficiencies of >50%. Our green-, yellow- and red-emitting nanocrystal quantum dots have molecular weights of 94, 140, 270 μg/nmol, and their corresponding diameters are around 3.3, 3.8 and 5.0 nm with a size dispersion of <5%, respectively. We deposit NCs films on MQW-NPs in a class-100 cleanroom to prevent any contamination of the nanopillar surfaces, which can negatively affect the energy transfer process. We deposit the films by drop-casting on top of the nanopillars and hold the samples on a hotplate at 100 ^{o}C for 1 hour to remove the excess solvent.

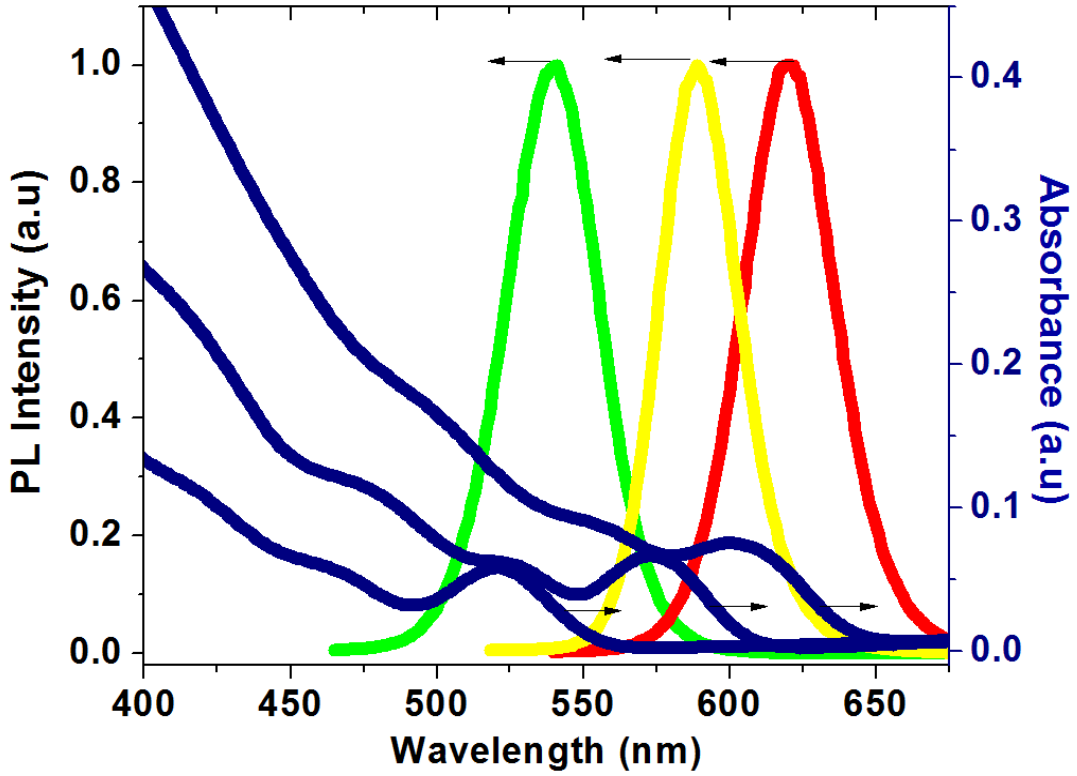

Figure 7.2.2 Absorption and emission spectra of CdSe/ZnS core/shell nanocrystal quantum dots (green-, yellow- and red-emitting ones).

We use a fluorescence lifetime system of FluoTime 200 spectrometer by PicoQuant to analyze exciton transfer dynamics of the hybrid samples. Our system achieves an instrument response function full-width-at-half-maximum of 200 ps, as shown in the inset of Figure 7.2.3. Because of the finite temporal response of IRF, the exhibited decays are the actual response of nanopillars convoluted with the IRF response. Thus, the time-resolved emission decays may not seem as perfect exponentials. In our analysis, we take this case into account in our calculations and make fits to the measured decays accordingly. For only nanopillar case in Figure 7.2.3, we use Equation (7.2.1), where IRF(t) is the instrument response function, A is the amplitude, and τ_{np} is the lifetime of the nanopillars. For the cases of MQW-NPs hybridized with nanocrystals in Figures 7.2.4-7.2.6, we use the Equation (7.2.2) (where τ_{NRET} is the Förster-type nonradiative energy transfer lifetime) because the generated electron-hole pairs near to nanocrystals (with a distance less than two Förster radius) experience

nonradiative energy transfer, but those farther away from the nanocrystals do not.

$$I_{ref}(t) = \int_{-\infty}^{t} IRF(t')\{A_1 e^{-\frac{(t-t')}{\tau_{np}}}\}dt' \qquad (7.2.1)$$

$$I_{sample}(t) = \int_{-\infty}^{t} IRF(t')\{A_1 e^{-\frac{(t-t')}{\tau_{np}}} + A_2 e^{-(\frac{1}{\tau_{np}}+\frac{1}{\tau_{nret}})(t-t')}\}dt' \qquad (7.2.2)$$

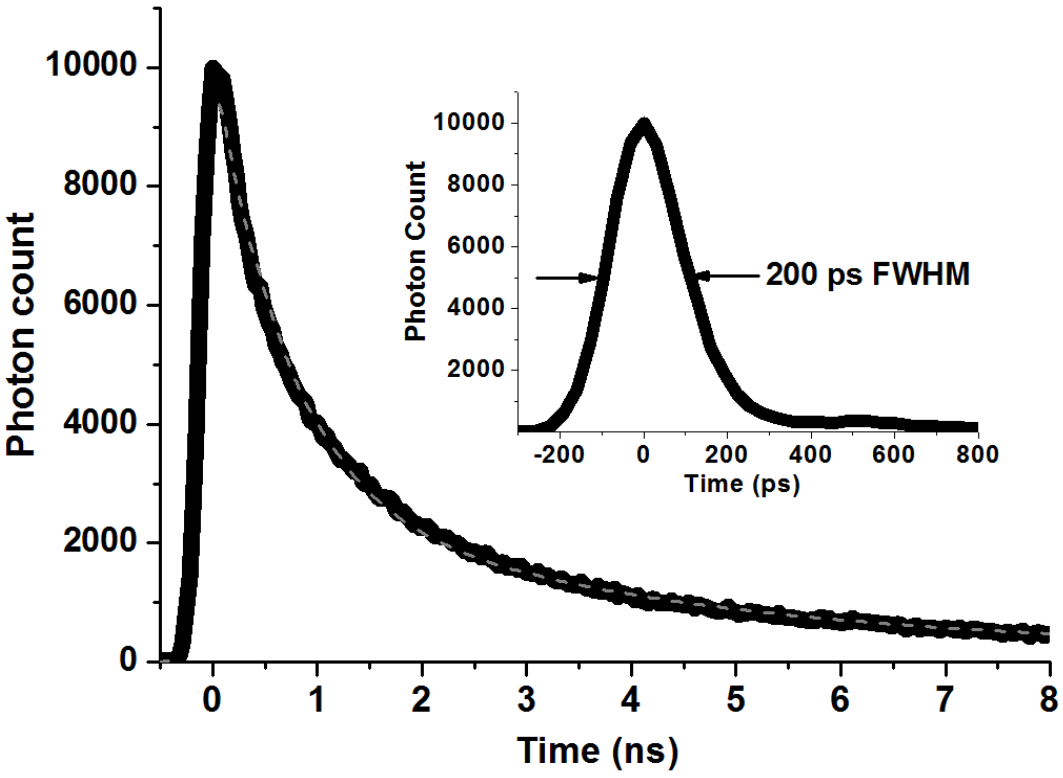

Figure 7.2.3 MQW-NPs photoluminescence decay (at λ= 450 nm) without nanocrystals. The dashed lines are the fits as described in text. Inset exhibits instrument response function and full-width-at-half-maximum (FWHM) of our time-resolved system.

7.2.3 Results and discussion

The time-resolved spectroscopy of only MQW-NPs is presented in Figure 7.2.3. We obtained a decay rate of $(0.944\ ns)^{-1}$ by using Equation (7.2.1). Strong spectral spectral overlap (J) between the emission of donor and the absorption of acceptor is important to achieve efficient nonradiative exciton transfer. The spectral overlap is calculated by using Equation (7.2.3), where $F_D(\lambda)$ is the corrected fluorescence intensity of the donor and $\varepsilon_A(\lambda)$ is the extinction coefficient of the acceptor at the wavelength λ [35]. The selection of the red-emitting nanocrystals allows us to obtain a strong spectral overlap of 4.421×10^{16} $M^{-1}cm^{-1}nm^4$ between the emission of the donor nanopillars and absorption of the acceptor quantum dots. Therefore, we integrate red-emitting CdSe/ZnS core/shell nanocrystals on InGaN/GaN multiple quantum well nanopillars. In Figure 7.2.4 the time-resolved fluorescence of MQW-NPs furnished with red-emitting nanocrystals at the donor emission wavelength (λ= 450 nm) is shown. It is clearly observable that the decay rate of the MQW nanopillars is increased because of the energy transfer from nanopillars to nanocrystals.

To extract the energy transfer rate and the percentage of the electron-hole pairs experiencing nonradiative exciton transfer, we use Equation (7.2.2). As a result of the numerical analysis, 41% of the generated electron-hole pairs in the MQW-NPs are found to be transferred to the nanocrystals while the rest of them make recombination in the NPs. For example, in the previous study by Chanyawadee *et al.* only 18% of the generated electron-hole pairs are transferred to the nanocrystals. Furthermore, the nonradiative exction transfer rate in our hybrid structure corresponds to $(0.192\ ns)^{-1}$. We also calculate transfer efficiency using Equation (7.2.4). As a result, an energy transfer efficiency of 83.0% is accomplished in MQW-NPs and nanocrystals hybrids. Although interspacing between the nanopillars and nanocrystals consisting of the ZnS shell (0.6 nm) and TOPO ligands (1.1 nm) decreases the transfer efficiency, the strong spectral overlap results in high energy transfer efficiency.

Here it is worth noting that the ZnS shell provides a large enough potential barrier that prevents the tunneling of the carriers so that the quenching cannot be due to a Dexter-type charge transfer process. Therefore, we can undoubtedly state that the shortening of the lifetime decay is as a result of the Förster-type nonradiative energy transfer. In the inset of Figure 7.2.4 the steady-state emission of the hybrid case is presented. The red emission generated by nanocrystals becomes significantly more dominant with respect to the MQW-NP emission because of the strong energy transfer, which is an important signature of the energy outflow from the nanopillars and energy inflow into the quantum dots. It is also an additional fact that the luminescence of nanocrystals without energy transfer also contributes to the overall emission of nanocrystals and makes it to be further stronger with respect to the NPs as well.

$$J(\lambda) = \int_0^\infty F_D(\lambda)\varepsilon_A(\lambda)\lambda^4 d\lambda \tag{7.2.3}$$

$$\eta_{FRET} = \frac{k_{FRET}}{(k_{FRET} + k_{NP})} \tag{7.2.4}$$

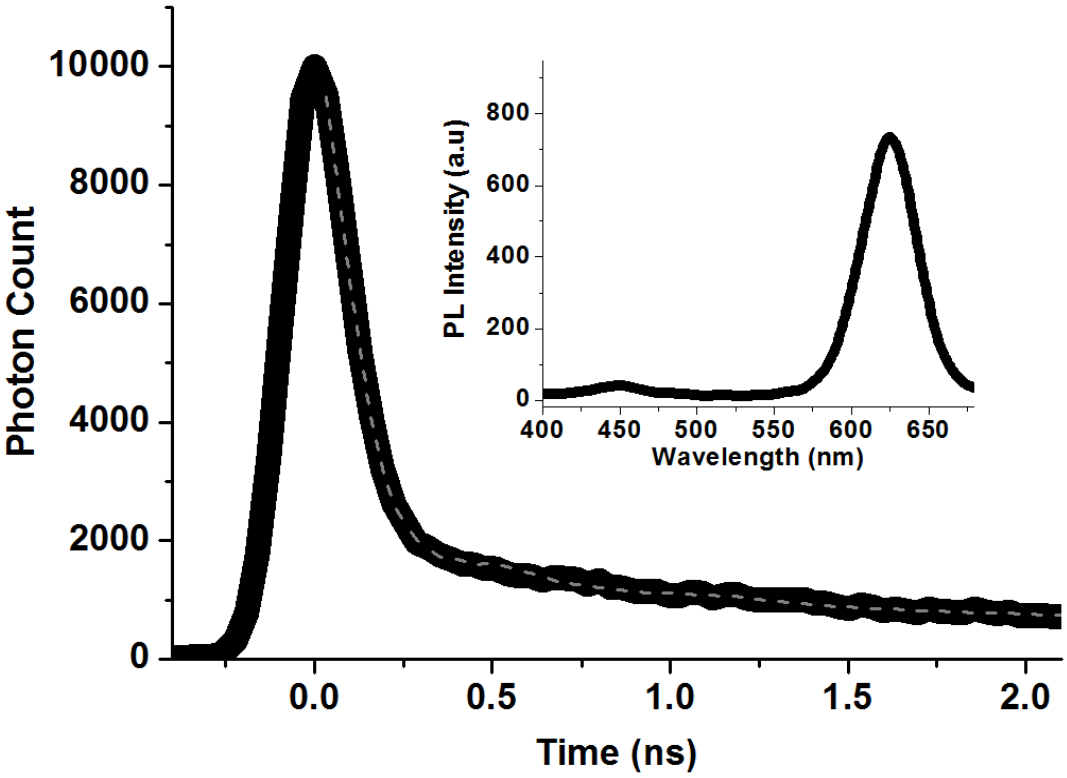

Figure 7.2.4 MQW-NPs photoluminescence decay (at λ= 450 nm) with red-emitting nanocrystals. The dashed lines are the fits as described in text. Inset exhibits steady-state photoluminescence spectrum of MQW-NPs with red-emitting nanocrystals.

To further understand exciton transfer process we vary the spectral overlap between the emission of MQW-NPs and absorption of nanocrystals. For that we hybridize yellow-emitting CdSe/ZnS core/shell nanocrystals with InGaN/GaN MQW nanopillars. The spectral overlap between emission of MQW-NPs and absorption of yellow-emitting nanocrystals decreases down to 1.491×10^{16} $M^{-1}cm^{-1}nm^{4}$. The time-resolved spectroscopy of the hybrid case is shown in Figure 7.2.5 and the decay rate increases due to the electron-hole pair transfer. According to our fit using Equation (7.2.2), we find that 40% of the electron-hole pairs are transferred from MQW-NPs to the yellow-emitting nanocrystals. The energy transfer rate and efficiency correspondingly become slightly lower, which are found to be $(0.237\ ns)^{-1}$ and 79.8%, respectively. Although the spectral overlap decreases for the cases of NPs with yellow-emitting

nanocrystals, the energy transfer efficiency does not significantly drop because the distance between nanocrystals and MQWs decreases, dot density around MQWs increases and the effective refractive index[20] decreases due to smaller size of yellow-emitting nanocrystals in comparison with red-emitting nanocrystals. As a result, a high energy transfer efficiency of 79.8% is obtained.

We also integrate green-emitting nanocrystals on MQW-NPs, for which the spectral overlap further reduces to 4.933×10^{15} $M^{-1}cm^{-1}nm^4$. The time-resolved spectroscopy of the hybrid case with green-emitting nanocrystals is shown in Figure 7.2.6. According to our fits, the transfer rate and efficiency decrease to $(0.253\ ns)^{-1}$ and 78.8%, and electron-hole pairs experiencing nonradiative energy transfer to nanocrystals slightly reduces to 39%. Both in the inset of Figure 7.2.5 and 7.2.6 the steady-state emission spectra are shown and according to them the nanocrystals emission suppresses the luminescence of MQW-NPs because of the energy migration from MQW-NPs into nanocrystals.

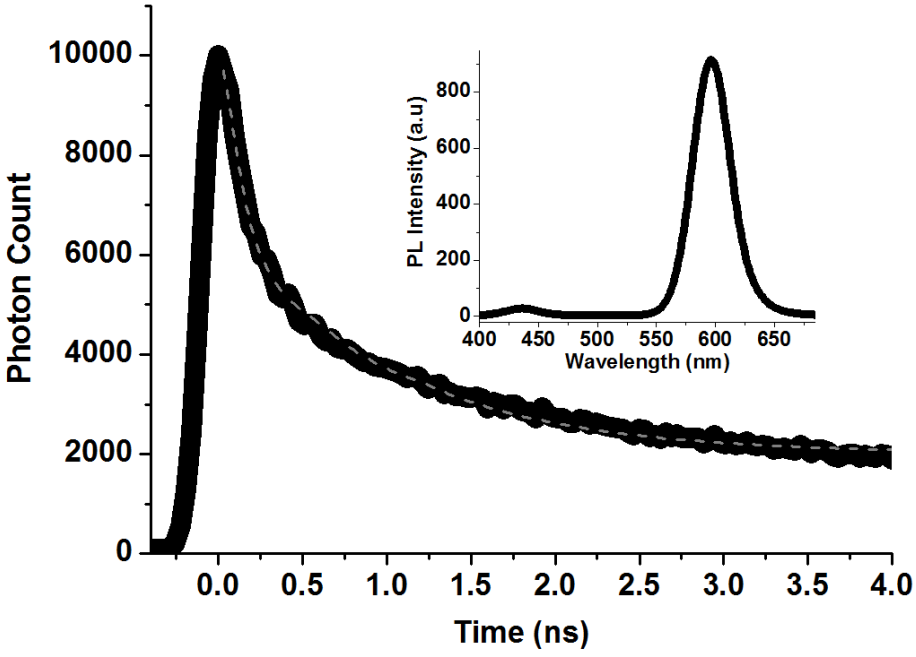

Figure 7.2.5 MQW-NPs photoluminescence decay (at λ= 450 nm) with yellow-emitting nanocrystals. The dashed lines are the fits as described in text. Inset exhibits steady-state photoluminescence spectrum of MQW-NPs with yellow-emitting nanocrystals.

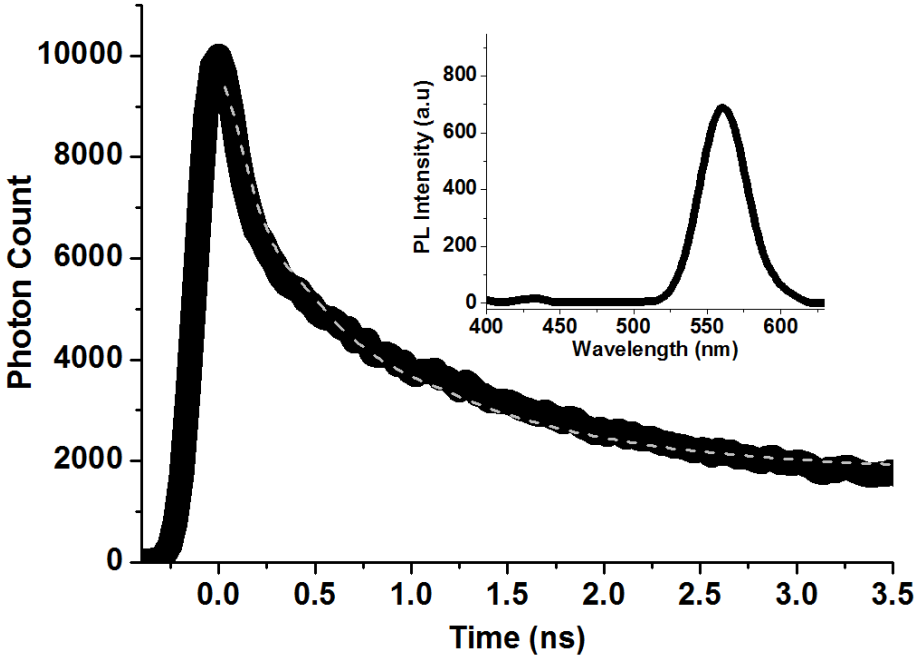

Figure 7.2.6 MQW-NPs photoluminescence decay (at λ= 450 nm) with green-emitting nanocrystals. The dashed lines are the fits as described in text. Inset exhibits steady-state photoluminescence spectrum of MQW-NPs with green-emitting nanocrystals.

7.2.4 Computational analysis of electron-hole pair transfer

We also make computational analysis of exciton transfer rates to further understand the energy transfer process and for that we derive the exciton transfer formula for our hybrid architectures. According to our model, MQWs transfer their excitons to NC layer at the surface of the nanopillars. We calculate the expected NRET rates by using Equations (7.2.5) - (7.2.7). For the hybrid case of red-emitting nanocrystals integrated on MQW-NPs, the spectral overlap (J) is calculated as 4.421×10^{16} $M^{-1}cm^{-1}nm^4$. The interspacing (d) between the center of the nanocrystal and quantum wells in NPs are taken to be 4.0 nm, which consists of 2.3 nm CdSe core radius, 0.6 nm ZnS shell radius, and 1.1 nm TOPO length. The refractive index (n) of 1.934 is estimated by averaging both refractive index of ligands surrounding nanocrystals as 1.468 and the refractive index of NC as

2.4 [148]. The quantum efficiency of donor multiple quantum well nanopillars is 20%. As a result, Förster radius (R_0) corresponds to 5.777 nm. We also know the decay rate of pure nanopillars (k_D) to be $(0.944\ ns)^{-1}$ and the dot density (σ) to be $2.100 \times 10^{12}\ cm^{-2}$. By putting all these parameters into Equation (7.2.7) for MQW-NPs with red-emitting nanocrystals, we obtain NRET rate of $(0.197\ ns)^{-1}$ and this calculated value is in good agreement with our measured NRET rate of $(0.192\ ns)^{-1}$. Similarly, we also calculated the ET rate for yellow- and green-emitting nanocrystals on the MQW-NPs and the used parameter values are summarized in Table 7.2.1. We obtained NRET rates of $(0.230\ ns)^{-1}$ and $(0.248\ ns)^{-1}$, respectively, and these values are also in good agreement with our measured NRET rates of $(0.237\ ns)^{-1}$ and $(0.253\ ns)^{-1}$, respectively. This further demonstrates that NRET between the nanopillar and nanocrystal quantum dots is originated by dipole-dipole interaction, which is in agreement with the Förster model.

$$R_o = 0.211(\kappa^2 n^{-4} Q_D J(\lambda))^{1/6} \qquad (7.2.5)\ [35]$$

$$C = k_D R_o^{\ 6} \qquad (7.2.6)\ [149]$$

$$\begin{aligned} k_{ET} &= CR^{-6} \\ &= \sigma R_0^{\ 6} \int_0^\infty k_{ET}\, dS \\ &= k_D \sigma R_0^{\ 6} \int_0^\infty \frac{2\pi\rho}{(d^2+\rho^2)^3} d\rho \qquad (7.2.7) \\ &= k_D \sigma R_0^{\ 6} 2\pi(-1)\left[\frac{1}{4(d^2+\rho^2)^2}\right]_0^\infty \\ &= \frac{k_D 0.5\pi\sigma R_0^{\ 6}}{d^4} \end{aligned}$$

7.2.5 Conclusion

In this section, we studied nonradiative exciton migration from blue-emitting InGaN/GaN multiple quantum well nanopillar structures to green-, yellow- and red-emitting CdSe/ZnS core/shell nanocrystal quantum dots. We observed fast

nonradiative exciton transfer from blue-emitting InGaN/GaN MQW-NPs to red-emitting CdSe/ZnS nanocrystals with a rate of $(0.192\ ns)^{-1}$. Furthermore, we showed tuning of the energy transfer rate to $(0.237\ ns)^{-1}$ and $(0.253\ ns)^{-1}$ for the yellow- and green-emitting CdSe/ZnS core/shell nanocrystals integrated layers, respectively. In all of these hybrid cases, 41%-39% of the generated electron-hole pairs in the NPs are found to be transferred to the nanocrystals. Our calculated and measured ET rates are in good agreement.

7.3 Observation of efficient transfer from Mott-Wannier to Frenkel excitons at room temperature in a hybrid semiconductor quantum dot/polymer composite

This section is based on the publication "Observation of efficient transfer from Mott-Wannier to Frenkel excitons at room temperature in a hybrid semiconductor quantum dot/polymer composite" **S. Nizamoglu**, X. W. Sun and H. V. Demir, Applied Physics Letters 97, 263106 (2010). Reproduced (or 'Reproduced in part') with permission from American Institute of Physics. Copyright 2010 American Institute of Physics.

Efficient conversion from Mott-Wannier to Frenkel excitons is observed at room temperature. The time-resolved photoluminescence shows that the energy transfer rate and efficiency reach 0.262 ns^{-1} and 80.9%, respectively. The energy transfer is enabled by strong dipole-dipole coupling in a hybrid inorganic/organic system of CdSe/ZnS core/shell heteronanocrystal and poly[2-methoxy-5-(3,7-dimethyl-octyloxy)-1,4-phenylenevinylene] MDMO-PPV homopolymer composite, and the measured energy transfer efficiencies are consistent with the analytical model.

7.3.1 Introduction

The Mott-Wannier (MW) and Frenkel (FR) excitons are the fundamental Coulomb-correlated light-generation tools in dielectric medium. The interactions of Mott-Wannier and Frenkel excitons provide opportunities in inorganic/organic composite devices [150], [151]. These interactions can be achieved either in a coherent or incoherent way [111]. For coherent coupling, the electron and hole wavefunctions in separate systems should strongly interact.

However, this condition requires a high degree of structural order. Alternatively, the other interaction channel is the incoherent coupling of Mott-Wannier and Frenkel excitons via Förster-type nonradiative energy transfer. Such NRET between organic/inorganic hybrids leads to a nonradiative conversion of Mott-Wannier excitons to Frenkel excitons. In a recent study, Blumentengel *et al*. showed this kind of exciton conversion process [150]. However, this process was observed only up to a maximum temperature of 100 K with a moderate energy transfer efficiency level of 50%; the energy transfer was terminated above 100 K because the excitons were reported to dissociate.

To make an efficient system, though, the energy transfer efficiency should be higher than 50% (*i.e.*, most of the excitons in inorganic substance should migrate to the organic domain) and this migration is desired to be achieved at room temperature for potential optoelectronic applications. But, efficient exciton conversion at room temperature has not been shown to date. To address this issue, in this section, we investigate and demonstrate a highly efficient conversion from Mott-Wannier to Frenkel excitons at room temperature. This opens up possibilities for high-efficiency hybrid inorganic/organic devices.

For efficient NRET, the energy transfer is expected to be comparable to or faster than the recombination lifetime of the donor. If this condition is satisfied, then a significant fraction of the excitation energy can possibly be transferred to the acceptor [152]. Thus, it is desired to select an inorganic material having Mott-Wannier-type excitons as the donor and organics with Frenkel-type excitons as the acceptor. Since inorganic semiconductor quantum dot nanocrystals show recombination lifetimes of tens of nanoseconds, they are suitable candidates as the donors for organic substances. Furthermore, the interface between the organic and inorganic materials is required to have a high purity and electronic perfection. If this condition is not satisfied, then the excitons can be trapped in defect states leading to nonradiative recombination. For strong energy transfer,

NCs and polymers are favorable candidates with their advantageous properties [8], [31], [45], [100], [101], [113], [130], [137], [138], [153].

7.3.2 Materials and spectroscopy

To compose a hybrid organic/inorganic structure with high NRET efficiency, we choose cyan-emitting CdSe/ZnS core/shell heteronanocrystal with Mott-Wannier excitons as donors and orange-emitting poly[2-methoxy-5-(3,7-dimethyl-octyloxy)-1,4-phenylenevinylene] MDMO-PPV homopolymer with Frenkel excitons as acceptors. Here it is worth mentioning that a true Mott-Wannier exciton refers to a hydrogen-like bound state intrinsically with its Bohr radius exceeding the crystal lattice constant. However, in our NCs investigated in this section, such a hydrogen-like bound state cannot truly exist because the exciton Bohr radius is comparable to the nanocrystal radius. Nevertheless, the bound electron-hole pair state in these quantum dots is characterized by strong Coulomb interaction, and the notion of exciton can be applied. The character of this Mott-Wannier-like exciton is still fundamentally different than that of a Frenkel exciton. This was previously discussed at length by Gaponenko [81], [154]. Throughout this section, with the term of Mott-Wannier exciton, we refer to Mott-Wannier-like exciton in a quantum dot.

The emission peak of the heteronanocrystals overlaps the absorption peak of the homopolymer, beneficial for efficient exciton migration (shown in Figure 7.3.1). We prepared thin films of hybrid inorganic/organic blends by spin-coating at 2,000 rpm on quartz substrates (with an acceleration of ca. 700 rpm/s). The homopolymer concentration was controlled with great care; the polymer concentrations were approximately 1.5×10^{17}, 2.9×10^{17}, 4.4×10^{17}, and 5.3×10^{17} cm^{-3} in Samples 1, 2, 3 and 4, respectively, and the heteronanocrystal concentration in all the samples was around 10^{18} cm^{-3}.

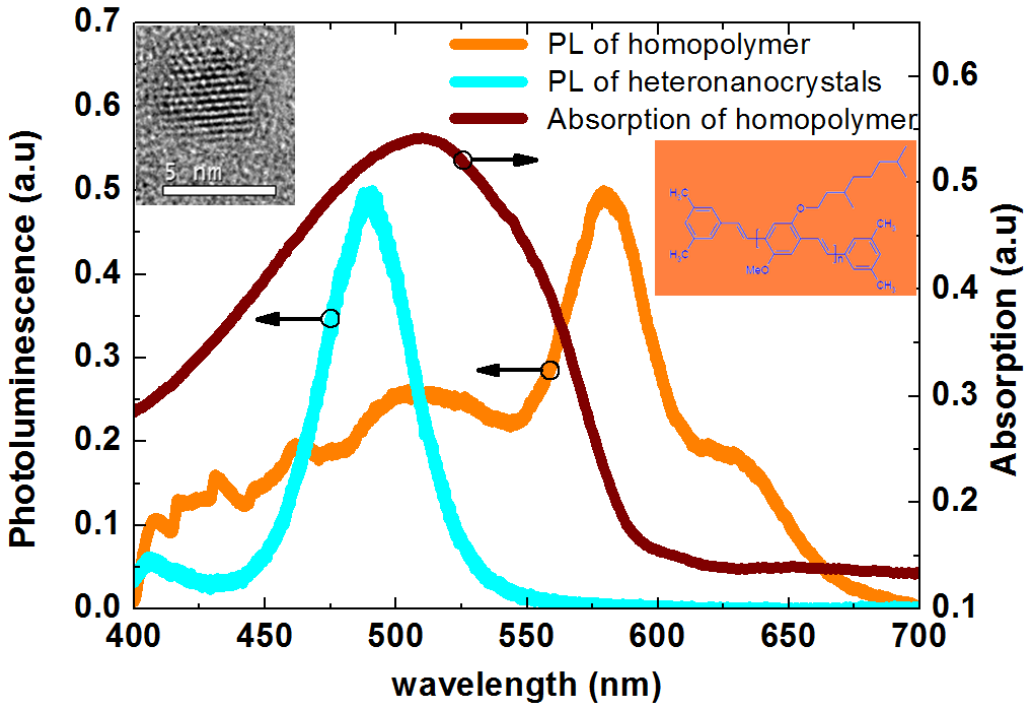

Figure 7.3.1 Absorption and photoluminescence spectra of MDMO-PPV homopolymer along with the PL spectrum of CdSe/ZnS core/shell heteronanocrystals. Inset: TEM (transmission electron microscopy) image of the heteronanocrystal and chemical structure of the homopolymer.

The response of the laser pulse on the photon multiplier tube is shown in the inset of Figure 7.3.2. The resolution of our experimental apparatus can be adjusted from 4 to 512 ps. For heteronanocrystals, we use a resolution of 32 ps, and for polymers, we use a resolution of 4 ps (because of their relatively fast decay). It is worth mentioning that the homopolymer also emits at around 495 nm (overlapping the NC emission), which could possibly affect the time-resolved behavior, but at the wavelength of 495 nm, the emission of the NCs is much stronger compared to the emission of the homopolymer (see the inset of Figure 7.3.3). So the lifetime of the heteronanocrystals can be clearly distinguished. For the data analysis, a multiexponential least-squares error model was adopted, which is convoluted with the laser diode response (instrument response function - IRF) as shown in Equation (7.3.1).

7.3.3 Results and discussion

Figure 7.3.2 shows the time-resolved spectroscopy of our hybrid homopolymer-heteronanocrystal composites along with that of NC-only solids on quartz substrates at the nanocrystal donor emission (495 nm). For the NC-only sample, we fit the photoluminescence decay using Equation (7.3.2) with a single lifetime component of 16.16 ns at room temperature (Table 7.3.1), which is the general lifetime of nanocrystals at room temperature (around tens of nanoseconds). This serves as the reference decay to distinguish the migration of excitons in the hybrid systems, which corresponds to a decay rate of 0.061 ns^{-1} (*i.e.*, $\Gamma_{nc} = 0.061$ ns^{-1}). In Sample 1, when the NCs are blended with MDMO-PPV homopolymers, the photoluminescence of NCs starts to quench because of the exciton migration from NCs to polymers. Thus, in addition to the interband recombination process, an extra decay component begins to be observed as shown in Equation (7.3.3) as a result of the nonradiative energy transfer in the hybrid inorganic-organic sample, where A_i, i=1,2, are the fitting amplitudes for lifetime components of τ_{NC} and τ_{NRET}.

$$I(t) = \int_{-\infty}^{t} IRF(t') \sum_{i=1}^{n} A_i e^{-\frac{(t-t')}{\tau_i}} dt' \qquad (7.3.1)$$

$$I_{ref}(t) = \int_{-\infty}^{t} IRF(t') \{A_1 e^{-\frac{(t-t')}{\tau_{NC}}}\} dt' \qquad (7.3.2)$$

$$I_{sample}(t) = \int_{-\infty}^{t} IRF(t`) \{A_1 e^{-\frac{(t-t`)}{\tau_{NC}}} + A_2 e^{-(\frac{1}{\tau_{NC}} + \frac{1}{\tau_{NRET}})(t-t`)}\} dt` \qquad (7.3.3)$$

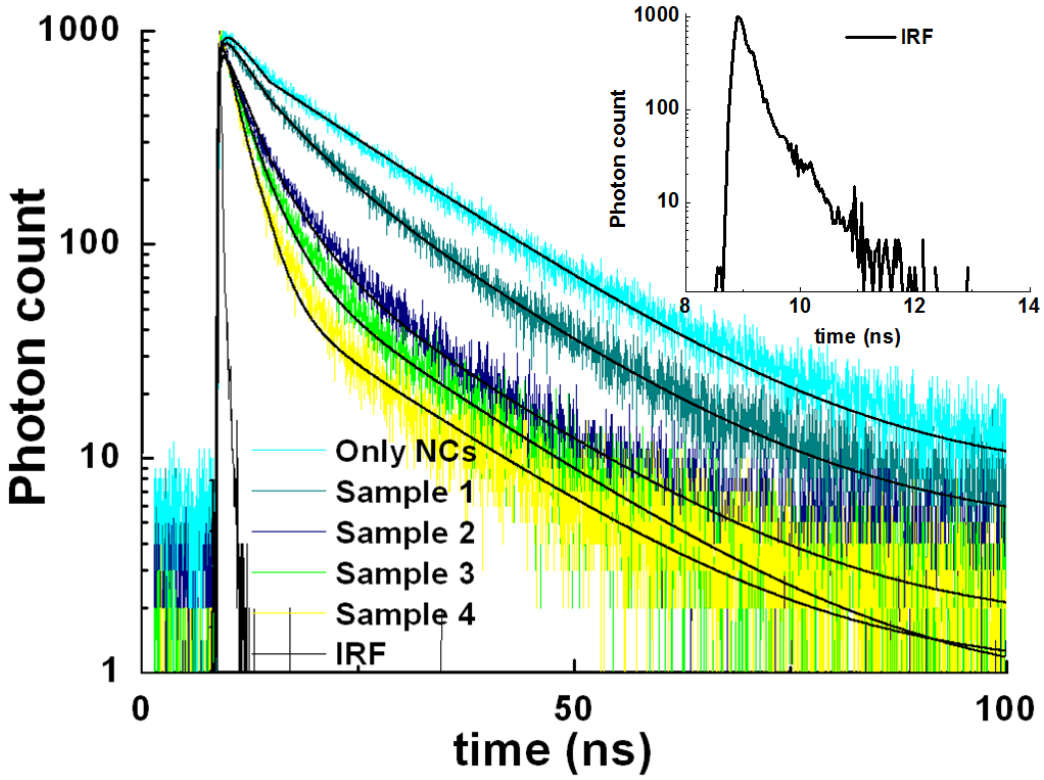

Figure 7.3.2 Time-resolved spectroscopy measurement at the peak heteronanocrystal emission wavelength (495 nm) for the hybrid composite system consisting of heteronanocrystals and homopolymers together (Samples 1-4), only nanocrystals on quartz substrate (only NCs) and instrument response function (IRF) of the laser diode at 375 nm using a time-correlated single photon counting (TCSPC) system of PicoHarp 300 with a time resolution of 32 ps at room temperature. The black lines are the fits as described in text.

For Sample 1, this additional lifetime component (*i.e.*, τ_2) is 7.00 ns, which is faster than the recombination lifetime of heteronanocrystals alone. This fast decay rate for Sample 1 (*i.e.*, $\Gamma_{sample1}$) becomes 0.142 ns^{-1} because of the energy transfer from NCs to homopolymers. We thus determine NRET rate as $\Gamma_{NRET} = \Gamma_{sample1} - \Gamma_{nc} = 0.142 - 0.061 = 0.081$ ns^{-1}. Furthermore, as the acceptor concentration increases in Samples 2, 3 and 4, the resulting quenching increases as well. Thus, this fast lifetime component compared with the recombination of heteronanocrystals is shifted from 7.00 to 5.87, 4.15 and 3.08 ns for Samples 2, 3 and 4 at room temperature as a result of the increased NRET from heteronanocrystals to homopolymers, respectively. The corresponding decay

rates for Samples 2 and 3 are 0.170 and 0.241 ns^{-1} and we extract their NRET rates 0.108 and 0.179 ns^{-1}, respectively. Finally, for Sample 4, the decay rate reaches a level of 0.324 ns^{-1}, achieving a NRET rate of 0.262 ns^{-1}. Furthermore, the relative amplitude A_2 arising from the energy transfer increases in comparison to that of the recombination component A_1 showing that the NCs with NRET becomes more dominant over the NCs without NRET (see Table 7.3.1 in the supplementary information). However, although we observe quenching in nanocrystals here, a possible question is whether the energy is really transferred to polymers or to the surface traps due to the defect states of nanocrystals. Therefore, one also needs to investigate the decay behavior of polymers.

Table 7.4.1 The multiexponential fitting parameters of only heteronanocrystal (only NCs) as the reference group and the hybrid composite systems consisting of both heteronanocrystals-homopolymers (Samples 1-4) at nanocrystal emission peak wavelength (λ=495 nm), presented along with their associated nonradiative energy transfer efficiency (η) and χ2.

	A_1	τ_1 (ns)	A_2	τ_2 (ns)	η	χ^2
Only NCs	1162.40	16.16	-	-	-	1.006
Sample 1	736.70	16.16	406.4	7.00	0.566	1.003
Sample 2	465.20	16.16	642.7	5.87	0.636	1.482
Sample 3	165.75	16.16	844.8	4.15	0.743	1.276
Sample 4	114.42	16.16	947.6	3.08	0.809	1.124

Figure 7.3.3 shows the time-resolved spectroscopy of our hybrid heteronanocrystal-homopolymer samples (from Sample 1 to Sample 4) and the case of only homopolymers at the polymer acceptor emission (585 nm). In the reference group, the lifetime decay of the MDMO-PPV homopolymers can be represented as biexponentials [155], with τ_1= 0.228 ns and τ_2=1.079 ns because of their Frenkel type excitonic behavior. Here the ultrafast recombination of polymers with lifetimes even shorter than 1 ns is mainly because of the strong electron and hole coupling. This enables the localization of their Frenkel-type exciton in one molecule, in contrast to the case of Mott-Wannier excitons where they can spread (delocalize) over many unit cells of the crystal in the quantum dot, so that their lifetimes are around tens of nanoseconds because of the weaker Coulomb attraction (<0.1 eV). As the acceptor homopolymer concentration increases in the composite, their lifetime increases in contrast to the decreasing lifetime of donor heteronanocrystals.

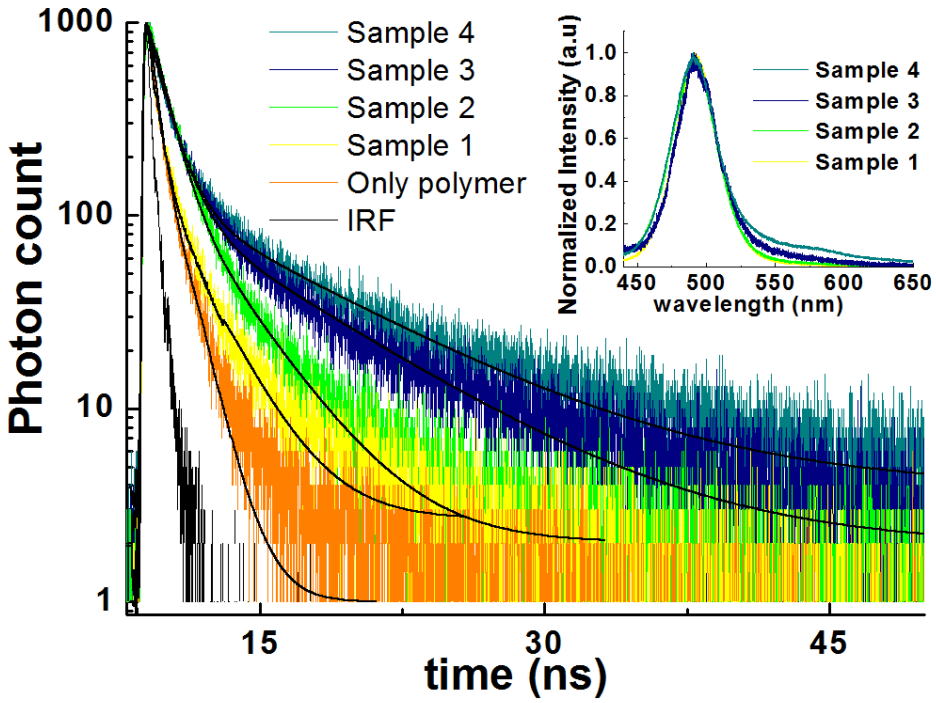

Figure 7.3.3 Time-resolved spectroscopy measurement at the peak homopolymer emission wavelength (585 nm) for the hybrid composite system consisting of heteronanocrystals and homopolymer together (Samples 1-4), only homopolymer on quartz substrate, and instrument response function (IRF) of the laser diode at 375 nm using a time-correlated single photon counting (TCSPC) system of PicoHarp 300 with a time resolution of 4 ps at room temperature and the steady-state photoluminescence from Samples 1 to 4 is given in the inset. The black lines are the fits as described in the text.

Moreover, in our hybrid system, this lifetime modification cannot be due to the charge transfer (*i.e.*, Dexter type transfer) because ZnS barriers (about three monolayers) in the core/shell heteronanocrystals provide full electronic isolation and prevent tunneling of the electron and hole wavefunctions [138]. Furthermore, in the inset of Figure 7.3.3, the steady-state luminescence of the heteronanocrystal-homopolymer composite is shown and the transfer is also visible in the luminescence spectra. From Sample 1 to 4, the emission above the wavelength 550 nm coming from the homopolymer is increasing, which is consistent with the decreasing donor lifetime and increasing acceptor lifetime. Thus, we can undoubtedly conclude that this is the result of Förster-type

nonradiative energy transfer from heteronanocrystals to homopolymers at room temperature.

Here the energy transfer efficiency was calculated $\eta=(\Gamma_{sample}-\Gamma_{NC})/\Gamma_{sample}=\Gamma_{NRET}/\Gamma_{sample}$ [91]. The efficiency for Sample 1 corresponds to 56.6%. As we increase the acceptor concentration for Samples 2, 3 and 4, the energy transfer efficiency increases to 63.6%, 74.3%, and finally 80.9%, respectively, and for all samples more than half of the excitation energy of heteronanocrystals is transferred to homopolymers at room temperature. Therefore, in our hybrid inorganic/organic structure, the energy is efficiently transformed from the weak Coulomb coupled carriers (Mott-Wannier excitons) to strong Coulomb coupled carriers (Frenkel excitons) at room temperature.

7.3.4 Analytical model

To investigate NRET efficiency (η) in our hybrid system, we applied an analytical. In a previous work, Zapunidi *et al.* studied quenching of steady-state photoluminescence of donors for varying donor concentration via NRET [156]. Using both NRET among heteronanocrystals and NRET between heteronanocrystal and homopolymer in our case, we derived the equation for η given in Equation (7.3.4).

$$\eta = 1 - \frac{1}{B^2 - 1}\left(\frac{B^2 + (Cq)^2}{1 + (Cq)^2} \exp\left\{ Cq\pi\left(\frac{1}{B} - 1\right) + 2Cq\left[\arctan(Cq) - \frac{\arctan(Cq/B)}{B} \right] \right\} - 1 \right) \tag{7.3.4}$$

where $C = \frac{4\pi R_o^{\,3}}{3}\sqrt{Q}$, and R_o is the Förster radius for the heteronanocrystal-homopolymer interaction, q is the homopolymer concentration, Q is the quantum efficiency of the heteronanocrystal, and B is the parameter representing the strength of NRET between heteronanocrystals (*i.e.*, if NRET among heteronanocrystals is weak, then $B \rightarrow 1$ and if NRET between heteronanocrystals is strong, then $B \rightarrow \infty$). The quantum efficiency of heteronanocrystals is 0.4 and

the Förster radius between heteronanocrystal and homopolymer is 9 x 10^{-7} cm. Figure 7.3.4 shows the calculated and measured NRET efficiencies for different B values, which shows the strength of NRET among NCs. As shown in the figure as the polymer concentration increases, the NRET efficiency becomes closer to B→1 because the intra-dot energy transfer becomes weaker due to the increased polymer concentration. It can be observed that the experimental results are consistent with the calculated NRET efficiencies, confirming the measured efficiencies and analytical model.

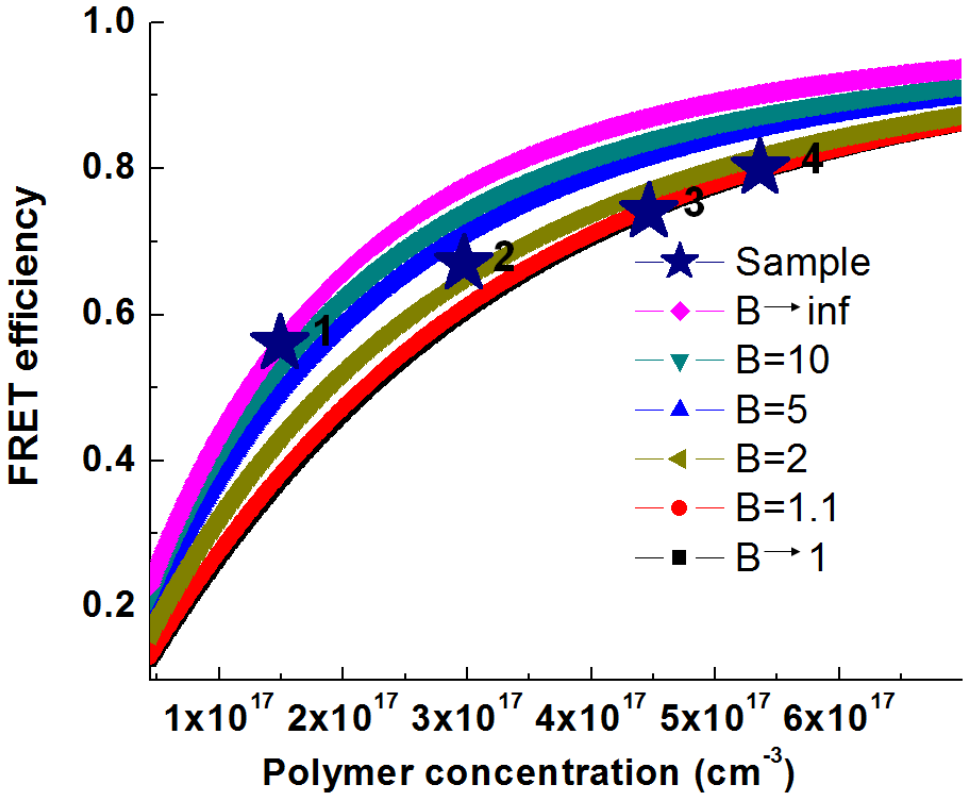

Figure 7.3.4 Calculated NRET efficiencies using the analytical model for different B values and measured NRET efficiencies.

7.4.5 Conclusion

In this section, efficient conversion from Mott-Wannier to Frenkel excitons at room temperature has been demonstrated by NRET using a hybrid composite system composed of CdSe/ZnS core/shell heteronanocrystals and MDMO-PPV homopolymers. NRET rate of 0.262 ns^{-1} and an efficiency of 80.9% were

realized. These experimental demonstrations undertaken at room temperature indicate that efficient excitonic interactions of Mott-Wannier and Frenkel excitons are possible in such inorganic/organic hybrids and hold great promise for future hybrid solid state devices.

Chapter 8

Conclusions

Around the world, about one fifth of the global electricity production is currently consumed for lighting. Significant amount of energy saving and carbon emission reduction can be achieved if light emitting diodes meet target device performance and replace the conventional light sources. Because of its economic and environmental potential, solid state lighting has attracted enormous interest both in academia and industry in the past two decades.

To date different approaches of solid state lighting including monolithic, multi-chip and color-conversion white LEDs have extensively been investigated. Among them, the phosphor based color conversion approach has drawn significant attention. However, there exist major drawbacks to use phosphor-based light emitting diodes. Phosphors do not allow for optimal photometric design due to their broad emission covering from blue to red. It is difficult to fully tune the properties of the generated white light, as is required to achieve optimal lighting conditions specific to particular applications (*e.g.,* indoors lighting, street lighting).

Alternatively, we proposed, developed and demonstrated a new class of white light emitting diodes integrated with nanophosphors of semiconductor

nanocrystals for efficient and high-quality lighting. Furthermore, we investigated novel device and hybrid structure designs using Förster-type nonradiative resonance energy transfer.

To summarize, in this thesis work,

- We experimentally showed nanocrystal hybridized white LEDs with high performance, which exhibit a high luminous efficacy of optical radiation exceeding 350 lm/W_{opt} and a high color rendering index close to 90 at a low correlated color temperature <3000 K. According to the best of our knowledge, these nanocrystal integrated white LEDs achieve the best photometric performance ever reported to date, outperforming conventional phosphor powders.

- To increase the rod activity and energy efficiency, we demonstrated scotopically-enhanced white LEDs leading to tristimulus coordinates *(x,y)*=(0.251,0.246), *LER*=266.83 lm/W_{opt}, *S/P*=3.04, *CRI*=71.7, and *CCT*=45 kK. This white light spectrum satisfies both of the figure-of-merits simultaneously for scotopic enhancement and reasonable color rendering for the first time, by achieving an *S/P* ratio above the *S/P*=2.50 barrier.

- We quantum-mechanically investigated multi-color spontaneous emission from quantum-dot-quantum-well heteronanocrystals made of onion-like (CdSe)ZnS/CdSe/ZnS (core)shell/shell/shell structures, with our theoretical results explaining experimental measurements for the first time. We discovered that the carrier localization is tuned from type-I-like to type-II-like localization by controlling CdSe and ZnS shell thicknesses, and that three-monolayer ZnS barriers are not necessarily sufficient for carrier localization, unlike in conventional (CdSe)ZnS (core)shell structures. Exciton localization in distinct layers of (CdSe)ZnS/CdSe/ZnS heteronanocrystals with high transition

probability (for n=1 states in CdSe core and n=2 states in CdSe shell) is key to their multi-color emission.

- We investigated energy gradient mixture of nanocrystal solids for recycling their trapped excitons by varying their donor-acceptor nanocrystal ratios and study the resulting quantum efficiency enhancement as a function of the donor-acceptor ratio in the solid film for hybrid LEDs. We achieved a maximum quantum efficiency enhancement of 17% in these nanocrystal solids when the donor-acceptor ratio is 1:1, demonstrating their highly-modified time-resolved photoluminescence decays to reveal the kinetics of strong energy transfer between them.

- We demonstrated the first nanocrystal hybridized light emitting diodes with enhanced color conversion and efficiency via recycling of trapped excitons.

- We showed white light generation based on nonradiative pumping of nanocrystals by quantum wells.

- To enhance the color conversion via NRET, we hybridized nanocrystals with multiple quantum well nanopillars and exhibited that energy transfer efficiency increased to 83%.

- We reported on Förster-type nonradiative resonance energy transfer directed from colloidal quantum dots (QDs) to epitaxial quantum wells (QWs) with an efficiency of 69.6% at a rate of 1.527 ns^{-1} for potential application in III-nitride based photovoltaics.

- We investigated and observed efficient energy conversion from Mott-Wannier to Frenkel excitons at room temperature in a hybrid semiconductor quantum dot/polymer with an transfer rate and efficiency that reach 0.262 ns^{-1} and 80.9%, respectively.

8.1 Innovation and impact

Our research work has innovatively contributed to color-conversion LEDs in major directions. We proposed, developed and demonstrated this new class of white LEDs based on nanophosphors of semiconductor nanocrystal quantum dots for efficient and high-quality lighting. For that, new simulation models have been developed, InGaN/GaN LEDs have been designed and fabricated, semiconductor nanocrystals (using hot injection method) have been synthesized and hybridized on LEDs, and these white LEDs have been characterized and tested. Furthermore, these nanocrystal emitters have been quantum mechanically simulated to be integrated on LEDs and the color rendering and efficiency optimization of these color conversion nanocrystal-LEDs have been studied.

This research work has led to successful demonstrators of semiconductor nanophosphors of colloidal quantum dots that photometrically outperform conventional phosphor powders in terms of color rendering, luminous efficacy of optical radiation, color temperature and scotopic/photopic ratio for the first time. These results indicate that such nanophosphors hold great promise for use in future high-quality solid state lighting and displays.

We proposed in 2005 and showed in 2006 that nanocrystal integrated LEDs hold great promise for lighting, which appeared and was highlighted on the front cover of Nanotechnology in 2007 [45]. Today in 2011, such hybrid LED products are on the market and there is an increasing commercial interest in these light emitting diodes by companies including Samsung, QD Vision, Lemnis Lighting, Nanoco Group PLC and others.

Novel light emitting device designs are also significant for adding new and superior functions to hybrid LEDs. We used Förster-type nonradiative energy transfer to realize novel hybrid systems. By using this energy transfer process, we showed enhanced color conversion via recycling of trapped excitons in

nanocrystals and demonstrated nonradiative pumping of nanocrystal quantum dots for color conversion. Furthermore, according to the best of our knowledge, we observed the first efficient energy conversion from Mott-Wannier to Frenkel excitons at room temperature.

As a result of this work, I received the Photonics21 Student Innovation Award by The European Commission Technology Platform of Photonics21, IEEE Photonics Society Graduate Student Fellowship, and SPIE Scholarship Award in Optical Science and Engineering. We published over 30 journal articles in major science-citation index journals including Applied Physics Letters, Optics Letters, Optics Express, ACS Nano, Nanotechnology, Journal of Applied Physics, New Journal of Physics, and IEEE Journal of Special Topics in Quantum Electronics. One of this research work entitled "White Light Generation Using CdSe/ZnS Core-Shell Nanocrystals Hybridized with InGaN/GaN Light Emitting Diodes" has been highlighted as a featured article on the front cover of the scientific journal Nanotechnology [45]. We presented more than 40 invited and contributed, refereed international conference talks and submitted 2 patent applications.

BIBLIOGRAPHY

[1] The Promise of Solid State Lighting for General Illumination Light Emitting Diodes (LEDs) and Organic Light Emitting Diodes (OLEDs), Optoelectronics Industry Development Association, Washington, DC http://www.netl.doe.gov/ssl/PDFs/oida_led-oled_rpt.pdf,

[2] M. R. Krames, O. B. Shchekin, R. Mueller–Mach, G. O. Mueller, L. Zhou, G. Harbers and M. G. Craford, "Status and Future of High-Power Light-Emitting Diodes for Solid-State Lighting," *Journal of Display Technology,* **3**, 160-175 (2007).

[3] S. Pimputkar, J. S. Speck, S. P. DenBaars and S. Nakamura, "Prospects for LED lighting," *Nature Photonics*, **3**, 180-182 (2009).

[4] E. F. Schubert, "Light-Emitting Diodes," Cambridge University Press, (2006).

[5] M.Yamada, Y. Narukawa, H. Tamaki, Y. Murazaki and T. Mukai, "A methodological study of the best solution for generating white light," *IEICE Transactions on Electronics*, **E88-C**, 1860-1871 (2005).

[6] H. Chen, D. Yeh, C. Lu, C. Huang, W. Shiao, J. Huang, C. C. Yang, I. Liu and W. Su, "White Light Generation With CdSe–ZnS Nanocrystals Coated on an InGaN–GaN Quantum-Well Blue/Green Two-Wavelength Light-Emitting Diode," *IEEE Photonics Technology Letters*, **18**, 1430 (2006).

[7] S. Nakamura and G. Fasol, "The Blue Laser Diode," Springer, (1997).

[8] G. Heliotis, E. Gu, C. Griffin, C. W. Jeon, P. N. Stavrinou, M. D. Dawson and D. D. C. Bradley, "Wavelength-tunable and white-light emission from polymer-converted micropixellated InGaN ultraviolet light-emitting diodes," *Journal of Optics A: Pure and Applied Optics*, **8**, 445 (2006).

[9] J. Y. Tsao, "Solid-state lighting: lamps, chips, and materials for tomorrow," *IEEE Circuits Devices Magazine*, **20**, 28-37 (2004).

[10] S. V. Gaponenko, U. Woggon, M. Saleh, W. Langbein, A. Uhrig and C. Klingshirn, "Nonlinear-optical properties of semiconductor quantum dots and their correlation with the precipitation stage," *Journal of Optical Society America B,* **10**, 1947 (1993).

[11] A. P. Allivisatos, "Semiconductor Clusters, Nanocrystals, and Quantum Dots," *Science,* **271**, 933 – 937 (1996).

[12] D. B. Judd, "Report of US Secretariat Committee on Colorimetry and Artificial Daylight," *Proceedings of the 12th Session of the CIE,* **1**, 11 (1951).

[13] J. J. Vos, "Colorimetric and photometric properties of a 2-degree fundamental observer," *Color Research & Application,* **3**, 125 (1978).

[14] G. Wyszecki and W. S. Stiles, "Color Science – Concepts and Methods, Quantitative Data and Formulae," *John Wiley and Sons, 2nd edition,* (2000).

[15] CIE, "Method of Measuring and Specifying Color-Rendering of Light Sources " *CIE publication,* 13.13 (1995).

[16] Y. Ohno, "Color Rendering and Luminous Efficacy of White LED Spectra," *Proceedings of SPIE,* **5530**, 88-98 (2004).

[17] Y. Ohno, "Spectral Design Considerations for Color Rendering of White LED Light Sources,"*Optical Engineering,* **44**, 111302 (2005).

[18] W. Davis and Y. Ohno, "Toward an Improved Color Rendering Metric," *Proceedings of SPIE,* **5941**, 59411G (2005).

[19] PNNL, "Spectrally enhanced lighting program implementation for energy savings: Field evaluation," 1-118 (2006).

[20] S. M. Berman, G. Fein, D. L. Jewett, B. R. B. T. M. Law, A. W. Myers and M. A. Bullimore, "Lighting spectral effects on Landolt C performance is enhanced by blur and abolished by mydriasis," *Journal of the Illuminating Engineering Society,* **25**, 42- 50 (1996).

[21] S. M. Berman, G. Fein, D. L. Jewett, B. R. Benson, T. M. Law and A. W. Myers, "Luminance controlled pupil size affects word reading accuracy," *Journal of the Illuminating Engineering Society,* **25**, 51-59 (1996).

[22] S. M. Berman, G. Fein, D. L. Jewett and F. Ashford, "Luminance controlled pupil size affects Landolt C test performance," *Journal of the Illuminating Engineering Society*, **22**, 150-165 (1993).

[23] S. M. Berman, G. Fein, D. L. Jewett and F. Ashford, "Landolt C recognition in elderly subjects is affected by scotopic intensity of surround illuminants," *Journal of the Illuminating Engineering Society*, **23**, 123-130 (1994).

[24] S. M. Berman, "Energy efficiency consequences of scotopic sensitivity," *Journal of the Illuminating Engineering Society*, **21**, 1 (1992).

[25] CIE, "Recommended system for mesopic photometry based on visual performance," *CIE Technical Report 191:2010*, (2010).

[26] K. Lewotsky, "Solid-state lighting faces challenges, opportunities in industrial applications," *SPIE Newsroom*, (2006).

[27] M. Arik, J. Petroskf and S. Weavery, "Thermal challenges in the future generation solid state lighting applications: light emitting diodes," *Inter Society Conf. on Thermal Phenomena*, 112-120 (2002).

[28] S. N. Lee, H. S. Paek, H. Kim, T. Jang and Y. Park, "Monolithic InGaN-based white light-emitting diodes with blue, green, and amber emissions," *Applied Physics Letters*, **92**, 081107 (2008).

[29] *Alexa Fluor, http://www.invitrogen.com/site/us/en/home/References/Molecular-Probes-The-Handbook/Fluorophores-and-Their-Amine-Reactive-Derivatives/Alexa-Fluor-Dyes-Spanning-the-Visible-and-Infrared-Spectrum.html#head4*.

[30] *American dye source Inc., http://www.adsdyes.com/*.

[31] M. Achermann, M. A. Petruska, S. A. Crooker and V. I. Klimov, "Picosecond energy transfer in quantum dot Langmuir-Blodgett nanoassemblies," *Journal of Physical Chemistery B*, **107**, 13782 (2003).

[32] W. Tan, X. Fang, J. Li and X. Liu, "Molecular Beacons: A Novel DNA Probe for Nucleic Acid and Protein Studies," *Chemistry - A European Journal*, **6**, 1107–1111 (2000).

[33] T. W. Gadella, G. N. Krogt and T. Bisseling, "GFP-Based FRET Microscopy in Living Plant Cells," *Trends in Plant Science,* **4**, 287–291 (1999).

[34] J. Yuan, L. Peng, B. E. Bouma and G. J. Tearney, "Quantitative FRET measurement by high-speed fluorescence excitation and emission spectrometer," *Optics Express,* **18**, 18839-18851 (2010).

[35] J. R. Lakowicz, "Principles of Fluorescence Spectroscopy ", Springer, (2006).

[36] B. O. Dabbousi, J. Rodriguez-Viejo, F. V. Mikulec, J. R. Heine, H. Mattoussi, R. Ober, K. F. Jensen and M. G. Bawendi, "(CdSe)ZnS Core-Shell Quantum Dots: Synthesis and Optical and Structural Characterization of a Size Series of Highly Luminescent Materials," *Journal of Physical Chemistry B,* **101**, 9463-9475 (1997).

[37] D. Dorfs and A. Eychmüller, "Multishell Semiconductor Nanocrystals," *Zeitschrift für Physikalische Chemie,* **220**, 1539-1552 (2006).

[38] A. L. Rogach, "Semiconductor Nanocrystal Quantum Dots: Synthesis, Assembly, Spectroscopy and Application," Springer, (2008).

[39] S. A. Ivanov, A. Piryatinski, J. Nanda, S. Tretiak, K. R. Zavadil, W. O. Wallace, D. Werder and V. I. Klimov, "Type-II core/shell CdS/ZnSe nanocrystals: synthesis, electronic structures, and spectroscopic properties," *Journal of American Chemical Society,* **129**, 11708-11719 (2007).

[40] A. Piryatinski, S. A. Ivanov, S. Tretiak and V. I. Klimov, "Effect of quantum and dielectric confinement on the exciton-exciton interaction energy in type II core/shell semiconductor nanocrystals," *Nano Letters,* **7**, 108-115 (2007).

[41] V. L. Colvin, M. C. Schlamp and A. P. Alivisatos, "Light-Emitting-Diodes Made from Cadmium Selenide Nanocrystals and a Semiconducting Polymer," *Nature,* **370**, 354-357 (1994).

[42] R. Osovsky, D. Cheskis, V. Kloper, A. Sashchiuk, M. Kroner and E. Lifshitz, "Continuous-Wave Pumping of Multiexciton Bands in the

Photoluminescence Spectrum of a Single CdTe-CdSe Core-Shell Colloidal Quantum Dot," *Physical Review Letters,* **102,** 197401 (2009).

[43] C. B. Murray, C. R. Kagan and M. G. Bawendi, "Synthesis and characterization of monodisperse nanocrystals and close-packed nanocrystal assemblies," *Annual Review of Materials Science,* **30**, 545-610 (2000).

[44] S. V. Gaponenko, "Introduction to Nanophotonics," Cambridge University Press, (2010).

[45] S. Nizamoglu, T. Ozel, E. Sari and H. V. Demir, "White light generation using CdSe/ZnS core-shell nanocrystals hybridized with InGaN/GaN light emitting diodes," *Nanotechnology,* **18**, 065709 (2007).

[46] W. W. Yu, L. Qu, W. Guo and X. Peng, "Experimental Determination of the Extinction Coefficient of CdTe, CdSe, and CdS Nanocrystals," *Chemical Materials*, **15**, 2854-2860 (2003).

[47] S. Sapra and D. D. Sarma, "Evolution of the electronic structure with size in II-VI semiconductor nanocrystals," *Phyical Review B,* **69**, 125304 (2004).

[48] Y. Chen, J. Vela, H. Htoon, J. L. Casson, D. J. Werder, D. A. Bussian, V. I. Klimov and J. A. Hollingsworth, ""Giant" multishell CdSe nanocrystal quantum dots with suppressed blinking," *Journal of American Chemical Society,* **130**, 5026–5027 (2008).

[49] L. Qu, Z. A. Peng and X. G. Peng, "Alternative Routes toward High Quality CdSe Nanocrystals," *Nano Letters,* **1**, 333 (2001).

[50] R. Viswanatha, S. Sapra, T. Saha-Dasgupta and D. D. Sarma, "Electronic structure of and quantum size effect in III-V and II-VI semiconducting nanocrystals using a realistic tight binding approach," *Phyical Review B,* **72**, 045333 (2005).

[51] S. Sapra, S. Mayilo, T. A. Klar, A. L. Rogach and J. Feldmann, "Bright white light emission from semiconductor nanocrystals: by chance and by design," *Advanced Materials,* **19**, 569 (2007).

[52] F. Koberling, U. Kolb, G. Philipp, I. Potapova, T. Basche and A. Mews, "Fluorescence Anisotropy and Crystal Structure of Individual Semiconductor Nanocrystals," *Journal of Physical Chemistery B,* **107**, 7463-7471 (2003).

[53] M. G. Burt, "The justification for applying the effective-mass approximation to microstructures," *Journal of Physics: Condensed Matter*, **4**, 6651 (1992).

[54] A. Eychmüller, A. Mews and H. Weller, "A Quantum Dot Quantum Well: CdS/HgS/CdS," *Chemical Physics Letters,* **208**, 59 (1993).

[55] D. Dorfs, H. Henschel, J. Kolny and A. Eychmuller, "Multilayered Nanoheterostructures: Theory and Experiment," *Journal of Physical Chemistery B,* **108**, 1578 (2004).

[56] V. I. Klimov, S. A. Ivanov, J. Nanda, M. Achermann, I. Bezel, J. A. McGuire and A.Piryatinski, "Single-exciton optical gain in semiconductor nanocrystals," *Nature*, **447**, 441 (2007).

[57] L. P. Balet, S. A. Ivanov, A. Piryatinski, M. Achermann and V. I. Klimov, "Inverted core/shell nanocrystals continuously tunable between Type-I and Type-II localization regimes," *Nano Letters*, **4**, 1485 (2004).

[58] D. Schoss, A. Mews, A. Eychmüller and H. Weller, "The Quantum Dot Quantum Well CdS/HgS/CdS: Theory and Experiment," *Physical Review B,* **49**, 24 (1994).

[59] X. G. Peng, M. C. Schlamp, A. V. Kadavanich and A. P. Alivisatos, "Epitaxial Growth of Highly Luminescent CdSe/CdS Core/Shell Nanocrystals with Photostability and Electronic Accessibility," *Journal of the American Chemical Society*, **119**, 7019 (1997).

[60] K. Chang and J. Xia, "Spatially separated excitons in quantum-dot quantum well structures," *Physical Review B,* **57**, 16 (1998).

[61] U. Hotje, C. Rose and M. Binnewies, "Lattice constants and molar volumes in the system ZnS, ZnSe, CdS, CdSe," *Surface State Sciences,* **5**, 1259 (2003).

[62] S. Q. Wang, "First-principles study of the anisotropic thermal expansion of wurtzite ZnS," *Applied Physics Letters,* **88**, 061902 (2006).

[63] Picoquant, http://www.picoquant.com/

[64] H. Chen, C. Hsu and H. Hong, "InGaN-CdSe-ZnSe Quantum Dots White LEDs," *IEEE Photonics Technology Letters*, **18**, 193 (2006).

[65] H. V. Demir, S. Nizamoglu, T. Ozel, E. Mutlugun, I. O. Huyal, E. Sari, E. Holder and N. Tian, "White light generation tuned by dual hybridization of nanocrystals and conjugated polymers," *New Journal of Physics,* **9**, 362 (2007).

[66] M. Ali, S. Chattopadhyay, A. Nag, A. Kumar, S. Sapra, S. Chakraborty and D. D.Sarma, "White light emission from a blend of CdSeS nanocrystals of different Se:S ratio," *Nanotechnology,* **18**, 075401 (2007).

[67] S. Nizamoglu and H. V. Demir, "Nanocrystal based hybrid white light generation with tunable color parameters," *Journal of Optics A: Pure and Applied Optics,* **9**, S419-S424 (2007).

[68] S. Nizamoglu and H. V. Demir, "Hybrid white light sources based on layer-by-layer assembly of nanocrystals on near-UV emitting diodes," *Nanotechnology*, **18**, 405702 (2007).

[69] E. Sari, S. Nizamoglu, T. Ozel and H. V. Demir, "Blue quantum electroabsorption modulators based on reversed quantum confined Stark effect with blue shift," *Applied Physics Letters,* **90**, 011101 (2007).

[70] V. A. Sabnis, H. V. Demir, O. Fidaner, J. S. Harris, D. A. B. Miller, J. F. Zheng, N. Li, T. C. Wu, H. T. Chen and Y. M. Houng, "Optically-controlled electroabsorption modulators for unconstrained wavelength conversion," *Applied Physics Letters,* **84**, 469-471 (2004).

[71] H. V. Demir, V. A. Sabnis, J. F. Zheng, O. Fidaner, J. S. Harris and D. A. B. Miller, "Scalable wavelength-converting crossbar switches," *IEEE Photonics Technology Letters,* **16**, 2305-2307 (2004).

[72] J. M. Phillips, M. E. Coltrin, M. H. Crawford, A. J. Fischer, M. R. Krames, R. Mueller-Mach, G. O. Mueller, Y. Ohno, L. E. S. Rohwer, J. A. Simmons and J. Y. Tsao, "Research challenges to ultra-efficient

inorganic solid-state lighting," *Laser & Photonics Reviews,* **1**, 307-333 (2007).

[73] J. Y. Tsao, "Ultra-Efficient Solid-State Lighting: Performance Frontier, Progress, Challenges," *The 21st Annual Meeting of The IEEE Lasers & Electro-Optics Society Conference Proceedings,* **WU4**, (2008).

[74] A. Žukauskas, R. Vaicekauskas, F. Ivanauskas, R. Gaska and M. S. Shur, "Optimization of white polychromatic semiconductor lamps," *Applied Physics Letters,* **80**, 234-236 (2002).

[75] T. Erdem, S. Nizamoglu, X. W. Sun and H. V. Demir, "A photometric investigation of ultra-efficient LEDs with high color rendering index and high luminous efficacy employing nanocrystal quantum dot luminophores," *Optics Express,* **18**, 340-347 (2010).

[76] S. Nizamoglu, G. Zengin and H. V. Demir, "Color-converting combinations of nanocrystal emitters for warm-white light generation with high color rendering index," *Applied Physics Letters,* **92**, 031102 (2008).

[77] S. M. Berman, M. Navvab, M. J. Martin, J. Sheedy and W. Tithof, "A comparison of traditional and high colour temperature lighting on the near acuity of elementary school children," *Lighting Research and Technology,* **38**, 41-52 (2006).

[78] J. A. Borton and K. A. Daley, "A comparision of light sources for the petrochemical industry," *IEEE Industry Application Magazine,* **3**, 54-62 (1997).

[79] D. J. Norris and M. G. Bawendi, "Measurement and assignment of the size-dependent optical spectrum in CdSe quantum dots," *Physical Review B,* **53**, 16338-16346 (1996).

[80] V. I. Klimov, "Semiconductor and Metal Nanocrystals: Synthesis and Electronic and Optical Properties," Marcel Dekker, (2003).

[81] S. V. Gaponenko, "Optical properties of semiconductor nanocrystals," Cambridge University Press, (1998).

[82] V. I. Klimov, A. A. Mikhailovsky, D. W. McBranch, C. A. Leatherdale and M. G. Bawendi, "Quantization of multi-particle Auger rates in semiconductor quantum dots," *Science,* **287**, 1011-1013 (2000).

[83] U. Banin, "Light-Emitting Diodes - Bright and Stable," *Nature Photonics,* **2**, 209-210 (2008).

[84] J. M. Caruge, J. E. Halpert, V. Wood, V. Bulovic and M. G. Bawendi, "Colloidal quantum-dot light-emitting diodes with metal-oxide charge transport layers," *Nature Photonics,* **2**, 247-250 (2008).

[85] Q. Sun, Y. A. Wang, L. S. Li, D. Wang, T. Zhu, J. Xu, C. Yang and Y. Li, "Bright, multicoloured light-emitting diodes based on quantum dots," *Nature Photonics,* **1**, 717-722 (2007).

[86] P. O. Anikeeva, J. E. Halpert, M. G. Bawendi and V. Bulovic, "Electroluminescence from a mixed red-green-blue colloidal quantum dot monolayer," *Nano Letters,* **7**, 2196-2200 (2007).

[87] N. Tessler, V. Medvedev, M. Kazes, S. Kan and U. Banin, "Efficient Near-Infrared Polymer Nanocrystal Light-Emitting Diodes," *Science,* **295**, 1506-1508 (2002).

[88] S. Nizamoglu, E. Sari, J.-H. Baek, I.-H. Lee and H. V. Demir, "White light generation by resonant nonradiative energy transfer from epitaxial InGaN/GaN quantum wells to colloidal CdSe/ZnS core/shell quantum dots," *New Journal of Physics,* **10**, 123001 (2008).

[89] B. Guilhabert, D. Elfström, A. J. C. Kuehne, D. Massoubre, H. X. Zhang, S. R. Jin, A. R. Mackintosh, E. Gu, R. A. Pethrick and M. D. Dawson, "Integration by self-aligned writing of nanocrystal/epoxy composites on InGaN micropixelated light-emitting diodes," *Optics Express,* **16**, 18933 (2009).

[90] R. D. Schaller, J. M. Pietryga, S. V. Goupalov, M. A. Petruska, S. A. Ivanov and V. I. Klimov, "Breaking the phonon bottleneck in semiconductor nanocrystals via multiphonon emission induced by intrinsic nonadiabatic interactions," *Physical Review Letters,* **95**, 196401 (2005).

[91] M. Achermann, M. A. Petruska, S. Kos, D. L. Smith, D. D. Koleske and V. I. Klimov, "Energy-transfer pumping of semiconductor nanocrystals using an epitaxial quantum well," *Nature,* **429**, 642-646 (2004).

[92] E. Mutlugun, I. M. Soganci and H. V. Demir, "Nanocrystal hybridized scintillators for enhanced detection and imaging on Si platforms in UV," *Optics Express,* **15**, 1128-1134 (2007).

[93] I. M. Soganci, S. Nizamoglu, E. Mutlugun, O. Akin and H. V. Demir, "Localized plasmon-engineered spontaneous emission of CdSe/ZnS nanocrystals closely-packed in the proximity of Ag nanoisland films for controlling emission linewidth, peak, and intensity," *Optics Express,* **15**, 14289-14298 (2007).

[94] D. Battaglia, J. J. Li, Y. Wang and X. Peng, "Colloidal two-dimensional systems: CdSe quantum shells and wells," *Angewandte Chemie International Edition,* **42**, 5035-5039 (2003).

[95] R. B. Little, M. A. El-Sayed, G. W. Bryant and S. J. Burke, "Formation of quantum-dot quantum-well heteronanostructures with large latticemismatch: ZnS/CdS/ZnS," *Chemical Physics,* **114**, 1813 (2001).

[96] S. A. Ivanov, J. Nanda, A. Piryatinski, M. Achermann, L. P. Balet, I. V. Bezel, P. O. Anikeeva, S. Tretiak and V. I. Klimov, "Light Amplification Using Inverted Core/Shell Nanocrystals: Towards Lasing in the Single-Exciton Regime," *Journal of Physical Chemistery B,* **108**, 10625 (2004).

[97] D. Battaglia, B. Blackman and X. Peng, "Coupled and Decoupled Dual Quantum Systems in One Semiconductor Nanocrystal," *Journal of American Chemical Society,* **127**, 10889 (2005).

[98] D. V. Talapin, A. L. Rogach, A. Kornowski, M. Haase and H. Weller, "Highly Luminescent Monodisperse CdSe and CdSe/ZnS Nanocrystals Synthesized in a Hexadecylamine – Trioctylphosphine Oxide – Trioctylphospine Mixture," *Nano Letters,* **1**, 207-211 (2001).

[99] R. C. Somers, M. G. Bawendi and D. G. Nocera, "CdSe nanocrystal based chem-/bio- sensors," *Chemical Society Reviews,* **36**, 579-591 (2007).

[100] V. Klimov, A. Mihkailovsky, S. Xu, A. Malko, J. Hollingsworth, C. Leatherdale and M. Bawendi, "Optical gain and stimulated emission in nanocrystal quantum dots," *Science,* **290**, 314–317 (2000).

[101] A. A. Chistyakov, I. L. Martynov, K. E. Mochalov, V. A. Oleinikov, S. V. Sizova, E. A. Ustinovich and K. V. Zakharchenko, "Interaction of CdSe/ZnS core-shell semiconductor nanocrystals in solid thin films," *Laser Physics,* **16**, 1625-1632 (2006).

[102] T. Ozel, E. Sari, S. Nizamoglu and H. V. Demir, "Violet to deep-ultraviolet InGaN/GaN and GaN/AlGaN quantum structures for UV electroabsorption modulators," *Journal of Applied Physics,* **102**, 113101 (2007).

[103] S. Nizamoglu, E. Mutlugun, T. Özel, H. V. Demir, S. Sapra, N. Gaponik and A. Eychmüller, "Dual-color emitting quantum-dot-quantum-well CdSe-ZnS heteronanocrystals hybridized on InGaN/GaN light emitting diodes for high-quality white light generation," *Applied Physics Letters,* **92**, 113110 (2008).

[104] A. L. Rogach, A. Eychmüller, S. G. Hickey and S. V. Kershaw, "Infrared emitting colloidal nanocrystals: synthesis, assembly, spectroscopy, and applications," *Small,* **3**, 536 (2007).

[105] J. H. Ahn, C. Bertoni, S. Dunn, C. Wang, D. V. Talapin, N. Gaponik, A. Eychmüller, Y. Hua, M. R. Bryce and M. C. Petty, "White Organic Light Emitting Devices Incorporating Nanoparticles of II-VI Semiconductors," *Nanotechnology,* **18**, 335202 (2007).

[106] I. Gur, N. A. Fromer, M. L. Geier and A. P. Alivisatos, "Air-Stable All-Inorganic Nanocrystal Solar Cells Processed from Solution," *Science,* **310**, 462-465 (2005).

[107] O. Kulakovich, N. Strekal, A. Yaroshevich, S. Maskevich, S. Gaponenko, I. Nabiev, U. Woggon and M. Artemyev, "Enhanced luminescence of CdSe quantum dots on gold colloids," *Nano Letters,* **2**, 1449-1452 (2002).

[108] T. A. Klar, T. Franzl, A. L. Rogach and J. Feldmann, "Super efficient exciton funneling in layer-by-layer semiconductor nanocrystal structures," *Advanced Materials,* **17***,* 769 (2005).

[109] C. R. Kagan, C. B. Murray, M. Nirmal and M. G. Bawendi, "Electronic Energy Transfer in CdSe Quantum Dot Solids," *Physical Review Letters,* **76**, 1517 (1996).

[110] C. R. Kagan, C. B. Murray and M. G. Bawendi, "Long Range Resonance Transfer of Electronic Excitations in Close Packed CdSe Quantum Dot Solids," *Physical Review B,* **54**, 8633-8643 (1996).

[111] S. A. Crooker, J. A. Hollingsworth, S. Tretiak and V. I. Klimov, "Spectrally resolved dynamics of energy transfer in quantum-dot assemblies: towards engineered energy flows in artificial materials," *Physical Review Letters,* **89**, 186802 (2002).

[112] T. Franzl, D. S. Koktysh, T. A. Klar, A. L. Rogach, J. Feldmann and N. Gaponik, "Fast energy transfer in layer-by-layer assembled CdTe nanocrystal bilayers," *Applied Physics Letters,* **84**, 2904 (2004).

[113] T. Franzl, A. Shavel, A. L. Rogach, N. Gaponik, T. A. Klar, A. Eychmüller and J. Feldmann, "High rate unidirectional energy transfer in directly assembled CdTe nanocrystal bilayers," *Small,* **1**, 392 (2005).

[114] T. Franzl, T. A. Klar, S. Schietinger, A. L. Rogach and J. Feldmann, "Exciton recycling in graded gap nanocrystal structures," *Nano Letters,* **4**, 1599 (2004).

[115] J. Malicka, I. Gryczynski, J. Fang, J. Kusba and J. R. Lakowicz, "Increased resonance energy transfer between fluorophores bound to DNA in proximity to metallic silver particles," *Analytical Biochemistery,* **315**, 160 (2003).

[116] S. J. Rosentha, "Bar-coding biomolecules with fluorescent nanocrystals," *Nature biotechnology,* **19**, 621 (2001).

[117] J. Kimura, S. Maenosono and Y. Yamaguchi, "Near-field optical recording on a CdSe nanocrystal thin film," *Nanotechnology,* **14**, 69 (2003).

[118] S. Maenosono, E. Ozaki, K. Yoshie and Y. Yamaguchi, "Nonlinear photoluminescence behavior in closely packed CdSe nanocrystal thin films," *Japanese Journal of Applied Physics,* **40**, L .638 (2001).

[119] M. B. Yairi, H. V. Demir and D. A. B. Miller, "Optically controlled optical gate with an optoelectronic dual diode structure: theory and experiment," *Journal of Optical and Quantum Electronics,* **33**, 1035-1054 (2001).

[120] H. V. Demir, V. A. Sabnis, O. Fidaner, J. S. H. Jr., D. A. B. Miller and J.-F. Zheng, "Dual-diode quantum-well modulator for C-band wavelength conversion and broadcasting," *Optics Express,* **12**, 310-316 (2004).

[121] I. K. Park, M. K. Kwon, J. O. Kim, S. B. Seo, J. Y. Kim, J. H. Lim, S. J. Park and Y. S. Kim, "Green light-emitting diodes with self-assembled In-rich InGaN quantum dots," *Applied Physics Letters,* **91**, 133105 (2007).

[122] Y. H. Cho, Y. H. Cho, S. K. Lee, H. S. Kwack, J. Y. Kim, K. S. Lim, H. M. Kim, T. W. Kang, S. N. Lee, M. S. Seon, O. H. Nam and Y. J. Park, "Carrier loss and luminescence degradation in green-light-emitting InGaN quantum wells with micron-scale indium clusters," *Applied Physics Letters,* **83**, 2578 (2003).

[123] C. Bayram, F. H. Teherani, D. J. Rogers and M. Razeghi, "A hybrid green light-emitting diode comprised of n-ZnO/(InGaN/GaN) multi-quantum-wells/p-GaN," *Applied Physics Letters,* **93**, 081111 (2008).

[124] S. Nizamoglu and H. V. Demir, "Resonant nonradiative energy transfer in CdSe/ZnS core/shell nanocrystal solids enhances hybrid white light emitting diodes," *Optics Express,* **16**, 13961-13968 (2008).

[125] S. Nizamoglu, E. Sari, J.-H. Baek, I.-H. Lee and H. V. Demir, "Green/yellow solid-state lighting via radiative and non-radiative transfer involving colloidal semiconductor nanocrystals," *IEEE Journal of Special Topics in Quantum Electronics,* **15**, 1163-1170 (2009).

[126] Evident Technologies , http://www.evidenttech.com/products/evidots/evidot-

specifications.html?searched=shelf+lifetime&highlight=ajaxSearch_highlight+ajaxSearch_highlight1+ajaxSearch_highlight2,

[127] S. Nizamoglu, O. Akin and H. V. Demir, "Quantum efficiency enhancement in nanocrystal solids using nanoradiative energy transfer with optimized donor-acceptor ratio for hybrid white light emitting diodes," *Applied Physics Letters*, **94**, 243107 (2009).

[128] D. M. Yeh, C. F. Huang, Y. C. Lu and C. C. Yang, "Making white-light-emitting diodes without phosphors," *SPIE Newsroom 10.1117/2.1200802.1069,* (2008).

[129] D. M. Yeh, C. F. Huang, Y. C. Lu and C. C. Yang, "White-light light-emitting device based on surface plasmon-enhanced CdSe/ZnS nanocrystal wavelength conversion on a blue/green two-color light-emitting diode," *Applied Physics Letters,* **92**, 091112 (2008).

[130] A. R. Clapp, I. L. Medintz and H. Mattoussi, "Förster Resonance Energy Transfer Investigations Using Quantum-Dot Fluorophores," *ChemPhysChem*, **14**, 47–57 (2006).

[131] S. Rohrmoser, J. Baldauf, R. T. Harley, P. G. Lagoudakis, S. Sapra, A. Eychmüller and I. M. Watson, "Temperature dependence of exciton transfer in hybrid quantum well/nanocrystal heterostructures," *Applied Physics Letters,* **91** 092126 (2007).

[132] M. Achermann, M. A. Petruska, D. D. Koleske, M. H. Crawford and V. I. Klimov, "Nanocrystal-based light-emitting diodes utilizing high-efficiency nonradiative energy transfer for color conversion," *Nano Letters*, **6**, 1396-1400 (2006).

[133] M. Şahin and M. Tomak, "Electronic structure of a many-electron spherical quantum dot with an impurity," *Physical Review B,* **72**, 125323 (2005).

[134] N. P. Gaponik, D. V.Talapin and A. L. Rogach, "A Light-Emitting Device Based on a CdTe Nanocrystal/Polyaniline Composite," *Physical Chemistry Chemical Physics*, **1**, 1787-1790 (1999).

[135] M. Sahin, "Photoionization cross section and intersublevel transitions in a one- and two-electron spherical quantum dot with a hydrogenic impurity," *Phyical Review B,* **77**, 045317 (2008).

[136] M. V. Artemyev, A. I. Bibik, L. I. Gurinovich, S. V. Gaponenko and U. Woggon, "Evolution from individual to collective electron states in a dense quantum dot ensemble," *Phyical Review B,* **60**, 1504 (1999).

[137] S. V. Gaponenko, V. N. Bogomolov, E. P. Petrov, A. M. Kapitonov, A. Eychmueller, A. L. Rogach, I. I. Kalosha and U. Woggon, "Spontaneous emission of organic molecules and semiconductor nanocrystals in a photonic crystal," *Journal of Luminescence,* **87-89**, (2000).

[138] S. Nizamoglu and H.V.Demir, "Onion-like (CdSe)ZnS/CdSe/ZnS quantum-dot-quantum-well heteronanocrystals for investigation of multi-color emission," *Optics Express,* **16**, 3515-3526 (2008).

[139] A. P. Alivisatos, W. W. Gu and C. Larabell, "Quantum dots as cellular probes," *Annual Review of Biomedical Engineering*, **7**, 55-76 (2005).

[140] E. Lifshitz, I. Dag, I. Litvin, G. Hodes, S. Gorer, R. Reisfeld, M. Zelner and H. Minti, "Optically Detected Magnetic Resonance Study of Electron/Hole Traps on CdSe Quantum Dot Surfaces," *Chemical Physics Letters,* **288**, 188 (1998).

[141] A. H. Mueller, M. A. Petruska, M. Achermann, D. J. Werder, E. A. Akhadov, D. D. Koleske, M. A. Hoffbauer and V. I. Klimov, "Multicolor Light-Emitting Diodes Based on Semiconductor Nanocrystals Encapsulated in GaN Charge Injection Layers," *Nano Letters,* **5**, 1039 (2005).

[142] V. M. Agranovich, G. C. L. Rocca and F. Bassani, "Efficient electronic energy transfer from a semiconductor quantum well to an organic material," *Letters to Jounal of Experimental and Theoretical Physics,* **66**, 748-751 (1997).

[143] D. Basko, G. C. L. Rocca, F. Bassani and V. M. Agranovich, "Förster energy transfer from a semiconductor quantum well to an organic

material overlayer," *The European Physical Journal B,* **8**, 353-362 (1999).

[144] V. M. Agranovich, D. M. Basko, G. C. L. Rocca and F. Bassani, "New concept for organic LEDs: non-radiative electronic energy transfer from semiconductor quantum well to organic overlayer," *Synthetic Metals,* **116**, 349-351 (2001).

[145] S. Chanyawadee, P. G. Lagoudakis, R. T. Harley, M. D. B. Charlton, D. V. Talapin, H. W. Huang and C. H. Lin, "Increased Color-Conversion Efficiency in Hybrid Light-Emitting Diodes utilizing Non-Radiative Energy Transfer," *Advanced Materials,* **21**, 1 (2009).

[146] V. Ramesh, A. Kikuchi, K. Kishino, M. Funato and Y. Kawakami, "Strain relaxation effect by nanotexturing InGaN/GaN multiple quantum well," *Journal of Applied Physics,* **107**, 114303 (2010).

[147] Z. J. Hong, Z. S. Ming, S. Xian, Z. D. Gang, Z. J. Jun, L. Z. Shun, J. D. Sheng, D. L. Hong, W. Hai, S. Y. Sheng, L. S. Ying and Y. Hui, "Fabrication and Optical Characterization of GaN-Based Nanopillar Light Emitting Diodes," *Chinese Physics Letters,* **25**, 3485 (2008).

[148] L. W. Wang and A. Zunger, "Pseudopotential calculations of nanoscale CdSe quantum dots," *Phyical Review B,* **53**, 9579 (1996).

[149] D. Kim, S. Okahara, M. Nakayama and Y. Shim, "Experimental verification of Förster energy transfer between semiconductor quantum dots," *Physıcal Review B,* **78**, 153301 (2008).

[150] S. Blumentengel, S. Sadofev, C. Xu, J. Puls and F. Henneberger, "Converting Wannier into Frenkel Excitons in an Inorganic/Organic Hybrid Semiconductor Nanostructure," *Physical Review Letters,* **97**, 237401 (2006).

[151] V. M. Agranovich, D. M. Basko, G. C. L. Rocca and F. Bassani, "Excitons and optical nonlinearities in hybrid organic-inorganic nanostructures," *Journal of Physics: Condensed Matter,* **10**, 9369 (1998).

[152] D. M. Basko, V. M. Agranovich, F. Bassani and G. C. L. Rocca, "Energy transfer from a semiconductor quantum dot to an organic matrix," *The European Physical Journal B,* **13**, 653-659 (2000).

[153] H. Sirringhaus, N. Tessler and R. H. Friend, "Integrated Optoelectronic Devices Based on Conjugated Polymers," *Science,* **280**, 1741-1744 (1998).

[154] S.Gaponenko and U. Woggon, "Excitons in Quantum Dots," *Physica Status Solidi (b),* **189**, 286-343 (1995).

[155] M. Anni, L. Manna, R. Cingolani, D. Valerini, A. Cretí and M. Lomascolo, "Förster energy transfer from blue-emitting polymers to colloidal CdSe/ZnS core shell quantum dots," *Applied Physics Letters,* **4169**, 85 (2004).

[156] S. A. Zapunidi and Y. V. K. D. Yu, "Analytical model for photoluminescence quenching via Förster resonant energy transfer in a conjugated polymer doped by energy acceptors," *Physical Review B,* **79**, 205208 (2009).